THERMAL HISTORIES OF CHONDRULES IN SOLAR NEBULA SHOCKS, INCLUDING THE EFFECT OF MOLECULAR LINE COOLING

by

Melissa A. Morris

A Dissertation Presented in Partial Fulfillment
of the Requirements for the Degree
Doctor of Philosophy

ARIZONA STATE UNIVERSITY

August 2009

THERMAL HISTORIES OF CHONDRULES IN SOLAR NEBULA SHOCKS, INCLUDING THE EFFECT OF MOLECULAR LINE COOLING

by

Melissa A. Morris

has been approved

June 2009

Graduate Supervisory Committee:

Steven J. Desch, Chair
Richard Hervig
Thomas Sharp
Francis Timmes
Meenakshi Wadhwa

ACCEPTED BY THE GRADUATE COLLEGE

ABSTRACT

Chondrules are millimeter-sized, silicate (mostly ferromagnesian) igneous spheres found within chondritic meteorites. They are some of the oldest materials in our Solar System, having formed within a few million years of its birth. Chondrules were melted at high temperature (over 1800 K), while they were free-floating objects in the early solar nebula. Their petrology and chemistry constrain their formation, especially their thermal histories. Chondrules provide some of the most powerful constraints on conditions in the solar nebula. Models in which chondrule precursors melted by passage through solar nebula shocks are very promising, and meet most constraints on chondrule formation in broad brush. However, these models have been lacking in some of the relevant physics. Previous shock models have used incorrect approximations to the input radiation boundary condition, and the opacity of solids has been treated simply. Most important, a proper treatment of cooling due to molecular line emission has not been included. In this thesis, the shock model is significantly improved. The appropriate boundary condition for the input radiation and the proper method for calculation of the opacity of solids are determined. Additionally, a complete treatment of molecular line cooling due to water is included. Previous estimates of the effect of line cooling predicted chondrule cooling rates in excess of 10,000 K per hour. However, once molecular line cooling due to water was incorporated into the full shock model, it was found that line cooling has very little effect (typically, a difference of less than 10 K) on the thermal histories of gas and chondrules. This behavior is attributed mostly to the thermal buffering of the gas due to hydrogen dissociation and recombination, which tends to keep the gas temperature at approximately 2000 K until the column densities of water become optically thick to line emission. Chondrule cooling rates in the range of 10 - 1000 K per hr are predicted, consistent with observations.

For my mom, who I still miss every day, and for my dad, who taught all of us we could do anything we set our minds to, as long as we worked hard enough.

ACKNOWLEDGMENTS

I would like to thank all the members of my committee for their guidance, support, and patience. Thanks to Rick Hervig and Frank Timmes for stepping in when needed. Thanks to Mini Wadhwa and Tom Sharp, who have been there from the beginning. I would especially like to acknowledge the support, both financial and otherwise, of my advisor, Steve Desch, without whom this research would not have been possible. Particular thanks are extended to Frank Timmes for lending a hand during the summer of 2008. Thanks to Mike Lesniak for helping me out with my code when I was ready to pull my hair out, even if it meant simply looking over my shoulder while I found the problem. Thanks to Simon Porter for helpful computing suggestions. I would also like to thank the many good friends who provided encouragement and the occasional, but necessary, diversion (you know who you are...Jo, Brian, Rolf, Jason, Kevin...). Thanks to John and Dusty (Jo's mum and dad) for "adopting" me and making me feel *especially* special. Last, but not least, I would like to thank my son, Chase, for his unfailing support, and my daughter, Brooke, for never failing to make me laugh.

This work was supported by NASA Origins of Solar Systems grant NNG06GI65G.

TABLE OF CONTENTS

Page

Page

Page

LIST OF TABLES

LIST OF FIGURES

Figure Page

Figure Page

CHAPTER 1

INTRODUCTION

The parent bodies of the most primitive meteorites, the chondrites, $\sim$ 4.57 billion years ago (Wadhwa & Russell 2000). Bulk composition analyses of chondrites show that they closely approximate the composition of the Sun's photosphere, excluding the most volatile elements (Anders & Grevesse 1989; Lodders 2003; Palme & Jones 2005). This suggests that chondrites formed from the same material as the Sun, dating to the origin of our Solar System. Chondrites are generally categorized into five classes: Ordinary, Carbonaceous, Enstatite, Rumuruti, and Kakangari, based on their mineralogical and petrographic characteristics, as well as their whole-rock chemical and oxygen-isotopic compositions, and are sub-divided into various groups (Weisberg et al. 2006). Unequilibrated chondrites are the most primitive meteorites in our collection, in that they have suffered very little alteration since their formation, and therefore contain information about the conditions that existed in the early solar nebula. Chondrites are remarkable for containing calcium-rich, aluminum-rich inclusions (CAIs), the oldest solids in the Solar System, whose formation has been dated to between 4567 Ma (Amelin et al. 2002, 2006; Jacobsen et al. 2008; Connelly et al. 2008) and 4569 Ma (Bouvier et al. 2007; Burkhardt et al. 2008; Bouvier & Wadhwa 2009). Also found in abundance within all chondrites (except for CI carbonaceous chondrites) are sub-millimeter- to millimeter-sized, (mostly ferromagnesian) igneous spheres, called chondrules, from which the chondrites derive their name.

Chondrules formed, at most, $\sim$ 2-3 million years after CAIs (Amelin et al. 2002; Kita et al. 2005; Russell et al. 2006; Wadhwa et al. 2007; Connelly et al. 2008), as melt droplets that were heated to high temperatures while they were independent, free-floating objects in the early solar nebula (Lauretta et al. 2006). After they were heated, cooled, and crystallized, chondrules were incorporated into the parent bodies from which chondrites originate. Chondrules are capable of providing incredibly detailed information about conditions in the Solar System protoplanetary disk, if the process that led to their heating, melting and recrystallization could be understood (Lauretta et al. 2006). Chondrules make up to 80% of the volume of ordinary chondrites (Grossman 1988; Ciesla 2005; Lauretta et al. 2006), and it is estimated that $\sim 10^{24}$ g of chondrules exist in the

asteroid belt today (Levy 1988). Such a prevalence of chondrules suggests that chondrule-forming events were widespread in the solar nebula. A process that can melt 10^{24} g of rock is surely a dominant process in the solar nebula disk.

1. Chondrules and the Constraints on their Formation

Recall that there are five general classes of chondritic meteorites based on petrology and chemical composition: Ordinary, Carbonaceous, Enstatite, Rumaruti, and Kakangari (Brearley & Jones 1998). Chondrules are found in all but type CI carbonaceous chondrites, which may lack chondrules due to major alteration by water (Weisberg et al. 2006). Chondrules are sub-millimeter to millimeter in size, with the majority close to one millimeter in diameter (Grossman 1988; Ciesla 2005) and are classified based on their bulk density, mineralogy, and textural types.

1.1. *Chemistry of Chondrules*

Fe-, Mg-rich chondrules contain phases rich in FeO and MgO. They are found in all classes of chondrites and are the most abundant type of chondrules. The bulk composition of Fe-, Mg-rich chondrules is similar to CI chondrites, with respect to refractory and moderately volatile elements (Grossman et al. 1988; Hewins 1991; Connolly et al. 2001). These types of chondrules are usually designated either FeO-poor (Type I) or FeO-rich (Type II). Type I chondrules have < 10 wt % bulk FeO content and are metal-rich (Rubin et al. 1999). Type II chondrules have > 10 wt % bulk FeO content and are metal-poor, with Fe, Ni-metal in proportions up to ~ 30 vol % (Connolly et al. 2001). Subdivision within Type I and Type II chondrules depends on the abundance of olivine and low-Ca pyroxene. Type A chondrules have < 10 % low-Ca pyroxene and Type B chondrules have < 10 % olivine, with Type AB possessing intermediate amounts of both low-Ca pyroxene and olivine.

Al-rich chondrules are the second most abundant class of chondrule and are found in almost all types of chondrites (Connolly & Desch 2004). As defined by Bischoff & Keil (1984), Al-rich

chondrules are those with bulk $Al_2O_3 > 10$ wt % (up to 28 wt %) for ordinary chondrites and > 12 wt % (up to 29 wt %) for Kakangari. Sizes of Al-rich chondrules range between 50 to 1300 μm, with many different textural types observed. Other types of chondrules include chromite-rich, silica-bearing, fassaite-rich (Grossman et al. 1988; Brearley & Jones 1998; Zanda et al. 2004), and the unique chondrules found within type CH chondrites (Krot et al. 2000, 2002). No experimental constraints exist for the thermal histories of these other types of chondrules, therefore less is known about their formation conditions (Connolly & Desch 2004).

1.2. *Textures of Chondrules*

Porphyritic textured chondrules (those with large crystals, or phenocrysts, set in a matrix of smaller-grained material) make up $\sim$ 85 % of all chondrules in ordinary chondrites (Gooding & Keil 1981). Porphyritic textures include porphyritic olivine (PO) and porphyritic olivine-pyroxene (POP). Non-porphyritic chondrules make up the remaining $\sim$ 15 % of chondrules found in ordinary chondrites. The non-porphyritic chondrules are divided into subtypes: glass (G), cryptocrystalline (CC), radial pyroxene or olivine (RP and RO), radial pyroxene-olivine (RPO), and barred olivine or pyroxene (BO and BP) (Gooding & Keil 1981).

The textures and chemistry of chondrules can constrain their thermal histories, melt evolution, and precursor materials (Connolly et al. 2006). Experimental petrology determines the heating and cooling rates of chondrules by defining the constraints on crystal growth and evolution of the bulk composition during melting and cooling. Experimental petrology has shown that the most important determinants of texture during chondrule formation are peak temperature, cooling rates, and the presence of external seed nuclei. Cooling rates are constrained by texture, major and minor element abundances, and bulk chemistry (Connolly & Desch 2004; Connolly et al. 2006; Lauretta et al. 2006). Peak temperature is constrained by the number of nuclei remaining in the melt and/or the number of nuclei encountered as external seed nuclei (Lofgren 1983, 1989, 1996; Hewins & Connolly 1996; Hewins 1997; Connolly et al. 1998; Desch & Connolly 2002; Lauretta et al. 2006).

1.3. *Thermal Histories of Chondrules*

Thermal Histories of Fe-, Mg-rich Chondrules. According to furnace experiments, in which melt droplets with chondrule compositions are allowed to cool and crystallize, reproduction of chondrule textures requires specific ranges of cooling rates (see below) between the liquidus temperature ($\approx$ 1800 K) and solidus temperature ($\approx$ 1400 K; Hewins & Connolly 1996). The majority of chondrules experienced peak temperatures in the range of 1770 - 2120 K for several seconds to minutes (Lofgren and Lanier 1990; Radomsky and Hewins 1990; Hewins and Connolly 1996; Lofgren 1996; Hewins 1997; Connolly and Love 1998; Jones et al. 2000; Connolly and Desch 2004; Hewins et al. 2005; Ciesla 2005; Connolly et al. 2006; Lauretta et al 2006), although the peak temperatures of BO chondrules may have been as much as 2200 K (Connolly et al. 1998; Connolly et al. 2006). Chondrule textures (the arrangement and shape of their crystals) and the elemental zoning behavior within individual crystals constrain the cooling rates of chondrules (Connolly & Hewins 1991; Jones & Lofgren 1993; DeHart & Lofgren 1996; Desch & Connolly 2002; Connolly et al. 2006; Lauretta et al. 2006). Based on texture and chemistry, chondrules experienced cooling rates of 10 - 3000 K hr^{-1}, with most cooling at $\sim$ 100 K hr^{-1} or less through their crystallization range (Desch & Connolly 2002; Hewins et al. 2005; Connolly et al. 2006; Lauretta et al. 2006). Miyamoto et al. (2009) recently developed a model to calculate cooling rates using the Fe-Mg chemical zoning profiles of olivine. They found that for the type II porphorytic olivine chondrules in Semarkona, the cooling rates through crystallization temperatures are broadly consistent with furnace experiments (10 - 1000 K hr$-$1). Initial cooling above the liquidus was at least 5000 K hr^{-1} (Yu et al. 1996; Yu & Hewins 1998; Desch & Connolly 2002). Porphyritic chondrules cooled at about $10 - 10^3\,\mathrm{K\,hr}^{-1}$, and barred-olivine chondrules cooled at about $10^3\,\mathrm{K\,hr}^{-1}$ (Hewins et al. 2005; see also Desch & Connolly 2002). Additionally, chondrules retain volatile elements such as S, indicating that they did not remain above the liquidus for more than minutes, and cooled quite rapidly ($\gtrsim 10^4\,\mathrm{K\,hr}^{-1}$ while above the liquidus (Yu & Hewins 1998)). The presence of primary S tells us that chondrules did not experience prolonged heating between $\sim$ 650 - 1200K for more than

several minutes (Hewins et al. 1996; Connolly and Love 1998; Jones et al, 2000; Lauretta et al. 2001; Tachibana & Huss 2005; Connolly et al. 2006). Finally, there is no indication of the isotopic fractionation that would arise from the free evaporation of alkalis such as Na, which constrains the time spent at high temperature before melting (Tachibana et al. 2004). Modeling of isotopic fractionation has shown that chondrules must heat up from 1300 to 1600 K in times on the order of minutes or less in order to prevent isotopic fractionation of S (Tachibana & Huss 2005). The only alternative to such rapid heating is if the ambient nebular gas was enriched in volatile or moderately volatile elements (Connolly et al. 2006).

The time spent at the peak temperature also affects the amount of relict material that remains intact (Lofgren 1996; Connolly and Desch 2004; Hewins et al. 2005; Connolly et al. 2006; Lauretta et al. 2006). Approximately 15% of chondrules in ordinary chondrites contain relict grains (Jones 1996), the presence of which limits the duration of heating above the liquidus to tens of seconds to several minutes (Connolly et al. 2006). The texture and chemistry of these relict grains indicates that they are previous generations of chondrules, signifying that chondrules experienced multiple heating events (Jones et al. 2005; Connolly et al. 2006; Lauretta et al. 2006). Evidence for multiple heating events is also found by the presence of fine-grained, igneous rims around some chondrules; a layer of material that was heated and melted in an event that post-dated melting of the host chondrule (Hewins et al. 1996, Jones et al. 2005).

Thermal Histories of Al-rich Chondrules. Thermal histories of Al-rich chondrules are poorly understood, although Sheng (1992) and Sheng et al. (1992) present approximations for cooling rates for a class of Al-rich chondrules known as plagioclase-olivine inclusions, or POIs, when the maximum temperature achieved was $\sim$ 1800 K. It has been speculated that the formation history of Al-rich chondrules is similar to Fe-, Mg-rich chondrules (Connolly & Desch 2004).

1.4. *Additional Constraints on Chondrule Formation*

The combination of chondrules and the fine-grain matrix in chondritic meteorites results in a solar bulk composition, suggesting that the chondrules and matrix formed in the same vicinity

within the solar nebula (Palme et al. 1993; Klerner & Palme 2000; Scott & Krott 2005; Ebel et al. 2008; Hezel & Palme 2008), and must be considered as an additional constraint on chondrule formation models. Klerner & Palme (2000) found a sub-chondritic value for the Ti/Al ratio in the matrix of the CR chondrite, Renazzo, while the Ti/Al ratio in the chondrules are supra-chondritic. The same complementarity values for Ti/Al are found in Al Rais and the CV meteorites Kaba, Leoville, Mokoia, and Vigarano (Klerner & Palme 2000). Additionally, the Mg/Si ratio in Renazzo matrix was found to be sub-chondritic, while the ratio in the chondrules are supra-chondritic (Ebel et al. 2008). Hezel & Palme (2008) analyzed the Ca/Al ratios in the matrix and chondrules of Allende and Y-86751. These two CV meteorites are almost identical in bulk composition and structure. Hezel & Palme found the Ca/Al ratio in the matrix of Allende to be sub-chondritic and the ratio in the matrix to be super-chondritic. Yet the opposite is found for Y-86751. Hezel & Palme interpret this as ruling out redistribution of Ca during parent body alteration, and therefore is indicative of a difference in conditions during formation.

The frequency of compound chondrules, two or more chondrules that are fused together, allows an estimate of the density of chondrules during formation (Gooding & Keil 1981; Wasson et al. 1995; Hood & Kring 1996; Ciesla et al. 2004a; Ciesla 2005; Yasuda & Nakamoto 2008) and in some cases (enveloping compound chondrules) argues for multiple heating events (Wasson et al. 1995; Jones et al. 2005). Chondrule densities of ~ 10 m^{-3} over regions of $\sim 10^3$ km are needed in order to prevent the isotopic fractionation of volatiles during melting (Cuzzi & Alexander 2006). Additionally, the retention of volatiles, such as Na, places lower limits on chondrule density (Cuzzi & Alexander 2006; Fedkin et al. 2006; Alexander et. al. 2008, Kropf & Pack 2008). Lack of Rayleigh isotopic fractionation among major elements constrains the pressure in chondrule-forming regions to $\gtrsim 10^{-3}$ bar (Alexander 2004), Alternatively, this lack of fractionation may occur because chondrules come into equilibrium with gas evaporated from other chondrules, which would constrain the minimum concentration of chondrule precursors (Cuzzi & Alexander 2006). In addition, Cuzzi & Alexander (2006) found that to satisfy the constraints on isotopic fractionation

TABLE 1
Observational Constraints for Chondrule Formation Models - Essential Constraints for which a Model Must Account

Constraint	Supporting Observations
Widespread and efficient	high chondrule abundances
Nebular timescales only	isotopic dating
Low ambient temperature	presence of volatiles
Short heating time (minutes)	retention of volatiles
	preservation of relict grains
	experimental reproduction of textures
	lack of isotopic fractionation of S
Peak temperatures $\sim$ 2000 K	experimental reproduction of textures
Short cooling time (hours)	experimental reproduction of textures
	zoning in minerals
	presence of glass
Multiple episodes; recycling	relict grains
	compound chondrules
	igneous rims
Magnetic field	remanent magnetization
Size sorting	restricted size range in each chondrite group
Presence of dust that escapes heating	fine-grained rims

of major elements, the chondrule-forming region must be at least 150 - 6000 km in scale. The range in sizes of chondrules must also be addressed by formation models, as well as the partial pressure of elements, such as oxygen and the total pressure chondrules experienced (Connolly & Desch 2004).

Finally, under the assumption that ^{26}Al was homogeneous in the early Solar System, there is an apparent age gap between CAI and chondrule formation based on initial values of ^{26}Al/^{27}Al (Russell et al. 1997; Galy et al. 2000; Tachibana et al. 2003; Bizzarro et al. 2004; Russell et al. 2007). These same data suggest timescales for chondrule formation of several Myr (Huss et al. 2001; Tachibana et al. 2003; Wadhwa et al. 2007; Rudraswami et al. 2008; Hutcheon et al. 2009), as do Pb-Pb ages (Amelin et al. 2002; Kita et al. 2005; Russell et al. 2006; Connelly et al. 2008).

The majority of observational constraints for formation models of chondrules are summarized in Tables 1 and 2, which we have adapted from Table 1 of Jones et al. (2000).

TABLE 2
Observational Constraints for Chondrule Formation Models - Constraints less Widely Accepted by Meteoriticists

Constraint	Supporting Observations
Chondrule formation $\sim$ 2 Myr after CAI formation	short-lived radioisotope data Pb-Pb dating
Elevated gas pressure	stability of molten chondrule
Variable nebular oxidation states	variable oxidation states of chondrules

2. Chondrule Formation Models

The chondrule formation process, despite its obvious importance, has been a mystery in the field of meteoritics for two centuries, since the recognition that chondrules are igneous, " like drops of fiery rain" (Sorby 1877). Proposed mechanisms include interaction with the early active Sun, through jets (Liffman & Brown 1995; Liffman & Brown 1996) or solar flares (Shu et al. 1996, 1997, 2001), melting by lightning (Pilipp et al. 1998; Desch & Cuzzi 2000), and melting by planetesimal impacts (Urey & Craig 1953; Urey 1967; Sanders 1996; Lugmair & Shukolyukov 2001). The most widely-accepted hypothesis, though, is that chondrules were melted in shock waves in the protoplanetary disk (Hewins 1997; Jones et al. 2000; Connolly & Desch 2004; Connolly et al. 2006).

2.1. *Lightning*

The proposal that chondrules were melted by lightning in the asteroidal region of the solar nebula has been debated for some time (Cameron 1966; Whipple 1966; Morfill et al. 1993; Love et al. 1995; Horanyi et al. 1995; Horanyi & Robertson 1996; Pilipp et al. 1998; Gibbard et al. 1997; Desch & Cuzzi 2001; Güttler et al. 2008). In this model, gas turbulence, gas convection, and/or vertical solar gravity produces size-segregated motions of chondrule precursors, which are then assumed to transfer charge in a manner similar to how ice particles in terrestrial thunderstorms do. On Earth, the continuing rainout of positively charged hailstones leads to large-scale separation of

charge and an increasing vertical electric field. When the field reaches a critical value ($\sim 10^5$ V m^{-1}), the resistance of the air breaks down and current flows, in the form of a lightning bolt, to cancel the charge separation (Jones et al. 2000; Desch & Cuzzi 2001).

The nebular lightning model of chondrule formation has support in the form of widespread observations of lightning in volcanic plumes and dust storms, as well as in the atmospheres of the outer planets (Desch et al. 2002, and references therein). Additionally, lightning discharges have been observed at high altitude on Earth (Sentman et al. 1995), where the pressure is $\sim 10^{-5}$ bar, analogous to the pressure in the solar nebula (Bell et al. 1997).

The nebular lightning model of Morfill et al. (1993) resulted in discharges lasting $\sim$ 100 s, consistent with the peak heating times of chondrules. The spatial scale of discharges may have been large enough to produce chondrule cooling rates (Jones et al. 2000). However, Gibbard et al. (1997) pointed out that the electrical conductivity in the nebula may have been too high, effectively preventing discharges. Additionally, the energy flux may have been too small to melt silicates (Love et al. 1995). Desch & Cuzzi (2002) presented a model which would eliminate most of the problems with previous lightning models. Their model results in very large charges on particles and very high concentrations of those particles, leading to higher particle velocities. The greater velocities, combined with the large charges on the particles, result in very energetic bolts (Desch & Cuzzi 2002). However, the electrical discharge experiments of Güttler et al. (2008) found chondrule formation by lightning unlikely, at best. In most of their experimental results, dust aggregates exploded, rather than melting (Güttler et al. 2008). Additionally, the small scales over which lightning is expected to operate would seemingly result in cooling rates that are too rapid to meet constraints on the thermal history of chondrules (Desch 2000). A better understanding of the electrical properties of the solar nebula, as well as terrestrial lightning, and further modeling is necessary to demonstrate that lightning is a viable source of the transient heating events that formed chondrules (Jones et al. 2000).

2.2. *Interaction of Planetary Bodies*

Planetary settings for the formation of chondrules include magmatic processes (Brezina 1885; Wahl 1911; Roy 1957; Chen et al. 1998; Lugmair & Shukolyukov 2001), ejection by volcanoes (Merrill 1920), and collisions between planetary bodies (Urey & Craig 1953; Urey 1967; Sanders 1996; Symes et al. 1997). The arguments against chondrule formation in a planetary setting have been summarized by many authors (Taylor et al. 1983; Boss 1996; Hewins 1997; Jones et al. 2000; Ciesla 2005), most especially Taylor et al. (1983) and Boss (1996). These arguments include the observation that chondrules are very different from known volcanic and impact deposits that are found on Earth, the Moon, and in meteorites (Taylor et al. 1983). Taylor et al. (1983) also cite the small abundance of agglutinates in chondrites, absence of hypervelocity impact pits on chondrules, the presence of chondrule rims, the diversity of chondrule compositions, oxygen isotopic heterogeneities, unfractionated bulk silicate compositions, and the narrow size distribution of chondrules, as arguments against formation of chondrules in a planetary setting. The high abundance of chondrules indicates an extremely efficient mechanism, difficult to reconcile with formation by impacts (Taylor et al. 1983; Boss 1996; Keil et al. 1997; Hewins 1997; Ciesla 2005). Impacts are also likely to fracture material, rather than melt it (Ciesla 2005) and are inconsistent with multiple heating events (Taylor et al. 1983; Jones et al. 2000; Ciesla 2005). If formed through impacts, one would also expect a wider range in chondrule ages (Taylor et al. 1983; Ciesla 2005). However, the main problem with identifying a planetary setting with chondrule formation is the lack of any quantitative model which calculates the thermal histories of chondrules (Taylor et al. 1983; Grossman 1988; Hewins et al. 1996; Connolly & Desch 2004; Ciesla 2005; Connolly et al. 2006).

2.3. *Interaction of Chondrule Precursors with the Early Active Sun*

Many have suggested that chondrule formation occurred as a result of interaction with the early active Sun (Grossman 1988; Hewins et al. 1996), such as byproducts of bipolar outflows (Liffman & Brown 1995; Liffman & Brown 1996; Liffman 2009) or solar flares (Shu et al. 1996,

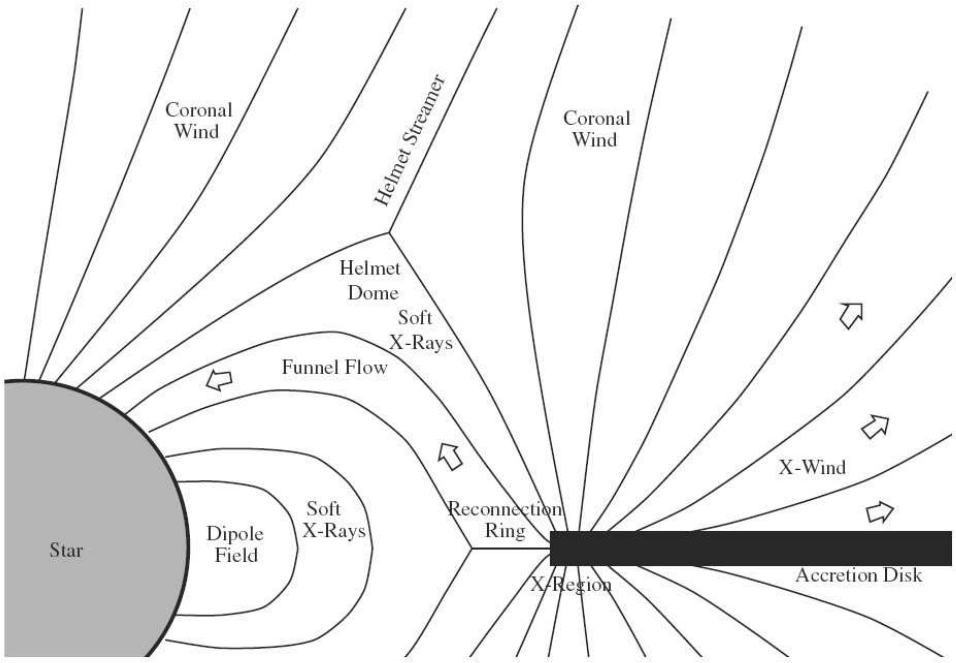

FIG. 1 — Cartoon drawing of the X-wind model. Figure from Shu et al. (2000).

1997, 2001). A major point in favor of these proposed formation mechanisms are the observations of these phenomena in young stars. The models of Liffman & Brown (1995, 1996), in which chondrules are produced by ablation from larger bodies entrained in outflows, predict cooling rates (a few thousand K hr^{-1}) that are considered too fast to produce porphyritic textures in chondrules (Connolly et al. 2006). Additionally, these models do not address multiple heating events or the total pressure or partial pressure of different elements during chondrule formation (Connolly et al. 2006).

X-wind. One proposed mechanism for chondrule formation involving interaction with the early active Sun that has received considerable attention is the X-wind model of Shu et al. (1996, 1997, 2001). The X-wind model of Shu et al. (1996, 1997, 2001) proposes that chondrule precursors located at $\sim$ 0.06 AU are lofted above the midplane of the disk by a magnetocentrifugally driven wind, where they are either irradiated and melted by energetic flares or optical photons from the early Sun (Figure 1). The newly formed chondrules are then transported via bipolar outflows to 2.5 AU (where chondritic parent bodies are believed to originate) and combined with local dust to form

the chondritic parent bodies. Theories of star formation indicate that a bipolar outflow is present in two of five stages of formation. During one of these stages, the central star is still embedded within an infalling envelope of gas and dust. During the other, later stage, the outflowing wind has reversed the flow of material, revealing the central star and surrounding accretion disk. The X-wind model proposes that CAIs were formed during the embedded stage and that chondrules were formed during both the embedded and revealed stages (Shu et al. 1996).

The presence of chondrules and the fine-grained matrix in chondritic meteorites, together, results in a solar bulk composition. This naturally suggests that the chondrules and matrix formed in the same vicinity within the solar nebula (Palme et al. 1993). The X-wind model does not explain this chondrule/matrix complementarity. In fact, the model would seem to argue against it. Micron-sized dust particles launched out of the midplane of the disk at $\sim$ 0.06 AU, would most certainly escape the planetary system, failing to follow the chondrules out to the asteroid belt at 2-3 AU. It seems incongruous that chondrules formed at $\sim$ 0.06 AU would be complementary to dust formed locally at 2-3 AU, resulting in a solar bulk composition, especially given the variations in composition among chondrites.

In the X-wind model, chondrule formation is attributed to x-ray flares from the young Sun. Although no detailed model (despite the substantial amount of literature on statistics of protostellar x-ray flares) has been developed to predict the thermal histories of chondrules in the context of the X-wind model, Jones et al. (2000) made some rough estimates of peak temperatures and cooling rates of chondrules melted by x-ray flares. The model provides for rapid melting of chondrules (tens of minutes) followed by cooling from peak temperatures over a period of days. This extended cooling period, with temperatures in excess of 1000 K, contradicts the evidence for partial retention of the volatile, Na, and is too slow to reproduce the textures observed in chondrules.

Additionally, the X-wind model provides no explanation for the evidence of multiple heating events experienced by many chondrules. In other words, the model does not demonstrate how chondrules heated near the Sun are flung out to 2-3 AU, then transported back to $\sim$ 0.06 AU to

be melted yet again.

2.4. *Nebular Shocks*

As noted previously, the dominant model of chondrule formation is that chondrules were melted in shock waves in the protoplanetary disk (Hewins 1997; Jones et al. 2000; Connolly & Desch 2004; Connolly et al. 2006). A shock wave, or shock front, is a sharp discontinuity between supersonic and subsonic gas, over an area only a few molecular mean free paths thick, typically only meters in the solar nebula. The gas is slowed, compressed, and heated by the time it reaches the other side of the shock front. Solids moving with the gas are heated not only by thermal exchange upon entering the shocked region, but also by friction as they are slowed to the post-shock gas speed, and by absorbing the infrared radiation emitted by other solids. The shock model of chondrule formation appears able to resolve the chondrule formation mystery, because it makes several detailed predictions about chondrule formation that are largely borne out by observation and experimentation, especially regarding chondrule thermal histories.

Passage through nebular shocks satisfies nearly all the experimental constraints on chondrule formation (Iida et al. 2001, hereafter INSN; Desch & Connolly 2002, hereafter DC02; Ciesla & Hood 2002, hereafter CH02; Desch et al. 2005; Connolly et al. 2006; Krot et al. 2009). Prior to passage through the shock front, chondrules are moderately heated by absorbing radiation emitted by chondrules which have already passed through the shock front. Upon passage through the shock front, the gas is immediately slowed, and compressed and heated, but the chondrules continue at supersonic speeds through the gas. They achieve their peak heating during this stage, due to absorption of radiation, thermal exchange with the gas, and especially supersonic frictional drag heating. This stage lasts until the chondrules slow to the gas velocity, which takes an aerodynamic stopping time, $t_{\rm stop} = \rho_{\rm p} a_{\rm p} / \rho_{\rm g} C_{\rm s} \sim 1$ minute (where $\rho_{\rm p}$ and $a_{\rm p}$ are the particle density and radius, and $\rho_{\rm g}$ and $C_{\rm s}$ are the post-shock gas density and sound speed). At this time, the gas and chondrules are dynamically coupled and chondrules are heated only by absorption of radiation and thermal exchange with the gas. Soon thereafter the solids and gas become thermally coupled as well, and

both components achieve similar temperatures. Although the chondrules pass through the first 100 km of the post-shock region more rapidly than the gas, once they do, they will thermally equilibrate to the gas temperature. Once this happens, the gas and chondrules cool together as fast as they can either radiate away energy or leave the source of infrared radiation that heats them.

Most of the constraints on chondrule formation have been met by nebular shock wave models. Shock waves produce the flash heating necessary for peak temperatures above the liquidus, while still allowing for the retention of volatiles and lack of isotopic fractionation. They are large in scale, leading to cooling rates consistent with observational constraints. Shock heating naturally results in the mixing of chondrules with local dust. (The dust either was in the vicinity and escaped heating, or recondensed from vapor after the shock, but before chondrite formation). Shock waves in the disk can occur more than once. Thermal histories, multiple heating events, retention of volatiles, and the complementarity of chondrules and matrix have all been addressed satisfactorily by shock models. Even so, objections to the model exist because there is no direct observational evidence for shocks in young stellar systems. However, many sources for nebular shocks have been proposed.

3. Shock Mechanisms

3.1. *Planetesimal Bow Shocks*

One possible source of shocks is a planetesimal in an eccentric orbit while gas is still present in the disk (Hood 1998; Weidenschilling 1998; Ciesla 2004; Nelson & Ruffert 2005; Hood et al. 2005; Hood et al. 2009). In this scenario, the gas and dust at 2.5 AU (including chondrule precursors) orbit the central star at the Keplerian velocity, $v_K = 20$ km s^{-1}. When at perihelion, the planetesimal orbits faster than the gas, with a relative velocity between the planetesimal and the gas of $\sim e\, v_K$, where e is the eccentricity of the planetesimal's orbit. Planetesimals in resonance with a proto-Jupiter can have eccentricities as high as $e \sim 0.3$ - 0.5 (Weidenschilling 1998; Marzari & Weidenschilling 2003; Hood et al. 2005; Hood et al. 2009). This results in a relative velocity of ~ 8 km s^{-1}, creating a bow shock around the planetesimal (Figure 2). Any solids in the region of

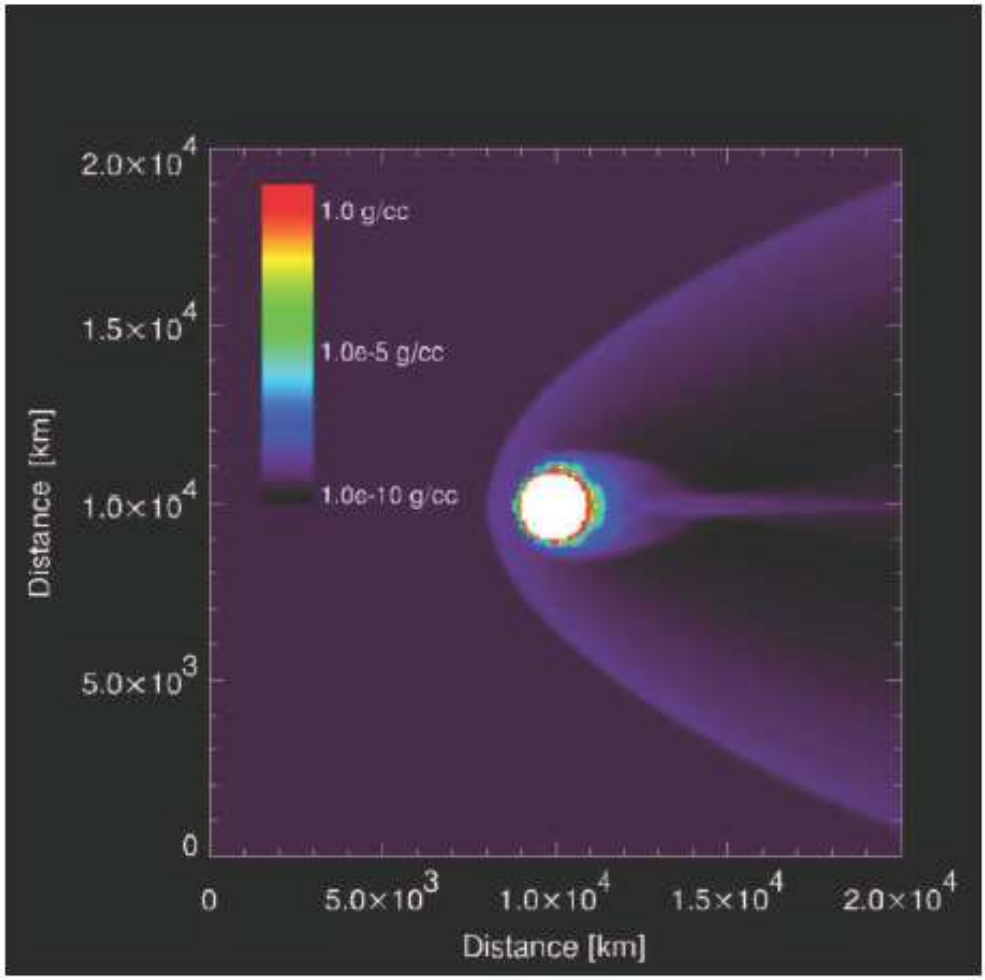

FIG. 2 —Simulation of gas flow around a 1000 km diameter planetesimal moving at a velocity of 8 km s^{-1} relative to nebular gas with an upstream density of 10^{-9} g cm^{-3} and temperature of 400 K. Figure from Ciesla et al. (2004b).

the bow shock will be heated.

The most important consideration regarding shocks created by planetesimal bow shocks is the scale of the region affected (Desch et al. 2005). The size of the bow shock will be comparable to the size of the planetesimal ($\lesssim 10^3$ km), which places constraints on the fraction of the nebula affected (Hood et al. 2005) and how long any entrained solids are heated (Ciesla et al. 2004b). Ciesla et al. (2004) have shown that solids pass through a bow shock in $\sim$ three minutes, resulting in cooling rates $> 10^3$ K hr^{-1}, inconsistent with the thermal histories of chondrules.

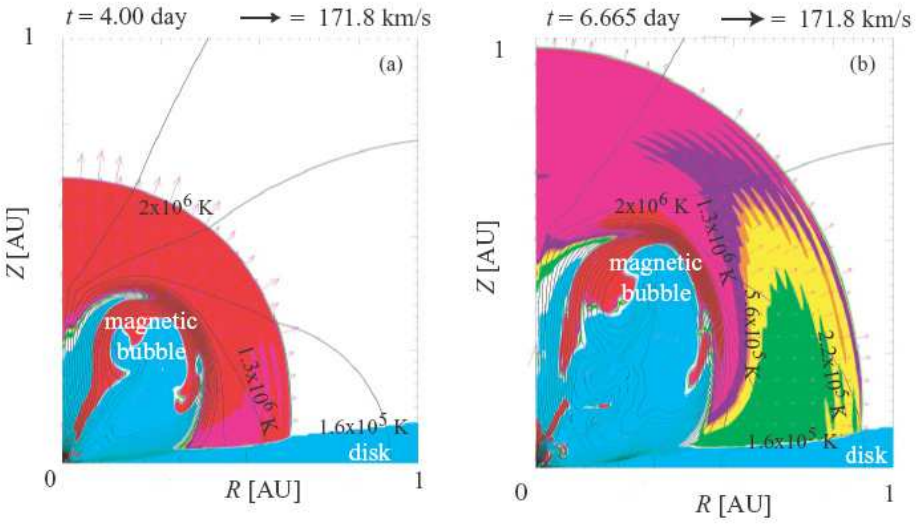

FIG. 3 — Results of MHD simulations of an X-ray flare event by Nakamoto et al. (2005). Global view of the temperature (gray contour), magnetic field lines (solid curves), and the velocity distribution (arrows) at (a) t = 4.00 days and (b) t = 6.665 days, respectively, after an X-ray flare event. The X-ray luminosity of the X-ray flare is about 10^{25} W, which is close to the maximum value of the observed X-ray flares in T Tauri stars. The major part of the momentum flows upward, and a small fraction of it flows toward the disk, which generates shock waves in the disk. Figure from Nakamoto et al. (2005).

3.2. *X-ray Flares*

Observations show T Tauri stars exhibit strong X-ray emission due to flares from the young star (Feigelson & Montemerle 1999), many with energies of $\sim 10^{36}$ erg (Feigelson et al. 2002). Although most of the energy from X-ray flares is directed perpendicular to the disk, modeling has shown that some fraction of energy is carried by gas directed toward the disk (Figure 3; Nakamoto et al. 2005). Shocks can be induced by collisions between this gas, which has been accelerated by X-ray flares, and the disk gas (Nakamoto et al. 2005). Shocks triggered by X-ray flares are expected to have velocities tens of km s^{-1}, with densities on the order of 10^{-10} g cm^{-3} (Nakamoto et al. 2005). Large energy flares, such as those observed in T Tauri stars, usually dissipate within a few Myr, and may be the source of heating of solids early in the history of forming systems. However, X-ray flares probably only affect material high above the midplane of the disk, where micron-sized dust may be heated, but chondrule precursors are not likely to exist, due to settling to the midplane.

3.3. *Gravitational Instability*

It has been suggested that shocks due to gravitational disk instabilities may be responsible for chondrule formation (Boss 2001; Boss & Durisen 2005; Boley & Durisen 2008). When a disk's self-gravity exceeds the vertical gravity due to the central star, bars or spiral arm patterns form (Figure 4). These instabilities occur if the Toomre parameter, $Q = c_{\rm s}\Omega_{\rm K}/(\pi G\Sigma) \lesssim 1$, where $c_{\rm s}$ is the sound speed, $\Omega_{\rm K}$ is the orbital frequency, and Σ is the column density of gas at that location. These bar and spiral patterns arising from disk instability can spontaneously form in massive disks, and almost certainly occurred in the early solar nebula (Gammie 1996). In fact, Desch [2007] has argued for a minimum mass solar nebula ten times that of Hayashi [1981]. (Alternatively, Boley & Durisen (2008) found that mass can build up in dead zones, leading to gravitational instabilities in otherwise low-mass disks). The gas densities within these bar and spiral regions are higher by an order of magnitude than the rest of the disk and move at speeds that are a fraction of the Keplerian velocity. When gas orbiting the disk at the Keplerian velocity collides with these high-density, slow-moving regions, a shock results (Boss & Durisen 2005; Boley et al. 2005; Boley & Durisen 2008). Models including median accretion rates for T Tauri stars ($\sim 10^{-8}\ M_{\odot}\ {\rm yr}^{-1}$; Gullbring et al. 1998) and a turbulence parameter, $\alpha = 10^{-4}$, show that $Q \lesssim 1$ beyond 5 AU (Bell et al. 1997), likely for millions of years. Shocks due to gravitational instabilities propagate through the entire disk (right down to the protostar) and will be driven into the asteroid belt midplane (Boss 2001), where the gas density is $\sim 10^{-9}$ g cm^{-3} (Bell et al. 1997). At 2-3 AU, shock speeds of $\sim$ 6-10 km s^{-1} are predicted (Boss & Durisen 2005). In the simulations of Boley et al. (2005), chondrule-forming shocks (judged by the results of DC02) occurred between 1.5 and 2.5 AU for perturbations at $\sim$ 5 AU. The chondrule-forming nature of these shocks was set by the density and temperature, which is likely to change over time, shifting the location of the chondrule-forming region. This variation in formation location would naturally explain differences in chondrule types and isotopic ratios (Boley et al. 2005). The simulations of Boley & Durisen (2008) predict, however, that such high-speed shocks (5 - 11 km s^{-1}) should be rare, and must be triggered inside 2 AU, unless the disk was

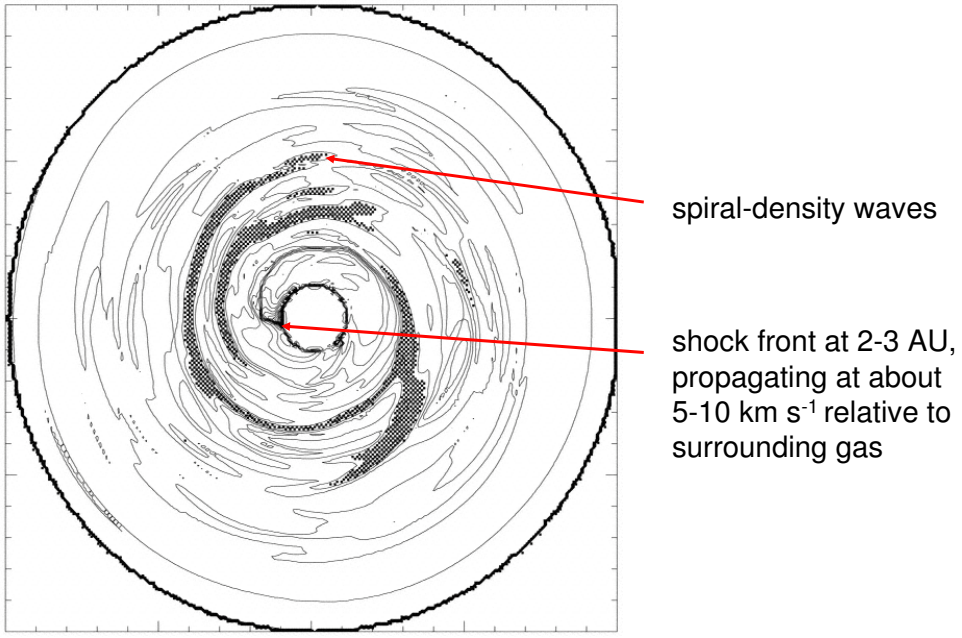

FIG. 4 — Density contours in the midplane of a gravitationally unstable disk. A strong transient shock front is shown at 9 o'clock, just outside the inner boundary of radius 2 AU. The radius of the entire region is 20 AU. Cross-hatched areas denote regions with densities above 10^{-10} g cm^{-3}. A solar-mass protostar lies at the center of the disk. Solids rotating in the counterclockwise direction between 2 and 3 AU encounter the shock front at a speed of $\sim$ 10 km s^{-1}. Figure from Boss & Durisen (2005).

on the verge of fragmentation. When gravitational instabilities did form in dead zones at 1-3 AU, they produced chondrule-forming shocks at asteroid belt and cometary distances (Boley & Durisen 2005).

Global spiral shocks due to gravitational instabilities are appealing as the mechanism that melted chondrules, because they meet many of the constraints on chondrule formation. They are likely to be repeated, depending on the formation mechanism for the spiral waves; they are global, but produce fairly local heating; they form chondrules in the disk; and they can work in the inner disk as well as the outer disk (Boley & Durisen 2008).

4. Shock Models

DC02 and CH02 assumed a one-dimensional (1-D) approximation, in which the gas properties vary only with x, the distance from the shock. In both models, changes in the properties of the gas and solids are complete in tens of hours, or within distances of $\lesssim 10^5$ km from the shock. In this case, the 1-D approximation is valid if the lateral scale of the shock front exceeds $\sim 10^5$ km. Shocks due to gravitational instabilities and X-ray flares are consistent with the 1-D approximation. However, shocks due to planetesimal bow shocks are not, as the scale of the shocks are $\sim 10^3$ km. This does not rule out such shocks, but they cannot be modeled with a 1-D approximation.

It is important to point out that in all compressive shocks in physical materials, a rarefaction wave follows the initial shock wave, during which time the medium experiences decompression. This holds true for nebular shocks. The post-shock computational boundary of models such as DC02 and CH02 are much smaller than the rarefaction wave. Prior to passage of the shock, the scale height of the disk is $H = c_{\rm s}/\Omega_{\rm K}$, where $c_{\rm s}$ is the sound speed and $\Omega_{\rm K}$ is the orbital frequency. As the temperature increases with the passage of the shock, so does the scale height. The increase in the scale height is $\sim c_{\rm s}'\Omega_{\rm K}$. Gas will expand at the sound speed, $c_{\rm s}$, to achieve this new scale height. It does so in a time $\sim 1/\ \Omega_{\rm K}$. At 2.5 AU, the time it takes to reach the new scale height is ≈ 1.5 years. In DC02, for example, it takes < 60 days for the material to reach the end of the computational domain.

A standard procedure in nebular shock models is to calculate the dynamical and thermal evolution of gas and chondrules separately, under the assumption of a fixed radiation field; once the temperatures of dust and chondrules are known, the emission of radiation can then be calculated and the radiation field updated. The solution is then iterated to convergence. While the nebular shock model successfully explains many aspects of chondrule formation, there remain differences between the models (INSN; DC02; CH02) that predict moderately different physical conditions in the site of chondrule formation, as reviewed by Desch et al. (2005). These differences all involve

the calculation of radiation effects, especially the radiative losses from molecular line emission, the opacity of solids, and the input radiation field.

DC02 and CH02 include radiative transfer of chondrule radiation, where INSN neglect this effect. The effect of line cooling—the cooling of gas by emission of so-called line photons by trace molecules in the gas such as CO and H_2O—in solar nebula shocks has been considered by INSN and by Miura & Nakamoto (2006). In both cases the cooling rates of Neufeld & Kaufman (1993) were used. INSN assumed a gas optically thin to the line radiation and found chondrule cooling rates $\sim 10^4\,\mathrm{K\,hr^{-1}}$ in many cases. Miura & Nakamoto (2006) allowed the gas to become optically thick to this line radiation. They found that for plausible parameters the cooling rates of chondrules and gas cluster around $5000\,\mathrm{K\,hr^{-1}}$, with line cooling playing an important role in the cooling of the gas. DC02 and CH02 ignored the effect of line cooling, assuming an optically thick limit to the line radiation.

A major input to calculations of the radiation field (more specifically, the frequency-integrated mean intensity J at all locations) is the input radiation field at the boundaries of the computational domain over which chondrule thermal histories are investigated. Far from the shock front, in the pre-shock region, the radiation field is set to a blackbody radiation field at the ambient temperature, T_{pre}, of the gas. The post-shock radiation field could also be set to the blackbody radiation field at temperature, T_{post}, but it is not clear what the temperature, T_{post}, far beyond the shock in the post-shock region should approach. Both INSN and CH02 set $T_{\mathrm{post}} = T_{\mathrm{pre}}$, while DC02 used the jump conditions of Hood & Horanyi (1991) to derive a much higher post-shock temperature ($T_{\mathrm{pre}} \approx 1100\,\mathrm{K}$ typically). The isothermal assumption $T_{\mathrm{post}} = T_{\mathrm{pre}}$, strictly speaking, violates the assumption of 1-D, but the jump conditions used by DC02 and Hood & Horanyi (1991) were incorrect.

The question of opacity is also complicated. Only the opacity due to chondrules was considered by CH02, INSN and Miura & Nakamoto (2006). In contrast, DC02 considered opacity due to both chondrules and a gray (no frequency or temperature dependence) opacity of micron-sized

dust, $\kappa = 1.14\,\mathrm{cm^2\,g^{-1}}$, up to a dust evaporation temperature $T_{\mathrm{evap}} = 2000\,\mathrm{K}$, above which the opacity vanished.

5. Purpose and Outline of Thesis

The purpose of this study is to investigate the formation of chondrules in solar nebula shocks. Although previous shock models for chondrule formation exist, these models have been lacking in some of the relevant physics. Previous shock models have used incorrect approximations to the input radiation boundary condition, and the opacity of solids has been treated simply. Most important, a proper treatment of cooling due to molecular line emission has not been included. In this study, we significantly improve the shock model. We determine the appropriate boundary condition for the input radiation, the proper method for calculation of the opacity of solids, and include a complete treatment of molecular line cooling due to H_2O.

In the following chapters we will discuss the physics of particle heating in nebular shocks, both with and without radiation effects. We present a description of the hydrodynamic shock code used in this study to predict the thermal histories of chondrules formed in nebular shocks, and describe in detail the improvements we have made over previous shock models. Results are presented and analyzed after each change is made to the model. New quantifications of line emission and its role in chondrule-forming shocks will be presented. Cooling rates due to line emission from H_2O in a dense gas are calculated exactly. Initially, the effects of line cooling in chondrule-forming shocks are estimated, through the use of a toy model. We then detail the complicated process of incorporating molecular line cooling into the hydrodynamic shock code. Final results, after the inclusion of line cooling, are presented and analyzed. Parameter studies are then performed to determine the effect of changing initial conditions, such as the density of the pre-shock gas, water abundance, and the concentration of chondrule precursors. Results of these parameter studies performed using the updated shock code are presented. These results act as constraints on the conditions in the early solar nebula, in order for chondrules to form in nebular shocks. Finally, we

discuss the insight we have gained from this study, the implications of our results, and future work planned in order to continue the investigation into the conditions during the birth of our Solar System, and by extension, other forming planetary systems.

CHAPTER 2

UPDATED SHOCK MODEL

The shock model used in this study is based on the models of DC02 and CH02, with substantial improvements. The discussion in §§1-3 largely follows that of DC02. As we have noted previously in Chapter 1, §4, the jump condition used by DC02 for the boundaries of the computational domain (far from the shock front) was incorrect, and the jump condition used by CH02 formally violates the 1-D assumption. In §4 of this Chapter, we derive the formal jump condition appropriate for use under the 1-D assumption, although we show that the CH02 condition is physically justified. Additionally, the model of CH02 neglected opacity due to fine-grained dust particles and DC02 assumed a constant dust opacity of 1.14 cm^2 g^{-1}. We have determined that neither of these choices is appropriate. We discuss dust opacity in detail in §5. Finally, the model of DC02 set the temperature at which dust evaporates at 2000 K. (CH02 did not consider evaporation of fine-grained dust, as the opacity in their model arose solely from chondrule precursors). We have determined that the temperature at which silicate dust evaporates is much lower than the 2000 K assumed by DC02. We discuss dust evaporation in §6. In §§1, 2, and 3, we discuss the physics of particle heating in shocks, as described by Desch et al. (2005), and the shock model of DC02 (similar to that of CH02), updated with new jump conditions at the computational boundary and improved treatment of the dust opacity and dust evaporation.

1. Physics of Particle Heating in Shocks

Any shock generated in the solar nebula will heat solids in three ways: 1) by thermal exchange between the hot, dense, post-shock gas and the particles in the post-shock region; 2) by frictional heating, as the particles are slowed to the reduced post-shock velocity in the post-shock region; and 3) by absorption of infrared radiation emitted by heated particles everywhere, in both the pre-shock and post-shock regions. Here, we discuss the dynamical and thermal evolution of gas and solids in shocks. Initially, we ignore absorption of radiation by solids.

1.1. *Basic Shock Equations Neglecting Radiation*

1.1.1. *Gas.* To describe the heating of solids passing through a shock front, we must constrain the temperature $T_{\rm g}$, pressure $P_{\rm g}$, density $\rho_{\rm g}$ and velocity $v_{\rm g}$ of the gas as it crosses the shock front. We make the assumption that these quantities vary only with x, perpendicular to the shock front. This assumption is known as the one-dimensional (1-D) approximation. We define $x = 0$ at the shock front, with $x < 0$ in the pre-shock region and $x > 0$ in the post-shock region. In what follows, we label the quantities that have not passed the shock front with the subscript "1", and label the quantities that have passed the shock front with the subscript "2". In all cases, we measure velocities in the frame of the shock.

In a one-dimensional, steady-state flow, the equation of conservation of mass (the "continuity" equation) is (e.g., Shore 1992)

$$\frac{\partial}{\partial x}\left(\rho_{\rm g} v_{\rm g}\right) = 0. \tag{2.1}$$

This tells us that the quantity $\rho_{\rm g} v_{\rm g}$ is constant and that $\rho_{\rm g_1} v_{\rm g_1} = \rho_{\rm g_2} v_{\rm g_2}$. We know that the gas will slow from supersonic to subsonic speeds across the shock front. Since $\rho_{\rm g_1} v_{\rm g_1} = \rho_{\rm g_2} v_{\rm g_2}$ this means that the gas must be compressed in the post-shock region. The equation of conservation of momentum (the "force" equation) is

$$\frac{\partial}{\partial x}\left(P_{\rm g} + \rho_{\rm g} {v_{\rm g}}^2\right) = 0. \tag{2.2}$$

Since the gas is compressed following passage through the shock front, it follows that it will be heated, but its final temperature depends on the nature of energy transfer. If no exchange of energy occurs between the gas and its surroundings, conservation of energy (including kinetic energy, internal energy, and mechanical work done by pressure) demands

$$\left(\rho_{\rm g} v_{\rm g}\right) \frac{\partial}{\partial x}\left[\frac{\gamma}{\gamma - 1}\frac{P_{\rm g}}{\rho_{\rm g}} + \frac{1}{2}{v_{\rm g}}^2\right] = 0, \tag{2.3}$$

where γ is the adiabatic index, or ratio of specific heats (e.g. $\gamma = 7/5$ for H_2 gas). With these three equations, one can solve for the three unknowns $v_{\rm g}$, $\rho_{\rm g}$ and $P_{\rm g}$ as functions of x.

In this simple example, in which radiation is neglected, the pre-shock gas does not experience any physical effects until it crosses the shock front. The pre-shock gas density and temperature ρ_{g_1} and T_{g_1} equal the ambient gas density and temperature, and the pre-shock gas velocity $v_{g_1} = v_s$, the speed of the shock. Upon crossing the shock front, the gas density, temperature, and velocity attain new values ρ_{g_2}, T_{g_2}, and v_{g_2}. These post-shock values are related to the pre-shock values using the Rankine-Hugoniot relations, or jump conditions, which are discussed in detail in §3.2. These jump conditions describe the state of the gas immediately after it passes through the shock front. In the absence of radiation, the post-shock gas properties do not vary with x.

1.1.2. *Particles.* Once the properties of the gas are known, the thermal histories of particles passing through the shock front can be calculated. In the pre-shock region, solid particles, such as chondrule precursors, move with the gas at a speed $v_{p_1} = V_s$ (in the frame of the shock front). Neglecting radiation, the particle is in thermal equilibrium with the surrounding gas, at temperature, T_{g_1}. Upon passage through the shock front, the gas is suddenly slowed, compressed, and heated. The shock front itself is only a few molecular mean free paths thick, or $\sim 1/(n\sigma)$, where n is the number density and σ is the collisional cross section of the gas molecules. Typical values for the solar nebula are $n \sim 10^{14}\,\mathrm{cm}^{-3}$, and $\sigma \approx 5 \times 10^{-16}\,\mathrm{cm}^2$, giving a mean free path of $\lesssim 1$ meter. Therefore, the shock front is only meters thick and the deceleration of the gas occurs in much less than 1 ms. As such, particles are suddenly out of dynamical and thermal equilibrium with the gas.

The continuity equation for particles, in analogy to equation 2.1 for the gas, assumes that both the total mass and number of particles are conserved:

$$\frac{\partial}{\partial x}\left(n_p v_p\right) = 0, \tag{2.4}$$

where n_p is the number density of particles. Immediately after passing through the shock front, the particle continues to move at speed $v_p \approx V_s$, as opposed to the gas, which has slowed almost immediately to a speed $\approx V_s/6$. This results in the exertion of a drag force on the particle, which is dependent on the relative velocity between the gas and particle. The force equation for the

particles, reflecting conservation of momentum, therefore includes the drag force, rather than a pressure force ($\partial P_{\rm g}/\partial x$), as in equation 2.2 for the gas. The drag force, $F_{\rm drag}$, the rate at which momentum is transferred from the gas to dust grains, has been calculated by Probstein (1968):

$$F_{\rm drag} = -\pi a_{\rm p}^2 \frac{C_{\rm D}}{2} \rho_{\rm g2} \left(v_{\rm p} - v_{\rm g2}\right) \left|v_{\rm p} - v_{\rm g2}\right|, \tag{2.5}$$

where $a_{\rm p}$ is the radius of the (spherical) particle , and $C_{\rm D}$ is the drag coefficient. The drag coefficient is a complicated function of particle speed and temperature. The mean free paths of gas molecules in the solar nebula (~ 1 meter) greatly exceed the typical sizes of particles, so the mean molecular flow approximation can be used (Cuzzi *et al.* 1996). In this approximation, molecules tend to interact (exchanging momentum) with the particles by sticking to them, leaving the surface in a random direction once they have reached equilibrium temperature with the particle. Upon leaving the surface, the molecules possess kinetic energy set by the particle temperature, $T_{\rm p}$. Under these conditions,

$$C_{\rm D} = \frac{2}{3s}\left(\frac{\pi T_{\rm p}}{T_{\rm g}}\right)^{1/2} + \frac{2s^2+1}{\pi^{1/2}s^3}\exp\left(-s^2\right) + \frac{4s^4+4s^2-1}{2s^4}{\rm erf}(s), \tag{2.6}$$

where $s \equiv \left|v_{\rm p} - v_{\rm g}\right| / (2kT_{\rm g}/\bar{m})^{1/2}$ and erf denotes the error function (Probstein 1968; Gombosi et al. 1986). In the supersonic limit $s \gg 1$, $C_{\rm D} \rightarrow 2$, while in the limit $s \ll 1$, $C_{\rm D} \approx 3/s$. The force equation for the particles can now be written:

$$n_{\rm p} m_{\rm p} v_{\rm p} \frac{\partial v_{\rm p}}{\partial x} = n_{\rm p} F_{\rm drag}, \tag{2.7}$$

where $m_{\rm p} = 4\pi\rho_{\rm p} a_{\rm p}^3/3$ is the particle mass, and $\rho_{\rm p}$ its internal density.

As the solids are slowed due to the drag force, the gas is accelerated, due to the exertion of a force on the gas by the solids that is equal and opposite to the drag force. As such, the momentum of the gas is no longer conserved and equation 2.2 must be replaced with

$$\frac{\partial}{\partial x}\left(P_{\rm g} + \rho_{\rm g} {v_{\rm g}}^2\right) = -n_{\rm p} F_{\rm drag}. \tag{2.8}$$

In the post-shock region, solids are heated by frictional drag and thermal collisions with hot

gas. The rate at which particles are heated by the gas is

$$q = \rho_{g2}\, C_{\rm H}\, \left(T_{\rm rec} - T_{g2}\right)\, \left|v_{\rm p} - v_{g2}\right|, \tag{2.9}$$

where

$$C_{\rm H} = \frac{\gamma+1}{\gamma-1}\,\frac{k}{8\bar{m}s^2}\left[\frac{s}{\pi^{1/2}}\exp(-s^2) + \left(\frac{1}{2}+s^2\right)\mathrm{erf}(s)\right],$$

and

$$T_{\rm rec} = T_{g2}\left(\frac{\gamma-1}{\gamma+1}\right)\left[\frac{2\gamma}{\gamma-1} + 2s^2 - \left(\frac{1}{2}+s^2+\frac{s}{\pi^{1/2}}\exp(-s^2)\mathrm{erf}^{-1}(s)\right)^{-1}\right]$$

where $\mathrm{erf}^{-1}(s) = 1/\mathrm{erf}(s)$ (Probstein 1968; Gombosi et al. 1986). When determining the heating rate, q, the same gas temperature, $T_{\rm gas}$, is used for each species, but $\gamma = 7/5$ for H_2 and SiO and $\gamma = 5/3$ for H and He. Additionally, s will be different for each species as well, since $\bar{m} = 1m_{\rm H}$ for H, $2m_{\rm H}$ for H_2, $4m_{\rm H}$ for He, and $44m_{\rm H}$ for SiO. In the limit $s \gg 1$,

$$q \rightarrow \rho_{g2}\left(v_{\rm p} - v_{g2}\right)^3 / \,8, \tag{2.10}$$

In this case, gas-drag heating dominates over thermal exchange and is seen to scale as the cube of the relative velocity. In the opposite limit $s \ll 1$, thermal exchange dominates over gas-drag heating, $T_{\rm rec} \rightarrow T_{g2}$, and the particle's temperature is forced to come into equilibrium with the gas temperature. In this case,

$$q \rightarrow \left(\frac{\rho_{\rm g}}{\bar{m}}\right)\,\frac{1}{4}\left(\frac{8kT_{\rm g}}{\pi\bar{m}}\right)^{1/2}\,\frac{1}{2}\left(\frac{\gamma+1}{\gamma-1}\right)k\left(T_{\rm g} - T_j\right). \tag{2.11}$$

Drag heating will dominate the heating of a particle while it is moving supersonically with respect to the gas, for a time $\approx t_{\rm stop}$, after which thermal exchange dominates. In either limit, the energy absorbed by solid particles is balanced by a loss of energy from the gas.

If the particles do not radiate, then the energy equation for the particles becomes

$$n_{\rm p} m_{\rm p} v_{\rm p} \frac{\partial}{\partial x}\left(C_{\rm P} T_{\rm p}\right) = n_{\rm p}\, 4\pi a_{\rm p}^2\, q, \tag{2.12}$$

where $C_{\rm P} \sim 10^7\,\mathrm{erg\,g^{-1}\,K^{-1}}$ is the specific heat capacity of the particle (Wasson 1996) .

Including interactions with solids, the gas energy flux equation becomes

$$(\rho_{\rm g} v_{\rm g}) \frac{\partial}{\partial x} \left[\frac{\gamma}{\gamma - 1} \frac{P_{\rm g}}{\rho_{\rm g}} + \frac{1}{2} {v_{\rm g}}^2 \right] = -n_{\rm p} v_{\rm p} F_{\rm drag} - n_{\rm p}\, 4\pi a_{\rm p}^2\, q. \tag{2.13}$$

The term, $-n_{\rm p} v_{\rm p} F_{\rm drag}$, accounts for increased kinetic energy of the gas due to interactions with the particles via the drag force, while the term that includes q accounts for direct energy exchanges. Combining the energy equations for the gas and particles demonstrates that energy is conserved:

$$(\rho_{\rm g} v_{\rm g}) \frac{\partial}{\partial x} \left[\frac{\gamma}{\gamma - 1} \frac{P_{\rm g}}{\rho_{\rm g}} + \frac{1}{2} {v_{\rm g}}^2 \right] + n_{\rm p} m_{\rm p} v_{\rm p} \frac{\partial}{\partial x} \left(C_{\rm P} T_{\rm p} \right) = -n_{\rm p} v_{\rm p} F_{\rm drag}. \tag{2.14}$$

Neglecting radiation, the gas and particle properties are determined entirely by their exchange of momentum and energy. Both gas and particles enter the shock front with temperature $T_{\rm g1}$ and speed $V_{\rm s}$. The gas, however, rapidly slows, compresses, and heats. The particles initially continue at speed $V_{\rm s}$, but in a time, $\sim t_{\rm stop}$, come into dynamical equilibrium with the gas. They eventually come into thermal equilibrium with the gas as well. Until the particles come into complete equilibrium with the gas, their velocities and temperatures are found by integrating the gas equations 2.1, 2.8, and 2.13, and the particle equations 2.4, 2.7 and 2.12. After the particles reach thermal and dynamical equilibrium with the gas, both gas and solids continue onward at the same velocity and temperature.

2. Radiation Effects

Both gas and solids will radiate away excess energy, mostly in the infrared. This radiation will affect the temperature and density of the gas, which in turn will affect the heating and cooling of chondrule precursors and chondrules embedded in the gas. In the case of solar nebula shocks, this radiation carries negligible mass and momentum, and the equations of mass flux and momentum flux for both gas and solids will not change (equations 2.1, 2.8, 2.4 and 2.7) i.e., it is not necessary to adopt a radiation hydrodynamics approach. However, the equations of energy flux for both gas and solids (equations 2.12 and 2.13) will change, due to the effects of this radiation. Because of the

difference in the way gas and solids radiate away excess energy, we treat each of the two equations of energy flux separately.

2.1. *Effects of Gas Radiation*

Gas molecules emit radiation at very specific wavelengths. Shocked nebular gas tends to be heated to $\lesssim$ 2500 K, which is too low to excite molecules to higher electronic states but sufficient to excite them to higher vibrational or rotational states. Because these states are quantized, transitions between excited states emit photons at very specific infrared wavelengths. These photons are known as line photons, and their emission is known as line emission. The most common gas molecules in a nebular gas, hydrogen molecules (H_2), lack a permanent electric dipole moment and are rather inefficient emitters of line photons. However, CO and H_2O, the next most abundant molecules in the gas, do have permanent electric dipoles. The line photons these molecules emit can carry away sufficient energy to cool the gas. In the context of a solar nebula shock, we are concerned with whether CO and H_2O molecules in the hot, post-shock gas ($x > 0$), in particular, emit line photons and cool the gas. In order to cool the post-shock gas, line photons must escape to the pre-shock region ($x < 0$). These line photons appear Doppler-shifted to the pre-shock molecules, because the molecules in the post-shock region move relative to the pre-shock gas by several km/s. Because of this frequency discrepancy, the line photons cannot be absorbed by the pre-shock molecules and may be lost from the system, thereby cooling the gas. Solids, however, *can* absorb these line photons. Line photons emitted by the hot, post-shock gas, therefore, are either absorbed by nearby gas molecules, absorbed by solids, or they escape to the pre-shock region and their energy is, for all practical purposes, lost from the region. We discuss the calculation of line cooling in detail in Chapter 3.

2.2. *Effects of Particle Radiation*

Unlike gas molecules, solid particles emit and absorb radiation over a continuous range of wavelengths. This means that Doppler shifts of the radiation are irrelevant. Radiation emitted by solid particles can be absorbed by solid particles anywhere else in the region. Particles that

absorb this radiation will heat and, as a consequence, emit more radiation. This feedback requires an entirely different approach to the treatment of radiation by solid particles.

2.3. *Radiative Transfer*

In our model, the gas is divided into four populations: atomic hydrogen (H), molecular hydrogen (H_2), helium atoms (He), and molecules resulting from the evaporation of solids, which we represent with SiO. The adiabatic index, γ, is defined as 5/3 for the two atomic species, and 7/5 for the two molecular species. There is a chemical energy of 4.48 eV associated with the dissociation of each H_2 molecule. The properties of solids are the number density, $n_{\rm p}$, the velocity, $V_{\rm p}$, the temperature, $T_{\rm p}$, the radii, $a_{\rm p}$, the material density, $\rho_{\rm p}$, and the heat capacity, $C_{\rm P}$. We must also define the latent heat of fusion, $l_{\rm melt}$, and the temperature range, ΔT_p, over which melting of solids takes place, as well as the latent heat of evaporation, $l_{\rm evap}$, and the temperature, $T_{\rm evap}$, at which evaporation occurs. Melting effectively increases the heat capacity over the range of temperatures at which melting occurs, by an amount $l_{\rm melt}/\Delta T_p$. We make the following assumptions: $C_{\rm P} = 1.0 \times 10^7\,{\rm erg\,g^{-1}\,K^{-1}}$, $l_{\rm melt} = 5.0 \times 10^9\,{\rm erg\,g^{-1}}$, and $l_{\rm evap} = 1.1 \times 10^{11}\,{\rm erg\,g^{-1}}$ (Wasson 1996). We discuss $T_{\rm evap}$ in §6. Melting is assumed to take place between temperatures of 1400 K and 1820 K, so that $\Delta T_p = 420\,{\rm K}$. Over this temperature range, the heat capacity is effectively $2.19 \times 10^7\,{\rm K}$. The fraction of the chondrule melted is assumed 0% at 1400 K, and rises linearly to 100% at 1820 K. A final needed parameter is the radiative emissivity ϵ. Since the chondrule precursors are heated to temperatures $1500 - 2000\,{\rm K}$, the wavelength of peak thermal emission is (by Wien's law) $\approx 2\,\mu{\rm m}$. The Planck-averaged emissivity ϵ is proportional to the particle radius a for small silicate particles, but independent of size for large particles (Draine and Lee 1984). We adopt the following emissivity, to conform with the results of Draine and Lee (1984):

$$\epsilon = 0.8 \times \min\left[1, \left(\frac{a_{\rm p}}{2\,\mu{\rm m}}\right)\right]. \tag{2.15}$$

We adopt the same wavelength-averaged emissivity for absorption and emission since the absorption spectra and emission spectra for solids are both in the near infrared.

We also include the effects of dust, fine-grained (radii $< 1\,\mu$m) silicate particles. Because of their small sizes, the thermal and aerodynamic timescales of the dust are too small to explicitly follow their evolution in our numerical code. We therefore assume that the fine-grained dust is thermally and dynamically well-coupled to the gas. The assumption of good dynamical coupling between gas and dust underestimates the temperature reached by the dust, as it neglects the effect of frictional drag heating. Using an emissivity $\epsilon = 0.2$, appropriate for grains of radii ~ 0.5 μm (and in agreement with the NIR albedo of interstellar dust; Li & Greenberg 1997), we calculate the temperature of the dust particles using equation 2.24, with the derivative set to zero. Within the code, we modify the particle temperature. If the equilibrium temperature is greater than $T_{\rm evap}$, we assume that dust is destroyed by evaporation from that point on, until the end of the post-shock region. The presence or absence of dust is crucial in the calculation of the opacity of the gas, which in turn, is used to properly calculate the radiation field.

Solids are allowed to absorb and emit radiation, affecting their total energy budget. The radiation emitted by some particles may be absorbed by other particles at a distant location. The determination of the radiation field at all locations is therefore a critical calculation. As discussed above, the gas itself may also radiate, primarily due to vibrational modes of H_2O near $6\,\mu$m (Neufeld and Kaufman 1993; Morris et al. 2009). Treatment of the especially difficult problem of line radiation in a dusty medium has been discussed in Hollenbach and McKee (1979) and Morris et al. (2009). Initially, we neglect cooling of the gas due to line emission in our treatment of the radiation field. Discussion of line cooling and its treatment in our numerical code is discussed in Chapter 3. Here, we follow the approach outlined in Mihalas (1978) for radiation emergent from a plane-parallel, temperature-stratified slab atmosphere.

In order to describe the radiation field, the first parameter to be defined is the (frequency-averaged) optical depth at all locations. At the beginning of our computational boundary, the optical depth $\tau(x = -x_{\rm pre}) = 0$, increasing to a maximum value $\tau(x = +x_{\rm post}) = \tau_{\rm m}$ at the

post-shock computational boundary. At other locations,

$$\tau(x) = \int_0^x \left[\rho_{\rm g}\kappa + n_{\rm p}(x)\,\pi a_{\rm p}^2 \epsilon_{\rm p}(\lambda)\right]\,{\rm d}x, \tag{2.16}$$

where κ is the opacity of the gas (with density, $\rho_{\rm g}$) due to dust associated with the gas. A complete treatment of the dust opacity is given in §5. If at some point the dust is destroyed through evaporation (§6), then κ, from that point on, is set to 0.001 times the value it would have by Eqn. 2.63. It is not set to zero, in order to account for ultra-refractories (Lenzuni et al. 1995).

The second parameter to be defined is the (frequency-integrated) source function, S. The source function from a blackbody at temperature T is the Planck function B, which after integrating over wavelength is $B = \sigma T^4/\pi$, where σ is the Stefan-Boltzmann constant. If *all* the particles in a region are held at temperature T, the source function must approach B, regardless of the emissivities of the particles. If the particles are at different temperatures, the source function is weighted according to their emissivities:

$$S = \frac{\rho_{\rm g}\kappa\sigma T_{\rm g}^4 + n_{\rm p}\pi a_{\rm p}^2 \epsilon\,\sigma T_{\rm p}^4}{\rho_{\rm g}\kappa + n_{\rm p}\pi a_{\rm p}^2 \epsilon}. \tag{2.17}$$

This reduces to $\sigma T_{\rm g}^4/\pi$ in the event that $T_{\rm p} = T_{\rm g}$. (Although the temperature of dust is approximated in the code, the gas temperature is used for the source function from dust to avoid numerical instabilities, as well as for the reason that the two temperatures are very similar.) The last parameter to be specified is the radiation entering through the two computational boundaries (integrated over wavelength). The radiation field entering the pre-shock computational boundary is given by $I_{\rm pre} = \sigma T_0^4/\pi$, where T_0 is the temperature of the ambient medium. The specific intensity of the radiation field entering the post-shock boundary is given by $I_{\rm post} = \sigma T_{\rm post}^4/\pi$, where $T_{\rm post}$ is the post-shock equilibrium temperature, using the radiative jump conditions of §4.

Given the incident radiation fields and the source function at all optical depths, $S(\tau)$, the mean intensity of radiation, $J(\tau)$ (integrated over wavelength) can be found:

$$J(\tau) = \frac{I_{\rm pre}}{2}{\rm E}_2(\tau) + \frac{I_{\rm post}}{2}{\rm E}_2(\tau_{\rm m} - \tau) + \frac{1}{2}\int_0^\tau S(t){\rm E}_1(\tau - t)\,{\rm d}t$$

$$+\frac{1}{2}\int_{\tau}^{\tau_{\rm m}} S(t)\mathrm{E}_1(t-\tau)\,\mathrm{d}t, \tag{2.18}$$

where E_1 and E_2 are exponential integrals. Using the properties of the exponential integrals, namely that $\mathrm{d}\mathrm{E}_n(x)/\mathrm{d}x = -\mathrm{E}_{n-1}(x)$, it can be shown by direct integration that if $S(t) = I_{\rm pre} = I_{\rm post} = I_0$ everywhere, then $J(\tau) = I_0$. We can also solve for the net flux of radiation energy, $F_{\rm rad}(\tau)$:

$$F_{\rm rad}(\tau) = 2\pi I_{\rm pre}\mathrm{E}_3(\tau) - 2\pi\int_{\tau}^{\tau_{\rm m}} S(t)\mathrm{E}_2(t-\tau)\,\mathrm{d}t$$
$$-2\pi I_{\rm post}\,\mathrm{E}_3(\tau_{\rm m}-\tau) + 2\pi\int_{0}^{\tau} S(t)\mathrm{E}_2(\tau-t)\,\mathrm{d}t. \tag{2.19}$$

It is again possible to show by direct integration that in the case $S(t) = I_{\rm pre} = I_{\rm post} = I_0$ everywhere that the net flux $F_{\rm rad} = 0$. It is also straightforward to demonstrate that in general

$$\frac{\partial F_{\rm rad}}{\partial x} = -4\pi\rho_{\rm g}\kappa\left[J_r - \sigma T_{\rm g}^4/\pi\right] - n_{\rm p}4\pi^2 a_{\rm p}^2\,\epsilon\left[J_r - \sigma T_{\rm p}^4/\pi\right], \tag{2.20}$$

where κ is the opacity of the gas (via the well-coupled dust component). That is, changes in radiative flux are due to net absorption of radiation by gas and dust.

2.4. *Basic Shock Equations Including Radiation*

In practice, we treat the four gas species (H, H_2, He, SiO) separately, then combine their separate heating rates into one overall heating rate. The net particle heating rate per unit surface area is then q (equation 2.9) plus the radiative terms: $q+\epsilon(J_r-\sigma T_{\rm p}^4/\pi)$. This net heating rate goes into raising the particle's temperature, thereby melting it or causing it to evaporate. If $T_{\rm p} < T_{\rm evap}$, or if $T_{\rm p} = T_{\rm evap}$ and the net heating is negative, then there is no evaporation, $m_{\rm p}$ is constant, and

$$\frac{\partial a_{\rm p}}{\partial x} = 0, \tag{2.21}$$

$$\frac{\partial}{\partial x}\left(C_{\rm P}T_{\rm p}\right) = \frac{3}{\rho_{\rm p}a_{\rm p}V_{\rm p}}\left[q + \epsilon\left(J_r - \sigma T_{\rm p}^4/\pi\right)\right]. \tag{2.22}$$

If $T_{\rm p} \geq T_{\rm evap}$ and the net heating is positive, then all the heat goes into evaporating the particle:

$$\frac{\partial a_{\rm p}}{\partial x} = -\frac{1}{\rho_{\rm p}l_{\rm evap}V_{\rm p}}\left[q + \epsilon\left(J_r - \sigma T_{\rm p}^4/\pi\right)\right], \tag{2.23}$$

and

$$\frac{\partial T_{\rm p}}{\partial x} = 0. \tag{2.24}$$

(That is, $T_{\rm p}$ is held constant at $T_{\rm evap}$.) These four equations can be used to immediately solve for the four unknowns for solids, $n_{\rm p}$, $V_{\rm p}$, $a_{\rm p}$ and $T_{\rm p}$. (In reality, of course, evaporation is over a range of temperatures, and is not a step function).

The gas equations, modified for dissociation and recombination, are as follows. Hydrogen atoms and molecules obey the following continuity equations:

$$\frac{\partial}{\partial x}\left(n_{\rm H} V_{\rm g}\right) = -2R, \tag{2.25}$$

and

$$\frac{\partial}{\partial x}\left(n_{\rm H_2} V_{\rm g}\right) = +R, \tag{2.26}$$

where R is the net rate (per unit volume and unit time) of the reactions $\rm H + H \rightarrow H_2$, given in Appendix B. The total number of hydrogen nuclei are conserved. Helium atoms are neither created or destroyed:

$$\frac{\partial}{\partial x}\left(n_{\rm He} V_{\rm g}\right) = 0. \tag{2.27}$$

Other molecules formed by the evaporation of solids are created at a rate

$$\frac{\partial}{\partial x}\left(n_{\rm SiO} V_{\rm g}\right) = -\frac{n_{\rm p} V_{\rm p} 4\pi \rho_{\rm p} a_{\rm p}^2}{44 m_{\rm H}} \frac{\partial a_{\rm p}}{\partial x} \equiv \dot{N}_{\rm SiO}. \tag{2.28}$$

Because the gas species are assumed to be dynamically and thermally well-coupled and to share the same velocity and temperature, we need just one force equation for the gas.

$$\left[\rho_{\rm g} V_{\rm g}^2 - P_{\rm g}\right]\left(\frac{1}{V_{\rm g}}\frac{\partial V_{\rm g}}{\partial x}\right) + \left[P_{\rm g}\right]\left(\frac{1}{T_{\rm g}}\frac{\partial T_{\rm g}}{\partial x}\right) = F_{{\rm drag},j} - \frac{RkT_{\rm g}}{V_{\rm g}} + \frac{\dot{N}_{\rm SiO} k T_{\rm g}}{V_{\rm g}}. \tag{2.29}$$

The last term accounts for the momentum flux lost from the particles as they evaporate and lose mass. (This evaporated mass transfers momentum to the gas as it becomes part of the gas).

We now turn to the energy equation to complete our description of the evolution of the gas. Like the solids, the gas can be heated by frictional drag as well as by collisional transfers of thermal

energy. Because total energy must be conserved, we first begin with a combined energy equation for the solids and gas. All stores of energy are moving with the gas or particles, except for the radiation, so that, in terms of number densities:

$$\begin{aligned}\frac{\partial}{\partial x}\Bigg[&n_{\rm H}V_{\rm g}\left(\frac{1}{2}m_{\rm H}V_{\rm g}^2+\frac{5}{2}kT_{\rm g}\right)+n_{\rm H}V_{\rm g}e_{\rm diss}+n_{\rm H_2}V_{\rm g}\left(\frac{1}{2}2m_{\rm H}V_{\rm g}^2+\frac{7}{2}kT_{\rm g}\right)\\&+n_{\rm He}V_{\rm g}\left(\frac{1}{2}4m_{\rm H}V_{\rm g}^2+\frac{5}{2}kT_{\rm g}\right)+n_{\rm SiO}V_{\rm g}\left(\frac{1}{2}44m_{\rm H}V_{\rm g}^2+\frac{7}{2}kT_{\rm g}\right)\\&+n_{\rm p}m_{\rm p}V_{\rm p}\left(\frac{1}{2}V_{\rm p}^2+C_{\rm P}T_{\rm p}\right)\Bigg]=-\frac{\partial F_{\rm rad}}{\partial x}+\dot{e}\\&=+4\rho_{\rm g}\kappa\left(J_r-\sigma T_{\rm g}^4/\pi\right)+n_{\rm p}4\pi a_{\rm p}^2\epsilon\left(J_r-\sigma T_{\rm p}^4/\pi\right)+\dot{e},\end{aligned}\tag{2.30}$$

where $e_{\rm diss}=2.24\,{\rm eV}$ and $\dot{e}$ is the net energy due to molecular line emission (for now, $\dot{e}=0$). After subtracting the terms that describe the dust energy evolution (and simplifying using the continuity equations) all the radiative terms involving particle opacities drop out, and only the terms involving gas opacity remain. What remains is

$$\left(n_{\rm H}+n_{\rm H_2}+n_{\rm He}+n_{\rm SiO}\right)V_{\rm g}^2\left(\frac{\partial V_{\rm g}}{\partial x}\right)+\left(\frac{5}{2}n_{\rm H}+\frac{7}{2}n_{\rm H_2}+\frac{5}{2}n_{\rm He}+\frac{7}{2}n_{\rm SiO}\right)V_{\rm g}\left(\frac{\partial C^2}{\partial x}\right)$$

$$=+\frac{4\rho_{\rm g}\kappa}{m_{\rm H}}\left(J_r-\sigma T_{\rm g}^4/\pi\right)-n_{\rm p}4\pi a_{\rm p}^2\frac{q}{m_{\rm H}}-n_{\rm p}V_{\rm p}\frac{F_{\rm drag}}{m_{\rm H}}$$

$$-n_{\rm p}V_{\rm p}\left(\frac{4\pi a_{\rm p}^2\rho_{\rm p}}{m_{\rm H}}\frac{\partial a_{\rm p}}{\partial x}\right)\left(\frac{1}{2}V_{\rm p}^2-\frac{1}{2}V_{\rm g}^2\right)+R\left(\frac{3}{2}C^2-\frac{2e_{\rm diss}}{m_{\rm H}}\right)-\dot{N}_{\rm SiO}\left(\frac{7}{2}C^2\right)+\dot{e}. \qquad (2.31)$$

The first term on the right-hand side of equation 2.31 accounts for energy absorbed by the gas from the radiation field, and radiation emitted by the gas (through the well-coupled dust component). The second term accounts for the loss of thermal energy from the gas to the particles. The third term includes work done by the gas on the particles via the drag force. The fourth term accounts for changes in the gas kinetic energy due to the creation of new gas molecules by evaporation. The fifth term accounts for changes in the thermal and chemical energy due to dissociation and recombination of molecules. The sixth term accounts for changes in the thermal energy due to the addition of new molecules by evaporation of solids. Finally, the seventh term is the net energy due to molecular line emission.

Expressing the energy equation in terms of pressure, as opposed to number densities, gives:

$$\rho_{\rm g}V_{\rm g}^2\left(\frac{1}{V_{\rm g}}\frac{\partial V_{\rm g}}{\partial x}\right)+\left[\frac{5}{2}P_{\rm g}+n_{\rm H_2}kT_{\rm g}\right]\left(\frac{1}{T_{\rm g}}\frac{\partial T_{\rm g}}{\partial x}\right)$$

$$=\frac{1}{V_{\rm g}}\left[4\rho_{\rm g}\kappa\left(J_r-\sigma T_{\rm g}^4/\pi\right)-n_{\rm p}4\pi a_{\rm p}^2q-n_{\rm p}V_{\rm p}F_{\rm drag}-n_{\rm p}V_{\rm p}\left(4\pi a_{\rm p}^2\rho_{\rm p}\frac{\partial a_{\rm p}}{\partial x}\right)\left(\frac{1}{2}V_{\rm p}^2-\frac{1}{2}V_{\rm g}^2\right)\right.$$

$$\left.-R\left(\frac{3}{2}kT_{\rm g}+e_{\rm diss}\right)+\dot{N}_{\rm SiO}\left(\frac{7}{2}kT_{\rm g}\right)+\dot{e}\right]. \qquad (2.32)$$

3. Hydrodynamic Shock Code

3.1. *Inputs*

Our calculation of the evolution of gas and solids encountering a shock is restricted to a range of distances, x, from the shock front. Our computational domain extends a distance $x=-x_{\rm pre}$ in the pre-shock region, to $x=+x_{\rm post}$ in the post-shock region, with $x=0$ at the shock front. The lateral extent of the shock front is assumed to greatly exceed either of these two values, so that the

one-dimensional approximation can be assumed. We typically use $x_{\rm pre} \sim x_{\rm post} \sim$ a few $\times 10^6$ km, regions that are much smaller than the scale height of the nebula at $2-3$ AU ($\sim$ a few $\times 10^7$ km), so that our one-dimensional calculation is applicable to nebular shocks generated by diskwide gravitational instabilities, but not to bow shocks of planetesimals. (We remind the reader that the post-shock region is well within the rarefaction wave of the shock). Our computational domain is divided into 1000 zones.

The particles and gas are started at the pre-shock computational boundary with imposed initial conditions. Both gas and solids begin with the same temperature, T_0, and velocity, $V_{\rm s}$. There is initially no SiO vapor or atomic H. The number density of He atoms is 0.2 times the density of H_2 molecules. All necessary equations are numerically integrated using a fourth-order Runge-Kutta routine with variable step size. The variable step size refers to the steps needed to integrate across each grid zone. Integration using the Runge-Kutta routine relies on solving for the spatial derivatives of each variable in the proper order. First the particles' radii, temperatures and velocities are found directly from equations 2.22 and 2.7, and the particle densities are found from the continuity equation 2.4. Next, equations 2.32 and 2.29 are combined to solve for the two unknowns, $V_{\rm g}$ and $T_{\rm g}$. Substituting the derivative of $V_{\rm g}$ allows us to find the derivatives of all the gas densities, except at the shock front, where the jump conditions (§3.2) result in a near-instantaneous change in the gas properties. (The properties of solids do not changed across the shock front). Additionally, if the relative velocity between gas and solids drops under $1\,{\rm m\,s^{-1}}$ in the post-shock region, the relative velocity is set to zero, resulting in the movement of the particles and the gas together from that point on. The numerical integration has an internal accuracy of 10^{-6}.

During the integrations, the radiation field is considered fixed. Initially, $J = \sigma T_{\rm pre}^4/\pi$ in the pre-shock region, and $J = \sigma T_{\rm post}^4/\pi$ (§4) in the post-shock region. After all other variables have been integrated across the entire computational domain, the radiation field is then recalculated based on the updated particle densities, radii and temperatures. The temperatures of both gas

and solids are then recalculated based on the new radiation field. The solution is iterated until the radiation field and the particle temperatures are self-consistent. Our convergence criteria is set so that, in all zones, particle temperatures converge to within 1% (2.5 - 5 K) and the mean intensity, J_r, converges to within 0.2%. In the standard ("canonical") run, convergence is achieved in less than 800 iterations.

3.2. *Jump Conditions at the Shock Front*

Jump conditions are needed to specify how the gas properties change across the shock front, the viscous layer in which the velocity of the gas changes from supersonic to subsonic and kinetic energy is converted into heat. The shock front is only a few gas mean-free-paths thick. The cross section of an H_2 molecule is $\sim 5\times10^{-16}\,\mathrm{cm}^2$, so that for typical densities $n_{H_2} \sim 10^{14}\,\mathrm{cm}^{-3}$, the shock front is only meters thick. Gas and solids will pass through this layer in $\sim 10\,\mu$s. By integrating equation 2.30 across the shock front, starting only a few meters ahead and ending a few meters behind, there is not enough time for many of the terms in equation 2.30 to change appreciably. The dissociation of hydrogen takes $\gtrsim 1\,$s, and no evaporation occurs in the first several seconds. Likewise, the flux, $F_{\rm rad}$, just ahead of the shock front will be virtually identical to the flux behind it. Finally, the particles are unable to heat a significant amount in less than a millisecond, and their velocities do not vary on timescales less than $\sim 10\,$s. So we need only consider the species H, H_2 and He. Although their densities will increase behind the shock, the proportions of these three species will not change. Thus we can use the standard jump conditions (e.g., Shore 1992, pp. 107-108):

$$\rho_2 = \rho_1 \frac{(\gamma+1)\mathrm{M}^2}{(\gamma-1)\mathrm{M}^2+2} \tag{2.33}$$

$$V_2 = V_1 \frac{n_1}{n_2} \tag{2.34}$$

$$T_2 = T_1 \frac{\left[2\gamma\mathrm{M}^2-(\gamma-1)\right]\left[(\gamma-1)\mathrm{M}^2+2\right]}{(\gamma+1)^2\mathrm{M}^2}, \tag{2.35}$$

where

$$\mathrm{M}^2 = \frac{V^2}{\gamma P/\rho} = \frac{1}{\gamma}\left[\frac{n_{\mathrm{H}} + 2n_{\mathrm{H}_2} + 4n_{\mathrm{He}}}{n_{\mathrm{H}} + n_{\mathrm{H}_2} + n_{\mathrm{He}}}\right]\frac{m_{\mathrm{H}}V_1^2}{kT_1} \tag{2.36}$$

is the square of the Mach number (recall that the subscript 1 denotes pre-shock conditions and the subscript 2 describes post-shock conditions). To accommodate the multiple species of the gas, we need to interpret the ratio of specific heats, γ, correctly:

$$\gamma = \frac{\frac{5}{2}n_{\mathrm{H}} + \frac{7}{2}n_{\mathrm{H}_2} + \frac{5}{2}n_{\mathrm{He}}}{\frac{3}{2}n_{\mathrm{H}} + \frac{5}{2}n_{\mathrm{H}_2} + \frac{3}{2}n_{\mathrm{He}}}. \tag{2.37}$$

For a solar composition gas at $\approx 300\,\mathrm{K}$, $n_{\mathrm{H}} \approx 0$, and $n_{\mathrm{He}}/n_{\mathrm{H}_2} \approx 0.2$, so $\gamma \approx 1.429$. Immediately behind a very strong shock, the gas should be compressed by a factor of 5.67. Behind a shock with $V_s = 7\,\mathrm{km\,s^{-1}}$, $\rho_1 = 10^{-9}\,\mathrm{g\,cm^{-3}}$ and $T_1 = 300\,\mathrm{K}$, the density increases by a factor of 5.14, and the temperature increases by a factor of 10.51.

We discuss the jump condition needed far from the shock front in the next section.

4. Jump Conditions Far from the Shock

A major input to calculations of the radiation field (more specifically, the frequency-integrated mean intensity, J, at all locations) is the input radiation field at the boundaries of the computational domain over which chondrule thermal histories are investigated. Far from the shock front, in the pre-shock region, the radiation field is set to a blackbody radiation field at the ambient temperature, T_{pre}, of the gas; but it is not immediately clear what the temperature, T_{post}, in the post-shock region should approach. Both INSN and CH02 set $T_{\mathrm{post}} = T_{\mathrm{pre}}$, while DC02 used the jump conditions of Hood & Horanyi (1991) to derive a much higher post-shock temperature (typically, $T_{\mathrm{post}} \approx 1100\,\mathrm{K}$). The isothermal assumption, $T_{\mathrm{post}} = T_{\mathrm{pre}}$, violates the assumption of 1-D, but the jump conditions used by DC02 and Hood & Horanyi (1991) were incorrect. Their jump condition did not consider energy carried by solids and used an incorrect calculation for the radiative flux. Below we derive the proper jump conditions, then discuss why the isothermal assumption is probably best after all.

As discussed in the previous section, jump conditions relate physical conditions (e.g., density ρ, pressure P, temperature T, velocity V) at a point before the shock to those after the shock (see Mihalas & Mihalas 1996). Immediately before and after the shock (i.e., a few meters), the jump conditions are those of an "adiabatic" shock because insignificant energy is radiated in that interval. The compression of the gas is then $\rho_2/\rho_1 = \eta_{\rm AD}^{-1}$, where

$$\eta_{\rm AD} = \frac{2\gamma}{\gamma+1}\,\frac{1}{\gamma {\rm M}^2} + \frac{\gamma-1}{\gamma+1} \tag{2.38}$$

(Mihalas & Mihalas 1996). We have included radiative fluxes and the effects of solids in the equations of mass, momentum and energy conservation and have derived new jump conditions appropriate far from the shock. There are essentially three needed jump conditions. As is standard, brackets refer to a difference in the bracketed quantity between two positions; in this case, they are far before the shock and far after the shock. For mass:

$$[\rho_{\rm g} V_{\rm g} + \rho_{\rm c} V_{\rm c}] = 0. \tag{2.39}$$

For momentum:

$$\left[\rho_{\rm g} V_{\rm g}^2 + P_{\rm g} + \rho_{\rm c} V_{\rm c}^2\right] = 0. \tag{2.40}$$

Finally, for energy:

$$\left[\rho_{\rm g} V_{\rm g}\,\left(\frac{1}{2}V_{\rm g}^2 + \frac{\gamma}{\gamma-1}\frac{P_{\rm g}}{\rho_{\rm g}}\right) + \rho_{\rm c} V_{\rm c}\,\left(\frac{1}{2}V_{\rm c}^2 + C_{\rm P} T_{\rm c}\right) + F_{\rm rad}\right] = 0. \tag{2.41}$$

We now define

$$\frac{\gamma}{\gamma-1}P_{\rm g} + \rho_{\rm c} C_{\rm p} T_{\rm c} \equiv \frac{\gamma'}{\gamma'-1}P_{\rm g}. \tag{2.42}$$

Because solids quickly reach dynamical equilibrium with the gas, $V_g = V_c$, far from the shock $\equiv V$, so

$$\frac{\gamma'}{\gamma'-1}P_{\rm g} = \frac{\gamma}{\gamma-1} + \delta, \tag{2.43}$$

where

$$\delta = (\rho_{\rm c} C_{\rm p} T_{\rm c})_0 / P_0. \tag{2.44}$$

This results in a new effective adiabatic index

$$\gamma' = \frac{\gamma + \delta\,(\gamma - 1)}{1 + \delta\,(\gamma - 1)}, \tag{2.45}$$

As $\delta \to 0, \gamma' = \gamma$, and if $\delta \gg 1, \gamma' = 1$. We can now rewrite equation 2.41 as

$$\left[(\rho_{\rm g} V + \rho_{\rm c} V)\,\frac{1}{2} V_{\rm g}^2 + \frac{\gamma'}{\gamma' - 1} P_{\rm g} V + F_{\rm rad}\right] = 0. \tag{2.46}$$

In either case, dynamical, thermal, and chemical equilibria are achieved. We can assume that all hydrogen is molecular. Well before the shock, all components have identical velocity V_0 and temperature T_0; well after the shock, they have identical velocity $V_{\rm f}$ and temperature $T_{\rm f}$. By the equations of continuity, $n_{\rm H2} V$ and $n_{\rm He} V$ are conserved. We can therefore rewrite the jump conditions as

$$\left[(\rho_{\rm g} V_{\rm g}) + (\rho_{\rm c} V_{\rm c})\right]_0\,[V_0 - V_{\rm f}] = P_0\,\left[\left(\frac{V_0}{V_{\rm f}}\right)\,\left(\frac{T_{\rm g,f}}{T_{\rm g,0}}\right) - 1\right], \tag{2.47}$$

and

$$\begin{aligned}\left[\rho_{\rm g} V_{\rm g} + \rho_{\rm c} V_{\rm c}\right]_0 \left[\frac{1}{2} V_0^2 - \frac{1}{2} V_{\rm f}^2\right] + \frac{\gamma'}{\gamma' - 1} P_0 V_0 \left(1 - \frac{P_{\rm f} V_{\rm f}}{P_0 V_0}\right) \\ = F_{\rm rad}(\tau = \tau_{\rm m}) - F_{\rm rad}(\tau = 0) = \Delta F.\end{aligned} \tag{2.48}$$

Note that when written in this format, all terms in both equations are positive: $F_{\rm rad}(\tau = 0) < 0$ and $F_{\rm rad}(\tau = \tau_{\rm m}) > 0$, because radiation is emitted from the region near the shock front, and $V_0 > V_{\rm f}$ and $T_{\rm f} > T_0$.

We now simplify the equations using the following definitions:

$$\eta = \frac{V_{\rm f}}{V_0} < 1 \tag{2.49}$$

$$y = \frac{T_{\rm f}}{T_0} > 1 \tag{2.50}$$

$$\gamma {\rm M}^2 = \frac{(\rho_{\rm g} + \rho_{\rm c})\,V_0^2}{P_0} \tag{2.51}$$

Note that all quantities are dimensionless. Using these definitions, and combining the jump conditions, we arrive at the following quadratic for η:

$$\left(\gamma {\rm M}^2\right)\left(1 - \eta^2\right) + \frac{2\gamma'}{\gamma' - 1}\,(1 - y) = \frac{2\Delta F}{P_0 V_0}. \tag{2.52}$$

If $\Delta F = 0$, i.e., there are no radiative losses, then

$$\eta = \frac{\gamma' - 1}{\gamma' + 1} + \frac{2\gamma'}{\gamma' + 1} \frac{1}{\gamma \mathrm{M}^2} \equiv \eta_{\mathrm{AD}}. \tag{2.53}$$

For $\Delta F \neq 0$,

$$(\eta - \eta_{\mathrm{AD}})(1 - \eta) = -\frac{\gamma' - 1}{\gamma' + 1} \frac{1}{\gamma \mathrm{M}^2} \frac{2\Delta F}{P_0 V_0}, \tag{2.54}$$

so that

$$\eta = \frac{\eta_{\mathrm{AD}} + 1}{2} - \frac{1 - \eta_{\mathrm{AD}}}{2} (1 + \epsilon)^{1/2}, \tag{2.55}$$

where ϵ is the ratio of net outward radiative fluxes to kinetic energy flux, given by

$$\epsilon = \frac{\gamma' - 1}{\gamma' + 1} \frac{F_2 - F_1}{\rho_1 V_1^3 / 2}. \tag{2.56}$$

If radiation carries energy away from the shock front, the signs of F_2 and F_1 (or ΔF) guarantee $\epsilon > 0$. (The neglect of the sign of the radiative fluxes is one of the flaws of the jump conditions used by Hood & Horanyi (1991) and DC02 as described in Desch et al. (2005)). In terms of these quantities, the new compression is $\rho_2/\rho_1 = \eta^{-1}$, where η solves the quadratic equation

$$(1 - \eta)(\eta_{\mathrm{AD}} - \eta) = \epsilon. \tag{2.57}$$

The post-shock temperature is then easily found:

$$T_{\mathrm{post}} = T_{\mathrm{pre}}\, \eta\, [1 + \gamma \mathrm{M}^2 (1 - \eta)]. \tag{2.58}$$

Using the proper jump conditions for the 1-D approximation, we have calculated the final temperature for a range of initial densities and shock velocities and found the final temperature is always greater than the initial temperature, $T_{\mathrm{pre}} = 300$ K (Figure 5). In fact, the final temperature is usually quite large (> 1300 K), unless the shock speed is small. We can calculate the peak temperature achieved by solids using the relationship $\frac{1}{8} \rho_{\mathrm{g}} V_{\mathrm{rel}}^3 = \sigma T_{\mathrm{peak}}^4$, where V_{rel} is the relative velocity between the gas and solids. For chondrule formation to occur, solids need to reach a peak temperature, $T_{\mathrm{peak}} > 1800$ K and cool to $T_{\mathrm{final}} < 1400$ K. We find this condition occurs only in cases of high density and low initial shock velocity ($\rho_{\mathrm{g}} > 10^{-9}$ g cm^{-3} and $V_s \sim 4 - 7$ km s^{-1}; see

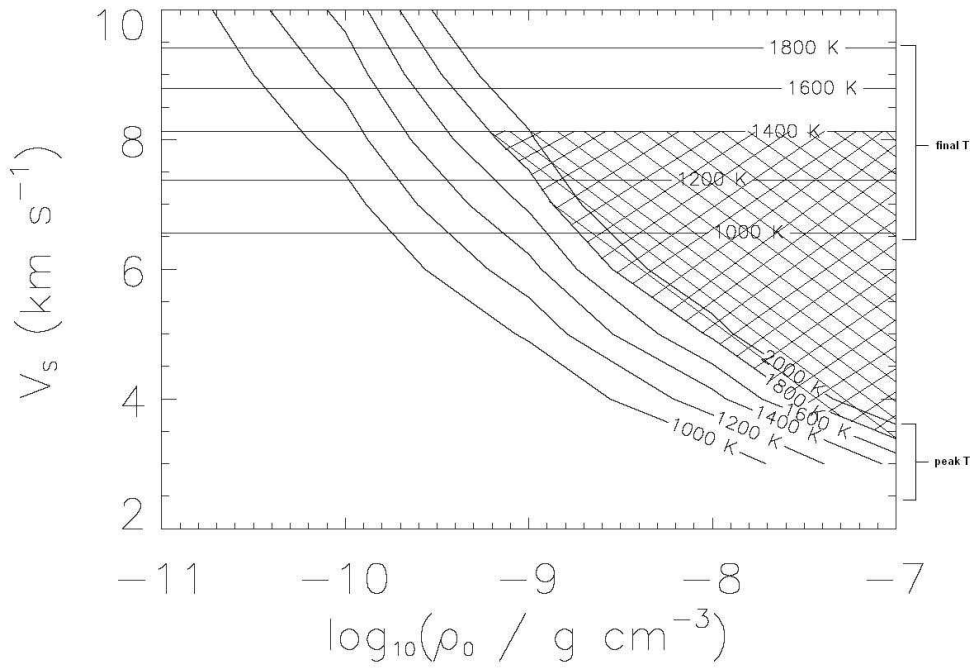

FIG. 5 —The limits on initial density, ρ_0, and shock velocity, V_s, necessary for chondrule-forming shocks in the 1-D approximation. The cross-hatched region is the area consistent with chondrule-formation, with $T_{\rm peak} > 1800$ K and $T_{\rm final} < 1400$ K.

Figure 1). These high densities and low shock speeds are largely incompatible with the formation of chondrules in the solar nebula. The minimum mass solar nebula is assumed to have a density of $\sim 10^{-10}$ g cm^{-3} at 2.5 AU according to Weidenschilling (1977), although Desch (2007) finds a more massive minimum mass solar nebula. We find that densities over 10 times that of the Weidenschilling (1977) minimum mass solar nebula ($\rho_{\rm g} > 10^{-9}$ g cm^{-3}) are needed in order for temperatures consistent with chondrule melting by shocks in a 1-D assumption with no radiative losses. Additionally, it has been demonstrated that shock speeds of 4-6 km s^{-1} will not sufficiently melt chondrules (DC02). So although there may be a small range of densities and initial shock speeds where chondrule formation is possible in the strict 1-D approximation (the extreme left "wedge" of the cross-hatched region in Figure 5), under most conditions, the 1-D approximation is not appropriate. We therefore abandon the strict 1-D assumption and explore the effect of radiative losses parallel to the shock.

In an adiabatic shock with no radiative losses, $\epsilon = 0$ and $\eta = \eta_{\rm AD}$, but as radiative losses increase, ϵ increases, η decreases, and the compression η^{-1} increases. When ϵ is such that $\eta^{-1} = \gamma {\rm M}^2$, the solution is the familiar "isothermal" shock.

The above solution for a shocked radiating flow is discussed in the gas-only case by Mihalas & Mihalas (1996), assuming there is no input radiation. This guarantees that $F_2 > 0$ and $F_1 < 0$ so $\epsilon > 0$. We are not aware of solutions for shocked radiating flows that include input radiation. To include input radiation, it would seem appropriate to alter the flux F_1 by an amount $-\sigma T_{\rm pre}^4$, and the flux F_2 by an amount $-\sigma T_{\rm post}^4$, so that the pre- and post-shock gas can radiative back into the computational domain. Unfortunately, this "reflecting" boundary condition typically drives ϵ to negative values, and is actually incompatible with a shock. It is therefore *not* appropriate to set the input radiation field to a blackbody at $T_{\rm post}$, with $T_{\rm post}$ calculated in the purely 1-D approximation. Violation of the 1-D approximation, at some level, may be necessary for maintenance of a shock in a radiating flow.

One easily understood violation of the 1-D approximation involves radiative diffusion carrying energy away parallel to the shock front (for example, out the tops and bottoms of a disk in which the shock propagation direction lies in the plane of the disk). The radiation generated by a nebular shock with lateral extent L will diffuse on a timescale

$$t_{\rm rd} = \frac{3\rho C_{\rm V} L^2}{64\pi^2\,\lambda\,\sigma T^3} \tag{2.59}$$

(Mihalas & Mihalas 1996), where λ is the mean free path of photons. For our preferred dust opacity (see §5), a post-shock density $\rho = 6\times10^{-9}\,{\rm g\,cm^{-3}}$ and temperature 2000 K, $t_{\rm rd} = 1.3\times10^7\,(L/H)^2\,{\rm s}$, where $H \approx 0.2\,{\rm AU}$ is the scale height of the disk. For opacity due to a solar composition of $300\,\mu{\rm m}$ chondrules, i.e., where dust evaporates, $t_{\rm rd}$ is lowered by a factor of 200. These are to be compared to the time for gas and chondrules to reach the computational boundary in simulations, typically $(5\times10^6\,{\rm km})/(1\,{\rm km\,s^{-1}}) \approx 5\times10^6\,{\rm s}$. If dust evaporates and $L < 0.3H$, then gas will definitely cool to the ambient temperature by the time the post-shock boundary is reached, and thereby justifies

setting $T_{\rm post}$ equal to $T_{\rm pre}$, as in CH02. If $L > 0.3H$, it is unlikely that $T_{\rm post}$ will drop to $T_{\rm pre}$ by the time the gas and chondrules reach the computational boundary, in the 1-D approximation. To model such a case, it would be necessary to model the whole disk, developing, at minimum, a 2-D simulation, and preferably a 3-D simulation.

5. Dust Opacities

Previous shock models have crudely estimated dust evaporation temperatures and dust opacities. Only the opacity due to chondrules was considered by CH02, INSN and Miura & Nakamoto (2006). In contrast, DC02 considered opacity due to both chondrules and a gray (no frequency or temperature dependence) opacity of micron-sized dust, $\kappa = 1.14\,{\rm cm^2\,g^{-1}}$, up to a dust evaporation temperature $T_{\rm evap} = 2000\,{\rm K}$, above which the opacity vanished. For meteoritic abundances of micron-sized dust and chondrules, dust opacity dominates over chondrules, so it is important to include dust opacity, especially as such opacity will be important in shutting off cooling by line emission (Morris et al. 2009). Ideally, the opacity is calculated at each wavelength. Assuming a dust-to-gas ratio $\rho_{\rm d}/\rho_{\rm g} = 5 \times 10^{-3}$, a particle radius $a_p = 0.5\,\mu{\rm m}$, and an absorptivity $Q_{\rm abs} = 1$ for $\lambda < 2\pi a_s$ and $Q_{\rm abs} = 2\pi a_s/\lambda$ for $\lambda > 2\pi a_s$, we derive

$$\kappa_\lambda = 30\ \min\left[1, (\lambda/3.1\,\mu{\rm m})^{-1}\right]\ {\rm cm^2\,g^{-1}} \tag{2.60}$$

Our estimates are similar to those derived by Henning & Stognienko (1996) using a particle size distribution, instead of our simplified monodispersion. We have found that the calculation of the opacity at each wavelength is prohibitively computationally expensive, however. Using only a range of 30 frequencies would increase our computational time for each simulation from ~ 10 days to > 30 days. We therefore desire an approximation to the opacity that is not wavelength-dependent. We use the Planck-averaged opacity and the Rosseland mean opacity as starting points in our search for such an approximation.

Both the Planck-averaged opacity and the Rosseland mean opacity are functions of both wavelength and temperature:

$$\kappa_{\rm P} = \frac{\int_\lambda \kappa_\lambda B_\lambda(T)\, d\lambda}{\int_\lambda B_\lambda(T)\, d\lambda}, \tag{2.61}$$

$$\kappa_{\rm R} = \frac{\int_\lambda \kappa_\lambda \frac{\partial B_\lambda}{\partial T}\, d\lambda}{\int_\lambda \frac{\partial B_\lambda}{\partial T}\, d\lambda}. \tag{2.62}$$

where κ_λ is the wavelength-dependent gas opacity due to dust and B_λ is the Planck function at temperature, T. The Rosseland mean intensity is important in modeling the radiative flux, and would be the most appropriate approximation to use in modeling stellar atmospheres. The Planck-averaged opacity is more appropriate for absorption of radiation. In all heating and cooling terms that involve using the mean intensity, J, the Planck-averaged opacity, $\kappa_{\rm P}$, should be used. In the calculation of the optical depths necessary to determine the mean intensity, J, at all zones, the Rosseland mean intensity, $\kappa_{\rm R}$, is appropriate. As we are most concerned with the absorption of radiation by solids, the Planck-averaged opacity is the logical choice, even at the expense of the flux calculation. Fortunately, we have determined that at a given opacity, κ_λ, $\kappa_{\rm P} \approx \kappa_{\rm R}$, as shown in Figure 2. Additionally, we have found a single, temperature-dependent approximation to the opacity that provides a good fit to the Planck-averaged opacity up to the evaporation temperature of 1500 K (see §6), as shown in Figure 3. This eliminates the need to calculate the opacity at each wavelength. For a solar composition ($\rho_{\rm d}/\rho_{\rm g} = 5 \times 10^{-3}$), our approximation to the opacity is

$$\kappa_{\rm app} = 12.161\ \ln(T) - 62.524\ {\rm cm}^2 \tag{2.63}$$

per gram of gas. We have used this approximation, dependent only on temperature, in the calculation of the dust opacity.

6. Dust Evaporation

Dust grains will typically evaporate in chondrule-forming shocks (Wasson 2008), affecting the opacity of the gas. In other words, the change in specific kinetic energy ($V^2/2$) exceeds the

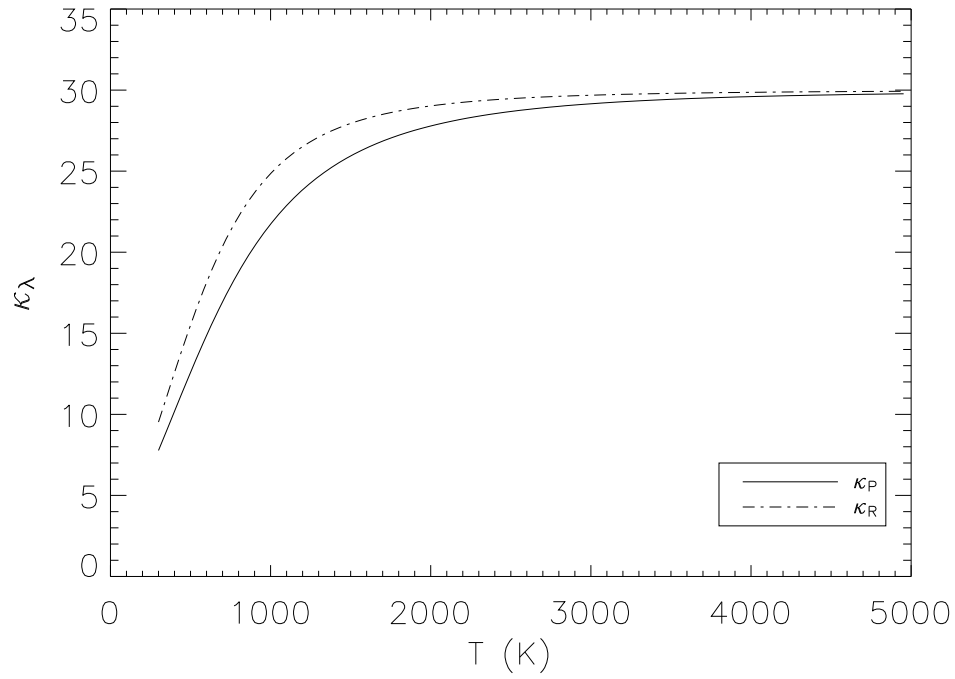

FIG. 6 — Planck-averaged opacity, $\kappa_{\rm P}$, and Rosseland mean opacity, $\kappa_{\rm R}$, as a function of temperature.

latent heat of evaporation ($l_{\rm evap} \sim 10^{11}\,{\rm erg\,g^{-1}}$) for chondrule-melting shock speeds ($\sim 7\,{\rm km\,s^{-1}}$).

Unlike chondrules, which take minutes to slow (during which time they can radiate), micron-sized dust grains slow in milliseconds and are very poor radiators (being smaller than the wavelength of maximum emission). Thus, most of their kinetic energy is converted into heat and they evaporate in milliseconds. So it is appropriate to assume dust grains instantaneously evaporate (as in DC02); however, the evaporation temperature of olivine dust should be taken as $\sim$ 1500 K, not 2000 K, as we show here.

Richter et al. (2002) present a temperature-dependent evaporation rate for materials,

$$J_i = \sum_{j=1}^{n} \frac{n_{ij}\gamma_{ij}P_{ij}^{sat}}{\sqrt{2\pi m_{ij}RT}}, \tag{2.64}$$

in units of mol cm^{-2} s^{-1}, where i is the isotope or element considered, j is the gas species containing i, n is the number density of i, γ is the evaporation coefficient of i, P^{sat} is the saturation vapor pressure for j, m is the molecular weight of j, R is the gas constant, and T is the temperature.

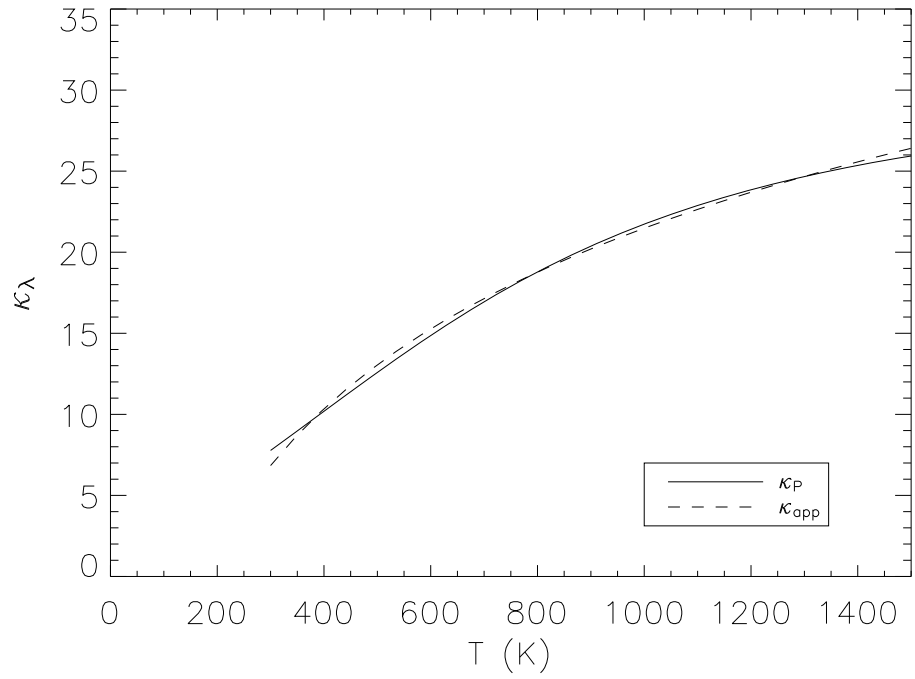

FIG. 7 — A comparison of our approximation to the opacity, $\kappa_{\rm app}$, (see text) with the Planck-averaged opacity, $\kappa_{\rm P}$, as a function of temperature, up to the evaporation temperature discussed in §6.

Davis & Richter (2005) give the temperature-dependent evaporation coefficients for forsterite, and calculate the vacuum evaporation rate as a function of temperature. They also calculate the evaporation rate at 1773 K as a function of pressure (Davis & Richter 2005). Neglecting any temperature-dependence of the saturation vapor pressure (a small effect; at most, a few times 10^{-2} g cm^{-2} s^{-1}), it can be seen from equation 2.64 that the only other quantities that will vary with temperature are the evaporation coefficient and, of course, the temperature. Therefore, we need only substitute the appropriate ratio γ/T into the given evaporation rate at 1773 K to calculate the evaporation rates at other temperatures. In so doing, we have determined the temperature-dependent evaporation rates for forsterite at pressures applicable to the solar nebula. The time it takes a grain to evaporate is given by

$$t_{\rm evap} = \frac{\rho_{\rm p} a_{\rm p}}{3JA}. \tag{2.65}$$

where A is the molar mass of the element considered. (The molar mass is needed to convert J from

TABLE 3
EVAPORATION RATES AND TIMESCALES FOR FINE-GRAINED SILICATE DUST AT 10^{-3} BAR

T (K)	J (g cm^{-2} s^{-1})[a]	$t_{\rm evap}$(s)
1473	1.7 x 10^{-8}	56.6
1573	5.3 x 10^{-8}	18.1
1673	9.3 x 10^{-8}	10.3
1773	10^{-7}	9.6
1873	1.2 x 10^{-7}	8.0
1973	1.7 x 10^{-7}	5.7
2073	2.1 x 10^{-7}	4.6

[a]The value J at T = 1773 K is given by Davis & Richter (2005).

mol cm^{-2} s^{-1} to g cm^{-2} s^{-1}). Tables 1-3 show the evaporation rate, J, and time to evaporation, $t_{\rm evap}$, for silicate dust particles of $a = 0.5$ μm.

This confirms that the dust grains will nearly instantaneously evaporate at the shock front (as in DC02), as the temperatures there will exceed 2000 K, decreasing the time to evaporate to milliseconds. Additionally, we have shown that at pressures typical of the solar nebula, it takes a matter of seconds for fine-grained dust to evaporate even at temperatures well below 2000 K. In many cases, temperatures in the pre-shock region will likely allow for these timescales to be achieved before the dust reaches the shock front. Although DC02 allowed for dust evaporation in the pre-shock region, temperatures in their model never reached their assumed high dust evaporation temperature (2000 K) prior to the shock front. Conversely, we have found that at all pressures considered here, upon reaching a temperature of $\sim$ 1500 K, the dust will evaporate before it travels one optical depth in the pre-shock region. In other words, $t_{\rm evap} < t_\tau = 1/\rho_{\rm g}\kappa V \sim 1$ minute. As a result, we have set the dust evaporation temperature to 1500 K, and allow for the evaporation of dust in the pre-shock region. This does not eliminate opacity due to dust entirely, however, as there will always be some opacity due to ultra-refractories, such as Al, (Lenzuni et al. 1995) and the chondrules themselves.

TABLE 4
EVAPORATION RATES AND TIMESCALES FOR FINE-GRAINED SILICATE DUST AT 10^{-4} BAR

T (K)	J (g cm^{-2} s^{-1})[a]	$t_{\rm evap}$(s)
1473	5.1 x 10^{-9}	188.6
1573	1.6 x 10^{-8}	60.1
1673	2.8 x 10^{-8}	34.3
1773	3.0 x 10^{-8}	32.1
1873	3.0 x 10^{-8}	32.1
1973	5.1 x 10^{-8}	18.9
2073	6.2 x 10^{-8}	15.5

[a]The value J at T = 1773 K is given by Davis & Richter (2005).

TABLE 5
EVAPORATION RATES AND TIMESCALES FOR FINE-GRAINED SILICATE DUST AT 10^{-2} BAR

T (K)	J (g cm^{-2} s^{-1})[a]	$t_{\rm evap}$(s)
1473	5.1 x 10^{-8}	18.8
1573	1.6 x 10^{-7}	6.0
1673	2.8 x 10^{-7}	3.4
1773	3.0 x 10^{-7}	3.2
1873	3.0 x 10^{-7}	3.2
1973	5.1 x 10^{-7}	1.9
2073	6.2 x 10^{-7}	1.6

[a]The value J at T = 1773 K is given by Davis & Richter (2005).

Dust evaporation past the shock front will have an effect on line cooling (Morris et al. 2009), as discussed in Chapter 3. However, because the opacity will not be exactly zero, because of chondrules and refractories, the line cooling will likely shut down after about 8 minutes, as shown in Morris et al. (2009).

CHAPTER 3

RESULTS WITH UPDATED INPUTS

We initially began with the original code of DC02, updated from Fortran 77 to Fortran 90, with small corrections for compatibility. To determine the veracity of the new version of the code, we first attempted to duplicate the results of DC02 (Table 6, Case 1). As demonstrated by Figures 8 and 9, our results are consistent with those of DC02. In fact, our figures are identical to their Figures 1 and 4. Once this important verification was made, we set out to include the improvements outlined in the previous chapter. Table 6 summarizes our results after each change to the model.

First, the new jump condition, as described in Chapter 2, §4, was implemented (Table 6, Case 2). All other parameters remain the same as in DC02 (pre-shock density, $\rho_g = 10^{-9}$ g cm^{-3}, $V_s = 7$ km s^{-1}, solids-to-gas ratio, $\rho_s/\rho_g = 5$ x 10^{-3}, and $\mathcal{C} = 1$, where $\mathcal{C} = (\rho_c/\rho_g)\,/3.75 \times 10^{-3}$ is the "concentration" of chondrules; with the chondrules-to-gas mass ratio normalized to 3.75×10^{-3} (where a chondrule radius $300\,\mu$m has been assumed). As expected, the gas temperature at the post-shock computational boundary has returned to the initial, ambient temperature of 300 K (Figure 10). Figures 11 and 12 show the gas properties, chondrule temperatures, and cooling rates after the inclusion of the new jump condition. Figure 11 shows that this change results in a higher density and a slightly slower shock velocity in the post-shock region than in the results of DC02. Because of the lower temperature, higher pressure results, thereby slowing the gas. Since, $\rho_1 V_1 = \rho_2 V_2$, this leads to higher density in the post-shock region. Because of the higher density, there is an increase in drag heating of chondrules in the post-shock region. This is clearly seen in Figure 12, which reflects a higher peak chondrule temperature (1900 K vs. $\sim$ 1860 K) than that of DC02. Cooling rates of chondrules have remained relatively unchanged, although the rapid initial cooling occurs at higher temperatures, naturally (Figure 12). The cooling rates of chondrules in this case are still well within the the chemical and petrological constraints.

It is important to recall that in a steady shock, upstream material is preheated by a radiation precursor over distances determined by the opacity (Mihalas & Mihalas 1984). In a "supercritical" shock (where the pre-shock temperature is equal to the temperature in the post-shock region

immediately following the initial temperature spike), a Marshak wave is driven into the pre-shock material from the shock front and flows until it reaches equilibrium with the surrounding gas. In opaque material, this radiation from the hot downstream material is absorbed in a layer within the cooler upstream material into which it can penetrate by diffusion. Mihalas & Mihalas (1984) derive the thickness of this layer by equating the time required for the radiation to diffuse a distance l from the shock front, $(l/\lambda_{\rm p})^2 \,/\, (\lambda_{\rm p}/c)$, to the time required for the material to be swept back into the shock front, (l/V_s), obtaining

$$l = (c/V_s)\lambda_{\rm p}, \tag{3.1}$$

where $\lambda_{\rm p}$ is the mean free path of a photon. However, this equation does not include the thermal inertia of the gas, assuming a diffusion coefficient, $D = 1/3\ \lambda\ c$. If we include the thermal inertia of the gas, we write l as

$$l = D/V_s, \tag{3.2}$$

where

$$D = V_{\rm eff}\lambda_{\rm p}, \tag{3.3}$$

with

$$V_{\rm eff} = \frac{1}{3}c, \tag{3.4}$$

if the radiation energy density $\gtrsim$ the gas energy density, or

$$V_{\rm eff} = \frac{c}{3}\,\frac{64\pi^2\sigma T^4/c}{\rho_g C_v T}, \tag{3.5}$$

if the gas energy density $\gtrsim$ the radiation energy density. We can use this formulation to determine the optical depth through which the Marshak wave travels, which essentially tells us the boundary location of the Marshak wave:

$$\tau_M = \frac{l}{\lambda_{\rm p}} = \frac{V_{\rm eff}}{V_s} = \frac{1}{3}\frac{c}{V_s}\ \min\ \left[1, \frac{64\pi^2\sigma T^4/c}{\rho_g C_v T}\right]. \tag{3.6}$$

Using a gas density of $\rho_g = 10^{-9}$ g cm^{-3} and $T = 1500$ K (the gas at which dust evaporates in our model) as inputs, this gives $\tau_M \sim 400$. In order to encompass the Marshak wave, we need a large

enough grid space to resolve this much optical depth.

When the upstream material is relatively transparent, the mean free path increases, and as a result, l increases. In this case, the net flow of radiation into the pre-shock material raises the pre-shock temperature and decreases the temperature jump and increases the density jump (Mihalas & Mihalas 1984). This is precisely the effect we see in Figure 13, which shows the results of the shock model after the dust evaporation temperature was lowered to 1500 K, as described in Chapter 2, §6 (Table 6, Case 3).

Additionally, because micron-sized dust evaporates prior to the shock front, the gas cools much more rapidly in the post-shock region (as opposed to the case where the dust does *not* evaporate in the pre-shock region). This is because the radiation generated at the shock is able to diffuse further into the pre-shock region. Although the higher density would normally result in more drag heating and, therefore, higher peak chondrule temperatures, the gas cools so rapidly that the peak chondrule temperature is actually substantially less in this case (Figure 14). Chondrule cooling rates are orders of magnitude higher than in the case where dust does not evaporate, and are inconsistent with experimental constraints. This is also the case when the concentration of chondrule precursors is increased by a factor of ten, as shown in Figures 15 and 16 (Table 6, Case 4). Accumulating evidence from the frequency of compound chondrules and the evidence for the retention of volatiles during chondrule formation (Cuzzi 2001; Ciesla et al. 2004a; Cuzzi & Alexander 2006; Alexander et al. 2008; Cuzzi 2008) increasingly has led to the belief that concentration of chondrule precursors were 10-100 times the solar value for solids, motivating this change in the model.

We next applied our approximation for the dust opacity, as described in §5 (Table 6, Case 5). With the inclusion of both the new dust evaporation temperature *and* the new dust opacity, the results are much more similar to those of DC02. However, the much higher dust opacity does not allow the radiation precursor to propagate far into the pre-shock region (l is small). As a result, less "pre-heating" of the upstream material occurs (Figure 15). Once the gas and dust reach the

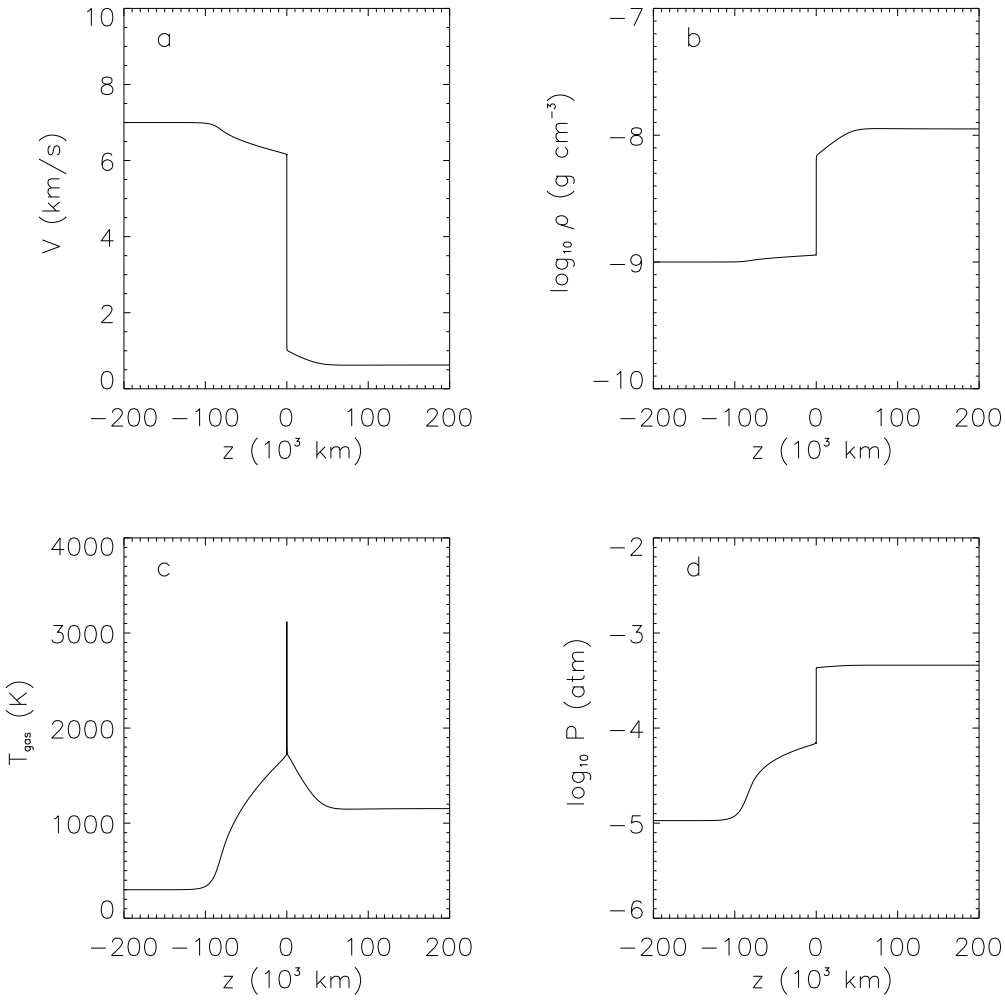

FIG. 8 — Case 1 (see Table 6). Gas properties [(a) velocity, (b) density, (c) temperature, and (d) pressure] as a function of the distance z from the shock front. The pre-shock region here is on the left. A steady state is assumed; the properties of an individual gas parcel as a function of time are found by reading these graphs from left to right. These results are consistent with those of DC02.

shock, the dust evaporates, resulting in lower peak temperatures for the chondrules (Figure 16). In this case, only partial melting of chondrules occurs, for the same shock speed, density, etc. Initial cooling rates are similar to those of DC02 (a few times 10^4 K hr^{-1}), however cooling rates are higher through the hotter end of the crystallization range, although they are mostly within the range matching experimental constraints. It is obvious that with the updated inputs, a shock speed slightly faster than 7 km s^{-1} is necessary to result in complete melting of chondrules.

We present the results of the updated model with an increased shock speed of 8 km s^{-1}

in Figures 19 and 20 (Table 6, Case 6). Micron-sized dust clearly evaporates in the pre-shock region, around 10^5 km ahead of the shock front (Figure 19c). In this case, the peak temperatures achieved by chondrules is $\sim$ 2000 K, resulting in complete melting. The cooling rates are consistent with experimental results. The chondrules experience rapid initial cooling at several times 10^4 K hr^{-1}, and experience cooling rates of 10-20 K hr^{-1} through their crystallization temperatures. We consider these to be the results of our "canonical" case: pre-shock density, $\rho_g = 10^{-9}$ g cm^{-3}, $V_s = 8$ km s^{-1}, $\rho_s/\rho_g = 5$ x 10^{-3}, and $\mathcal{C} = 10$.

The results of increasing the shock speed yet again, to 9 km s^{-1}, are shown in Figures 21 and 22 (Table 6, Case 7). The gas now reaches an initial peak temperature of $>$ 4500 K. The peak temperature of chondrules artificially remains at 2000 K, and does not climb any higher, because we have set the evaporation temperature of chondrule-sized particles to 2000 K. At this temperature, chondrules evaporate from an initial radius of 300 μm, to $\sim$ 210 μm by the end of the computational domain, losing 65% of their mass.

Leaving all other parameters unchanged from the canonical case, we then investigated the effect of increasing/decreasing the gas density (Table 6, Case 8). Figures 23 and 24 show the results when the density is decreased by a factor of 10. Chondrule precursors just barely begin to melt in this case, only reaching peak temperatures of $\sim$ 1500 K. Cooling rates are much too high to match the constraints on chondrule thermal histories. When we attempted to increase the density, the code became unstable, and no results were obtained.

We now have results in our canonical case (neglecting the effects of line cooling) that describe the thermal histories of chondrules in a manner consistent with the chemistry and petrology of chondrules. The task remains to investigate the effects of line cooling.

TABLE 6
RESULTS OF PARAMETER STUDY, NEGLECTING LINE COOLING

Case No.	$\mathcal{C}$	V_s	ρ_g (g cm^{-3})	H_2O[a]	$T_{\rm peak}$ (K)	Cooling rate (K hr^{-1})[b]	Cooling rate (K hr^{-1})[c]
1	1	7	10^{-9}	1	1800	> 2 x 10^4	14-50
2	1	7	10^{-9}	1	1900	> 2 x 10^4	24-40
3	1	7	10^{-9}	1	1500	> 3 x 10^5	N/A
4	10	7	10^{-9}	1	1500	> 3 x 10^5	N/A
5	10	7	10^{-9}	1	1640	> 2 x 10^4	37-100[e]
6	10	8	10^{-9}	1	2000	> 5 x 10^4	5-20
7	10	9	10^{-9}	1	2000[d]	1100	8-20
8	10	8	3 x 10^{-10}	1	1500	N/A	6 x 10^4

[a]Water abundance with respect to our assumed water-to-gas ratio, 8 x 10^{-4}.

[b]Cooling rates at $T_{\rm peak}$

[c]Cooling rates through 1400-1800 K, the crystallization temperature range of chondrules.

[d]Artificial peak temperature due to evaporation. See text for final radius of chondrules.

[e]Cooling rates through 1400-1499 K; rates are $\sim$ 2 x 10^4 from 1500-1640 K.

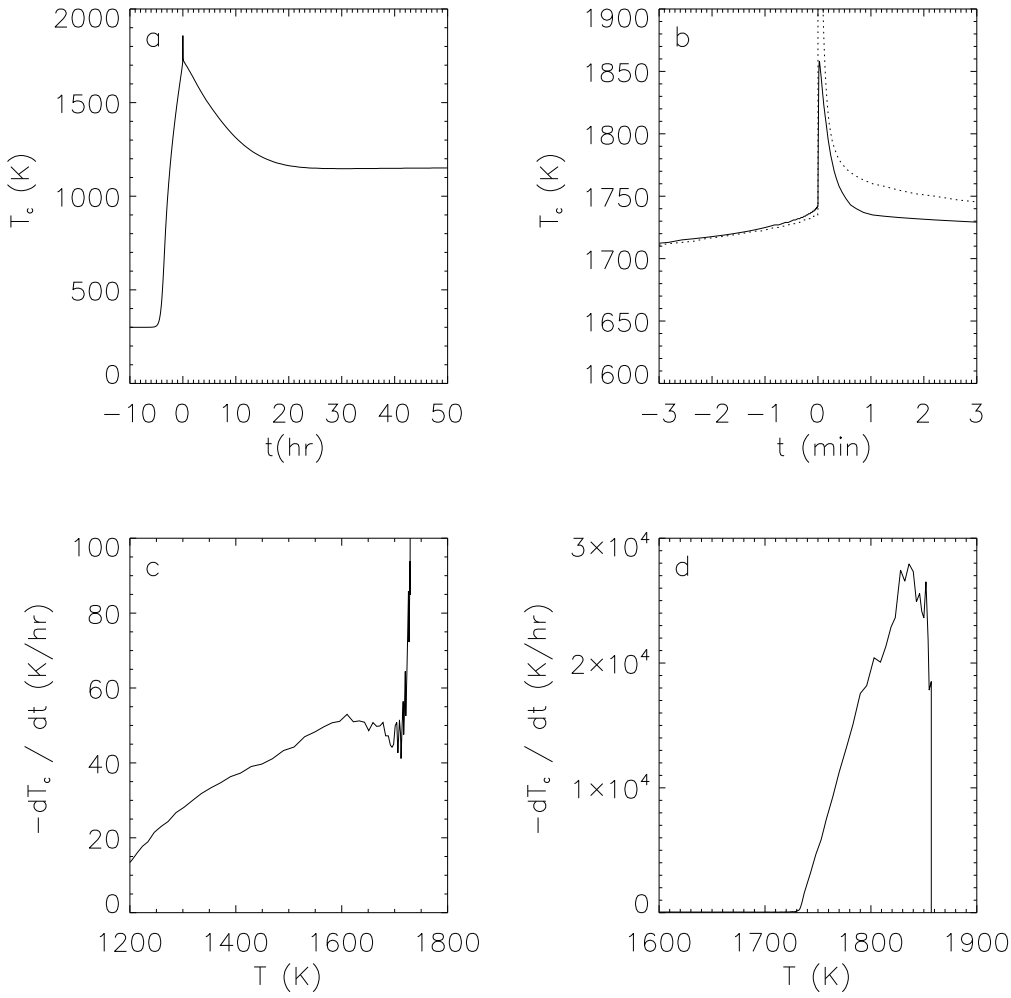

FIG. 9 — Case 1 (see Table 6). Thermal history of chondrules in a shock. The chondrules' temperatures (solid line) over the course of hours (a), and also minutes (b), where it is contrasted with the temperature of the gas (dotted line). Chondrules in the pre-shock region are heated by radiation. The cooling rates of chondrules as a function of temperature through the crystallization temperatures (c), and at higher temperatures (d), when heating is dominated by gas drag. These results are consistent with those of DC02.

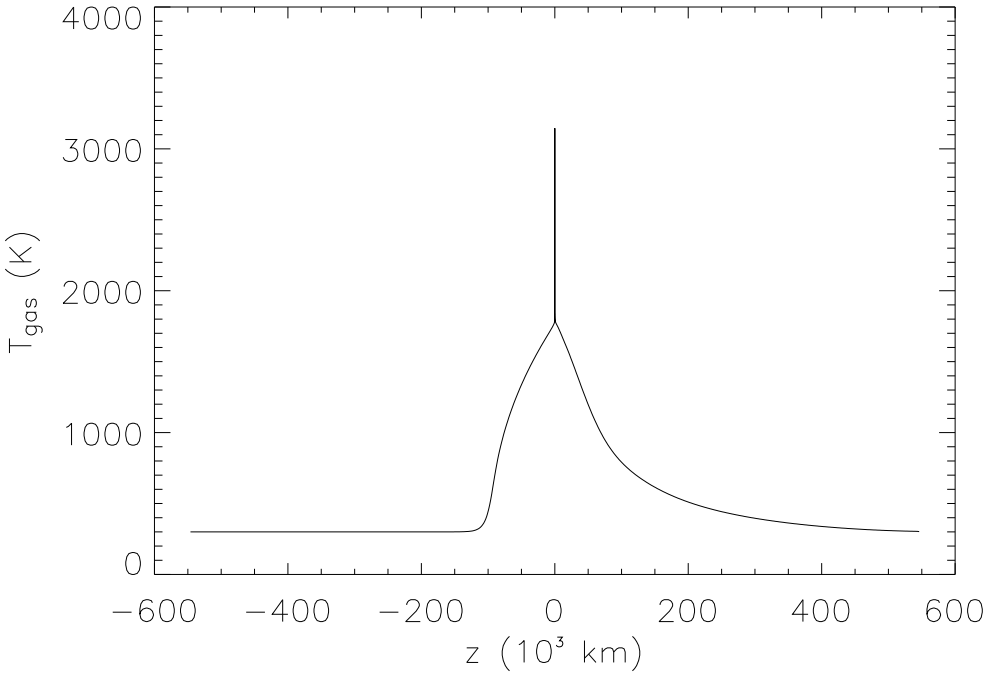

FIG. 10 — Gas temperature as a function of the distance z from the shock front.

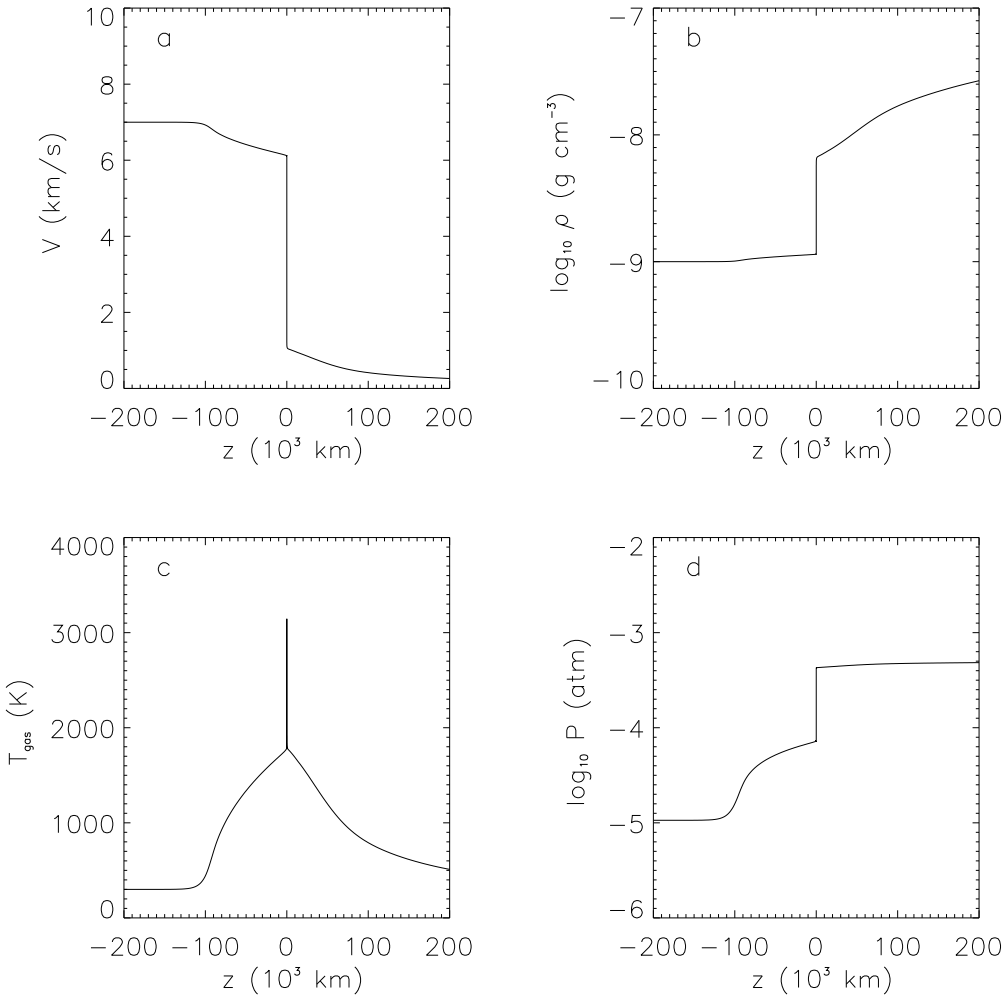

FIG. 11 — Case 2 (see Table 6). Same as Figure 8, except with $T_{\rm post} = T_{\rm pre} = 300$ K, as described in Chapter 2, §4.

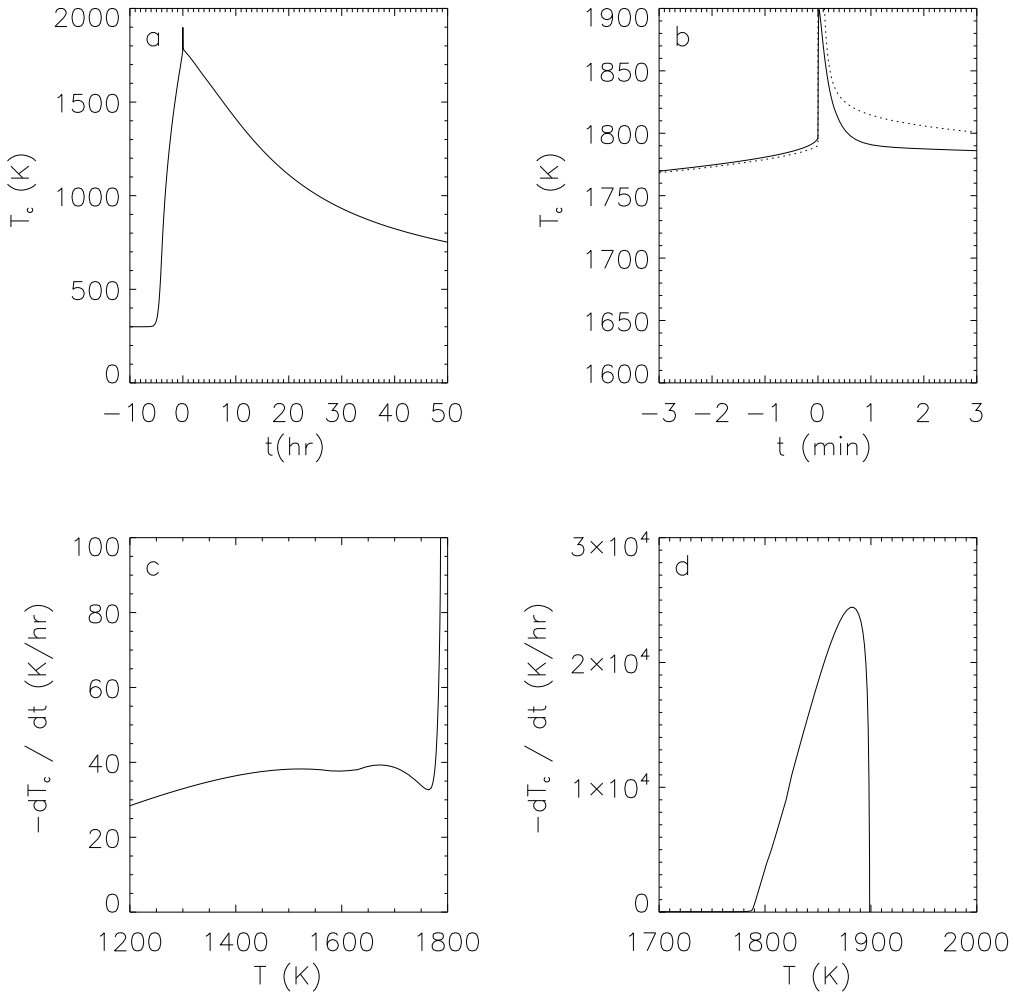

FIG. 12 — Case 2 (see Table 6). Same as Figure 9, except with $T_{\rm post} = T_{\rm pre} = 300$ K, as described in Chapter 2, §4.

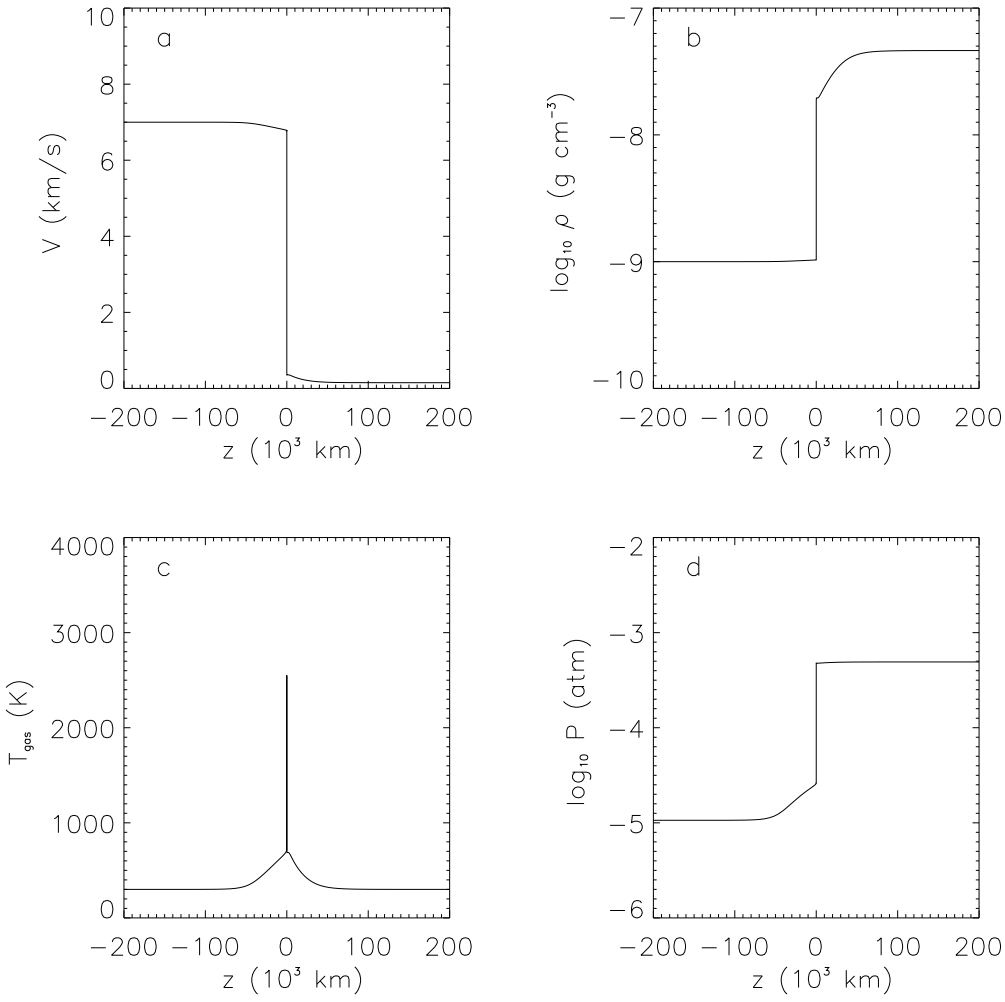

FIG. 13 — Case 3 (see Table 6). Same as Figure 11, except in this case, dust evaporates at 1500 K, as described in Chapter 2, §6.

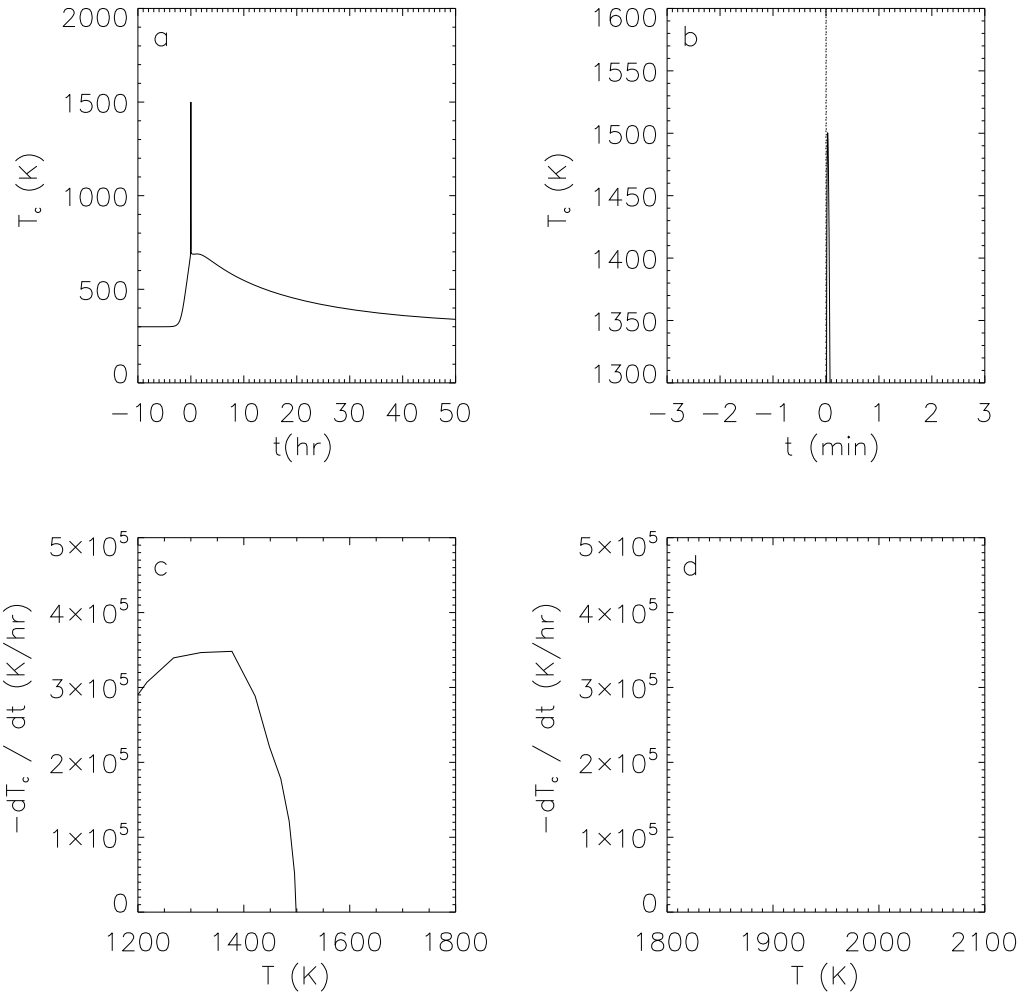

FIG. 14 — Case 3 (see Table 6). Same as Figure 12, except in this case, dust evaporates at 1500 K, as described in Chapter 2, §6.

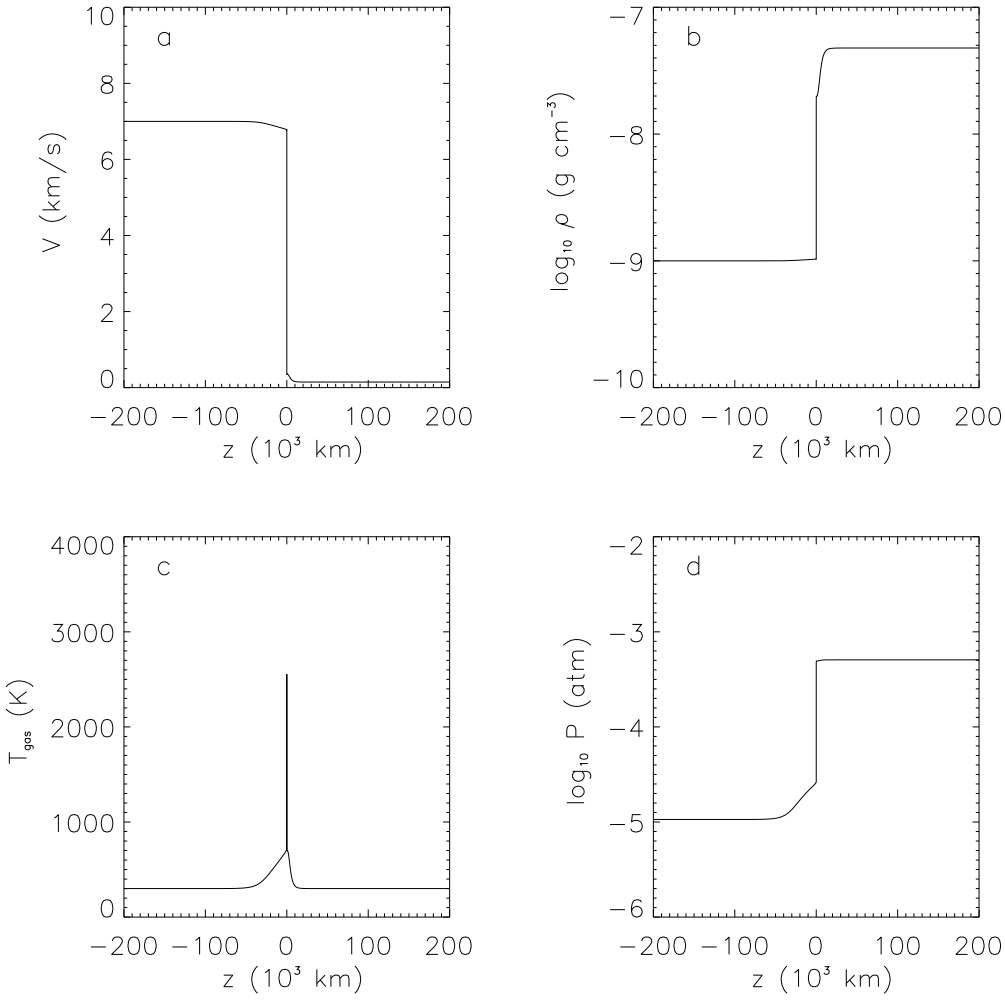

FIG. 15 — Case 4 (see Table 6). Same as Figure 13, except this case assumes a chondrule precursor concentration 10 times that of DC02 ($C = 10$).

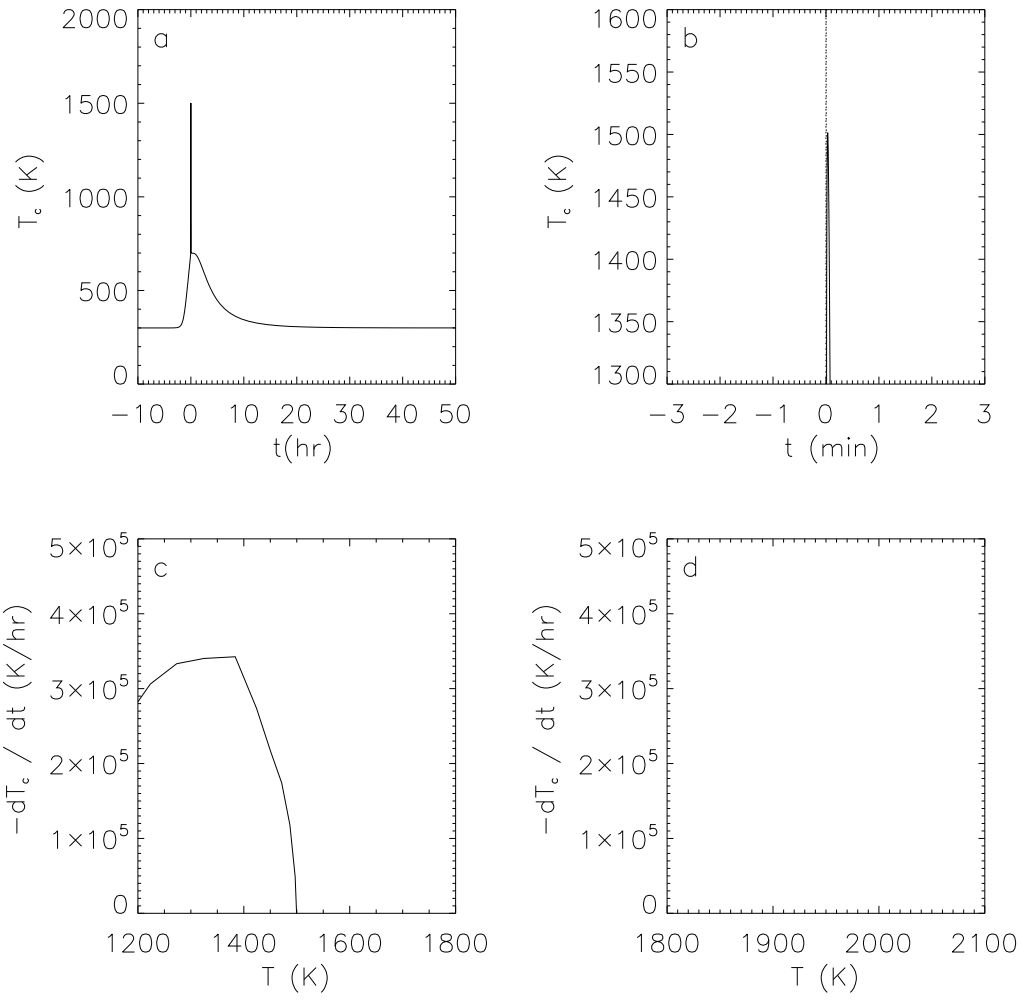

FIG. 16 — Case 4 (see Table 6). Same as Figure 14, except this case assumes a chondrule precursor concentration 10 times that of DC02 ($C = 10$).

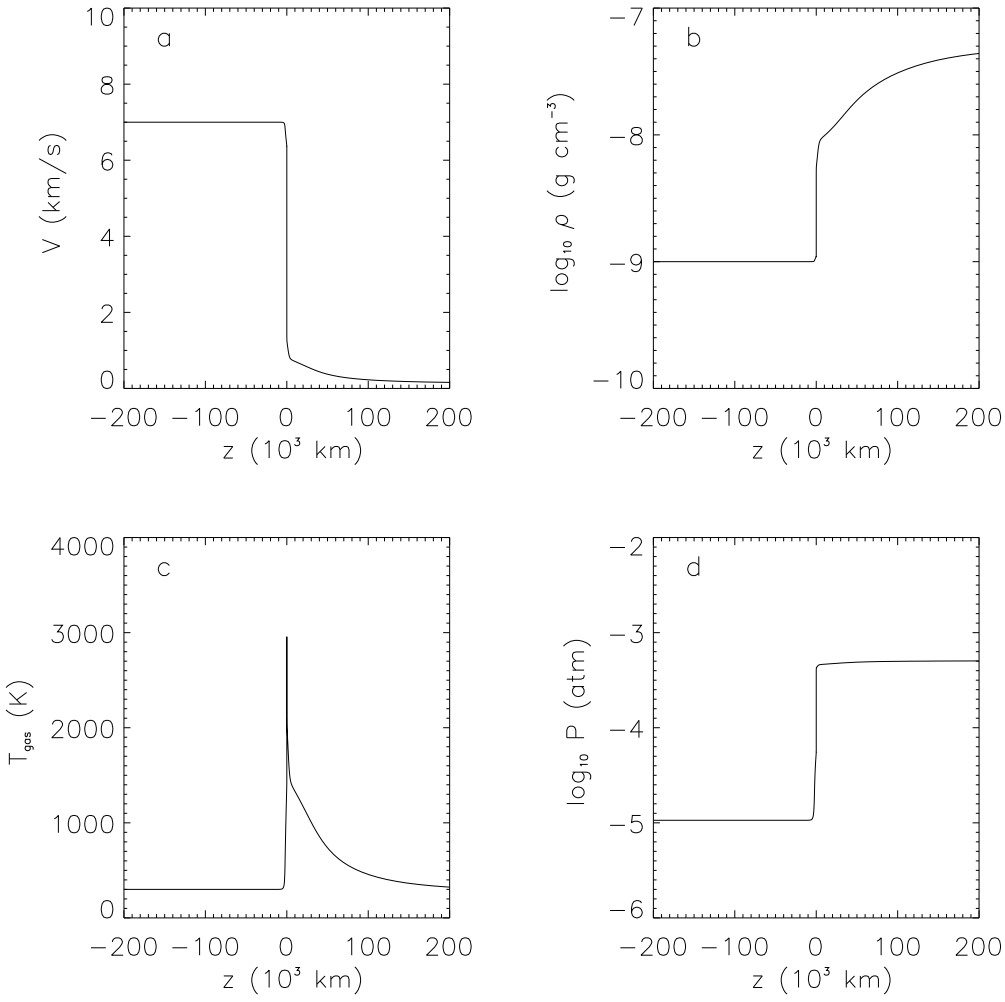

FIG. 17 — Case 5 (see Table 6). Same as Figure 15, except in this case, we use the new dust opacity as described in Chapter 2, §5.

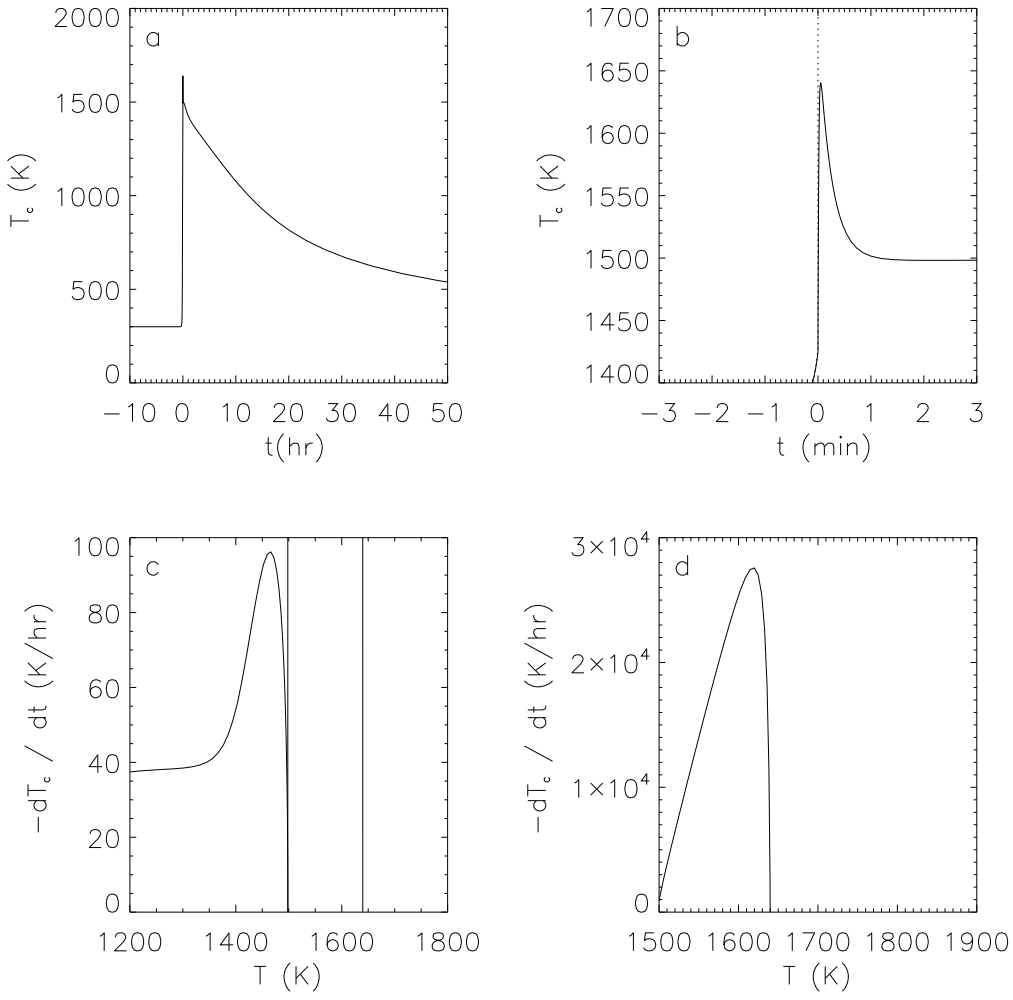

FIG. 18 — Case 5 (see Table 6). Same as Figure 16, except in this case, we use the new dust opacity as described in Chapter 2, §5.

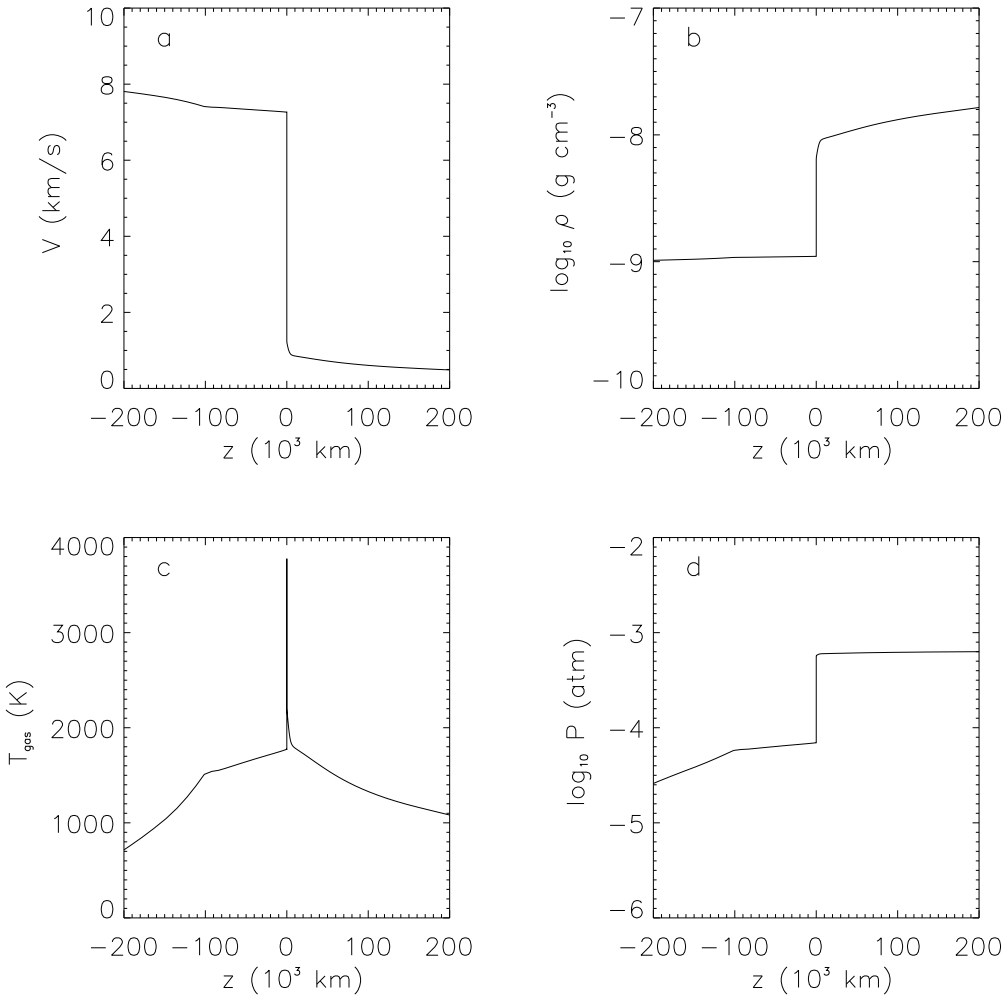

FIG. 19 — Case 6 (see Table 6). Same as Figure 17, except with a shock velocity, $V_s = 8$ km s^{-1}. This is our "canonical" case neglecting line cooling.

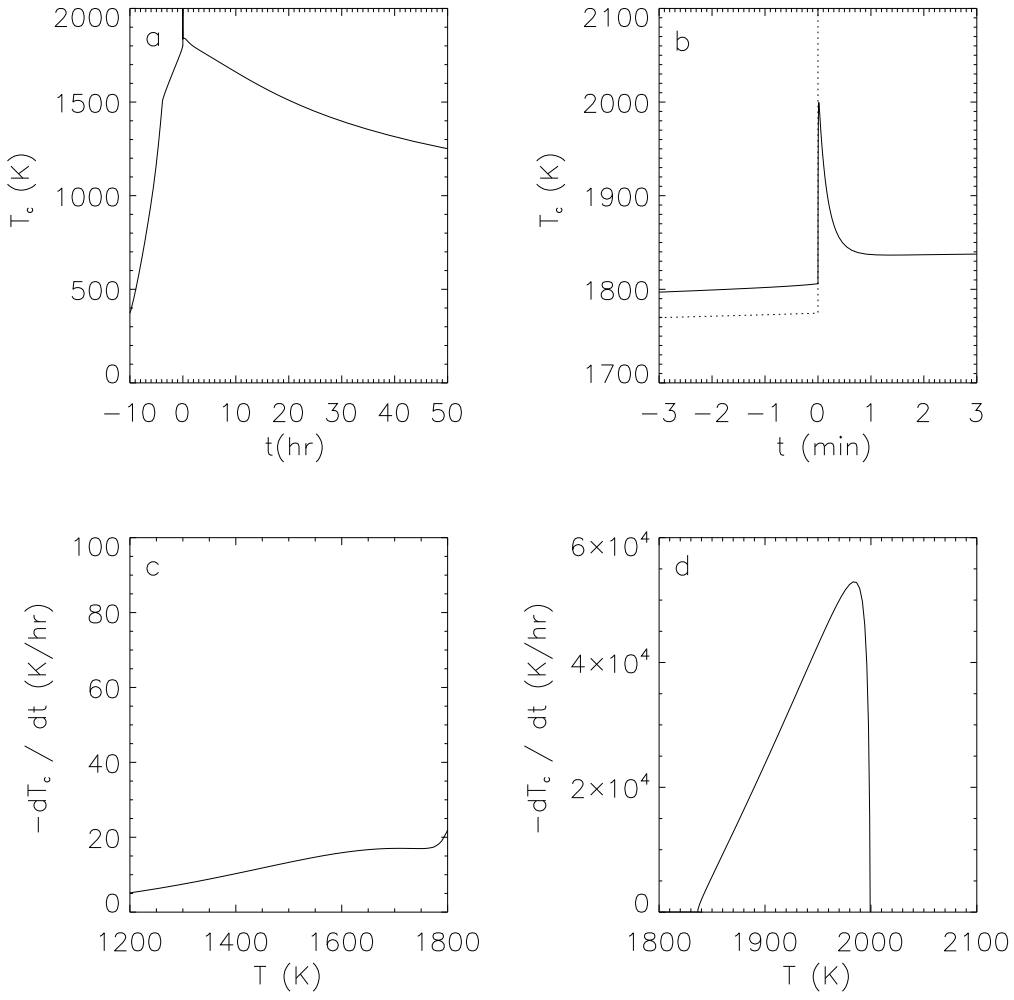

FIG. 20 — Case 6 (see Table 6). Same as Figure 18, except with a shock velocity, $V_s = 8$ km s^{-1}. This is our "canonical" case neglecting line cooling.

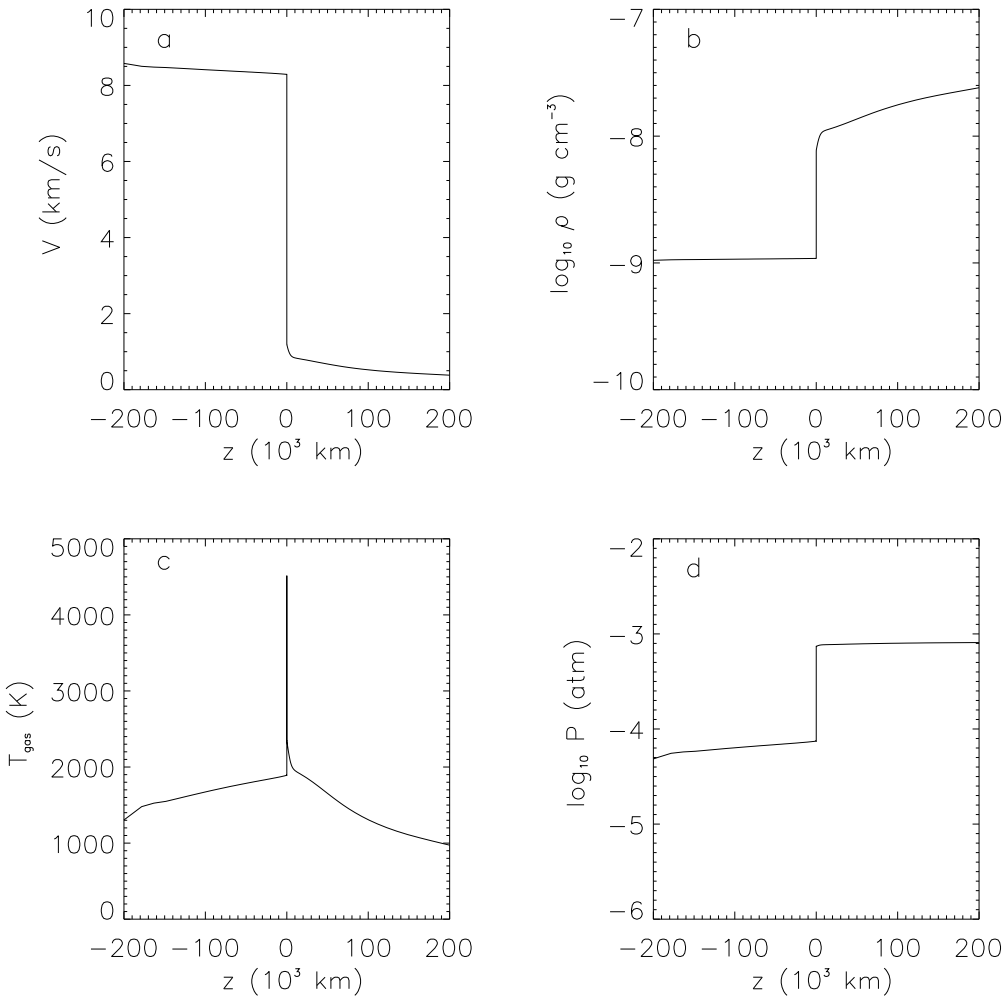

FIG. 21 — Case 7 (see Table 6). Same as Figure 19, except with shock speed, $V_{\rm s} = 9$ km s^{-1}.

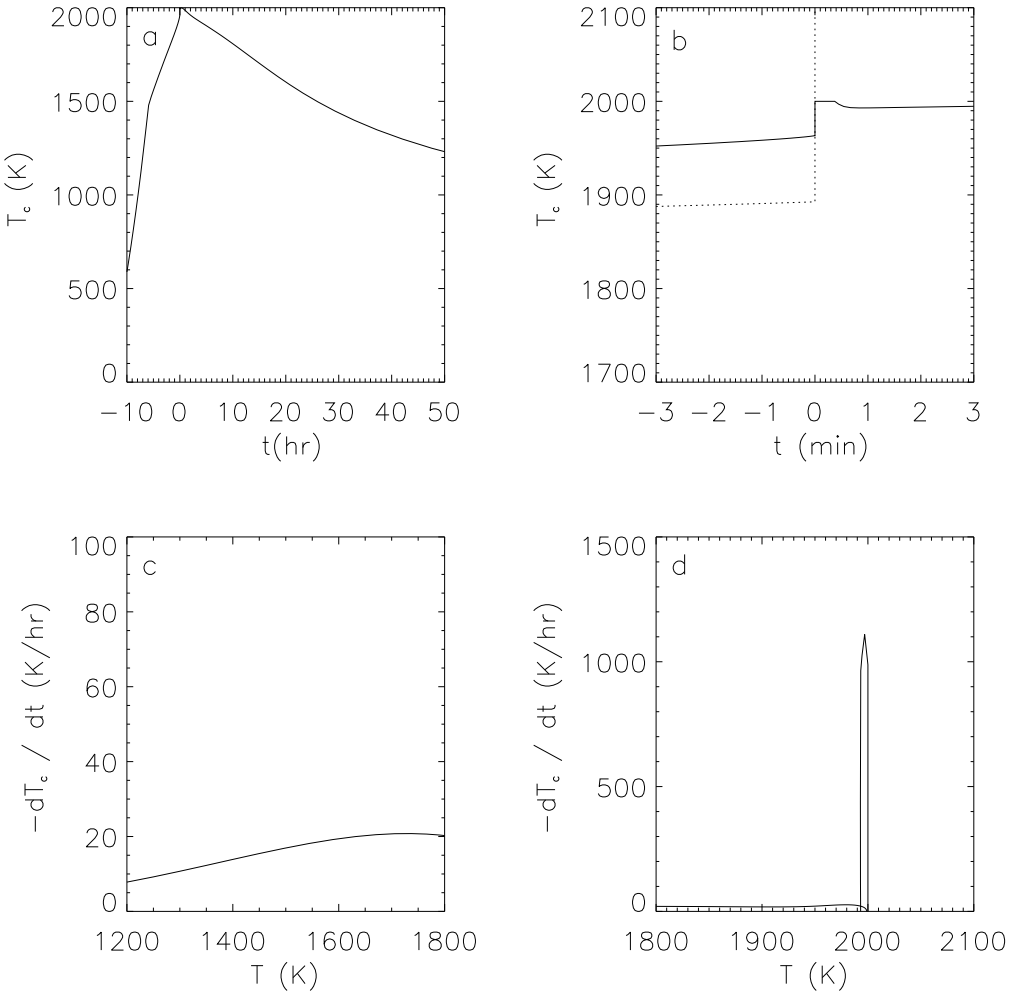

FIG. 22 — Case 7 (see Table 6). Same as Figure 20, except now the shock speed, $V_s = 9$ km s^{-1}.

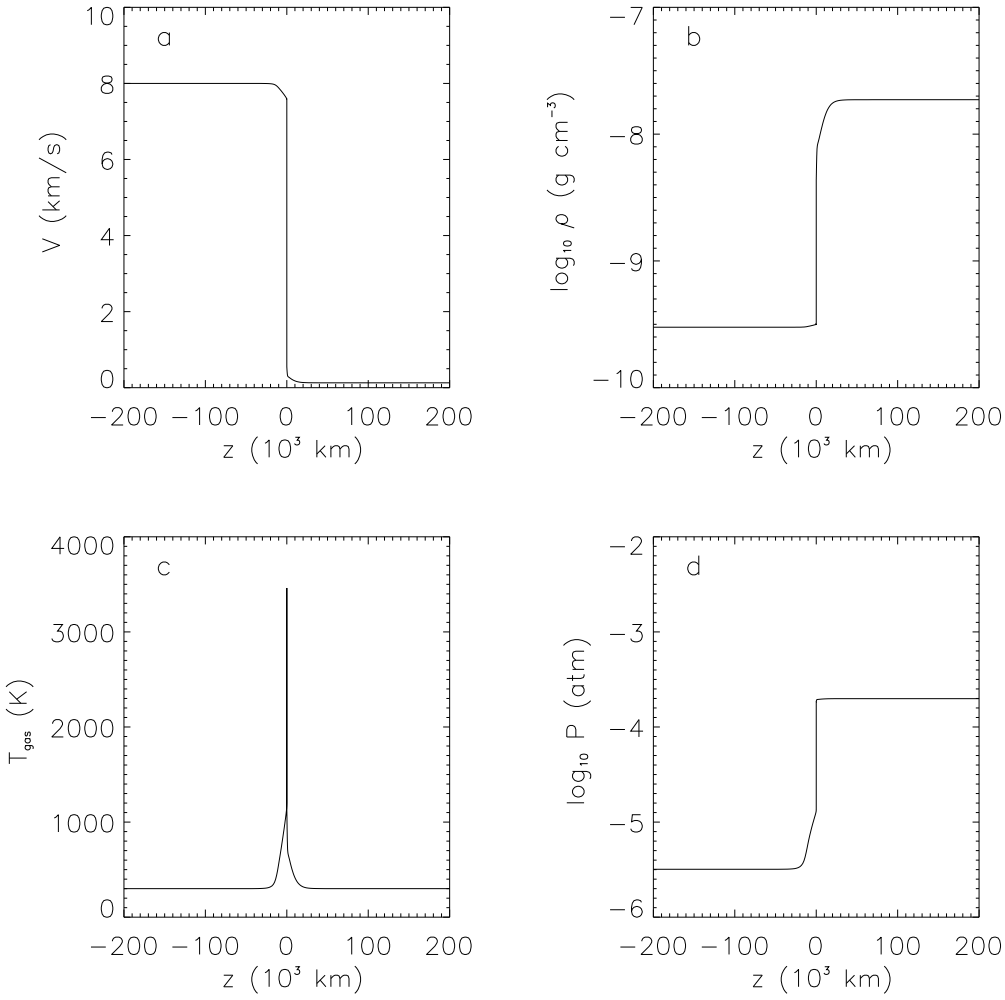

FIG. 23 — Case 8 (see Table 6). Same as Figure 19, except with $\rho_0 = 3 \text{ x } 10^{-10}$ g cm^{-3}.

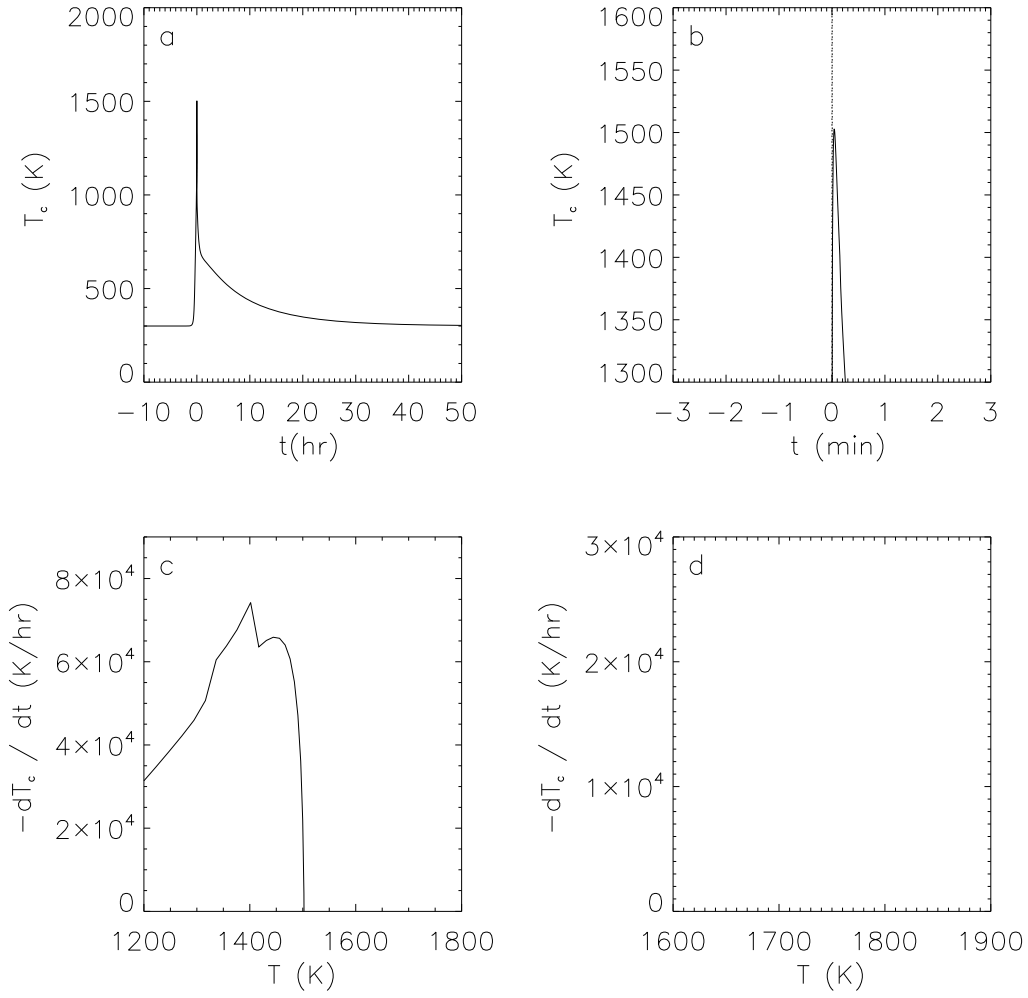

FIG. 24 — Case 8 (see Table 6). Same as Figure 20, except with $\rho_0 = 3$ x10^{-10} g cm^{-3}.

CHAPTER 4

LINE COOLING

1. Radiative Transfer and Line Cooling

NOTE: Material in this chapter was published in The Astrophysical Journal (Morris et al. 2009).

In many astrophysical settings, emission of radiation via rotational and vibrational transitions of molecules plays an important role in cooling warm gas. Because the emission of such radiation is in sharp spectral lines, this mechanism is referred to as line cooling. Line radiation from the water molecule H_2O, with its permanent electric dipole and its high cosmochemical abundance, is significant in a variety of settings ranging from molecular clouds to protostellar envelopes (e.g., Cernicharo & Crovisier 2005). More recently, line cooling from H_2O molecules has been recognized to play a pivotal role in the energetics following the passage of a shock wave through the dense gas in the solar nebula protoplanetary disk (see Desch et al. 2005).

The rate of emission of line radiation from a warm gas containing water molecules is difficult to calculate, because there are so many accessible rotational and vibrational energy levels, and therefore a great many transitions. In dense molecular gas ($n_{\rm H2} > 10^{10}\,{\rm cm}^{-3}$), these energy levels are populated according to Boltzmann statistics (i.e., are in local thermodynamic equilibrium, or LTE), but at lower densities the populations must be calculated by balancing transition rates. Finally, the cooling of gas by line radiation relies on the ability of the photons to escape the system without being reabsorbed, to the extent that other, nearby molecules can absorb the emitted photons, the gas does not cool. Photons generated during a molecular transition are emitted and also reabsorbed over a small range of frequencies centered on the line frequency, with an efficiency that depends on the frequency shift from the line center. Rather than integrating the equations of radiative transfer over all frequencies within the line, all standard treatments of the problem instead assume integration over this "line profile" and use a frequency-integrated escape probability of photons. This escape probability is a function of the column density of the molecule within the system. This is the approach taken by Neufeld & Kaufman (1993; hereafter NK93), in particular.

The calculation of NK93 of the rate of line cooling from H_2O molecules has remained the state of the art for 15 years; but, as we discuss below, several aspects of the NK93 calculation are now out of date. Their calculation uses a limited database of transitions, an oversimplified escape probability formulism, and ignores absorption by dust grains. It is one of the goals of the work here to update the H_2O line cooling rates to improve on the calculations of NK93. A second goal is to assess whether or not line cooling plays a significant role in cooling the gas following the passage of a shock through the dense gas of the solar nebula. As discussed by Desch et al. (2005), previous modeling has not determined whether or not line cooling can be neglected. This has significant implications for the issue of chondrule formation.

2. Estimates of Line Cooling in Shocks

Chondrules and gas are thermally coupled only a few minutes after passing through the shock front (INSN; DC02; CH02), so these chondrule cooling rates are controlled by the rate at which gas cools by emission of line radiation. To understand the essence of their results without reproducing all of their calculations in detail, we now estimate the cooling rate of chondrules and gas following the shock, using the tabulations of NK93.

We first examine how the cooling rates predicted by NK93 and used by INSN and Miura & Nakamoto (2006) are calculated. For a wide range of densities and temperatures, NK93 calculated the steady-state level populations of H_2O and CO molecules (denoted 'M'), and the rates of emission of photons. The escape of these photons from a system was considered under the large velocity gradient (Sobolev) approximation as a function of column density $n(M)d$, via use of the parameter

$$\tilde{N} \equiv \frac{n(M)}{dv_z/dz}, \tag{4.1}$$

These results were adapted to a large range of geometries of interest, including those not consistent with the Sobolev approximation, in particular the one of relevance to nebular shocks, a static, plane-parallel slab of thickness d. According to NK93, the cooling rate at the center of the slab (at

depth $d/2$) will depend on the similar parameter

$$\tilde{N} = \frac{n(M)\, d}{\Delta v}, \tag{4.2}$$

where Δv is the thermal velocity of the molecules M. An important assumption made by NK93 is that if the line photons can escape to the edge of the slab, then the gas is cooled; if the photons do not escape to the edge of the slab, they are essentially reabsorbed on the spot and there is no cooling. The cooling rate per volume is then $n(m)\mathcal{L}_{\rm LTE}(\tilde{N})$, where the subscript 'LTE' is the notation used by NK93 to denote cooling rates derived under the assumption that the population levels follow a Boltzmann distribution, which is the regime of interest for solar nebula shocks. NK93 have tabulated $\mathcal{L}_{\rm LTE}(\tilde{N})$ for both vibrational and rotational lines of H_2O and CO, for every decade in $\tilde{N}$.

The plane-parallel slab is equivalent to the nebula shock geometry because of the large velocity jump at the shock front. In a typical chondrule-forming shock, the gas velocity changes nearly instantaneously from $\approx 7\,{\rm km\,s^{-1}}$ to $\approx 1.6\,{\rm km\,s^{-1}}$, a jump of over $5\,{\rm km\,s^{-1}}$. This velocity difference is much larger than the thermal velocities of the H_2O molecules [$\Delta v = (2kT/m_{\rm H2O})^{1/2}$ $= 1.36\,{\rm km\,s^{-1}}$ at 2000 K] that control the width of the line profile. Essentially, once a line photon emitted from the post-shock gas escapes to the shock front, it will continue to travel relatively unimpeded by gas. Only one change to the NK93 formulation must be made before it is adopted to the nebular shock geometry. For gas a distance z past the shock front, the equivalent thickness of the slab is $d = 2z$, and the cooling rate is only half the cooling rate calculated by NK93, who assumed radiation could escape either side of the slab.

The cooling rate of the gas yields

$$\frac{\partial e}{\partial t} = \frac{\partial}{\partial t}\left(\frac{p}{\gamma - 1}\right) = 2.8\, n_{\rm H2}\, k\, \frac{\partial T}{\partial t} = -\frac{1}{2}\, n({\rm H_2O})\, \mathcal{L}_{\rm LTE}(\tilde{N}), \tag{4.3}$$

where we have ignored compression of the gas after passing through the shock front in this toy model, and we have assumed an abundance of He of 10% by number. Converting the time derivative to a

spatial derivative by assuming a constant gas velocity $V_{\rm g}$ past the shock front, we find

$$\frac{\partial T}{\partial \tilde{N}} = -\frac{\Delta v}{5.6 n_{\rm H2} V_{\rm g} k} \frac{\mathcal{L}_{\rm LTE}(\tilde{N})}{2}, \tag{4.4}$$

where we have assumed a constant Δv throughout the post-shock region. In actuality, Δv would decrease past the shock front, but that would merely reduce the total cooling, so our assumption overestimates the degree of cooling. This formula provides the gas temperature as a function of $\tilde{N}$, the effective column density past the shock front.

Fedkin & Grossman (2006) showed that the $n_{\rm H2O}/n_{\rm H2}$ ratio in the solar nebula probably varied with temperature, but found that $n_{\rm H2O}/n_{\rm H2} = 5 \times 10^{-4}$ was a good average for the temperatures of interest. We have adopted a canonical ratio $n_{\rm H2O}/n_{\rm H2} = 8 \times 10^{-4}$. This is only slightly higher than some commonly assumed canonical ratios but is consistent with the abundance of Lodders (2003), $n_{\rm H2O}/n_{\rm H2} = 8.88 \times 10^{-4}$. We note that the exact value of $n_{\rm H2O}/n_{\rm H2}$ in the chondrule formation environment is likely variable with time within the solar nebula (Ciesla & Cuzzi 2006), and consider variations in this ratio later in the paper. Some dissociation of H_2O is likely to occur at the peak post-shock temperatures we consider, but we are interested in the maximum cooling possible by line photons, so we neglect dissociation in our calculations.

Interpolating between the tabulated values of $\mathcal{L}_{\rm LTE}(\tilde{N})$ provided by NK93, we have integrated equation 4.4 to find the total drop in temperature by the time the gas is at the equivalent of $\tilde{N} = 10^{21}\,{\rm cm^{-2}\,km^{-1}\,s}$ past the shock front. For typical parameters (pre-shock density $n_{\rm H2} = 2 \times 10^{14}\,{\rm cm^{-3}}$ and velocity $V_{\rm g} = 7\,{\rm km\,s^{-1}}$; mixing ratio $n_{\rm H2O}/n_{\rm H2} = 8 \times 10^{-4}$; post-shock density $n_{\rm H2} = 1.2 \times 10^{15}\,{\rm cm^{-3}}$ and velocity $V_{\rm g} = 1.2\,{\rm km\,s^{-1}}$; and post-shock thermal velocity $\Delta v = 1.6\,{\rm km\,s^{-1}}$), this equates to $d = 1.3 \times 10^4\,{\rm km}$, a distance $z = 6.6 \times 10^3\,{\rm km}$, and a time 1.6 hours after passing through the shock front. (Again, this toy model neglects the compression and slowing of the gas. It also assumes wrongly that Δv is constant, whereas it should decrease slightly as the gas cools. It is nonetheless illustrative.) At these distances past the shock front, the total cooling due to rotational lines of H_2O and CO is completely negligible, $< 4\,{\rm K}$. This illustrates that

the rotational lines become optically thick so quickly that they are unable to escape the post-shock region and cool the gas. On the other hand, the total cooling from CO vibrational line photons is roughly 72 K. This leads to an average cooling rate of $\sim 40\,\mathrm{K\,hr^{-1}}$, which is important, but not significantly greater than the cooling rates of chondrules ($\sim 10^2\,\mathrm{K\,hr^{-1}}$). The assumption of INSN that the lines of H_2O and CO are optically thin is therefore invalidated, because these lines are indeed optically thick. The final line cooling mode (not considered by INSN, but considered by Miura & Nakamoto 2006) is vibrational line cooling from H_2O. We find a total cooling due to these line photons on the order of 800 K. This is a significant cooling of the gas: the average cooling over 1.6 hours is $\sim 500\,\mathrm{K\,hr^{-1}}$, with even higher cooling rates obtained early on. The cooling of the gas by vibrational line photons of H_2O, despite being somewhat optically thick, is the source of the high chondrule cooling rates predicted by Miura & Nakamoto (2006). We confirm the statement made by Miura & Nakamoto (2006) that "...line emission is important for the gas cooling." We hereafter focus on cooling due to H_2O alone, as the dominant coolant is expected to be water.

Clearly, any model of chondrule cooling rates in solar nebula shocks must account for the emission of line photons from H_2O. However, incorporating the cooling rates of NK93 directly into a shock code, as Miura & Nakamoto (2006) did, is not ideal. First, line cooling due to rotational and vibrational transitions of H_2O was calculated by NK93 using roughly 50,000 transitions from the HITRAN database (Rothman et al. 1987). While this was the best available data at the time, much more extensive databases now exist. Second, NK93 calculated escape probabilities under the large velocity gradient (Sobolev) approximation, and asserted, but did not demonstrate, that the results will apply to the case of a static, plane-parallel slab if $\tilde{N}$ is defined as described above. Third, NK93 assumed a one-sided escape probability for line photons equal to $0.5/(1+3\tau)$, where τ is the Sobolev optical depth; more exact escape probabilities exist, as described below. Fourth, it is not necessarily the case that if photons do not escape to the edge of the slab that the gas does not cool locally; photons reabsorbed halfway to the edge still cool the gas at the slab center. Finally, NK93 did not consider the absorption of line photons by intervening dust. Inclusion of dust is absolutely

mandatory, as the following argument makes clear: For a solar-composition gas with 0.5% of the mass in the form of $a = 0.5\,\mu$m radius grains (similar to the size of matrix dust grains in meteorites), the opacity to short-wavelength radiation is as high as $\kappa = (\rho_{\rm dust}/\rho_{\rm gas})\,(3/4\rho_{\rm s}a) = 30\,{\rm cm}^2\,{\rm g}^{-1}$, where the internal density of the dust grains is $\rho_{\rm s} \approx 2.5\,{\rm g\,cm}^{-3}$. Over the distance for which the optical depth in dust is unity, the parameter $\tilde{N}$ is therefore less than $10^{19}\,{\rm cm}^{-2}\,{\rm km}^{-1}\,{\rm s}$, assuming a ratio $n_{\rm H2O}/n_{\rm H2} = 8 \times 10^{-4}$. This corresponds to distances $\sim 10^3\,{\rm km}$, or times of about 10 minutes after passage through the shock front. As this is smaller than the $\tilde{N}$ for which the most significant cooling takes place, dust grains are capable of absorbing photons that would otherwise cool the gas. A thorough treatment of line cooling should improve on the calculations of NK93 in the areas identified above.

3. Calculation of H_2O Cooling Rates

We have used the SCAN-H_2O database of Jørgensen et al. (2001) of 1.2 million lines (rotational plus vibrational) of the H_2O molecule to calculate the cooling rates due to emission of line photons from H_2O. We continue to assume, as NK93 did, that if photons are not able to escape the region entirely, they are reabsorbed on the spot. This assumption will be relaxed in future work, but for now it allows a crude estimate of the importance of line radiation. In other respects, we improve on the NK93 calculation by more accurately calculating escape probabilities, and by including the possibility of absorption by dust grains.

3.1. *Escape Probabilities Without Dust*

The probability that a line photon will escape a semi-infinite volume, otherwise known as the one-sided escape probability, $P_{\rm esc}$, is given by

$$P_{\rm esc} = \frac{1}{2} \int_{-\infty}^{\infty} \Phi(x)\; E_2(\tau\Phi(x))\; dx, \tag{4.5}$$

$$x \equiv \frac{\lambda - \lambda_0}{\Delta\lambda_D}, \tag{4.6}$$

$$\Delta\lambda_D = \frac{c}{\lambda_0}\sqrt{\frac{2kT}{m_{\rm H2O}}} \tag{4.7}$$

(Avrett & Hummer 1965; Hummer & Rybicki 1971; Rybicki & Lightman 1979; Bowers & Deeming 1984). Here Φ(x) is the line profile, x is the frequency measured from line center in Doppler widths ($\Delta\lambda_D$), and E_2 is the second exponential integral. In equation 4.5, τ refers to the optical depth integrated over the line, which is $\sqrt{\pi}$ times the optical depth at line center. Considering the combined effect of both Doppler and Lorentz broadening, the line profile is given by the normalized Voigt profile

$$\Phi(x) = \frac{a}{\pi^{3/2}} \int_{-\infty}^{\infty} \frac{e^{-y^2}}{(x-y)^2 + a^2}\, dy, \tag{4.8}$$

(Avrett & Hummer 1965; Rybicki & Lightman 1979; Bowers & Deeming 1984), where a is the ratio of Lorentz to Doppler width (Avrett & Hummer 1965). In astrophysical situations $a \ll 1$, perhaps as large as 0.1 (Mihalas 1978; Bowers & Deeming 1984). In this study, the Voigt profile was calculated using the algorithm of Zaghloul (2007), where the Voigt function is written as a single proper integral with a damped sine integrand:

$$\Phi(x) = \exp\left(a^2\right)\mathrm{erfc}(a)\exp\left(-x^2\right)\cos(2ax) \;+\; \frac{2}{\sqrt{\pi}} \int_0^x \exp\left[-(x^2-y^2)\sin(2a(x-y)\right]\, dy, \tag{4.9}$$

where erfc is the complimentary error function. Using 4.9, Voigt functions were calculated for three different values of a and are shown in Figure 2. These results are consistent with the results of Zaghloul (2007). Utilizing these values for $\Phi(x)$, straightforward numerical integration was performed to calculate the "exact" one-sided escape probability $P_{\rm esc}$ in the absence of dust.

Besides the form adopted by NK93, several other approximations to the one-sided escape probability exist in the literature. Hollenbach & McKee (1979) give the following approximation to the one-sided escape probability:

$$P_{\rm esc} = \frac{1}{2}\,\frac{1}{1+\tau\left(2\ln\left(2.13+\tau^2/\pi\right)\right)^{1/2}}. \tag{4.10}$$

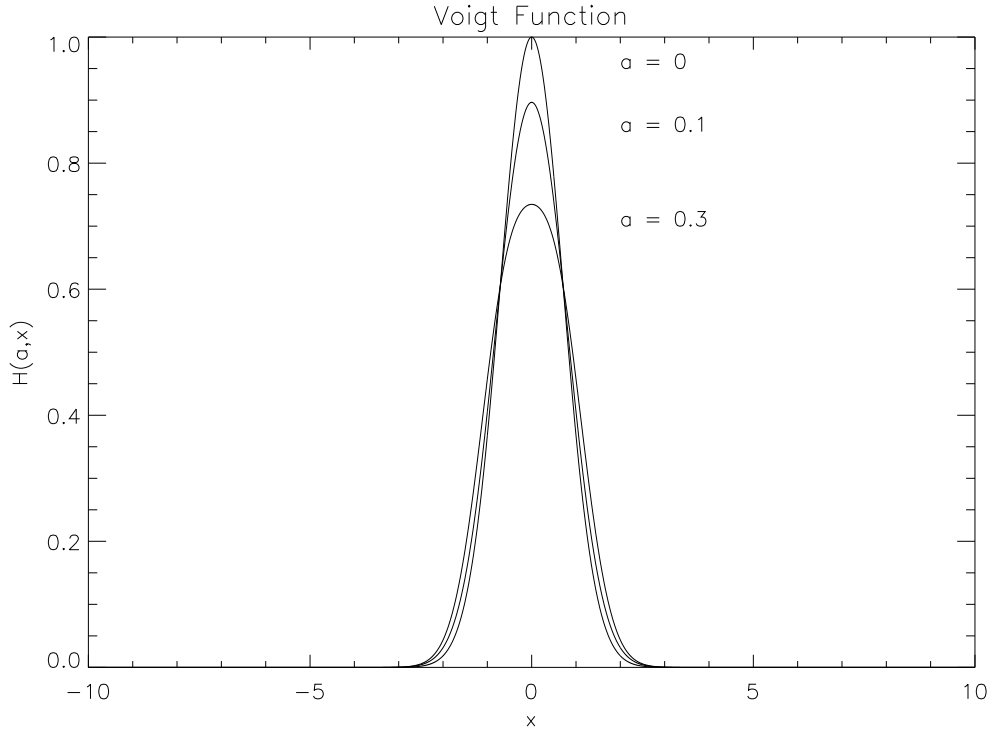

FIG. 25 — Voigt functions calculated using the formulation of Zaghloul (2007), for three values of a.

The approximation given by Collin-Souffrin et al. (1981) is

$$P_{\rm esc} = \frac{1}{2}\,\frac{1}{1+2\tau\left(\ln\left(\tau/\sqrt{\pi}+1\right)\right)^{1/2}}. \tag{4.11}$$

Mathews (1992) estimates

$$P_{\rm esc} = \frac{1}{2}\,\frac{1}{1+2\tau\left(\ln\left(\tau\sqrt{\pi}+1\right)\right)^{1/2}}, \tag{4.12}$$

and Dumont et al. (2003) give

$$P_{\rm esc} = \frac{1-e^{-2\tau}}{4\tau}, \qquad \tau < 1, \tag{4.13}$$

$$P_{\rm esc} = \frac{1}{2\sqrt{\pi}\,\tau\left(1.2+\ln\frac{\tau^{1/2}}{1+10^{-5}\tau}\right)}, \quad \tau > 1. \tag{4.14}$$

These approximations are all in the Doppler limit, in which $a = 0$ and the line profile is given by $\pi^{-1/2}\,e^{-x^2}$. We have evaluated the approximations to the escape probabilities of Hollenbach & McKee (1979), Collin-Souffrin et al. (1981), Mathews (1992), NK93, and Dumont et al. (2003), and compared the results to our "exact", numerically integrated, escape probabilities with $a = 0$

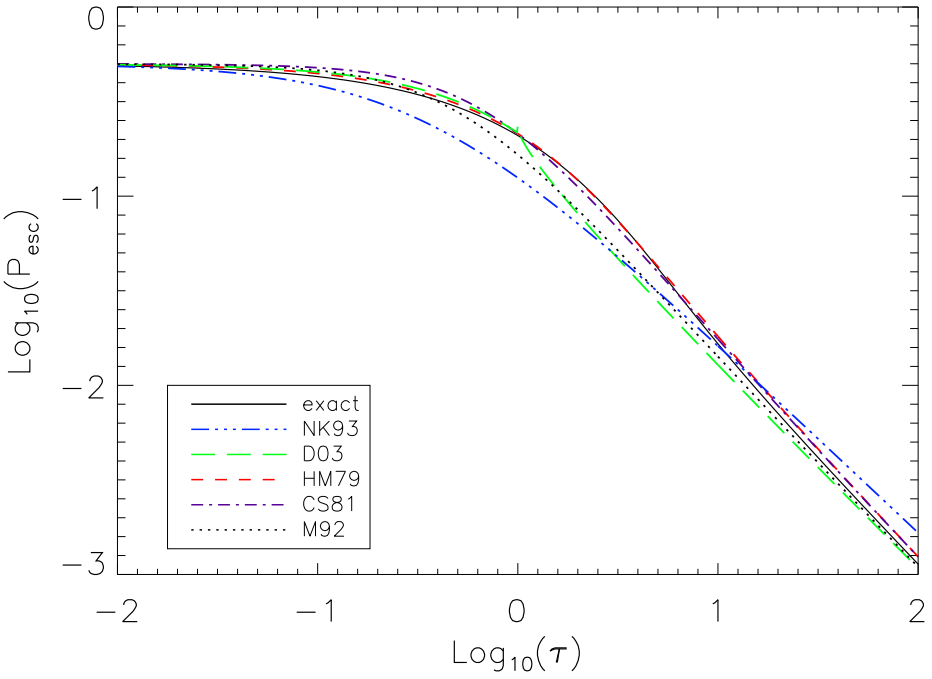

FIG. 26 — Escape probability approximations used by Hollenbach & McKee (1979), Collin-Souffrin et al. (1981), Mathews (1992), NK93, and Dumont et al. (2003), compared to the "exact" escape probability calculated here (see text).

(Figure 1). The maximum error between these approximations and the exact escape probability are as follows: 11.42% for Hollenbach & McKee (1979); 15.70% for Collin-Souffrin et al. (1981); 31.34% for Mathews (1992); and 37.22% for Dumont et al. (2003). The maximum error between the approximation used by NK93 and the exact escape probability is 46.44%, although it is not quite appropriate to make this comparison, as NK93 used the Sobolov optical depth in their calculations. The approximation of Hollenbach & McKee (1979) is superior to the others and provides a satisfactory fit; we will use this approximation in what follows.

Using the Hollenbach & McKee (1979) approximation to the escape probability, a parameter study was conducted to determine the effect of varying the value of a in the calculation of the Voigt function. It was found that varying the value of a between 0.0 and 0.1 increased the escape probability significantly for $\tau \gg 1$ (Figure 2), consistent with figures 4 and 5 of Hummer & Rybicki (1982). It is not immediately clear how this will affect the overall cooling rate, but we anticipate

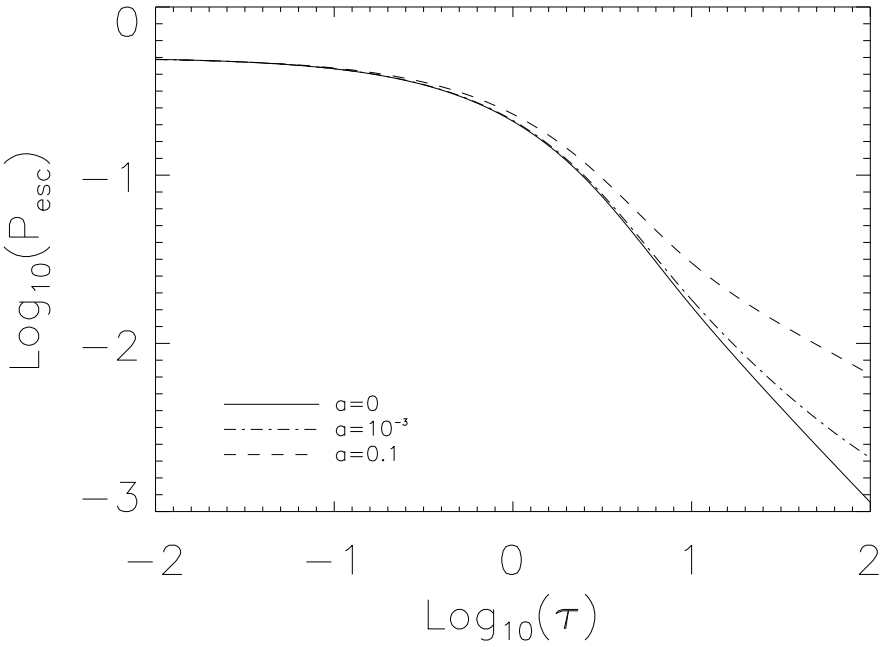

FIG. 27 — Exact escape probability for three different values of a (the ratio of Lorentz to Doppler width).

a small effect as the lines for which the escape probability is increased at higher a are optically thick anyway, leading to lower cooling rates. We investigate this effect of the Voigt function on the cooling rates in Section 3.

3.2. *Escape Probabilities With Dust*

Dust can also absorb photons, preventing their escape. Hence, the proper treatment of the escape probability must account for the absorption by dust, where the optical depth to line photons is now given by $\tau_d + \tau\Phi(x)$, and the exact escape probability is

$$P_{\rm esc} = \frac{1}{2} \int_{-\infty}^{\infty} \Phi(x)\ E_2(\tau_{\rm d} + \tau\Phi(x))\ dx. \tag{4.15}$$

This equation reflects the fact that dust grains provide a continuum opacity that is always capable of absorbing photons. We have used this equation to calculate the exact escape probabilities in the presence of dust (Figure 28). Because it is computationally burdensome to calculate the escape probability for all possible combinations of τ and $\tau_{\rm d}$, we seek an approximation such that the

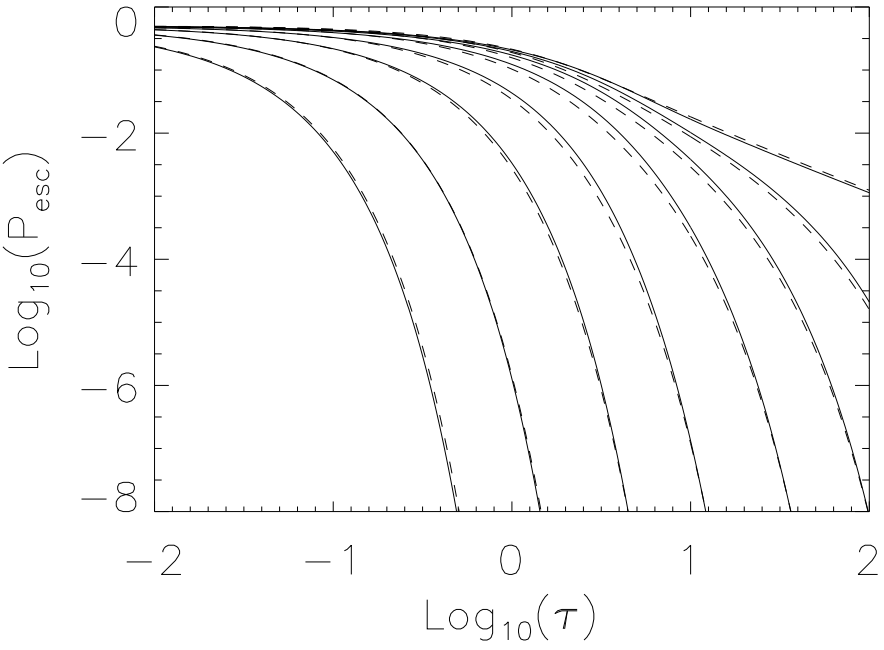

FIG. 28 — Approximations to the escape probability with the inclusion of dust (dashed lines), compared to exact escape probabilities, including dust (solid lines). From left to right, the values used for $\tau_{\rm d}/\tau_0$ are 30, 10, 3, 1, 0.3, 0.1, 0.03, and 0.

TABLE 7
MAXIMUM ERROR FOR $P_{\rm esc}$, WITH THE INCLUSION OF DUST.

τ_d/τ_0	maximum error (%)
0.0	11.42
0.03	24.52
0.1	25.02
0.3	47.51
1.0	54.27
3.0	47.73
10.0	65.20[a]
30.0	128.04[a]

[a]Maximum error was reached at high optical depth where the escape probability $< 10^{-8}$.

escape probability is the product of two separate, independent functions of τ and $\tau_{\rm d}$. On physical grounds, one expects this function to resemble $P_{\rm esc}(\tau, \tau_{\rm d}) \approx P_{\rm esc}(\tau_{\rm d} = 0) \times E_2(\tau_{\rm d})$. Clearly, this is the appropriate expression when $\tau_{\rm d} \approx 0$. It is also exact in the limit $\tau = 0$. The deviation is expected to be strongest when $\tau \approx \tau_{\rm d} \approx 1$, but happily the deviation is not great. Applying the slight modification,

$$P_{\rm esc}^{\rm appr}(\tau, \tau_{\rm d}) = P_{\rm esc}(\tau_{\rm d} = 0) \times E_2(0.95\tau_{\rm d}), \tag{4.16}$$

provides an excellent fit to the exact probability calculated using equation 4.15, as illustrated in Figure 28, and tabulated in Table 1. It can be seen that the approximations including dust fit very well in all regions except where $\tau \approx 1$ and $\tau_{\rm d} \approx 1$, as expected. We can apply these escape probabilities to the calculation of the cooling rate from water when dust is present.

3.3. *Line Cooling*

The cooling per line in the optically thin limit is given by

$$\frac{\Lambda_{ul}}{n_{H_2O}} = S(T) \cdot \frac{8\pi kT}{\lambda^2} \left(\frac{hc/\lambda kT}{e^{hc/\lambda kT} - 1} \right), \tag{4.17}$$

where $S(T)$ is the temperature-dependent line strength of the spectral line, and λ is the wavelength at line center (see Appendix A). In our calculations, we assume that level populations obey a Boltzmann distribution. This is justified if the number density of protoplanetary disks greatly exceeds the critical density of each transition. As NK93 found no variations in level populations when the density exceeded $\approx 10^{10}\,\mathrm{cm}^{-3}$, we assume that all level populations have critical densities below this value. Since we are motivated by chondrule formation, for which the gas densities exceed $\approx 10^{15}\,\mathrm{cm}^{-3}$, the use of a Boltzmann distribution is justified. Unfortunately, for other problems (e.g., molecular clouds), our approach is limited in applicability.

The cooling rate is reduced below its optically thin limit as the column densities are increased, due to the inability of photons to escape the system. Specifically, the total cooling, $\mathcal{L}_{\mathrm{LTE}}$, is given by the total cooling per line, summed over all lines, including the escape probabilities:

$$\mathcal{L}_{\mathrm{LTE}} = \sum \Lambda_{ul}\ P_{\mathrm{esc}}(\tau_{ul}, \tau_{\mathrm{d}}). \tag{4.18}$$

Based on the methods of Plume et al. (2004), the gas optical depth at line center, τ_0, can be found from the linestrength and column density of water

$$\tau_0 = \frac{S(T)\, N_{H_2O}}{(\Delta v/c)\, \nu}, \tag{4.19}$$

(see Appendix A), where the Doppler linewidth is given by

$$\Delta v = \left(\frac{2kT}{m_{H_2O}}\right)^{\frac{1}{2}}, \tag{4.20}$$

and is $\approx 1.36\,\mathrm{km\,s}^{-1}$ at $T = 2000\,\mathrm{K}$. In terms of the optical depth at line center, $\tau_{ul} = \tau_0 \times \sqrt{\pi}$.

The dust optical depth at a depth z into a semi-infinite volume is given by

$$\tau_{\mathrm{d}} = \rho_{\mathrm{g}}\, z\, \kappa(\lambda), \tag{4.21}$$

where $\kappa(\lambda)$ is the opacity per gram of gas. Assuming a dust-to-gas ratio $\rho_{\mathrm{d}}/\rho_{\mathrm{g}} = 5 \times 10^{-3}$, a particle radius $a_s = 0.5\,\mu\mathrm{m}$, and an absorptivity $Q_{\mathrm{abs}} = 1$ for $\lambda < 2\pi a_s$ and $Q_{\mathrm{abs}} = 2\pi a_s/\lambda$ for $\lambda > 2\pi a_s$, we derive

$$\kappa = 30\ \mathrm{min}\left[1, (\lambda/3.1\,\mu\mathrm{m})^{-1}\right]\ \mathrm{cm}^2\,\mathrm{g}^{-1} \tag{4.22}$$

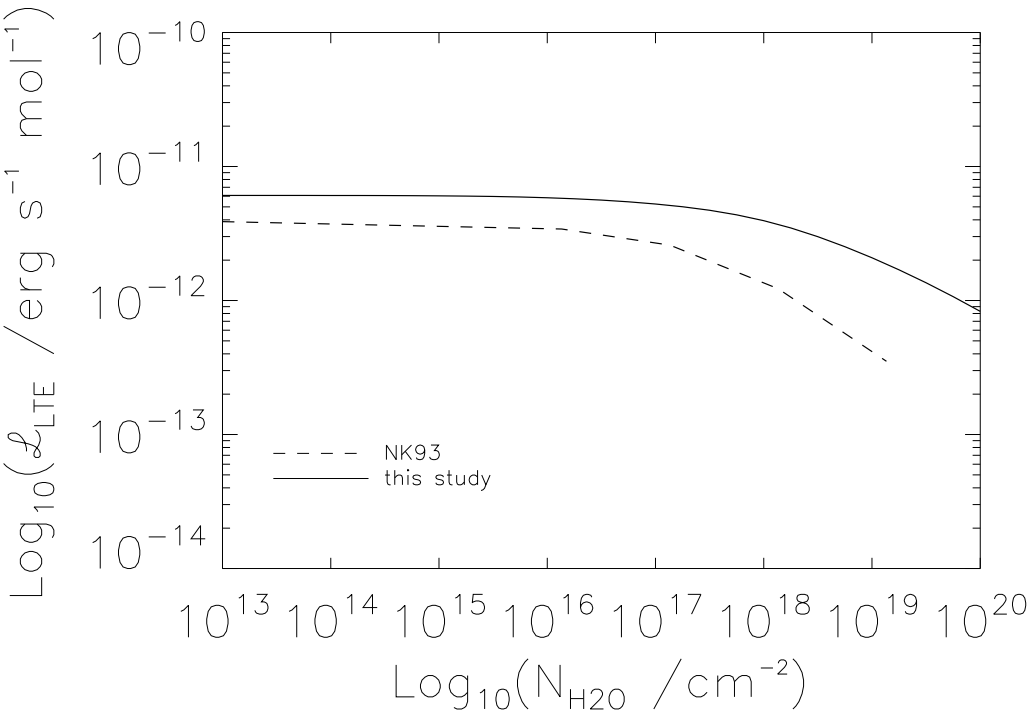

FIG. 29 — Cooling rates of NK93 compared to those of this study.

We have determined the Rosseland mean dust opacity to be $\kappa_{\mathrm{R}} = 28.76\,\mathrm{cm^2\,g^{-1}}$ at $T = 2000\,\mathrm{K}$. Our estimates are similar to those derived by Henning & Stognienko (1996) using a particle size distribution instead of our simplified monodispersion.

3.4. *Cooling Rates*

We first calculate the cooling rates in the absence of dust. Using many more transitions (and improved escape probabilities) we find that, in the absence of dust, our cooling rates are enhanced by about 30% over those calculated by NK93 (Figure 29). For the cooling without dust, we found a slight difference ($< 6\%$) in cooling rate between the cases where the escape probabilities are calculated exactly, and when we use the approximation of Hollenbach & McKee (1979). For consistency, we will quote cooling rates obtained using the Hollenbach & McKee (1979) approximation. The cooling rate for the $T = 2000\,\mathrm{K}$ case, in the absence of dust, is plotted as the rightmost curve in Figure 30. Also plotted in Figure 30 are the cases where the dust-to-water ratio is varied from 300 times to 1/300 times its canonical value. Here, the canonical case refers

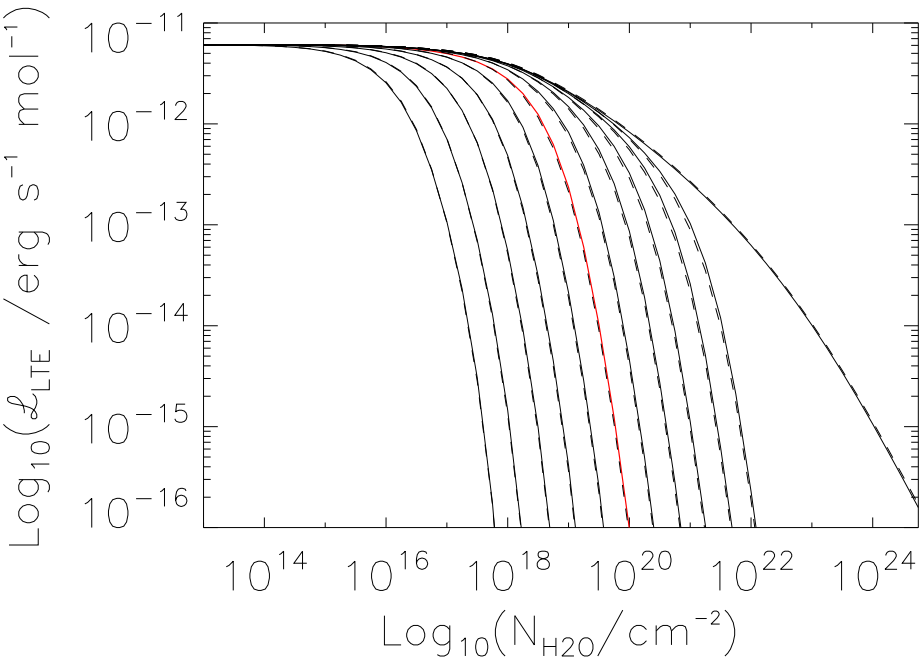

FIG. 30 — Exact cooling rates due to H_2O for various dust-to-water ratios (solid lines), as a function of water column density, and the cooling rates calculated using the approximation to the escape probability (dashed lines) for $T = 2000\,\mathrm{K}$. The rightmost curve is the case with no dust; the red curve is the canonical case (see text). The curves to the left of the canonical curve (from right to left) show cooling rates for 3, 10, 30, 100, and 300 times the canonical dust-to-water ratio. The curves to the right of the canonical curve (from left to right) are 1/3, 1/10, 1/30, 1/100, and 1/300 times the canonical dust-to-water ratio.

to a dust-to-gas mass ratio of 0.5%, yielding the opacity discussed above; the dust-to-water ratio effectively measures only the dust opacity per gram of water vapor. The canonical amount of water assumed here is a ratio $H_2O/H_2 = 8 \times 10^{-4}$. A higher dust-to-water ratio means dust grains are more likely to absorb line photons, and the cooling rate due to line emission is reduced below the optically thin limit at a smaller total column density of water. Surprisingly, even small amounts of dust (300 times smaller than the canonical limit, or a dust-to-gas ratio of $\sim 0.001\%$) will prevent the gas from cooling as freely as it would without dust at column densities $N_{\mathrm{H2O}} > 10^{22}\,\mathrm{cm^{-2}}$. The maximum error in each case between the exact value of the cooling rate (using the escape probability of equation 15) and that found using the approximation to the escape probability (equation 16) is shown in Table 2 (for $T = 2000\,\mathrm{K}$). Figure 31 gives the same information for the case when

TABLE 8
MAXIMUM DISCREPANCY BETWEEN "EXACT" AND APPROXIMATE COOLING RATES SHOWN IN FIGURE 30, AT $T = 2000\,\mathrm{K}$.

Dust-to-Water Ratio[a]	maximum error (%)
0.0	5.54
1.0	14.01
3.0	13.29
10.0	12.24
30.0	11.04
100.0	9.26
300.0	7.45
1/3	14.77
1/10	15.64
1/30	15.39
1/100	17.93
1/300	18.40

[a]Relative to the canonical value.

$T = 1500\,\mathrm{K}$. The cooling rates (assuming $a = 0$, the pure Doppler broadening case) for $T = 1250$ K, 1500 K, 1750 K, 2000 K, and 2250 K, both in the absence of dust and with the canonical abundance of dust, are tabulated in Tables 3-12.

Absorption of line photons by dust grains drastically affects the cooling of the gas. The dust opacity is a strong function of wavelength, so we investigate the effects of assuming a constant opacity. In the continuum opacity case it would be reasonable to assume the flux of photons propagating through a gas is equivalent to the flux derived assuming the gas had a wavelength-independent opacity equal to the Rosseland mean opacity. We therefore recalculated the cooling rate when the dust opacity equaled the Rosseland mean opacity cited above, at all wavelengths. For the canonical dust-to-water ratio, the results are plotted in Figure 32. The optical depth of dust is given by

$$\tau_{\mathrm{d}} = \frac{N_{\mathrm{H2O}}}{n_{\mathrm{H2O}}/n_{\mathrm{H2}}}\, 1.4 m_{\mathrm{H2}}\, \kappa. \tag{4.23}$$

Using the Rosseland mean opacity and canonical water-to-gas ratios cited above, we would estimate $\tau \approx 1$ when $N_{\mathrm{H2O}} \approx 6 \times 10^{18}\,\mathrm{cm}^{-2}$. This is indeed the point where the cooling rate

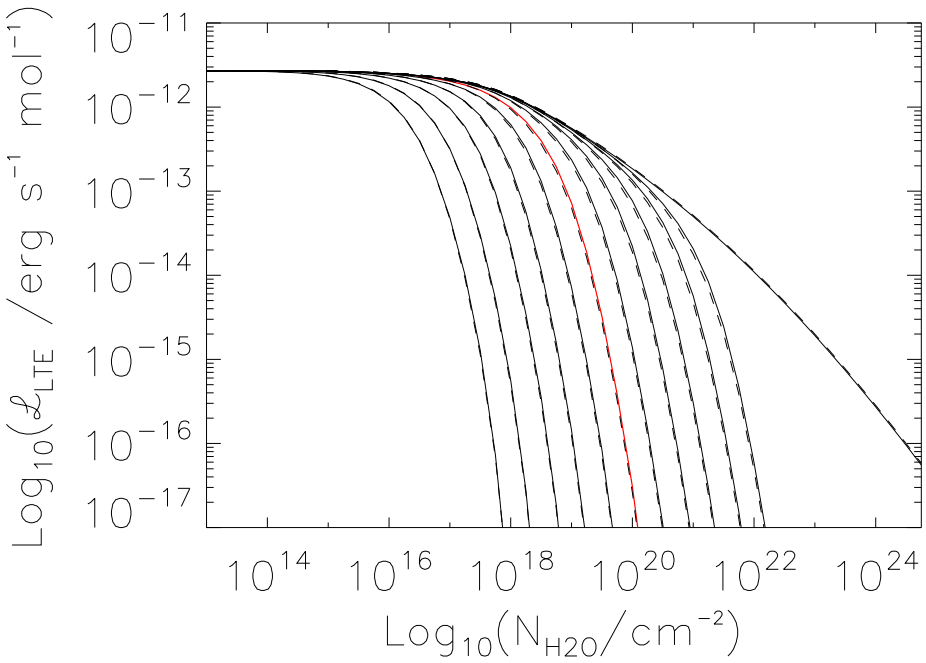

FIG. 31 — Same as Figure 30, but with T = 1500 K.

is significantly reduced due to absorption by dust grains. When the opacity is replaced by the wavelength-dependent opacity $\kappa(\lambda)$, however, the cooling is not effectively reduced until higher column densities are reached. This signifies that most of the cooling is effected by emission of line photons with wavelengths at which $\kappa(\lambda) < \kappa_{\mathrm{R}}$, i.e., $\lambda > 3\,\mu$m. Use of a wavelength-dependent opacity in conjunction with a calculation of the cooling at each H_2O wavelength is therefore necessary. We use the wavelength-dependent opacity in all cases cited here.

Finally, we investigate the effect of the line broadening parameter a on the cooling rate. Increasing a above the $a = 0$ pure Doppler broadening case has the effect of putting more emission in the optically thin wings of the line profile. Effectively, this should act like a reduction of the overall water column density. We have calculated the cooling rates assuming line profiles with $a = 0$ and $a = 0.1$, in the cases where no dust is present, and when it is present at the canonical value. These cooling rates are plotted in Figure 33. As expected, the cooling rate is slightly higher when $a = 0.1$, because the column density of water is effectively reduced; however, the difference

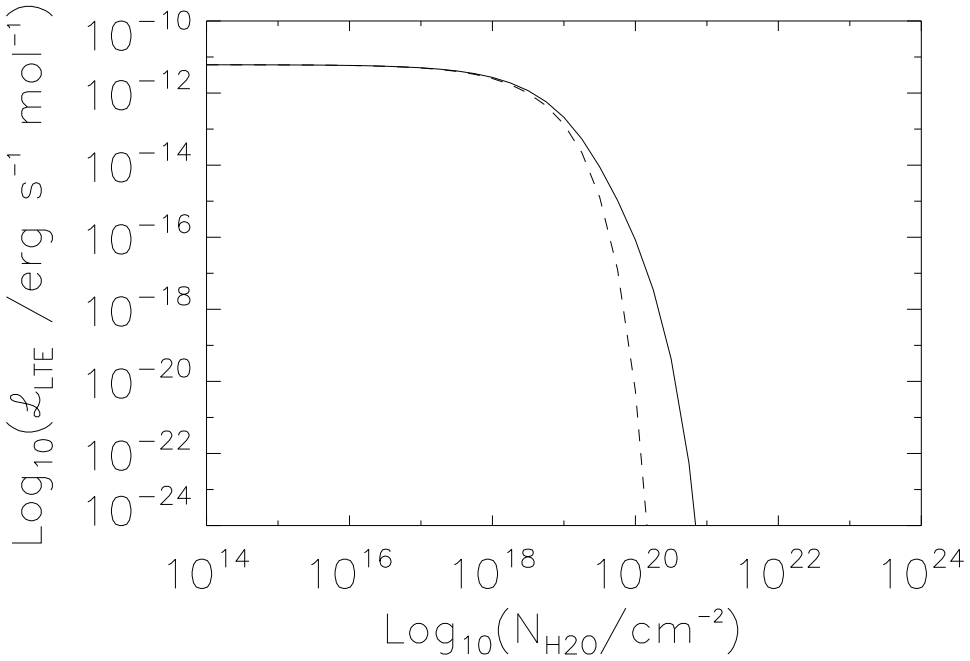

FIG. 32 — Cooling rates due to H_2O using the Rosseland mean dust opacity at $T = 2000\,\mathrm{K}$ (dashed line) and using the wavelength-dependent dust opacity (solid line). Most line cooling takes place at wavelengths longward of $3\,\mu$m, where the dust is relatively optically thin. Use of a single dust opacity at all wavelengths is not warranted.

is slight. In the case with no dust, the discrepancy between the $a = 0$ and $a = 0.1$ cases is $< 11\%$ for a column density of water of $N_{\mathrm{H2O}} < 10^{21}\,\mathrm{cm}^{-2}$, increasing to $\approx 41\%$ at a column density of $10^{24}\,\mathrm{cm}^{-2}$. In the case with dust, the discrepancy is $< 13\%$ at $N_{\mathrm{H2O}} < 10^{19}\,\mathrm{cm}^{-2}$. These calculations are computationally much more burdensome than the $a = 0$ pure Doppler broadening case, because of the need to calculate the Voigt function. Fortunately, it is seen that their effects on the cooling rates of gas are minimal, $< 10\%$ in the regime where cooling is significant, for a up to 0.1. As a is typically $\ll 1$ (Mihalas 1978; Bowers & Deeming 1984), we will assume $a = 0$ in the cases that follow.

TABLE 9

Cooling Rates Without the Inclusion of Dust, $a = 0.0$, $T = 1250\,\mathrm{K}$

N_{H_2O}	$\mathcal{L}_{\mathrm{LTE}_{\mathrm{exact}}}$	$\mathcal{L}_{\mathrm{LTE}_{\mathrm{approx}}}$	% error
10^{13}	1.547 x 10^{-12}	1.548 x 10^{-12}	0.03
10^{14}	1.543 x 10^{-12}	1.546 x 10^{-12}	0.16
10^{15}	1.517 x 10^{-12}	1.526 x 10^{-12}	0.61
10^{16}	1.405 x 10^{-12}	1.425 x 10^{-12}	1.44
10^{17}	1.128 x 10^{-12}	1.160 x 10^{-12}	2.82
10^{18}	6.259 x 10^{-13}	6.415 x 10^{-13}	2.95
10^{19}	2.227 x 10^{-13}	2.293 x 10^{-13}	2.96
10^{20}	6.611 x 10^{-14}	6.816 x 10^{-14}	3.10
10^{21}	1.615 x 10^{-14}	1.668 x 10^{-14}	3.33
10^{22}	3.318 x 10^{-14}	3.437 x 10^{-14}	3.58
10^{23}	5.750 x 10^{-16}	5.978 x 10^{-16}	3.95
10^{24}	8.587 x 10^{-17}	8.959 x 10^{-17}	4.34

TABLE 10

Cooling Rates With the Canonical Dust-to-water Ratio (see text), $a = 0.0$, $T = 1250\,\mathrm{K}$

N_{H_2O}	$\mathcal{L}_{\mathrm{LTE}_{\mathrm{exact}}}$	$\mathcal{L}_{\mathrm{LTE}_{\mathrm{approx}}}$	% error
10^{13}	1.547 x 10^{-12}	1.548 x 10^{-12}	0.03
10^{14}	1.543 x 10^{-12}	1.546 x 10^{-12}	0.16
10^{15}	1.516 x 10^{-12}	1.525 x 10^{-12}	0.59
10^{16}	1.397 x 10^{-12}	1.415 x 10^{-12}	1.26
10^{17}	1.083 x 10^{-12}	1.097 x 10^{-12}	1.62
10^{18}	4.686 x 10^{-13}	4.439 x 10^{-13}	5.27
10^{19}	3.204 x 10^{-14}	2.765 x 10^{-14}	13.71
10^{20}	1.459 x 10^{-17}	1.226 x 10^{-17}	15.98
10^{21}	1.101 x 10^{-28}	2.148 x 10^{-28}	95.04
10^{22}	0.00	0.00	0.00
10^{23}	0.00	0.00	0.00
10^{24}	0.00	0.00	0.00

TABLE 11

Cooling Rates Without the Inclusion of Dust, $a = 0.0$, $T = 1500\,\mathrm{K}$

N_{H_2O}	$\mathcal{L}_{\mathrm{LTE}_{\mathrm{exact}}}$	$\mathcal{L}_{\mathrm{LTE}_{\mathrm{approx}}}$	% error
10^{13}	2.704 x 10^{-12}	2.705 x 10^{-12}	0.02
10^{14}	2.700 x 10^{-12}	2.704 x 10^{-12}	0.12
10^{15}	2.667 x 10^{-12}	2.679 x 10^{-12}	0.47
10^{16}	2.519 x 10^{-12}	2.548 x 10^{-12}	1.15
10^{17}	2.127 x 10^{-12}	2.179 x 10^{-12}	2.47
10^{18}	1.347 x 10^{-12}	1.383 x 10^{-12}	2.81
10^{19}	5.597 x 10^{-13}	5.755 x 10^{-13}	2.84
10^{20}	1.850 x 10^{-13}	1.905 x 10^{-13}	3.00
10^{21}	4.992 x 10^{-14}	5.153 x 10^{-14}	3.26
10^{22}	1.094 x 10^{-14}	1.132 x 10^{-14}	3.45
10^{23}	1.917 x 10^{-15}	1.991 x 10^{-15}	3.86
10^{24}	2.715 x 10^{-16}	2.837 x 10^{-16}	4.48

TABLE 12

Cooling Rates With the Canonical Dust-to-water Ratio (see text), $a = 0.0$, $T = 1500\,\mathrm{K}$

N_{H_2O}	$\mathcal{L}_{\mathrm{LTE}_{\mathrm{exact}}}$	$\mathcal{L}_{\mathrm{LTE}_{\mathrm{approx}}}$	% error
10^{13}	2.704 x 10^{-12}	2.705 x 10^{-12}	0.02
10^{14}	2.699 x 10^{-12}	2.702 x 10^{-12}	0.12
10^{15}	2.664 x 10^{-12}	2.677 x 10^{-12}	0.46
10^{16}	2.502 x 10^{-12}	2.527 x 10^{-12}	1.01
10^{17}	2.031 x 10^{-12}	2.055 x 10^{-12}	1.36
10^{18}	9.849 x 10^{-13}	9.430 x 10^{-13}	4.26
10^{19}	7.223 x 10^{-13}	6.338 x 10^{-13}	12.26
10^{20}	3.081 x 10^{-17}	2.612 x 10^{-17}	15.23
10^{21}	2.210 x 10^{-28}	4.353 x 10^{-28}	97.01
10^{22}	0.00	0.00	0.00
10^{23}	0.00	0.00	0.00
10^{24}	0.00	0.00	0.00

TABLE 13

Cooling Rates Without the Inclusion of Dust, $a = 0.0$, $T = 1750\,\mathrm{K}$

N_{H_2O}	$\mathcal{L}_{\mathrm{LTE}_{\mathrm{exact}}}$	$\mathcal{L}_{\mathrm{LTE}_{\mathrm{approx}}}$	% error
10^{13}	4.219 x 10^{-12}	4.220 x 10^{-12}	0.01
10^{14}	4.214 x 10^{-12}	4.217 x 10^{-12}	0.08
10^{15}	4.177 x 10^{-12}	4.193 x 10^{-12}	0.37
10^{16}	4.002 x 10^{-12}	4.040 x 10^{-12}	0.94
10^{17}	3.501 x 10^{-12}	3.575 x 10^{-12}	2.11
10^{18}	2.446 x 10^{-12}	2.511 x 10^{-12}	2.68
10^{19}	1.158 x 10^{-12}	1.189 x 10^{-12}	2.74
10^{20}	4.219 x 10^{-13}	4.343 x 10^{-13}	2.93
10^{21}	1.240 x 10^{-13}	1.279 x 10^{-13}	3.15
10^{22}	2.863 x 10^{-14}	2.958 x 10^{-14}	3.35
10^{23}	4.913 x 10^{-15}	5.101 x 10^{-15}	3.83
10^{24}	6.215 x 10^{-16}	1.156 x 10^{-16}	5.75

TABLE 14

Cooling Rates for the Canonical Dust-to-water Ratio (see text), $a = 0.0$, $T = 1750\,\mathrm{K}$

N_{H_2O}	$\mathcal{L}_{\mathrm{LTE}_{\mathrm{exact}}}$	$\mathcal{L}_{\mathrm{LTE}_{\mathrm{approx}}}$	% error
10^{13}	4.219 x 10^{-12}	4.220 x 10^{-12}	0.01
10^{14}	4.213 x 10^{-12}	4.217 x 10^{-12}	0.08
10^{15}	4.173 x 10^{-12}	4.188 x 10^{-12}	0.35
10^{16}	3.973 x 10^{-12}	4.006 x 10^{-12}	0.82
10^{17}	3.329 x 10^{-12}	3.365 x 10^{-12}	1.15
10^{18}	1.754 x 10^{-12}	1.696 x 10^{-12}	3.27
10^{19}	1.383 x 10^{-12}	1.233 x 10^{-12}	10.84
10^{20}	5.735 x 10^{-17}	4.899 x 10^{-17}	14.57
10^{21}	3.973 x 10^{-28}	7.831 x 10^{-28}	97.13
10^{22}	0.00	0.00	0.00
10^{23}	0.00	0.00	0.00
10^{24}	0.00	0.00	0.00

TABLE 15

Cooling Rates Without the Inclusion of Dust, $a = 0.0$, $T = 2000\,\mathrm{K}$

N_{H_2O}	$\mathcal{L}_{\mathrm{LTE}_{\mathrm{exact}}}$	$\mathcal{L}_{\mathrm{LTE}_{\mathrm{approx}}}$	% error
10^{13}	6.083 x 10^{-12}	6.084 x 10^{-12}	0.01
10^{14}	6.078 x 10^{-12}	6.082 x 10^{-12}	0.02
10^{15}	6.040 x 10^{-12}	6.057 x 10^{-12}	0.28
10^{16}	5.847 x 10^{-12}	5.893 x 10^{-12}	0.78
10^{17}	5.250 x 10^{-12}	5.344 x 10^{-12}	1.79
10^{18}	3.943 x 10^{-12}	4.045 x 10^{-12}	2.58
10^{19}	2.084 x 10^{-12}	2.139 x 10^{-12}	2.68
10^{20}	8.297 x 10^{-13}	8.536 x 10^{-13}	2.89
10^{21}	2.617 x 10^{-13}	2.698 x 10^{-13}	3.12
10^{22}	6.260 x 10^{-14}	6.464 x 10^{-14}	3.26
10^{23}	1.013 x 10^{-14}	1.724 x 10^{-14}	3.83
10^{24}	1.060 x 10^{-14}	1.118 x 10^{-14}	5.54

TABLE 16

Cooling Rates for the Canonical Dust-to-water Ratio (see text), $a = 0.0$, $T = 2000\,\mathrm{K}$

N_{H_2O}	$\mathcal{L}_{\mathrm{LTE}_{\mathrm{exact}}}$	$\mathcal{L}_{\mathrm{LTE}_{\mathrm{approx}}}$	% error
10^{13}	6.083 x 10^{-12}	6.084 x 10^{-12}	0.01
10^{14}	6.077 x 10^{-12}	6.081 x 10^{-12}	0.06
10^{15}	6.034 x 10^{-12}	6.051 x 10^{-12}	0.28
10^{16}	5.803 x 10^{-12}	5.842 x 10^{-12}	0.69
10^{17}	4.977 x 10^{-12}	5.025 x 10^{-12}	0.98
10^{18}	2.783 x 10^{-12}	2.716 x 10^{-12}	2.39
10^{19}	2.351 x 10^{-12}	2.129 x 10^{-12}	9.45
10^{20}	9.721 x 10^{-17}	8.359 x 10^{-17}	14.01
10^{21}	6.497 x 10^{-28}	1.283 x 10^{-27}	97.59
10^{22}	0.00	0.00	0.00
10^{23}	0.00	0.00	0.00
10^{24}	0.00	0.00	0.00

TABLE 17

Cooling Rates Without the Inclusion of Dust, $a = 0.0$, $T = 2250\,\mathrm{K}$

N_{H_2O}	$\mathcal{L}_{\mathrm{LTE}_{\mathrm{exact}}}$	$\mathcal{L}_{\mathrm{LTE}_{\mathrm{approx}}}$	% error
10^{13}	8.284 x 10^{-12}	8.285 x 10^{-12}	0.01
10^{14}	8.279 x 10^{-12}	8.283 x 10^{-12}	0.04
10^{15}	8.241 x 10^{-12}	8.260 x 10^{-12}	0.22
10^{16}	8.040 x 10^{-12}	8.092 x 10^{-12}	0.65
10^{17}	7.364 x 10^{-12}	7.476 x 10^{-12}	1.52
10^{18}	5.835 x 10^{-12}	5.979 x 10^{-12}	2.47
10^{19}	3.383 x 10^{-12}	3.471 x 10^{-12}	2.63
10^{20}	1.457 x 10^{-12}	1.499 x 10^{-12}	2.85
10^{21}	4.870 x 10^{-13}	5.022 x 10^{-13}	3.11
10^{22}	1.185 x 10^{-13}	1.222 x 10^{-13}	3.20
10^{23}	1.726 x 10^{-14}	1.793 x 10^{-14}	3.87
10^{24}	1.440 x 10^{-15}	1.543 x 10^{-15}	7.14

TABLE 18

Cooling Rates for the Canonical Dust-to-water Ratio (see text), $a = 0.0$, $T = 2250\,\mathrm{K}$

N_{H_2O}	$\mathcal{L}_{\mathrm{LTE}_{\mathrm{exact}}}$	$\mathcal{L}_{\mathrm{LTE}_{\mathrm{approx}}}$	% error
10^{13}	8.284 x 10^{-12}	8.285 x 10^{-12}	0.01
10^{14}	8.279 x 10^{-12}	8.281 x 10^{-12}	0.04
10^{15}	8.233 x 10^{-12}	8.250 x 10^{-12}	0.22
10^{16}	7.976 x 10^{-12}	8.022 x 10^{-12}	0.58
10^{17}	6.963 x 10^{-12}	7.023 x 10^{-12}	0.86
10^{18}	4.065 x 10^{-12}	3.998 x 10^{-12}	1.64
10^{19}	3.658 x 10^{-12}	3.361 x 10^{-12}	8.11
10^{20}	1.532 x 10^{-16}	1.324 x 10^{-16}	13.56
10^{21}	9.895 x 10^{-28}	1.954 x 10^{-27}	97.46
10^{22}	0.00	0.00	0.00
10^{23}	0.00	0.00	0.00
10^{24}	0.00	0.00	0.00

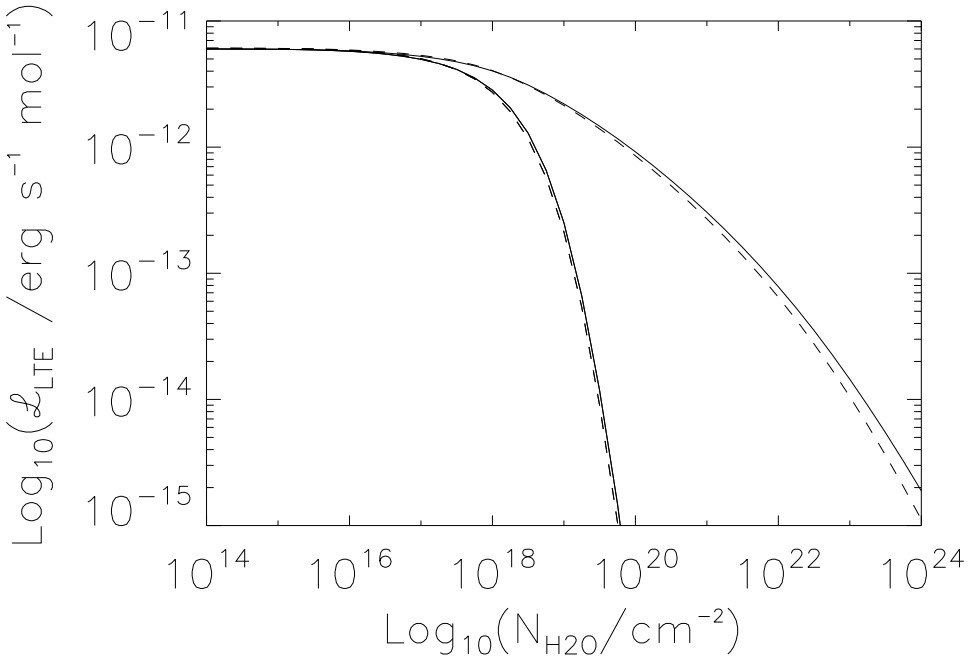

FIG. 33 — Cooling rates with a broadened line profile corresponding to $a = 0.1$ (solid curves), compared to those calculated assuming pure Doppler broadening $a = 0$ (dashed curves), both in the absence of dust (top curves) and with a canonical dust-to-water ratio (bottom curves).

4. Cooling During Chondrule-forming Shocks

Line cooling is effective at cooling gas, provided the line photons are not reabsorbed by H_2O molecules or dust grains before they can escape to the cool, pre-shock region. In a nebular shock, it is assured that sufficiently far from the shock front, no line photons can escape and the gas and dust will become thermally coupled and cool slowly, if at all. What is not clear is the degree to which line cooling is significant in the region immediately past the shock. Does line cooling lead to a significant drop in temperature ($> 10^2$ K) before dust grains begin to reabsorb line photons? Are the cooling rates of chondrules dominated by line cooling and therefore high ($\sim 10^4\,\mathrm{K\,hr^{-1}}$) at the temperatures at which chondrules crystallize, as found by INSN, or can line cooling be neglected, as DC02 and CH02 assume? To answer these questions we have constructed a toy model to assess the maximum possible importance of line cooling and to determine whether more detailed calculations

of chondrule formation in nebular shocks need to include line cooling.

Our toy model builds on the calculation presented in Section 1. We find it convenient to convert a time derivative $\partial/\partial t$ to a spatial derivative $V_{\rm g}\partial/\partial z$, and then convert the spatial variable z (distance past the shock front) into a column density of water past the shock front (assuming the water density remains constant). Then the cooling with column density of water is given by

$$\frac{\partial T}{\partial N_{H_20}} = -\left(\frac{1}{\rho_{\rm g} V_{\rm g}}\right)\left(\frac{m_{\rm H}}{k}\right)\mathcal{L}_{\rm LTE}\left(N_{H2O}\right). \tag{4.24}$$

The cooling rate is a function of the dust-to-water ratio (via $\mathcal{L}_{\rm LTE}$), as well as the water column density. Given a dust-to-water ratio, this equation can then be integrated to find T as a function of $N_{\rm H2O}$. Note that we have not accounted for the fact that the line broadening should decrease as the temperature drops, making it slightly harder for the gas to cool; our simplified analysis therefore overestimates the cooling somewhat.

We plot the results of this integration in Figure 34 for both the dust-free case and the case where the dust is one-tenth that of the canonical value (in order to show the effect of even a small amount of dust). For ease of comparison to chondrules, we have also assumed the canonical water-to-gas ratio (and other canonical values) to convert $N_{\rm H2O}$ to a time. Specifically, we assumed a pre-shock density of $\rho_{\rm g} = 10^{-9}\,{\rm g\,cm^{-3}}$, a shock velocity of $V_{\rm s} = 7\,{\rm km\,s^{-1}}$, assumed the density increased and the velocity decreased by a factor of $(\gamma+1)/(\gamma-1) = 6$ past the shock front, and used our canonical water-to-gas ratio of $n_{H2O}/n_{H2} = 8\times10^{-4}$. These parameters are consistent with our assumption of an initial post-shock temperature of 2200 K (DC02; CH02). In the absence of dust, the gas would cool below 1400 K in roughly 300 seconds, leading to a cooling rate of $> 1\times10^{4}\,{\rm K\,hr^{-1}}$. This cooling is attributable solely to effective cooling by water; by comparison to NK93 we infer these are mostly vibrational photons. As chondrules and gas are expected to be thermally well coupled more than 100 seconds past the shock front (DC02; CH02), this can be interpreted as a likely cooling rate of chondrules as well. The cooling rate begins to taper off as large column densities are reached, but not until times $> 10^{5}\,{\rm s}$, by which time the gas and

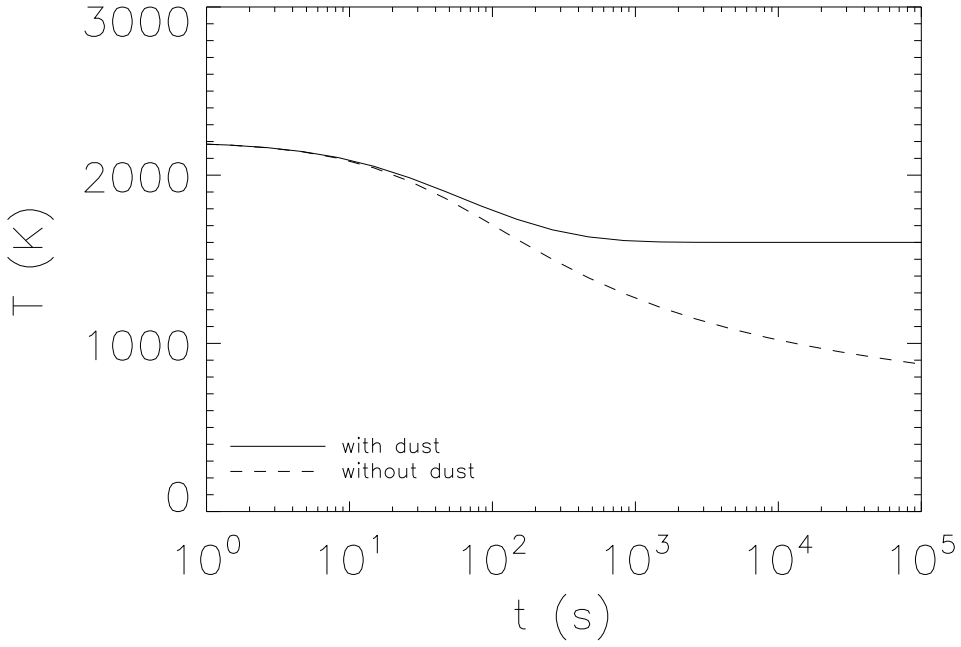

FIG. 34 — Gas temperature as a function of time, both with and without the inclusion of dust grains that can absorb line photons (see text for details).

chondrules have traveled roughly 10^{10} cm past the shock front, equivalent to a column density of water $> 10^{22}\,\mathrm{cm}^{-2}$.

Including the absorption of line photons by dust grains completely changes the thermal history of the gas and chondrules. Using an opacity of dust $\sim 30\,\mathrm{cm}^2\,\mathrm{g}^{-1}$ (at short wavelengths) and a post-shock gas density of $6\times10^{-9}\,\mathrm{g\,cm}^{-3}$, the optical depth of dust exceeds unity after only 55 km past the shock front, which is reached after traveling only 48 seconds. During this first minute or so past the shock front, the line photons emitted by H_2O molecules escape freely and effectively cool the gas; but after the first minute or so, they are absorbed by dust grains instead. Instead of H_2O line photons freely escaping to the shock front and cooling the gas and dust system, the photons are reabsorbed "on-the-spot" and do not cool the gas. This effect of the reduced cooling rate is clearly seen in Figure 34 beyond about 10^2 seconds. The trapping of line photons by dust grains becomes so effective that no further cooling by line emission is possible after a few minutes.

TABLE 19
Cooling Rates for Various Dust-to-gas and Water-to-gas Ratios

dust/gas[a]	water/gas[b]	T at 10^4 s (K)	Cooling Rate [c]
0.0	0.1	1275	2.7×10^2
0.0	1.0	1000	3.2×10^3
0.0	10.0	875	3.7×10^4
0.1	0.1	2000	N/A
0.1	1.0	1650	[d]
0.1	10.0	1225	2.3×10^4
1.0	0.1	2175	N/A
1.0	1.0	2000	N/A
1.0	10.0	1600	[e]
10.0	0.1	2200	N/A
10.0	1.0	2175	N/A
10.0	10.0	2000	N/A

[a]times the canonical dust/gas mass ratio 5×10^{-3}

[b]times the canonical water/gas ratio $n_{\rm H2O}/n_{\rm H2} = 8 \times 10^{-4}$

[c]the average cooling rate between 1800 and 1400 K, in $\rm K\,hr^{-1}$

[d]$490\,\rm K\,hr^{-1}$ between 1800 and 1650 K; never cooled below 1650 K

[e]$5000\,\rm K\,hr^{-1}$ between 1800 and 1600 K; never cooled below 1600 K

Ignoring the effects of cooling other than line photons, the temperature would stabilize at about 1600 K. For this particular choice of parameters, chondrules would *not* cool at rates $\sim 10^4\,\rm K\,hr^{-1}$ through their crystallization temperatures (1400 - 1800 K) as in INSN and Miura & Nakamoto (2006); in fact, they wouldn't cool at all under the assumptions of our toy model.

We have investigated the effect of varying the dust-to-gas and water-to-gas ratios on the cooling rates of chondrules. Their behaviors are similar to those depicted in Figure 34. In Table 4 we report only the average cooling rates of chondrules over their crystallization temperature range (i.e., from 1800 K to 1400 K). The gas density and shock velocity are not varied. The results of this parameter study show that even a small amount of dust very effectively shuts down the line cooling due to H_2O .

5. Estimated Effects of Line Cooling

We have built upon the line cooling work of NK93, by using a much-expanded database of spectral lines, improved escape probabilities, and the inclusion of dust grains. We have found that although the cooling rate due to H_2O line cooling is a complicated combination of gas and dust opacity, the cooling rate can be well approximated by $\mathcal{L}_{\rm LTE}(\tau, \tau_{\rm d}) \approx \mathcal{L}_{\rm LTE}(\tau_{\rm d} = 0) \times E_2(0.95\ \tau_{\rm d})$. This allows us to investigate the maximum cooling effect H_2O line cooling will have in chondrule-forming nebular shocks.

Because vibrational line photons from H_2O so effectively cool the gas, the high oxygen fugacities and H_2O densities inferred for the chondrule-forming environment (Fedkin & Grossman 2007) would seem incompatible with cooling rates < 100 K/hr, but we find that dust significantly reduces the photon escape probabilities and the cooling rates. Dust grains absorb the line photons that would escape and cool the gas. Without dust, H_2O line cooling reduces the temperature of the gas to 1400-1800 K in ≤ 0.1 hr and cooling continues at this rate ($>10^4$ K/hr). With dust, however, the grains absorb line photons and inhibit cooling, leading to a cessation of cooling after ~ 0.1 hr (~ 8 minutes). Line cooling is a very effective and important cooling agent in the first few minutes and must be included in any comprehensive shock model. After the first few minutes, however, the thermally well-coupled gas and chondrules cool together at a slow rate (only as fast as they travel ~ 1 optical depth through the dust), as in DC02 and CH02. INSN failed to note this effect; although they treat the gas and dust as well coupled ($T_{\rm gas} = T_{\rm dust}$), their system was effectively optically thin to line emission, allowing all line photons to escape the region and cool the gas.

As we are interested at this time only in the maximum cooling effects of line photons (the "worst-case scenario"), our calculations of cooling rates made no assumptions about radiative transfer; the chondrule temperatures followed the gas temperature. Thermal histories of chondrules including radiative transfer, line cooling, and other relevant effects will be reported later in this

work. Since we have assumed that line photons either escape completely or are absorbed immediately, the true situation will clearly be bracketed between the two extremes shown in Figure 34. In these calculations, we have assumed that the dust is thermodynamically coupled to the gas. All temperatures (gas, dust, and chondrules), in actuality, will be determined by dust/chondrule opacity and radiative transfer. DC02 showed that the cooling rates of chondrules (without the inclusion of line cooling) were given by the formula that appears above as Equation 1. In the case considered in Figure 34, the chondrule concentration may be considered to be low ($\mathcal{C} \ll 1$), and the dust opacity is characterized by $\delta = 0.1 \times 28.76/1.14 = 2.5$. This yields a total cooling rate of gas and dust through the crystallization range of about $125\,\mathrm{K\,hr^{-1}}$ after line cooling shuts off. Higher chondrule concentrations ($\mathcal{C} > 10^2$) appear to have been typical during chondrule formation (Cuzzi & Alexander 2006; Alexander et al. 2008). These would increase the cooling rate to several $\times 10^2\,\mathrm{K\,hr^{-1}}$. Line cooling is significant during the first few minutes past the shock, and more detailed calculations will be necessary to constrain the initial drop in temperature from the peak to below the liquidus. However, our results have shown that dust effectively shuts down line cooling within minutes and it then takes hours for chondrules to crystallize in a shock, consistent with DC02 and CH02.

As mentioned previously, we did not calculate line cooling due to CO, as it is a factor of $\sim$ 20 less effective than H_2O. CO also cools by emitting line photons, but dust will absorb these line photons as readily as those emitted by H_2O. Figure 34 shows a drop in temperature of $\sim$ 600 K. If CO were included, the temperature would probably drop an extra 5% ($\sim$ 630 K), which is within the uncertainties of the H_2O abundances we have assumed.

This study has shown that the gas and chondrules will cool much too rapidly to match the experimental constraints on chondrule cooling rates if dust is not present. The question of the dust abundance and its opacity therefore becomes paramount. But, significantly, we have found that enhancing only the amount of H_2O causes higher cooling rates, whereas enhancing the amount of H_2O and dust together does not. What affects the cooling rate the most, therefore, is not

the amount of water, but the dust-to-water ratio. Potential complications, though, include the possibility that dust will evaporate immediately upon passage of the shock, and the possibility that dust vapor may recondense in the post-shock region (e.g., Scott & Krot 2005).

In a related vein, we note an application of this work only tangentially related to chondrule formation. Ciesla et al. (2003) suggested that phyllosilicates found in the fine-grained accretionary rims of chondrules in CM meteorites may have resulted from rapid gas-phase reactions of water vapor with silicates. Previous studies indicated that phyllosilicate production would be kinetically inhibited in the solar nebula (Prinn & Fegley 1987); however, Ciesla et al. (2003) showed that nebular shocks could result in a local increase in the water vapor pressure, thereby increasing the rate of phyllosilicate formation, as well as increasing the temperature at which phyllosilicates become stable. Chondrule-forming shocks in icy regions of the solar nebula could therefore account for both the formation of chondrules and their fine-grained phyllosilicate rims. A possible objection to this hypothesis is that the high abundance of water vapor in the shocked region would cool the gas too rapidly to allow the production of much phyllosilicates. As our work here shows, however, rapid cooling by line photons will not be associated with shocked, water-rich nebula gas, as long as the dust-to-water ratio is close to the canonical value for the solar nebula. An investigation of this hypothesis is also planned for future work.

CHAPTER 5

INCLUSION OF LINE COOLING IN THE SHOCK CODE

Recall from Chapter 4 that molecular line cooling due to the presence of water is dependent, in a nonlinear fashion, on the column depth of water, (i.e., the opacity of the gas), the opacity of dust, and the gas temperature. Technically, each line should be treated separately. The calculation of the amount of emission and absorption of line cooling in each zone of our computational boundary, employing the complete methods of Morris et al. (2009), would result in many months of computational time for each run of the code. Therefore it was highly desirable to simplify the way in which line cooling was incorporated into the shock code. In particular, we wished to eliminate any wavelength-dependence. To that end, we searched for an approximation to the exact, wavelength-integrated cooling rates given in Morris et al. (2009) (see Figures 30 and 31) that provided a single, line-integrated cooling rate, dependent only on the column depth of water, temperature, and opacity. We found that for all temperatures, in all cases of interest (low dust opacity), the following approximation provides an excellent fit to the cooling rates (Figure 35).

$$\Lambda(N_{H_2O}, \Sigma_{\rm eff}) = \Lambda(N_{H_2O}, \Sigma_{\rm eff} = 0)\ \exp\left[-\frac{\Sigma_{\rm eff}}{1.2\ {\rm x}\ 10^{-4}\ {\rm g\ cm^{-2}}}\right] \tag{5.1}$$

where 1.2 x 10^{-4} g cm^{-2} is the column density of solids that gives $\tau_{\rm d} = 1$, assuming the opacity is due to solids in the form of our assumed micron-sized dust. To include other solids, we define $\Sigma_{\rm eff}$ as the *effective* column density of all solids, including micron-sized dust, chondrule precursors, and chondrules. For our chondrule parameters,

$$\Sigma_{\rm eff} = \Sigma_{\rm dust} + \Sigma_{\rm ch}/{\rm const.} \tag{5.2}$$

Utilizing the complete methods of Morris et al. (2009), lookup tables of exact cooling rates without dust, $\Lambda(N_{H_2O}, \Sigma_{\rm d} = 0)$, were generated for 48 column densities of H_2O ranging between 10^{13} and 10^{25} cm^{-2}, and temperatures of 250 - 4000 K (in increments of 250 K), for a total of 720 entries in the N_{H_2O} - T grid. A separate subroutine to the shock code was developed to calculate the proper line cooling rate, including solids, using Equation 5.1, given the temperature, column density of water, and the column density of solids. An initial test of the subroutine enabled an examination of the broad results of line cooling. To simplify the test, we calculated the column

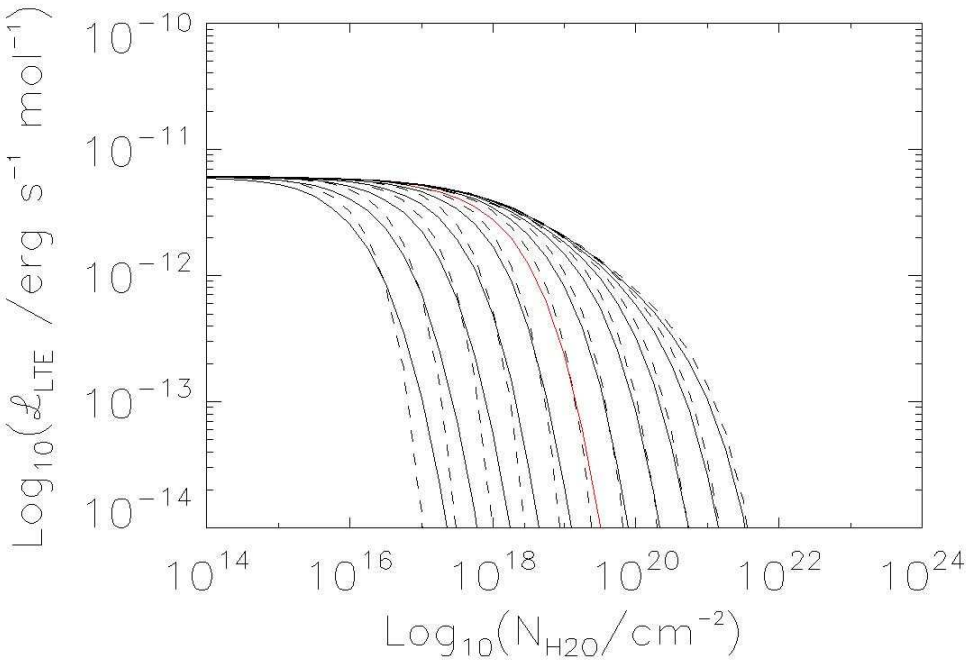

FIG. 35 — Exact cooling rates due to H_2O for various dust-to-water ratios (solid lines), as a function of water column density, and our approximation to the exact, wavelength-integrated cooling rates (dashed lines) for $T = 2000\,\mathrm{K}$. The rightmost curve is the case with no dust; the red curve is the canonical case (see text). The curves to the left of the canonical curve (from right to left) show cooling rates for 3, 10, 30, 100, and 300 times the canonical dust-to-water ratio. The curves to the right of the canonical curve (from left to right) are 1/3, 1/10, 1/30, 1/100, and 1/300 times the canonical dust-to-water ratio. Since dust is largely evaporated in the post-shock region, we are only interested in the cases with low dust-to-water ratios.

densities of dust and H_2O from each zone *to the shock front*, rather than zone to zone. Figures 36 and 37 show the results in the case considering gas opacity only and Figures 38 and 39 show the results in the case including opacity due to solids.

At first glance, there seems to be very little difference between the case which includes gas opacity only and the case which also includes opacity due to solids. However, a closer look (Figure 40) reveals that the case including solids results in a minutely higher peak temperature and slightly higher temperatures in the post-shock region.

This simplified test of our line cooling subroutine resulted in a dramatic increase in cooling rates over our canonical case because we were only accounting for *emission* due to line cooling. We

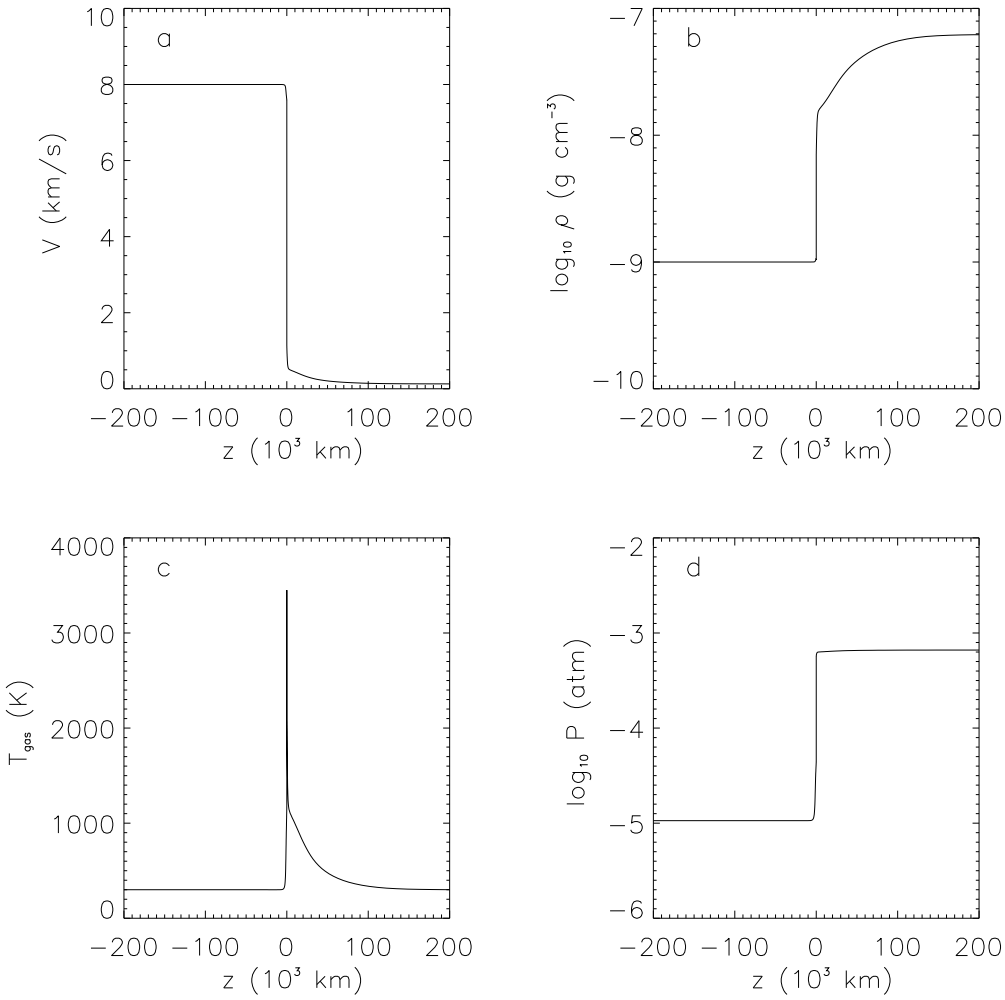

FIG. 36 — Same as Figure 19 (our canonical case neglecting line cooling), except we have included an approximation of the line cooling, considering gas opacity only. In each zone, column densities (both H_2O and solids) are calculated from that zone to/from the shock front.

have yet to account for the amount of this emission from each zone that is *absorbed* in other zones.

It is important to remember at this time, that line photons emitted by H_2O on one side of the shock will not be absorbed by H_2O molecules on the other side of the shock, as they appear significantly Doppler-shifted; the difference in gas velocity is ~ 5 km s^{-1}, many times the thermal speeds of < 1 km s^{-1}. The calculation of the column density of water in each zone must take this effect into account. In order to properly account for the zone-to-zone effects of line emission, it was necessary to create yet another subroutine to determine the transfer of line radiation from zone-to-zone (Figure 41). The first step in this process is to calculate the comoving column density

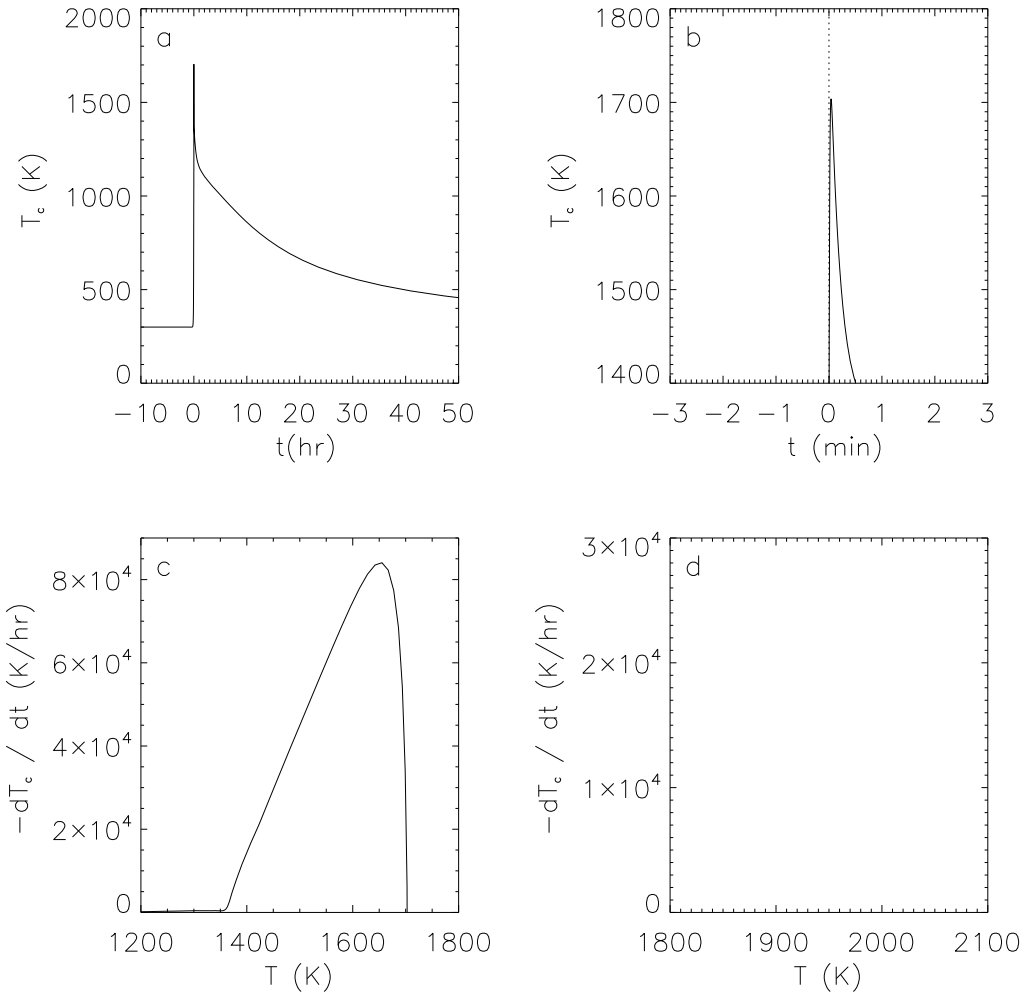

FIG. 37 — Same as Figure 20 (our canonical case neglecting line cooling), except we have included an approximation of the line cooling, considering gas opacity only. In each zone, column densities (both H_2O and solids) are calculated from that zone to/from the shock front.

of water and solids through which the radiation must pass. The column density from the edge of the computational domain ($x = x_{\rm pre}$) to point x_i is

$$N_{H_2O}(i) = \sum_{j=2}^{i} \left[\frac{n^*_{H_2O}(j) + n^*_{H_2O}(j-1)}{2} \right] \; x_j - x_{j-1}, \tag{5.3}$$

where $n^*_{H_2O} = n_{H_2O}$, if i and j are on the same side of the shock, and $n^*_{H_2O} = 0$, if they are not. The column density of solids must include both fine-grained dust and chondrules/chondrule precursors. First, it is necessary to determine the mass density of both dust and chondrules/chondrule

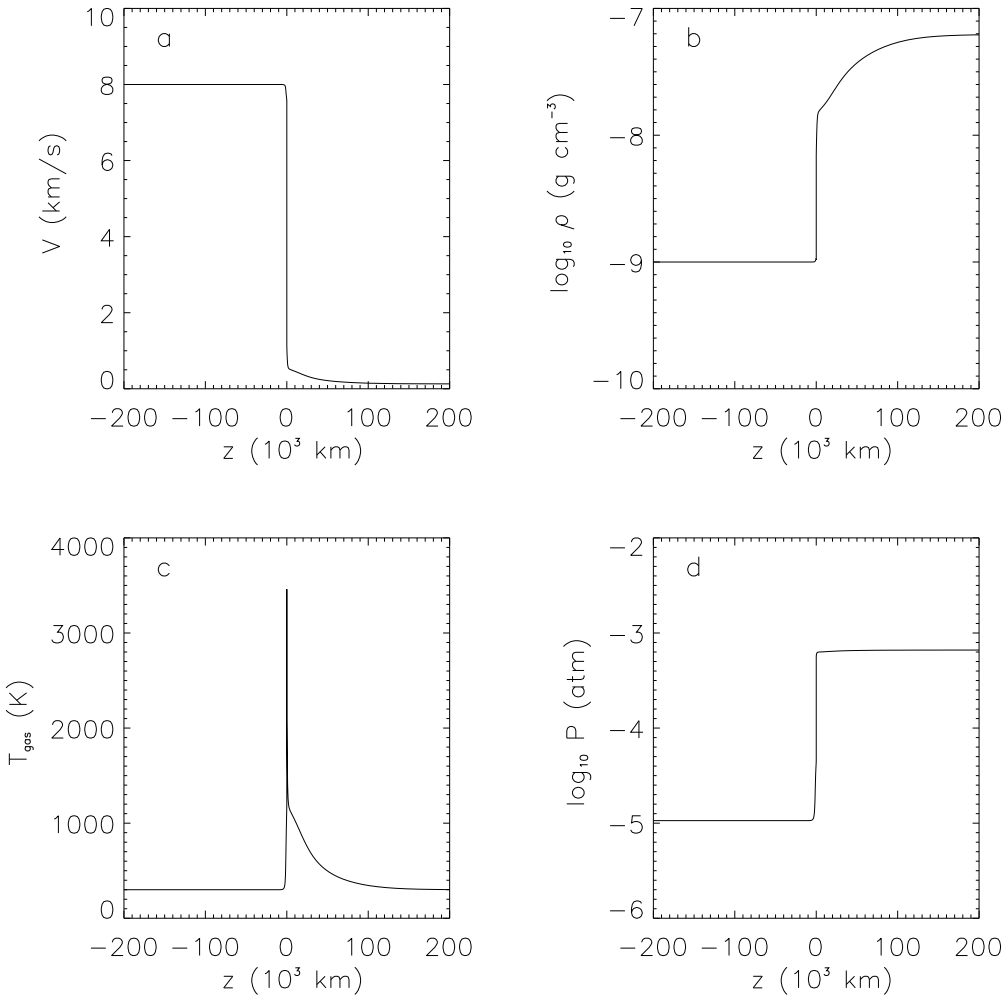

FIG. 38 — Same as Figure 36, except we have now considered opacity due to solids. Once again, in each zone, column densities (both H_2O and solids) are calculated from that zone to/from the shock front.

precursors. The mass density of dust, assuming a solar dust-to-gas ratio, is given by

$$\rho_{\rm d} = 5 \text{ x } 10^{-3} \, \rho_{\rm gas}. \tag{5.4}$$

If the dust evaporates (T_d exceeds $T_{\rm evap}$), then $\rho_{\rm d} = 0.001$ times the amount calculated by Eqn. 5.4.

The mass of chondrules/chondrule precursors is

$$m_{\rm ch} = \frac{4}{3}\pi\rho_{\rm p}a_{\rm p}^3. \tag{5.5}$$

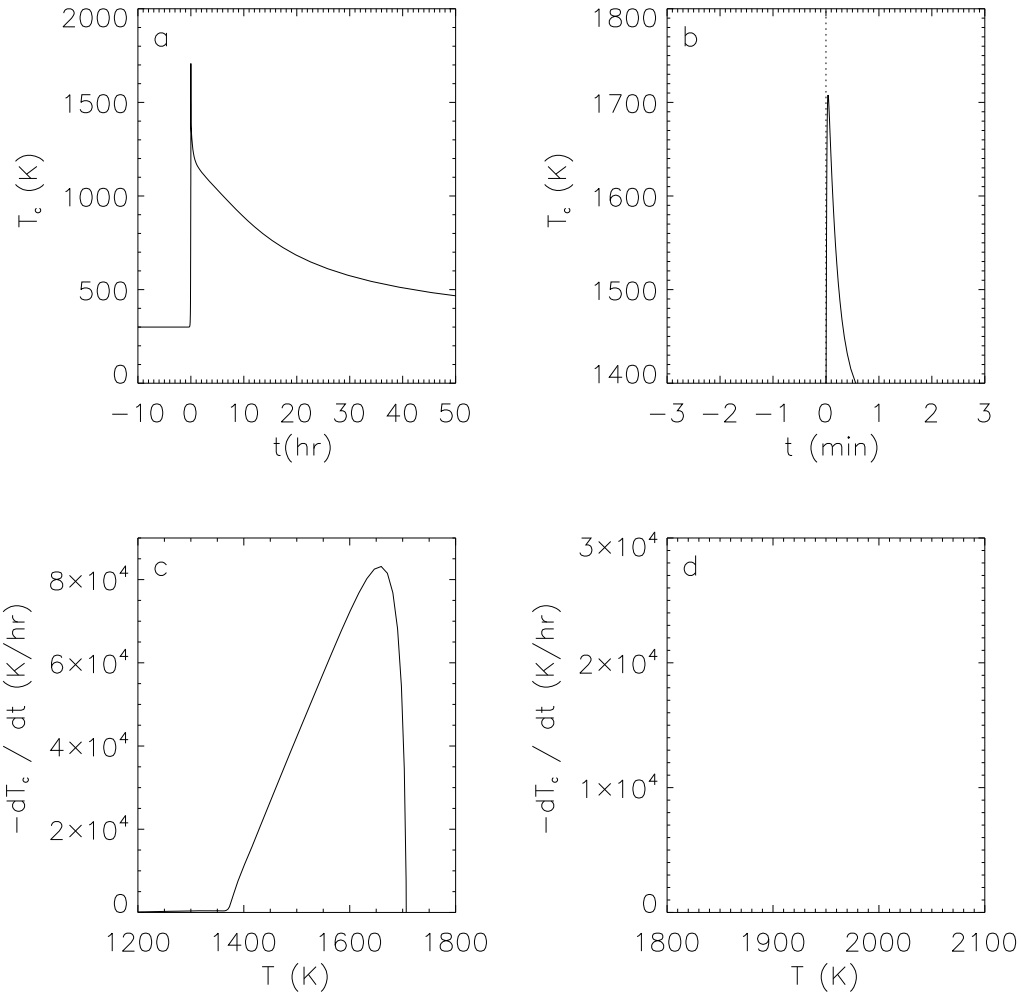

FIG. 39 — Same as Figure 37, except we have now considered opacity due to solids. Once again, in each zone, column densities (both H_2O and solids) are calculated from that zone to/from the shock front.

From ($x = x_{\rm pre}$) to ($x = x_i$), the column density of dust is then

$$\Sigma_{\rm d} = \sum_{j=2}^{i} \frac{1}{2} \left(\rho_{{\rm d},j} + \rho_{{\rm d},j-1}\right)\ x_j - x_{j-1}, \tag{5.6}$$

and the column density of chondrules/chondrule precursors is

$$\Sigma_{\rm ch} = \sum_{j=2}^{i} \frac{1}{2} \left(n_{{\rm ch},j} + n_{{\rm ch},j-1}\right) m_{\rm ch}\ x_j - x_{j-1}, \tag{5.7}$$

giving the effective column density of solids as

$$\Sigma_{\rm eff} = \Sigma_{\rm d} + 8\ {\rm x}10^{-4}\ \Sigma_{\rm ch}. \tag{5.8}$$

Once the column density of water, temperature, and the column density of solids in each zone is known, the amount of emission due to line cooling from that zone can be calculated using the line cooling subroutine. Utilizing the new line radiation transfer subroutine, the amount of this emission that is absorbed in other zones can then be determined. These two new subroutines to the shock code account for the fact that in any one zone, you may have a net increase or a net decrease in the amount of energy, due to line cooling. Using our approximation (Eqn. 5.1), the algorithm for calculating the change in energy due to line emission from zone i into zone $j \neq i$, is as follows:

for all i, if $j = 1$, then

$$\dot{E} = \frac{1}{2}\, n_{H_2O}\ \Big[\Lambda(N_{H_2O_i} - N_{H_2O_{j+1}}, \Sigma_{\mathrm{eff}_i} - \Sigma_{\mathrm{eff}_{j+1}}, T_i) - \Lambda(N_{H_2O_i} - N_{H_2O_j}, \Sigma_{\mathrm{eff}_i} - \Sigma_{\mathrm{eff}_j}, T_i)\Big]\ dx_i, \tag{5.9}$$

if $j = 2$ to $i - 1$, then

$$\dot{E} = \frac{1}{2}\, n_{H_2O}\ \Big[\Lambda(N_{H_2O_i} - N_{H_2O_{j+1}}, \Sigma_{\mathrm{eff}_i} - \Sigma_{\mathrm{eff}_{j+1}}, T_i) - \Lambda(N_{H_2O_i} - N_{H_2O_{j-1}}, \Sigma_{\mathrm{eff}_i} - \Sigma_{\mathrm{eff}_{j-1}}, T_i)\Big]\ dx_i, \tag{5.10}$$

if $i < n$ to $i - 1$, then

$$\dot{E} = \frac{1}{2}\, n_{H_2O}\ \Big[\Lambda(N_{H_2O_{j-1}} - N_{H_2O_i}, \Sigma_{\mathrm{eff}_{j-1}} - \Sigma_{\mathrm{eff}_i}, T_i) - \Lambda(N_{H_2O_j} - N_{H_2O_i}, \Sigma_{\mathrm{eff}_j} - \Sigma_{\mathrm{eff}_i}, T_i)\Big]\ dx_i, \tag{5.11}$$

if $j = i + 1$ to $n - 1$, then

$$\dot{E} = \frac{1}{2}\, n_{H_2O}\ \Big[\Lambda(N_{H_2O_{j-1}} - N_{H_2O_i}, \Sigma_{\mathrm{eff}_{j-1}} - \Sigma_{\mathrm{eff}_i}, T_i) - \Lambda(N_{H_2O_{j+1}} - N_{H_2O_i}, \Sigma_{\mathrm{eff}_{j+1}} - \Sigma_{\mathrm{eff}_i}, T_i)\Big]\ dx_i, \tag{5.12}$$

where

$$dx_i = \frac{x(i+1) - x(i-1)}{2}. \tag{5.13}$$

if $i = 1$, then

$$dx_i = \frac{x(2) - x(1)}{2}, \tag{5.14}$$

and if $i = n$, then

$$dx_i = \frac{x(n) - x(n-1)}{2}. \tag{5.15}$$

The net line cooling in any zone is then given by

$$\dot{e}_i = \frac{1}{dx_i} \sum_{j \neq i} \left(\dot{E}_{j \rightarrow i} - \dot{E}_{i \rightarrow j} \right). \tag{5.16}$$

The algorithm accounts for *backwarming*; line emission radiation is emitted in both directions from each zone, so that all zones will absorb line emission not only from succeeding zones, but also from preceding zones, including those in the pre-shock region. This net energy due to line cooling serves to cool or heat the gas in each zone, and must be accounted for as a part of the gas energy term (Eqn. 2.32) within the Runge Kutta solver. Recall that the line cooling, $\Lambda(N_{H_2O}, \Sigma_{\rm d}, T_i) \propto n_{H_2O}$. If, in any one zone, the column density of water, $N_{H_2O} = 0$, then the line emission from that zone, $\Lambda(N_{H_2O}, \Sigma_{\rm d}, T_i) = 0$. If the column density of dust, $\Sigma_{\rm dust} = 0$, then the effective column density, $\Sigma_{\rm eff}$, will only include the column density due to chondrules/chondrule precursors, and the line emission will be much greater than if dust were present. If the temperatures in any two zones are the same, then the net emission and absorption of line emission between those zones will be zero.

Our updated shock code now includes all the improvements suggested in Desch et al. (2005). Using the updated code, we were able to evaluate the effects of molecular line cooling.

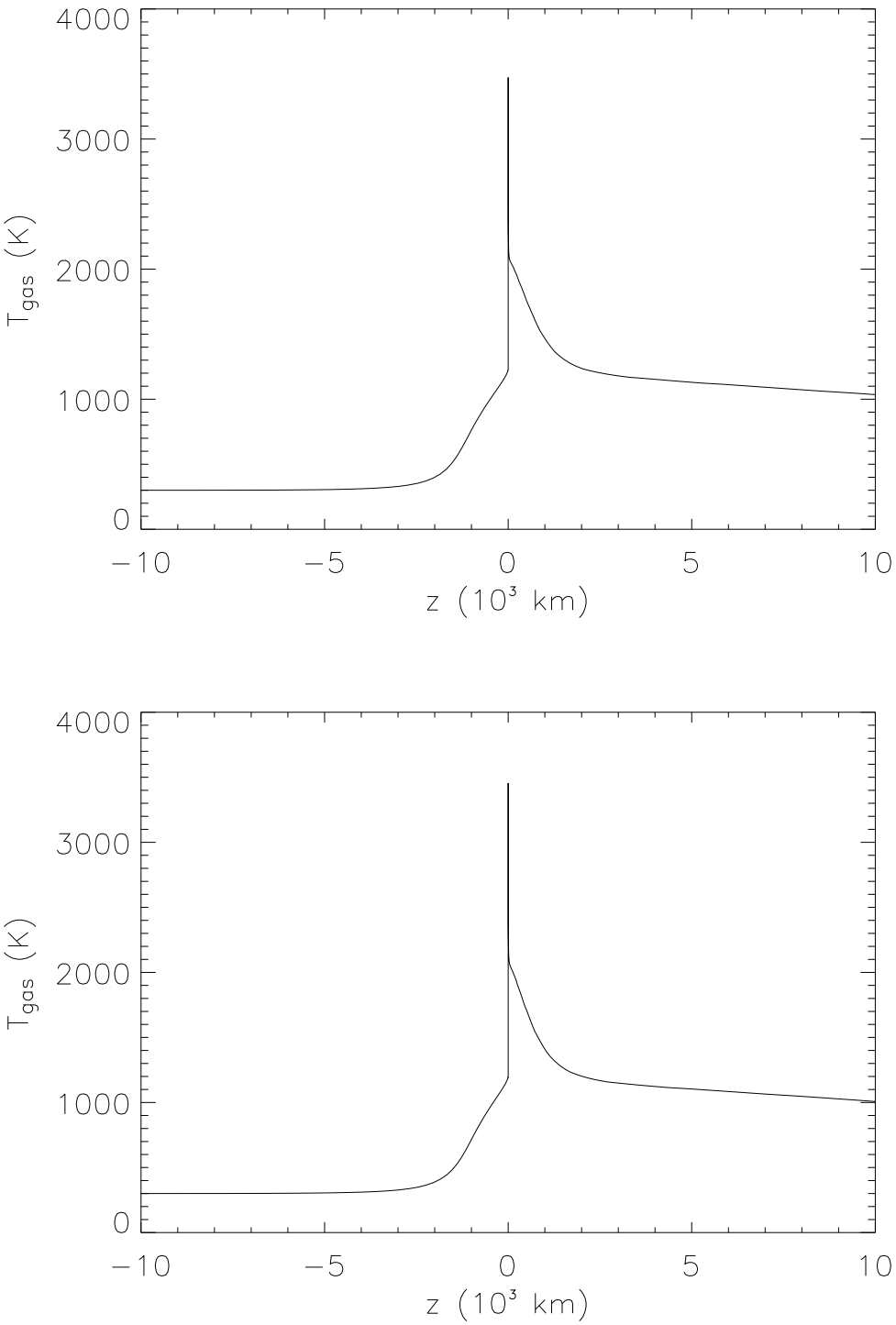

FIG. 40 — The figure on the top is the same as Figure 36 (c), where we have zoomed in on the area within 10^5 km of the shock front. The figure on the bottom is the same as Figure 38 (c), where, once again, we have zoomed in on the area within 10^5 km of the shock front.

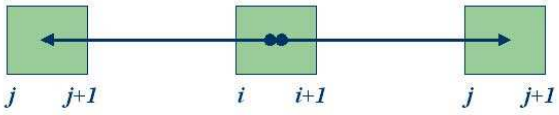

FIG. 41 — A cartoon of line emission from zone i into zone j.

CHAPTER 6

RESULTS INCLUDING LINE COOLING

Based on our toy model outlined in Chapter 4, we expected the inclusion of line cooling to result in a noticeable increase in cooling rates over our canonical case neglecting line cooling, from $\sim 10^2$ K hr^{-1} to $\sim 10^4$ K hr^{-1}. This is especially true when you consider that in our canonical case, dust begins to evaporate in the pre-shock region, and is completely evaporated at the shock front. The opacity of solids (chondrules and ultra-refractories) is a mere 0.03 cm^2 g^{-1} in the post-shock region, due to evaporation. This being the case, we would expect cooling rates of $> 10^4$ K hr^{-1}, not only immediately following the shock, but for as long as 10^5 seconds after the shock, similar to the "without dust" case of Figure 34. However, our results show that this is not the case, as shown in Figures 42 and 43, where we have included the effects of line cooling in our canonical shock (Table 20, Case 9). These figures are indistinguishable from Figures 19 and 20, our canonical case neglecting line cooling (Table 6, Case 6). Increasing the water abundance to 10 times the solar value (Figures 44 and 45;(Table 20, Case 10)) only results in an increase in the cooling rates of chondrules of $\sim$ 10 K through their crystallization temperatures. Clearly, something (other than dust opacity) that we did not account for in our toy model, is serving to drastically reduce the cooling rates due to line emission.

One physical effect not included in our original toy model is backwarming, or the radiation emitted from the pre-shock region. Another effect is the dissociation and recombination of hydrogen, as we were interested in isolating the effects of line cooling. Dissociation of hydrogen molecules is responsible for the rapid cooling rates immediately following the shock in the results of DC02, leading us to believe that inclusion of these effects would only serve to increase the cooling rates of the gas. However, recombination of hydrogen atoms convert stored chemical energy to heat in the gas, thereby slowing the cooling rates. It has become evident that dissociation and recombination of hydrogen following the shock must be examined more closely.

The fraction of the gas that is atomic hydrogen at any time is given by

$$f = \frac{n_{\mathrm{H}}}{n_{\mathrm{H}} + 2n_{\mathrm{H_2}}} \tag{6.1}$$

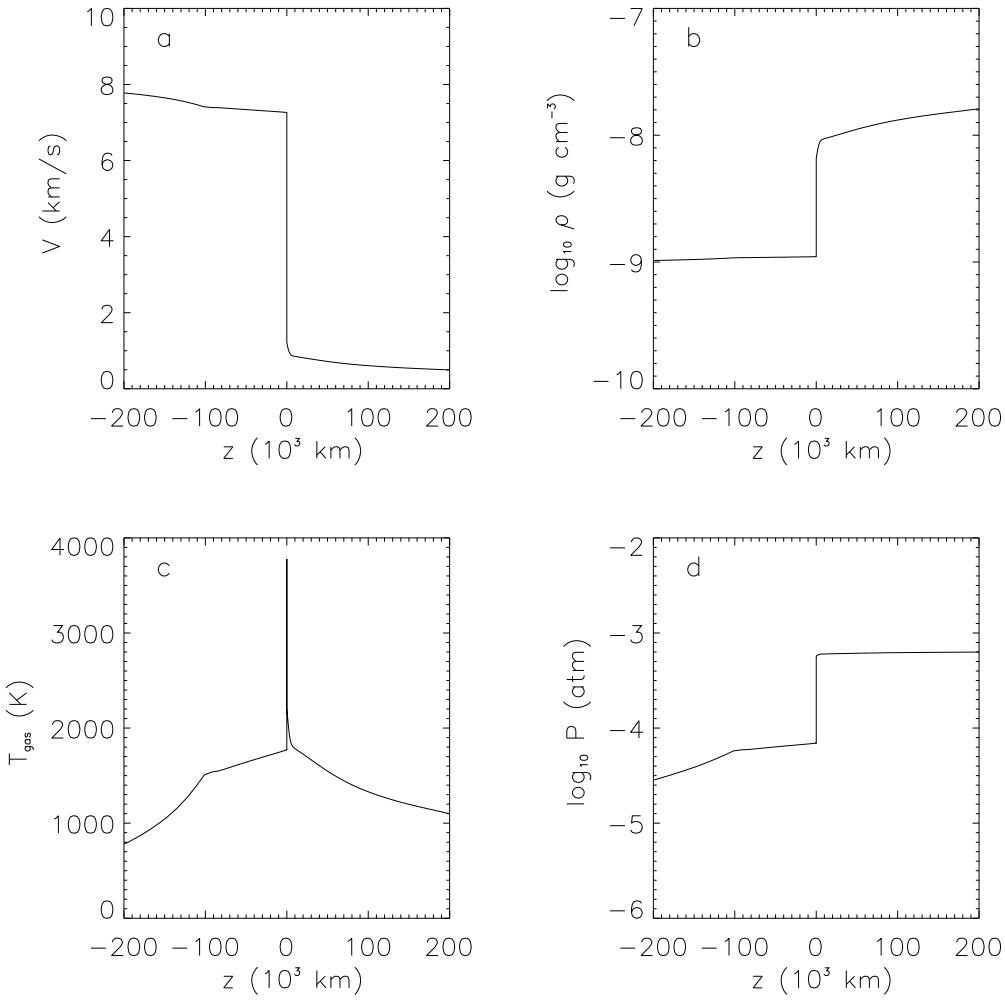

FIG. 42 — Case 9 (see Table 20). Same as Figure 19 (our canonical case neglecting line cooling), except now we have included detailed treatment of H_2O line cooling following the methods of Morris et al. (2009).

where $n_{\mathrm{H_{TOT}}} \equiv n_{\mathrm{H}} + 2n_{\mathrm{H_2}}$. The heating rate per recombination of hydrogen is

$$\Gamma \cong \frac{df}{dt} n_{\mathrm{H_{TOT}}} \left(\frac{\epsilon}{2}\right) \tag{6.2}$$

where $\epsilon = 4.48$ eV. As f increases (hydrogen is dissociating), Γ decreases (the gas is cooling). This heating due to recombination of hydrogen will result in a reduction in the cooling rate of the gas. The new cooling rate is found using the definition of internal energy (including the chemical energy

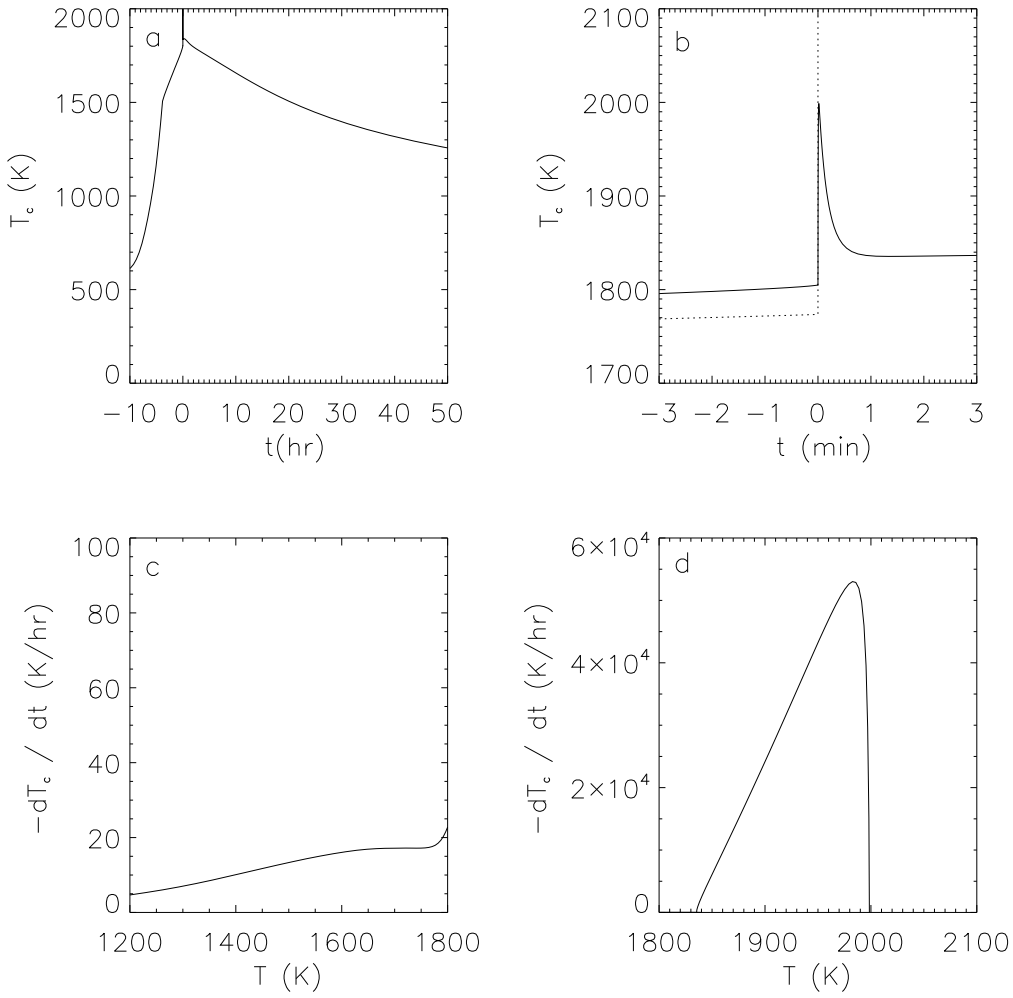

FIG. 43 — Case 9 (see Table 20). Same as Figure 20 (our canonical case neglecting line cooling), except now we have included detailed treatment of H_2O line cooling following the methods of Morris et al. (2009).

of dissociation):

$$\begin{aligned} e &= \frac{5}{2}n_{\rm H_2}kT + \frac{3}{2}n_{\rm H}kT + \frac{3}{2}n_{\rm He}kT + \frac{\epsilon}{2}n_{\rm H} \\ &= n_{\rm H_2}kT + \frac{3}{2}\left(n_{\rm H_2} + n_{\rm H} + n_{\rm He}\right)kT + \frac{\epsilon}{2}n_{\rm H} \\ &= n_{\rm H_2}kT + \frac{3}{2}P + \frac{\epsilon}{2}n_{\rm H} \\ &= \frac{1-f}{2}n_{\rm H_{TOT}}kT + \frac{3}{2}P + f\ n_{\rm H_{TOT}}\left(\frac{\epsilon}{2}\right). \end{aligned}$$

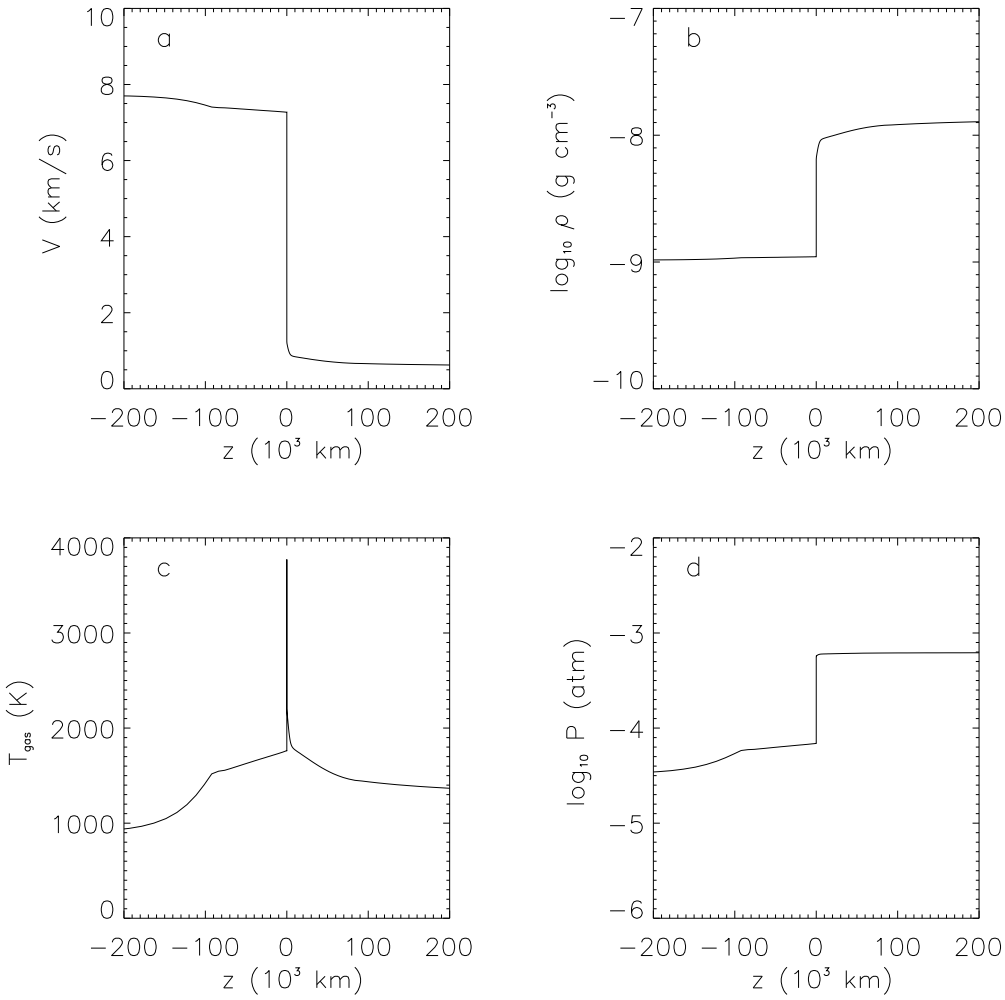

FIG. 44 — Case 10 (see Table 20). Same as Figure 42 (our canonical case including line cooling), except the water abundance has been increased by a factor of ten.

IF $n_{\rm H_2} \equiv n_{\rm H_{TOT}}$ = constant, $n_{\rm H} = 0$, and P is held constant

$$\left(\frac{dT}{dt}\right)_{\rm f=0} = \frac{1}{n_{\rm H_2} k} \frac{\partial e}{\partial t},$$

IF $n_{\rm H_{TOT}}$ and P are held constant, but f is allowed to vary, then $n_{\rm H_2} = (1-f)\, n_{\rm H_{TOT}}/2$, giving

$$\left(\frac{\partial e}{\partial t}\right) = \frac{n_{\rm H_{TOT}} k}{2} \left[(1-f) + \left(\frac{\epsilon}{k} - T\right) \frac{dF}{dT}\right] \frac{dT}{dt},$$

$$\left(\frac{\partial T}{\partial t}\right)_{f\neq 0} = \frac{2}{n_{\rm H_{TOT}} k} \left[(1-f) + \left(\frac{\epsilon}{k} - T\right) \frac{df}{dT}\right]^{-1} \frac{\partial e}{\partial t},$$

and

$$\left(\frac{\partial T}{\partial t}\right)_{f=0} = \frac{2}{n_{\rm H_{TOT}} k} \frac{\partial e}{\partial t},$$

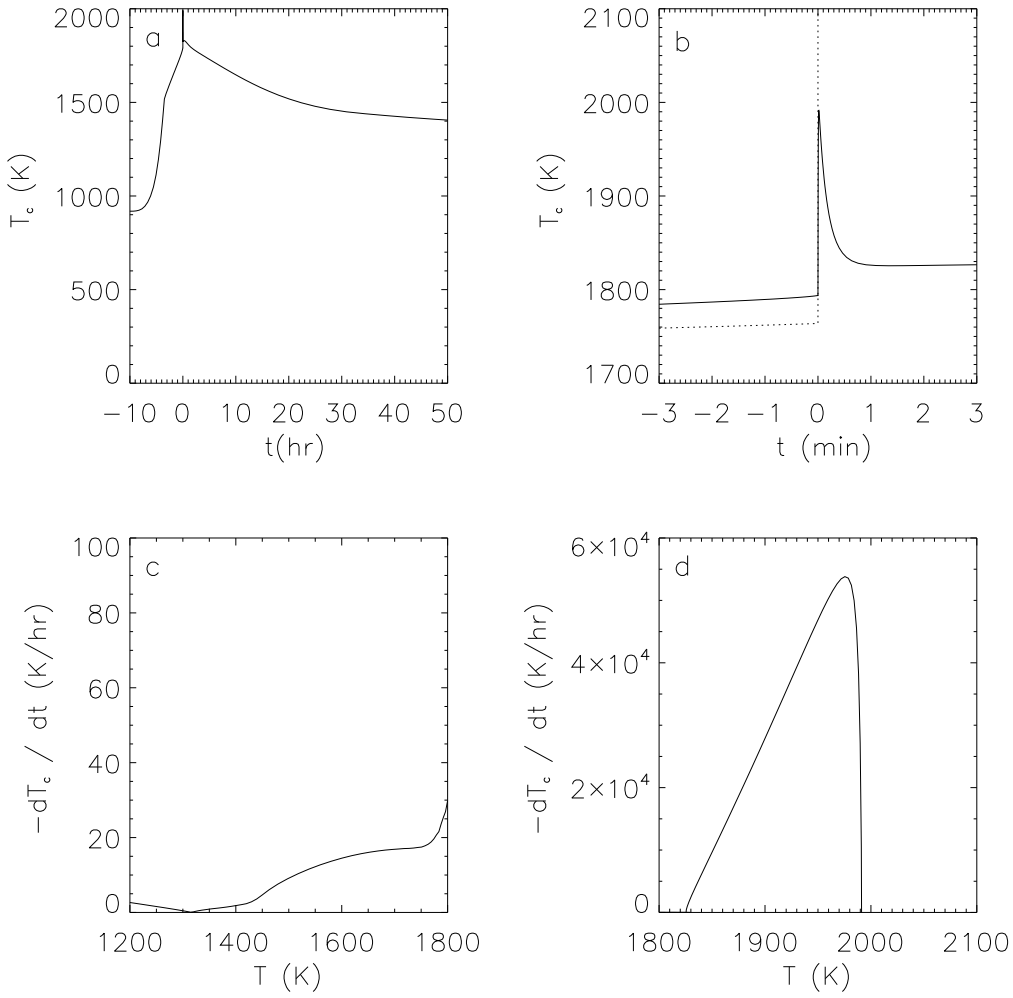

FIG. 45 — Case 10 (see Table 20). Same as Figure 43 (our canonical case including line cooling), except the water abundance has been increased by a factor of ten.

giving the new cooling rate after reduction due to hydrogen recombination.

$$\left(\frac{dT}{dt}\right) = \left(\frac{dT}{dt}\right)_{\rm f=0} \left[(1-f) + \left(\frac{\epsilon}{k} - T\right)\frac{df}{dT}\right]^{-1} \tag{6.3}$$

Assuming chemical equilibrium ($R_{\rm rec} = R_{\rm diss}$), we can use the dissociation and recombination rates given in Appendix B to determine the fraction of the gas that is atomic at any given time. To do so, it is necessary to balance the rates of dissociation and recombination, and solve the resulting cubic equation. Once this was done, it was necessary to find a temperature-dependent approximation to both the fraction, f, and its derivative with respect to temperature, df/dT, in order to incorporate the effects of dissociation and recombination into our toy model, as the toy model does not track

number densities of hydrogen. We are only concerned with the temperature range $\sim$ 1750 - 2200 K; in our canonical case, 2200 K is the post-shock gas temperature immediately following the spike at the shock front, cooling to 1750 K and reaching chemical equilibrium in minutes. The fraction of atomic hydrogen, f, its derivative, df/dT, and our approximations to both are shown in Figures 46 and 47. Figure 48 shows the dependence of the term

$$B \equiv \left[(1-f) + \left(\frac{\epsilon}{k} - T_{\rm g}\right)\ \frac{df}{dT_{\rm g}}\right] \tag{6.4}$$

on temperature, demonstrating the reduction in cooling rates. Figure 49 shows the gas temperature as a function of time in our toy model, after the inclusion of backwarming and the effects of hydrogen reactions. It is clearly evident that these two effects dramatically reduce the effect of line cooling, by factors of $\sim 10^2$. However, these results suggest that we should still see an increase in the cooling rates of the gas (between 2200 K and 1750 K) when line cooling is included.

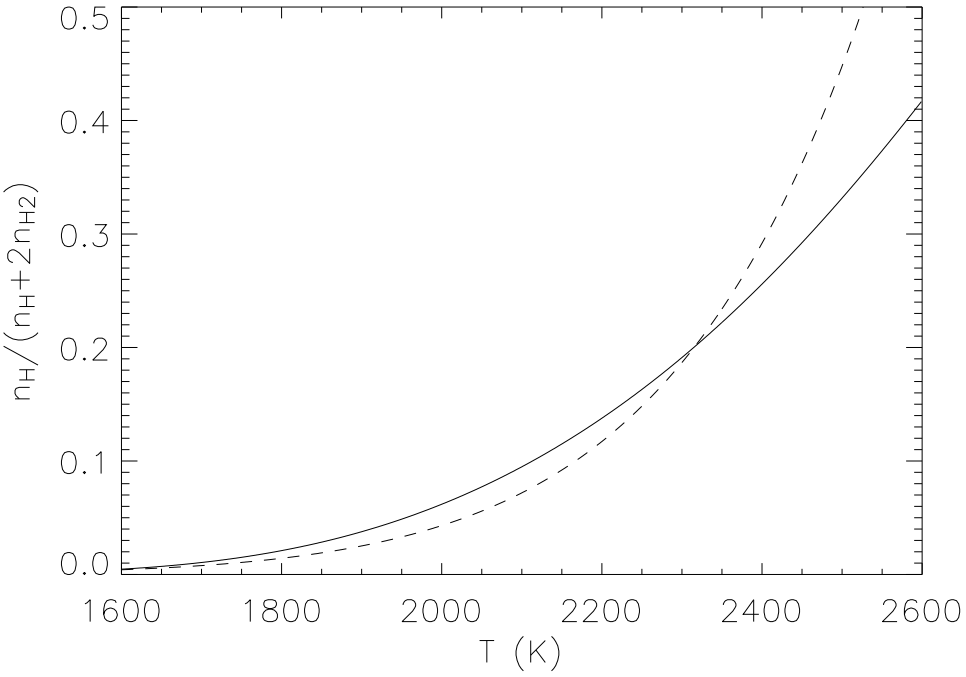

FIG. 46 — In chemical equilibrium, the fraction of atomic hydrogen (solid line) and our approximation ($10^{-36}\ T_g^{10.492}$; dashed line), assuming a post-shock density of 6 x 10^{-9} g cm−3.

Now we must examine the effects of the column density of water on the cooling rates. According to the tables of Morris et al. (2009), the cooling rate due to H_2O at $N_{H_2O} = 10^{19}\,cm^{-2}$ (in the case with no dust) is 38 % of the cooling rate at $N_{H_2O} = 10^{13}\,cm^{-2}$. This is the column density of H_2O reached only 100 s after the shock. This decreases the cooling rate from an initial 200 K hr^{-1} to 76 K hr^{-1} in those first 100 s. At $N_{H_2O} = 10^{20}\,cm^{-2}$, the cooling rate is 16 % of the original, and at $N_{H_2O} = 10^{21}\,cm^{-2}$, it has decreased to .05 %. This results in a reduction of the cooling rate to $\sim$ 30 K hr^{-1} after 1000 s, and it drops to $\sim$ 10 K hr^{-1} shortly thereafter. This equates to a drop in temperature of only around 20 K in the first 1000 s.

At temperatures where the cooling is dominated by line cooling (as opposed to dissociation of hydrogen molecules), we now expect to see, at most, a difference of 10 K hr^{-1} in the cooling rates of the gas. Comparing the cooling rates of the gas after the inclusion of line cooling (Figure 51c) to those without line cooling (Figure 50c), we see only a difference of $\sim$ 5 K hr^{-1}, consistent with

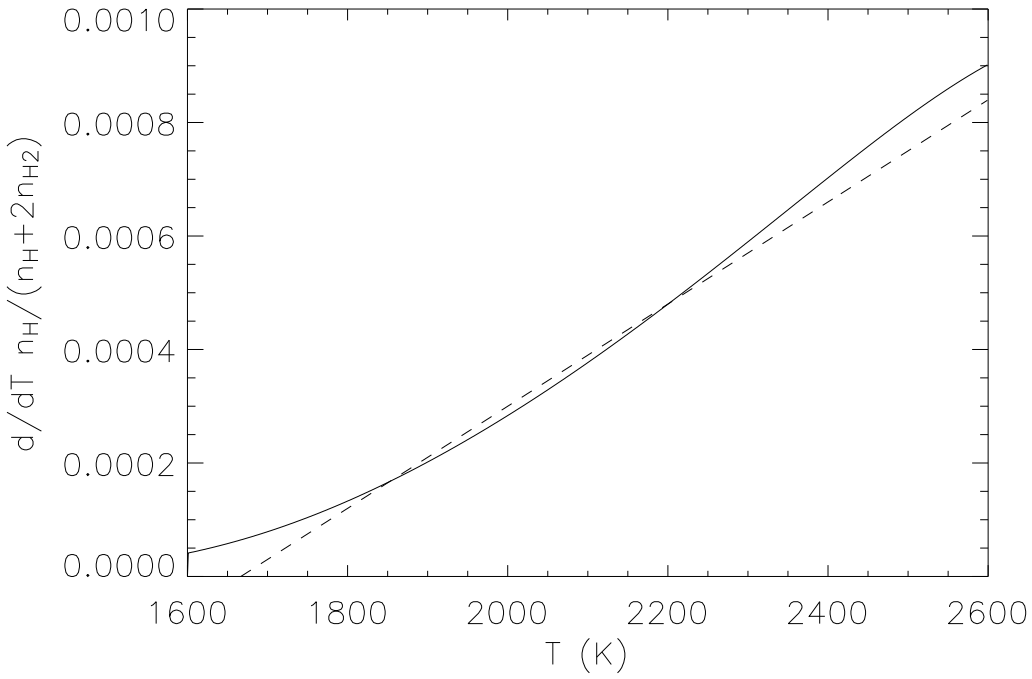

FIG. 47 — The temperature derivative of the fraction of atomic hydrogen (solid line) and our approximation (9 x $10^{-7}\ T_{\rm g} - 0.0015$; dashed line).

our calculations. Even when the water abundance is increased by a factor of ten, the cooling rates increase by only $\sim$ 30 K hr^{-1} (Figure 52c; the vertical line is a numerical artifact). (Figures 44 and 45 also show the case where the water abundance has been increased by a factor of ten over the canonical case). The combination of the addition of energy due to recombination of hydrogen, and reduced cooling rates due to higher column densities of H_2O, have almost eliminated the effect of line cooling on the gas.

We now ask ourselves: If line radiation barely affects the cooling rates of the gas, what effect can it have on the cooling rates of the chondrules? To get an idea, we must examine to what extent thermal exchange between the gas and chondrules affects the particle heating term in the post shock region. Recall that the heating term for the chondrules is $q\ +\ \epsilon\left(J_{\rm r} - \sigma T_{\rm p}^4/\pi\right)$, where q depends on the relative velocities of the gas and particles. Using this expression, we can compare the contribution of the the terms that are dependent on the gas properties with the

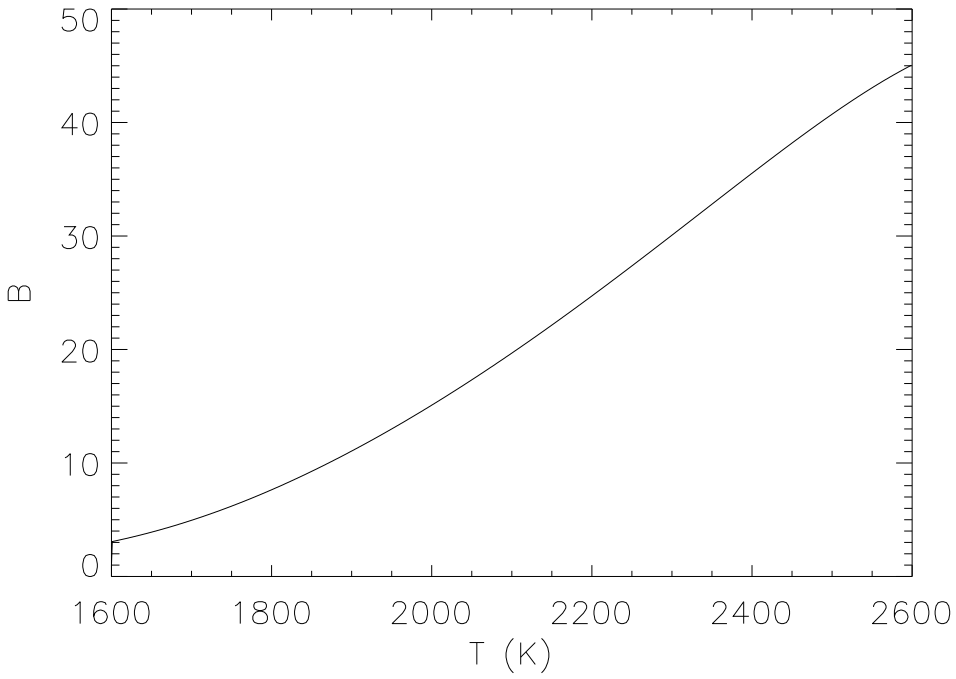

FIG. 48 — The reduction of cooling rates, $B \equiv [(1-f) + (\epsilon/k - T_{\rm g})\ df/dT_{\rm g}]$, due to hydrogen recombination.

term that depends only on the chondrule temperature. In doing so, we have found that by the time chemical equilibrium is achieved and line cooling exceeds the cooling due to dissociation of hydrogen, thermal exchange with the gas accounts for less than 10% of the particle heating term. Therefore, line cooling due to H_2O has a negligible effect on chondrule cooling rates.

We can also test the results summarized above by examining the case where we do not allow hydrogen to dissociate or recombine. We predict that without hydrogen dissociation the gas will not cool as rapidly immediately following the shock. Without the additional energy due to recombination, line cooling will be much more effective; so effective, in fact, that even at the 10% level, we should see some effect on the cooling rates of chondrules. In Figure 53c, we see that the gas does indeed cool much more rapidly due to line cooling in the post-shock region, therefore the gas does not heat as rapidly in the pre-shock region. Figure 54b shows that the chondrules would reach a higher peak temperature if they did not evaporate, because of lack of initial cooling due to hydrogen dissociation. Figure 54d shows that the initial cooling rates of chondrules ($\sim$ 8000 K

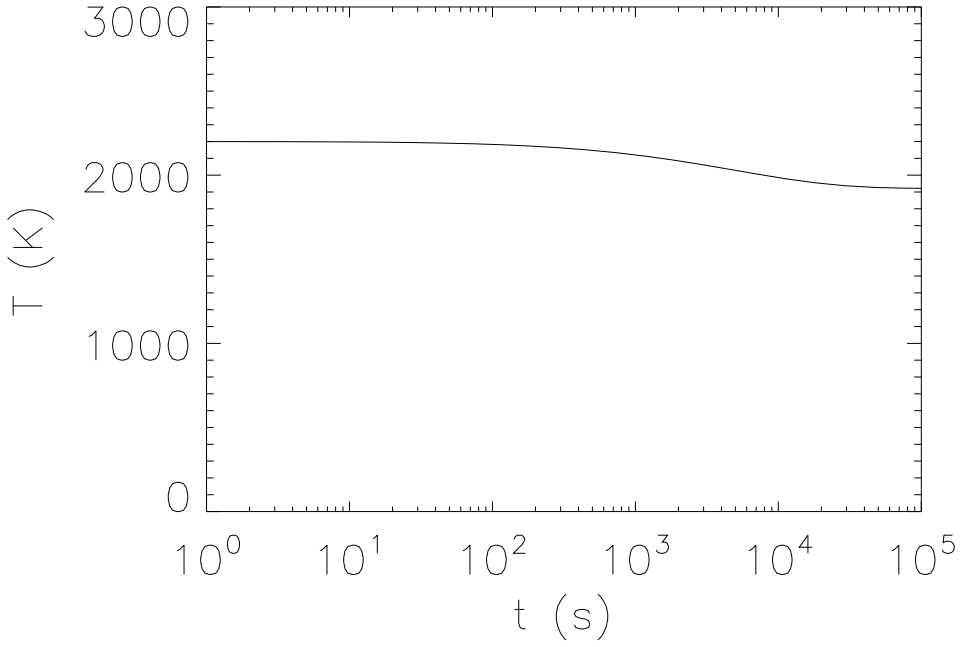

FIG. 49 — Gas temperature as a function of time in our toy model, after the inclusion of backwarming and the effects of hydrogen dissociation and recombination.

hr−1) is drastically reduced from the case in which hydrogen dissociation occurs (> 5 x 10^4 K hr^{-1}). As predicted, we see higher cooling rates of chondrules through their crystallization temperatures (Figure 54c).

1. Results of Parameter Study

As we now understand the effects of line cooling (or lack thereof), we wish to run the updated shock code with various input parameters in order to constrain the conditions under which chondrules form in solar nebula shocks. We have already examined the case where the water abundance is increase by a factor of 10 over the canonical value (Table 20, Case 10), with respect to the effect of line cooling; now let us look at the thermal histories of the chondrules. In this case (increased water abundance; Table 20, Case 10), chondrule precursors completely melt upon passage through the shock, but do not evaporate. Initial cooling rates are rapid (> 5 x 10^4 K hr^{-1}),

slowing to < 30 K hr^{-1} through the crystallization temperature range (Figures 44 and 45). These cooling rates are consistent with experimental constraints. As expected, when the water abundance is reduced to 1/10 the canonical value (Figures 55 and 56; Table 20, Case 11), we see no difference in the results from the canonical case.

We next reduced the shock speed to 7 km s^{-1} (Table 20, Case 12). Very little "pre-heating" of the upstream material occurs (Figure 57). Micron-sized dust begins to evaporate shortly before reaching the shock front. The lower shock speed results in less drag heating of chondrules upon passage through the shock, in turn resulting in lower peak temperatures for the chondrules (Figure 58). As in the case with no line cooling, only partial melting of chondrules occurs. Initial cooling rates meet the constraints necessary for the retention of volatiles (a few times 10^4 K hr^{-1}), and cooling rates are, for the most part, within the range necessary to match experimental constraints through the crystallization temperatures of chondrules.

We were unable to obtain results with a shock speed of 9 km s^{-1}. We cannot explain why, but with the addition of line cooling, the code became unstable at this shock speed. However, since we have determined that line cooling will have very little effect, for sound physical reasons that still apply, we can refer to our case at 9 km s^{-1}, without line cooling (Figures 21 and 22; Table 6, Case 7). We were able to obtain results (to within convergence of ~ 1 %) for a shock speed of 10 km s^{-1} (Table 20, Case 14). These results are shown in Figures 59 and 60. The gas now reaches a peak temperature of > 5400 K. Once again, akin to the 9 km s^{-1} case, the peak temperature of chondrules artificially remains at 2000 K, and does not climb any higher, due to the evaporation temperature of chondrules. At this shock speed (10 km s^{-1}), chondrules evaporate from an initial radius of 300 μm, to ~ 146 μm by the end of the computational domain, losing 88 % of their mass.

We now investigate the effect of increasing/decreasing the gas density. Figures 61 and 62 show the results when the density is decreased by a factor of 10 (Table 20, Case 15). We see the same results here as we did without line cooling. Chondrule precursors just barely begin to melt, only reaching peak temperatures of ~ 1500 K, and cooling rates are much too high to match the

constraints on chondrule thermal histories.

Leaving all other parameters unchanged from the canonical case, we turn to investigate the effect of increasing/decreasing the chondrule concentration, $\mathcal{C}$. Figures 63 and 64 show the results when the chondrule density is increased by a factor of 30 (Table 20, Case 16). As predicted by DC02, higher chondrule concentrations lead to higher cooling rates. However, DC02 also predict higher peak chondrule temperatures. Our results show that this is not the case. The lower shock velocity in the post-shock region actually leads to slightly lower peak chondrule temperatures. Regardless, the peak temperature reached by chondrules is still enough to completely melt the chondrule precursors, without leading to evaporation. Although cooling rates are higher than in the canonical case with a lower chondrule concentration, they still meet the constraints set by furnace experiments; initial rapid cooling, with cooling through the crystallization temperature range at rates < 1000 K hr^{-1}.

You will note that in our discussion of the results after the inclusion of line cooling, we have not yet addressed the constraints on the thermal histories of chondrules *before* they are melted by the shock wave. So far, we have only discussed how our results compare to the constraints on cooling rates of chondrules *after* they have melted. Recall that the presence of primary S limits the duration of heating above $\sim$ 650 - 1200 K to several minutes (Hewins et al. 1996; Connolly & Love 1998; Jones et al. 2000; Lauretta et al. 2001; Tachibana & Huss 2005. Additionally, the lack of isotopic fractionation of alkalis limits the time spent at high temperature (1300 - 1600 K) to minutes, or less, prior to melting (Tachibana et al. 2004; Tachibana & Huss 2005). In our canonical case (Figure 20), chondrules spend almost eight hours at temperatures > 650 K before reaching the shock wave and melting. Out of those eight hours, $\sim$ three and a half are spent between 1300 and 1600 K. Our canonical case clearly does not meet these constraints on the "pre-heating" of chondrules. Because micron-sized dust evaporates well before the shock front, the precursor radiation is able to penetrate further upstream and heat the gas and chondrule precursors much sooner, therefore, they are heated for much longer timescales before melting. However, in the case

TABLE 20
RESULTS OF PARAMETER STUDY, INCLUDING LINE COOLING

Case No.	$\mathcal{C}$	V_s	ρ_g (g cm^{-3})	H_2O[a]	$T_{\rm peak}$ (K)	Cooling rate (K hr^{-1})[b]	Cooling rate (K hr^{-1})[c]
9	10	8	10^{-9}	1	2000	> 5 x 10^4	10-25
10	10	8	10^{-9}	10	1900	> 5 x 10^4	3-30
11	10	8	10^{-9}	0.1	2000	> 5 x 10^4	10-25
12	10	7	10^{-9}	1	1720	> 2 x 10^4	15-45[e]
13	10	9	10^{-9}	1	2000[d]	1100	8-20
14	10	10	10^{-9}	1	2000[d]	1500	15-21
15	10	8	3 x 10^{-10}	1	1500	> 7 x 10^4	7 x 10^4
16	30	8	10^{-9}	1	1900	> 5 x 10^4	35-65
17	50	8	10^{-9}	1	2000	$> 10^4$	22-90

[a]Water abundance with respect to our assumed water-to-gas ratio, 8 x 10^{-4}.

[b]Cooling rates at $T_{\rm peak}$

[c]Cooling rates through 1400-1800 K, the crystallization temperature range of chondrules.

[d]Artificial peak temperature due to evaporation. See text for final radius of chondrules.

[e]Cooling rates through 1400-1599 K; rates are $\sim$ 2 x 10^4 from 1600-1800 K.

where we have increased the chondrule concentration to $\mathcal{C} = 30$ (Figures 63 and 64) (Table 20, Case 16), the dust does not evaporate as quickly, and the chondrules only spend about two and half hours at temperatures over 650 K, and only $\sim$ 40 minutes at temperatures between 1300 and 1600 K. We predict that at even higher chondrule concentrations, there will not be extended heating of chondrules in the pre-shock region and the constraint on "pre-heating" of chondrules will be met by the updated shock model, while still meeting the constraints on cooling rates after melting. The justification for such higher chondrule concentrations will be addressed in the next chapter. Table 20 shows the peak temperature reached by chondrules and the cooling rates through their crystallization temperature range, resulting from our parameter study.

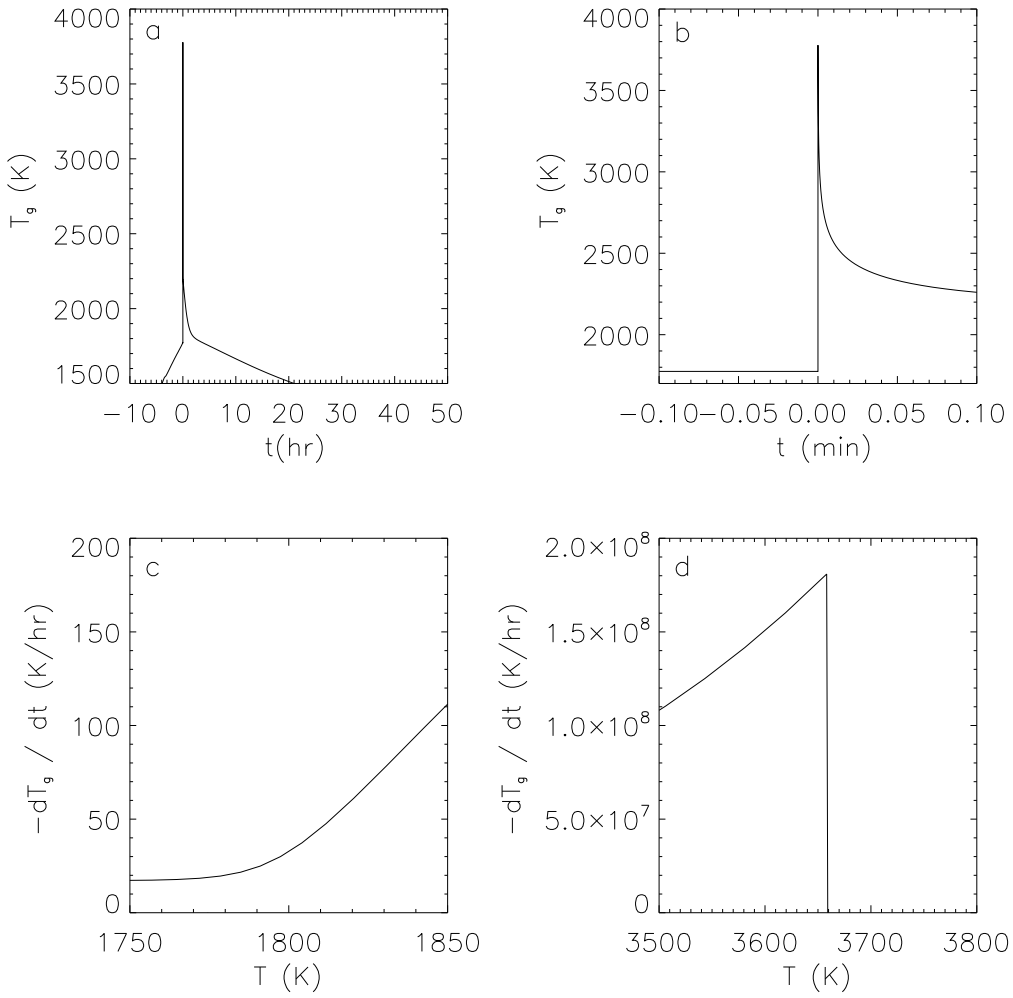

FIG. 50 — Case 6 (see Table 6). Gas temperatures in our canonical shock (neglecting line cooling), over the course of hours (a), and also fractions of a minute (b). The cooling rates of the gas as a function of temperature, in the regime where the effects of line cooling become important (c), and at higher temperatures (d), when the cooling rates are dominated by the dissociation of hydrogen molecules.

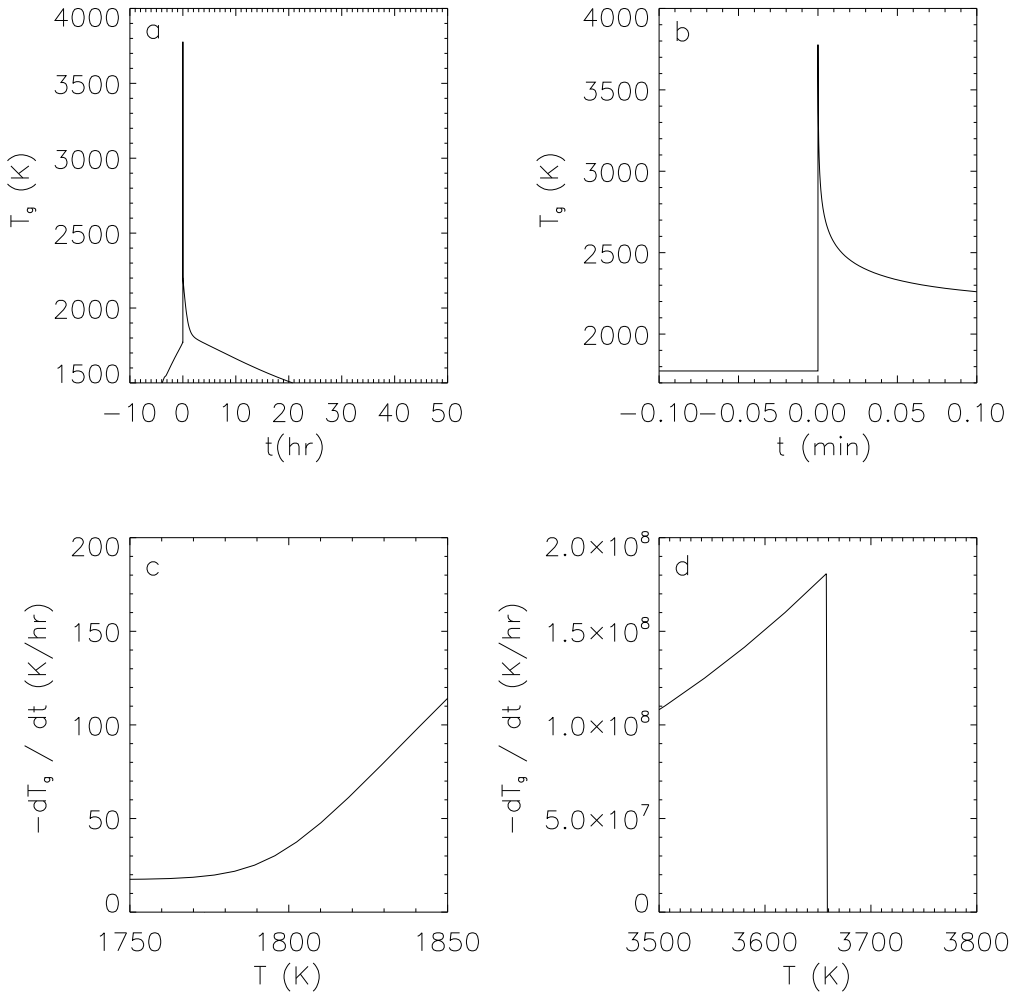

FIG. 51 — Case 9 (see Table 20). Same as Figure 50, except, in this case, the effects of line cooling on the gas are included.

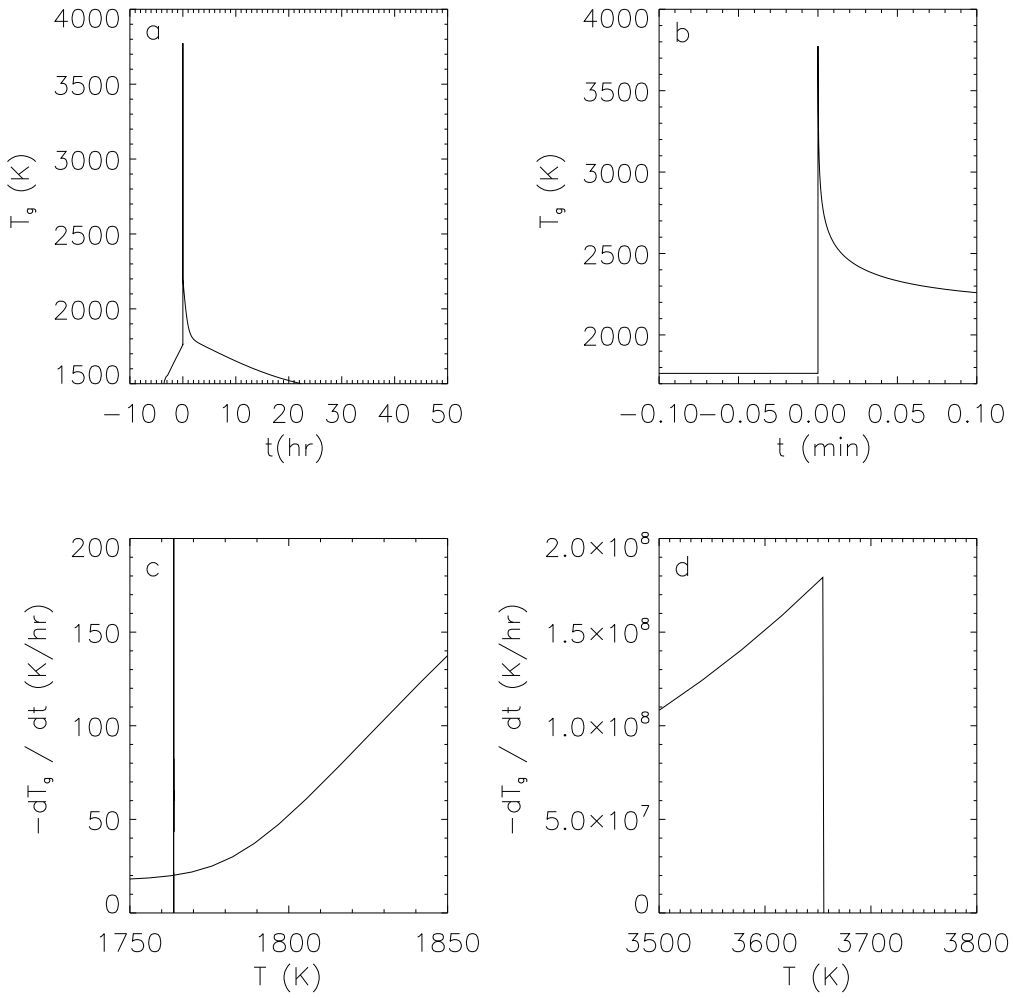

FIG. 52 — Case 10 (see Table 20). Same as Figure 51, except, in this case, the water abundance has been increased to 10 times the solar value.

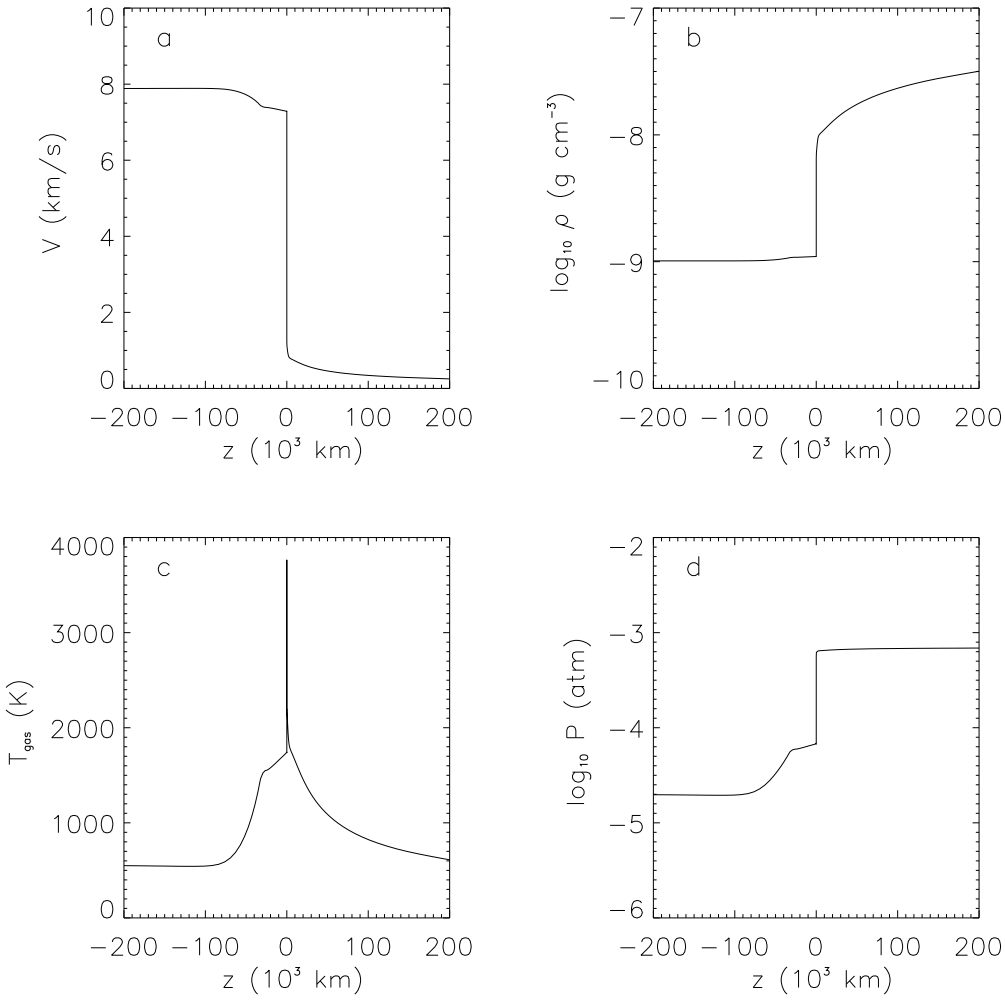

FIG. 53 — Same as Figure 42 (our canonical case including line cooling), except now we do not allow hydrogen to dissociate or recombine.

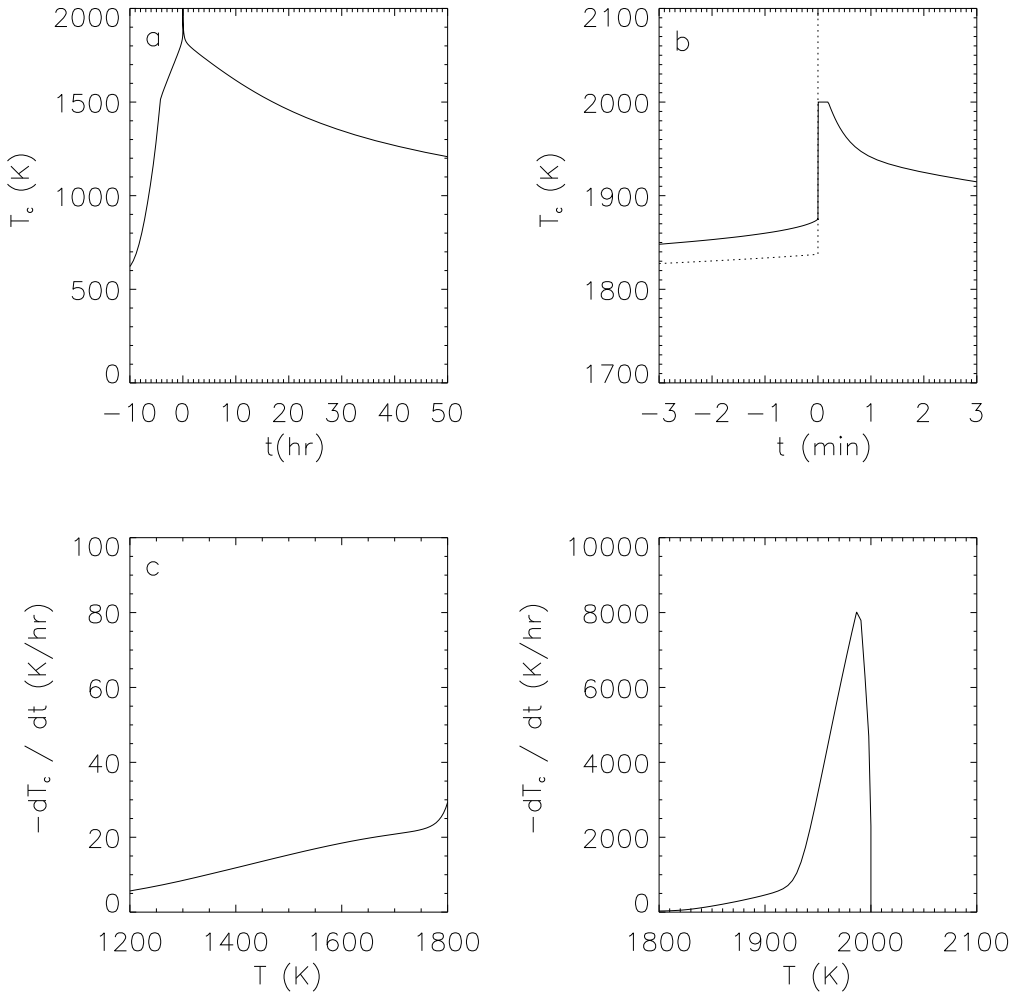

FIG. 54 — Same as Figure 43 (our canonical case including line cooling), except now we do not allow hydrogen to dissociate or recombine.

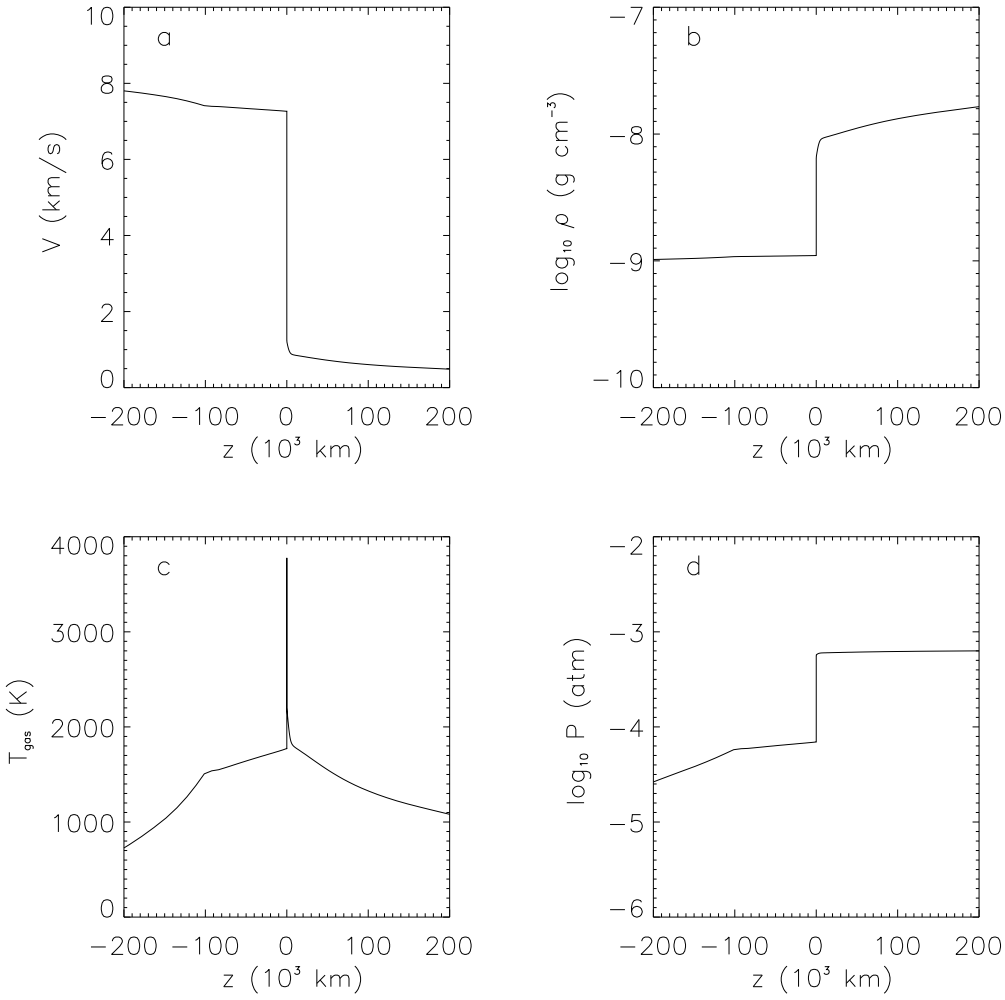

FIG. 55 — Case 11 (see Table 20). Same as Figure 42 (our canonical case including line cooling), except now the water abundance has been reduced to 1/10 the solar value.

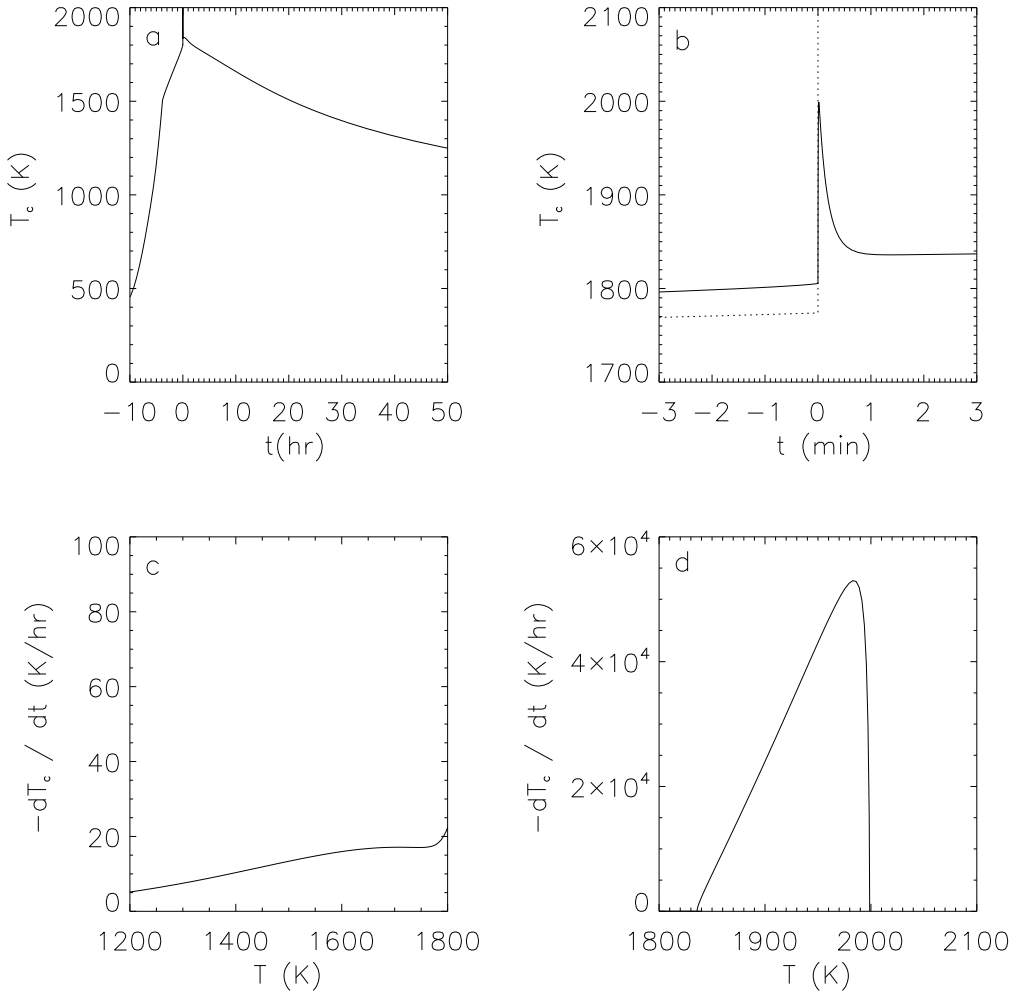

FIG. 56 — Case 11 (see Table 20). Same as Figure 43 (our canonical case including line cooling), except now the water abundance has been reduced to 1/10 times the solar value.

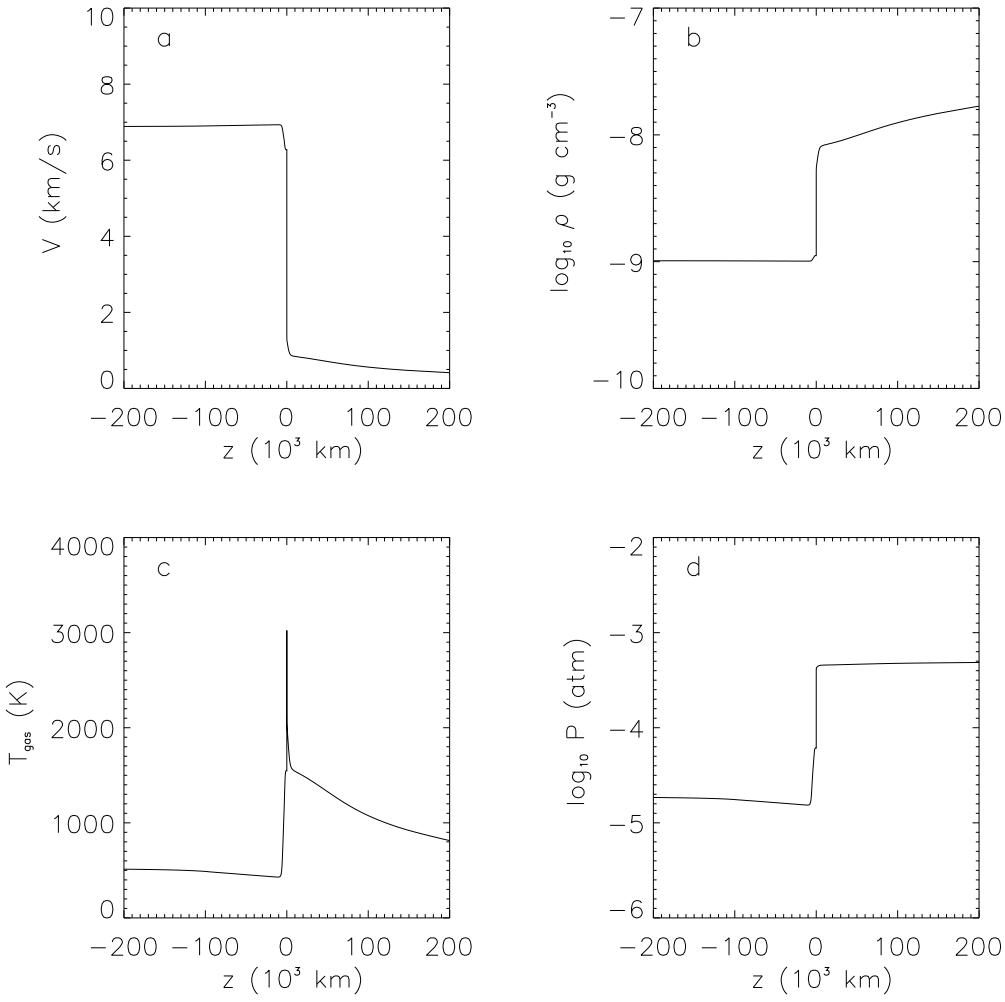

FIG. 57 — Case 12 (see Table 20). Same as Figure 42 (our canonical case including line cooling), except the shock speed has been reduced to $V_s = 7$ km s^{-1}.

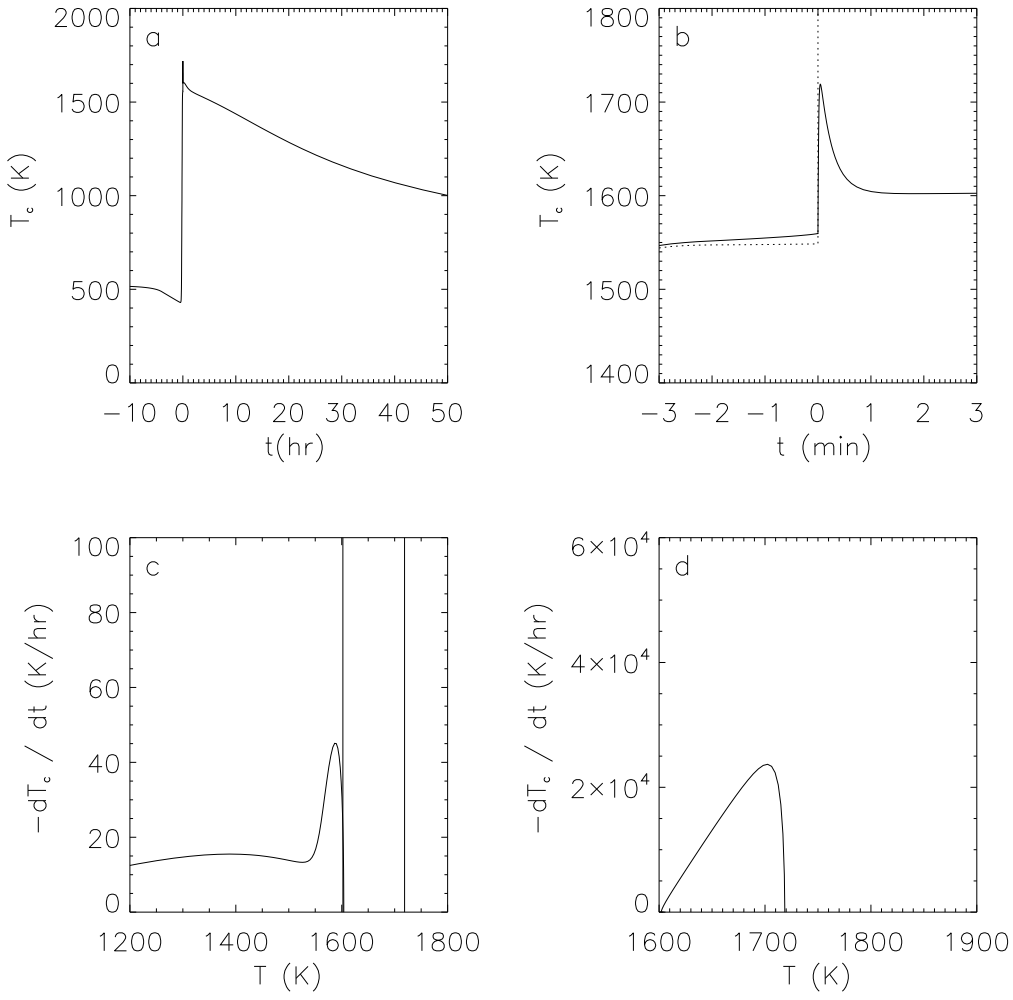

FIG. 58 — Case 12 (see Table 20). Same as Figure 43 (our canonical case including line cooling), except the shock speed has been reduced to $V_s = 7$ km s^{-1}.

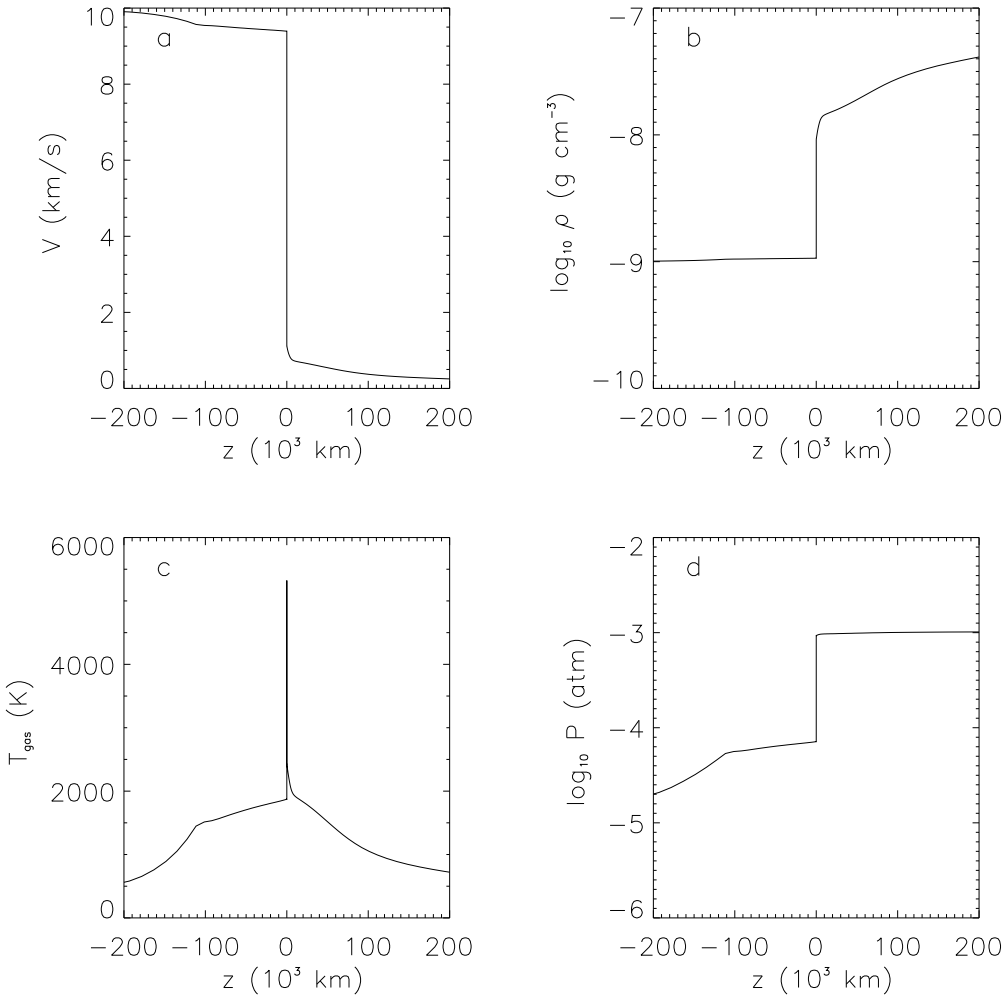

FIG. 59 — Case 14 (see Table 20). Same as Figure 42 (our canonical case including line cooling), except the shock speed has been increased to $V_s = 10$ km s^{-1}.

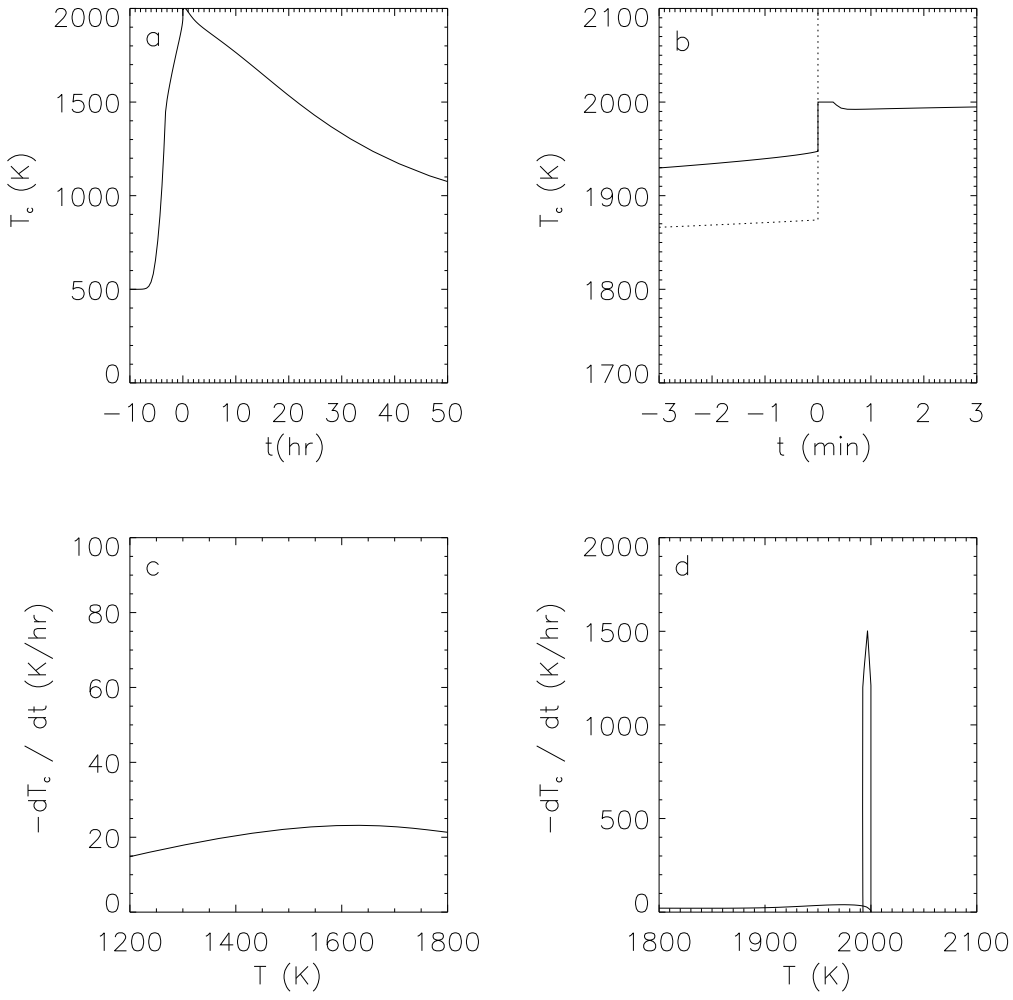

FIG. 60 — Case 14 (see Table 20). Same as Figure 43 (our canonical case including line cooling), except the shock speed has been increased to $V_s = 10$ km s^{-1}.

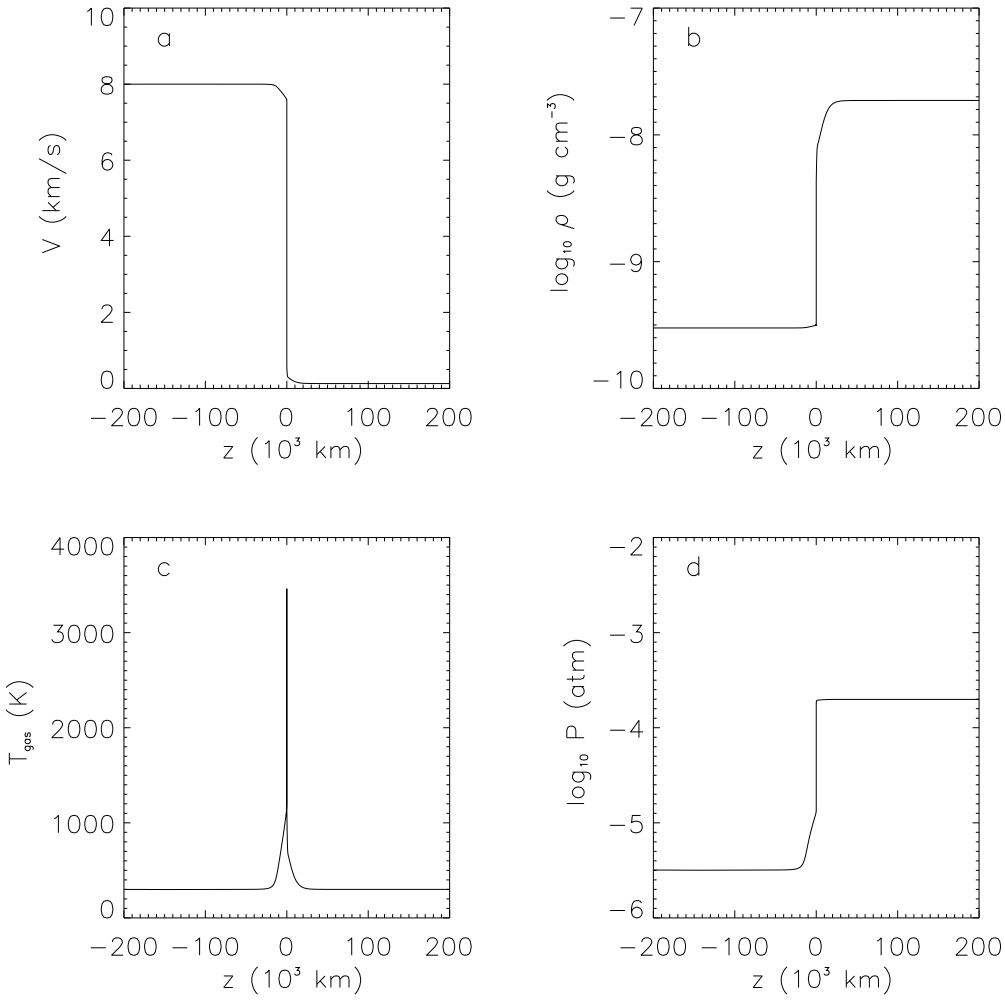

FIG. 61 — Case 15 (see Table 20). Same as Figure 42 (our canonical case including line cooling), except the pre-shock gas density has been reduced to $\rho_1 = 3 \text{ x } 10^{-10}$ g cm^{-3}.

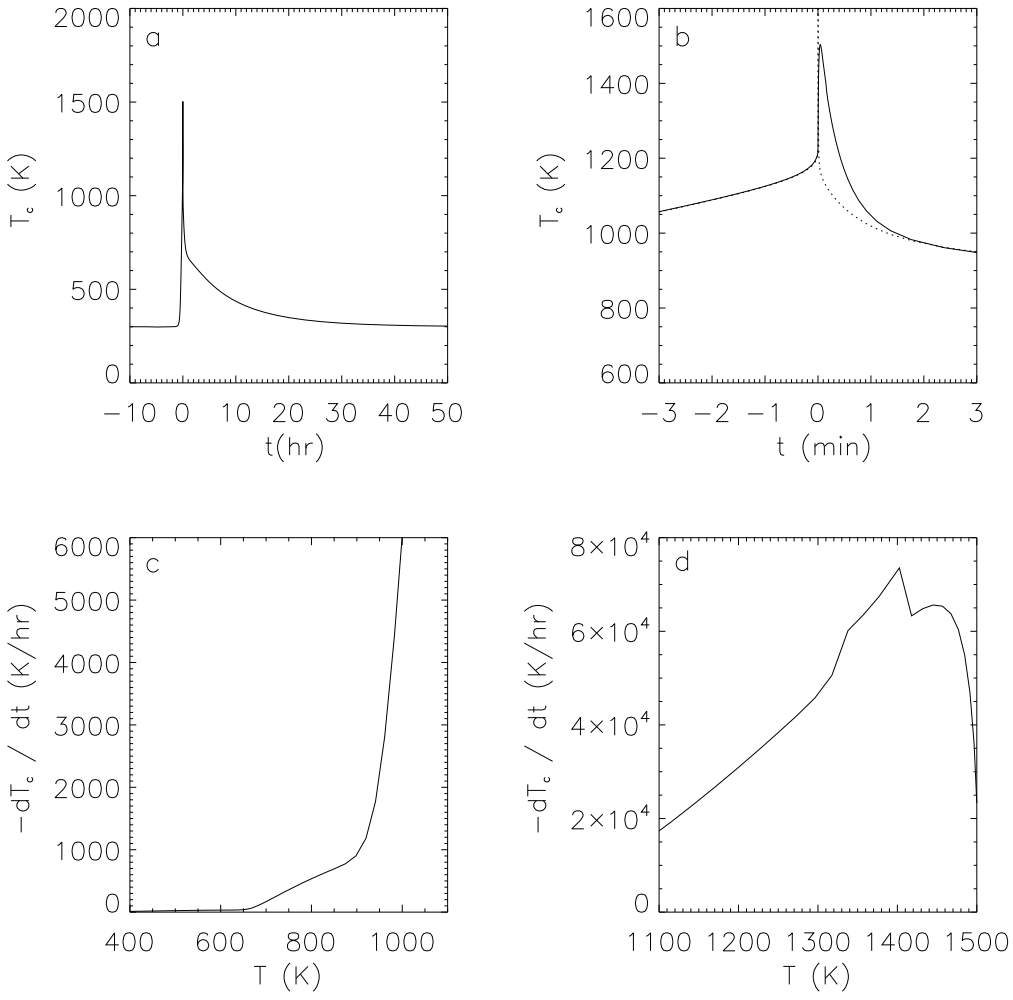

FIG. 62 — Case 15 (see Table 20). Same as Figure 43 (our canonical case including line cooling), except the pre-shock gas density has been reduced to $\rho_1 = 3 \times 10^{-10}$ g cm^{-3}.

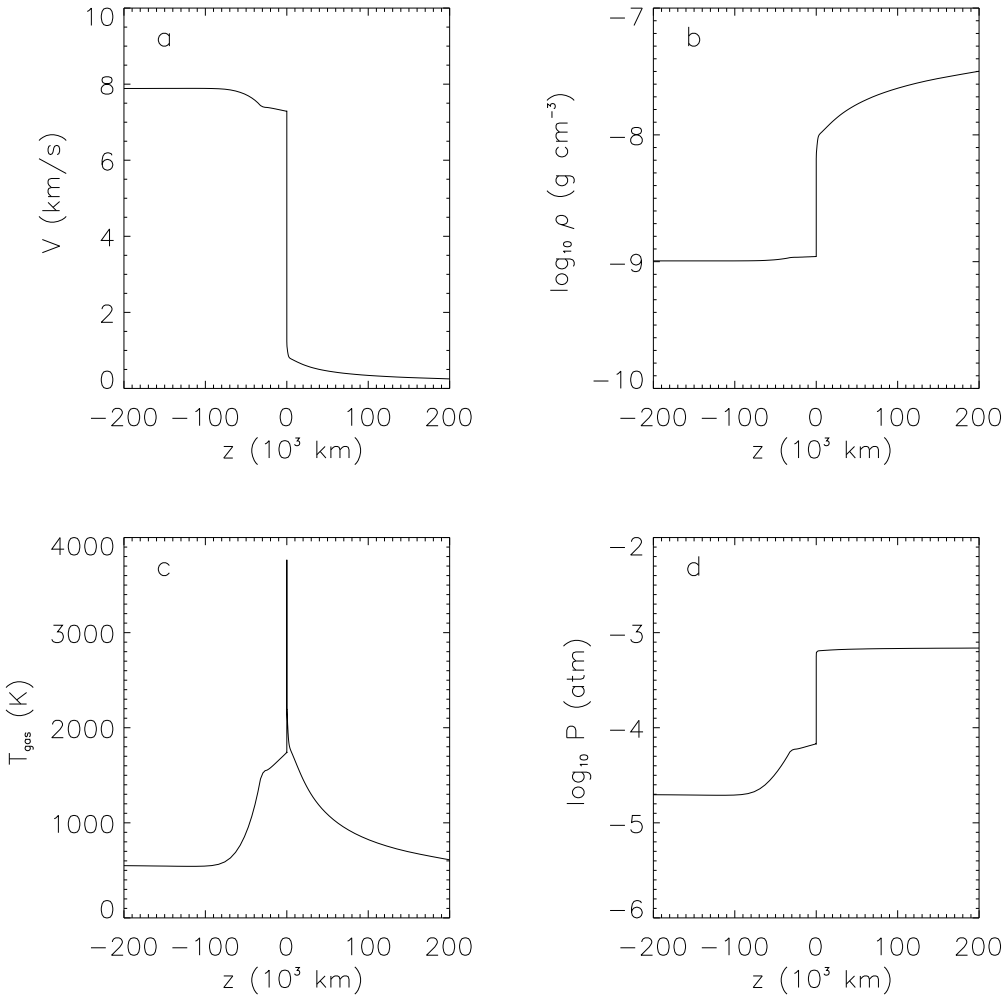

FIG. 63 — Case 16 (see Table 20). Same as Figure 42 (our canonical case including line cooling), except the chondrule concentration has been increased to $\mathcal{C} = 30$.

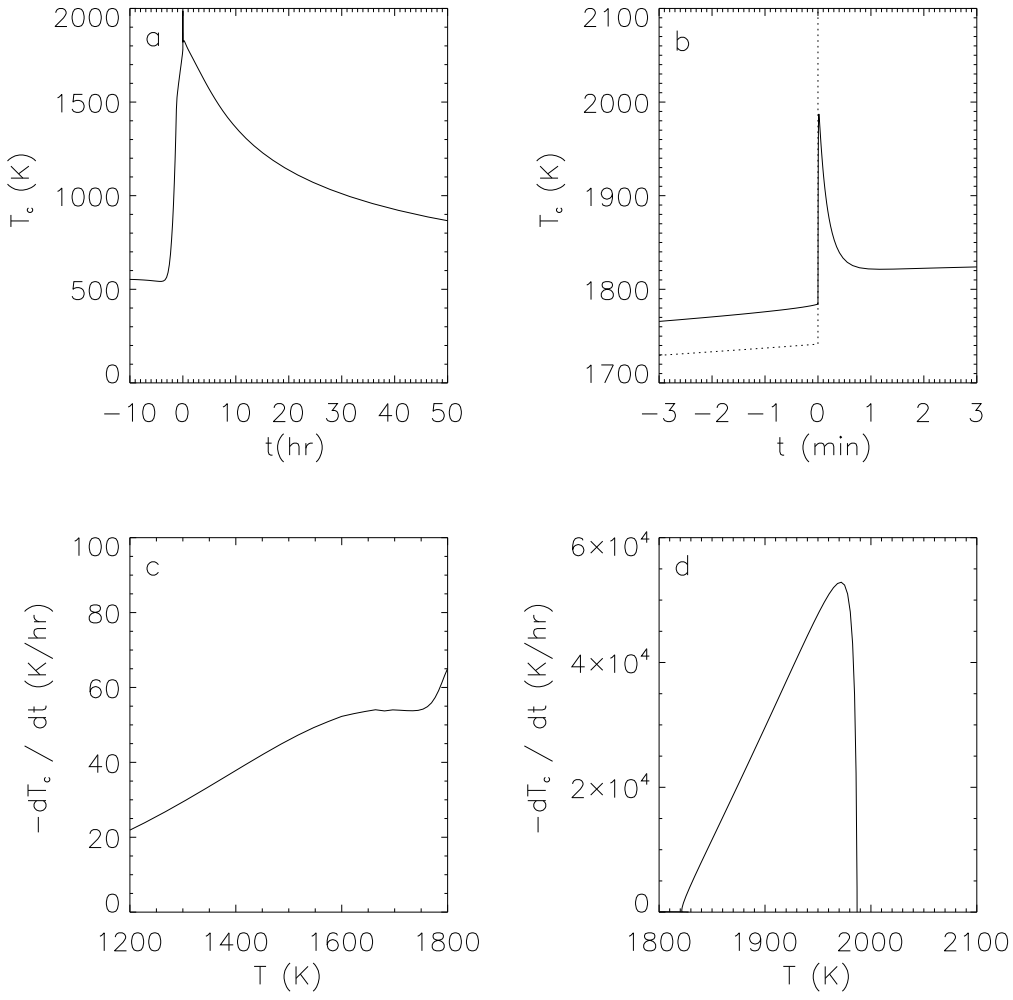

FIG. 64 — Case 16 (see Table 20). Same as Figure 43 (our canonical case including line cooling), except the chondrule concentration has been increased to $\mathcal{C} = 30$.

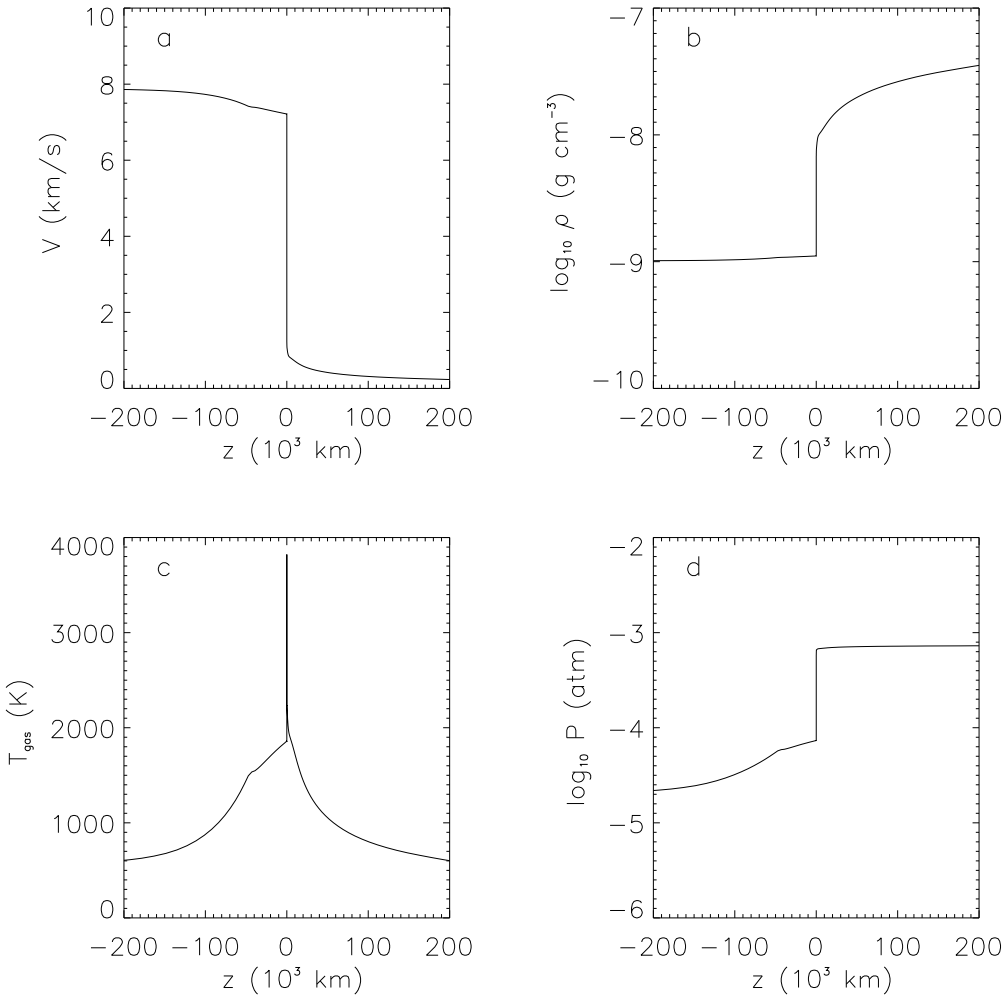

FIG. 65 — Case 16 (see Table 20). Same as Figure 42 (our canonical case including line cooling), except the chondrule concentration has been increased to $\mathcal{C} = 50$.

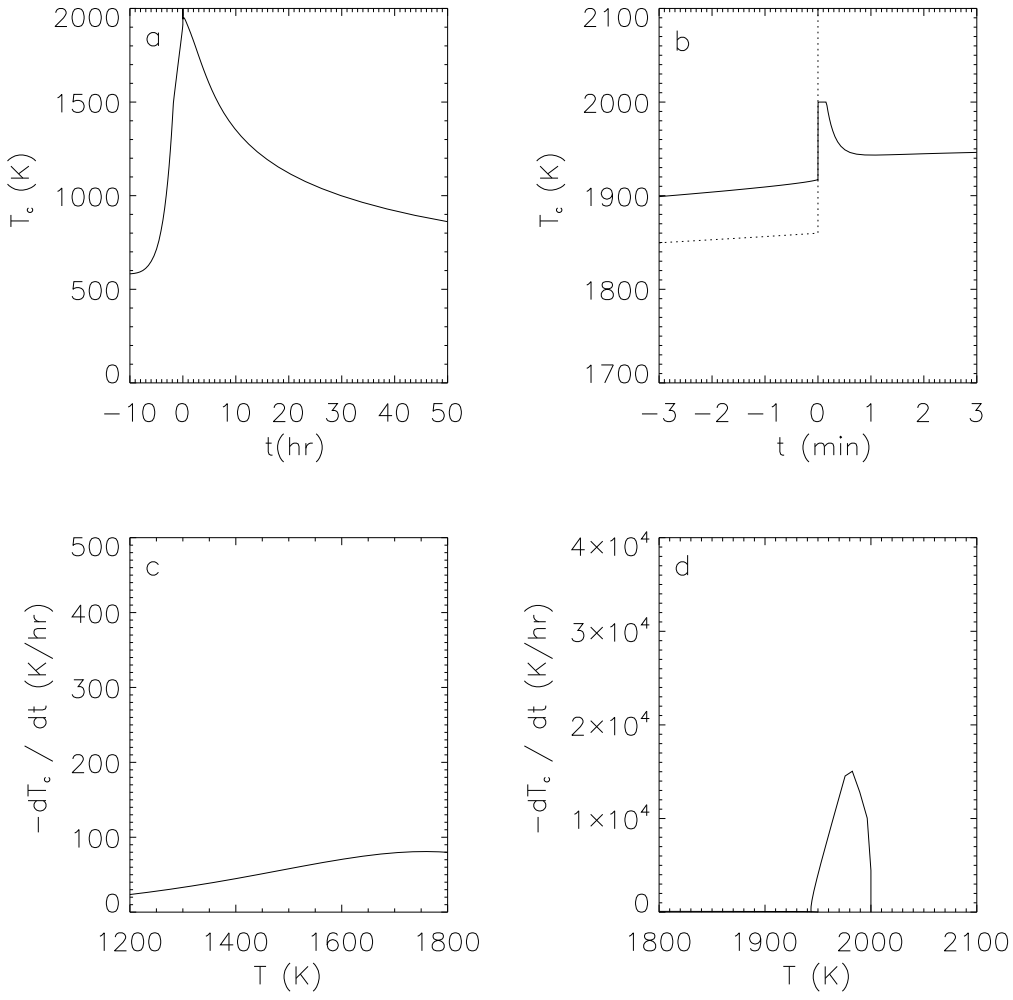

FIG. 66 — Case 16 (see Table 20). Same as Figure 43 (our canonical case including line cooling), except the chondrule concentration has been increased to $\mathcal{C} = 50$.

CHAPTER 7

SUMMARY, CONCLUSION, AND DISCUSSION

1. Formation of Chondrules

Chondrules are some of the oldest materials in our Solar System, forming within a few million years after its birth. Analyses of chondrules have yielded constraints on their thermal histories, and as such, chondrules can provide crucial information about the conditions in the early solar nebula.

As reviewed in Chapter 1, the complementarity of chondrules and the matrix in which they are embedded is considered an additional constraint. Although the composition of chondrules and the fine-grained matrix of the chondrites differ from chondrite to chondrite, the bulk composition of the meteorites is approximately solar (Wood 1985; Huss 1988; Palme et al. 1993; Klerner & Palme 2000; Hezel & Palme 2007). This complementarity of chondrules and matrix suggests that chondrules were combined with dust local to the region of their formation, prior to incorporation into the chondrite parent bodies.

The thermal histories of chondrules are remarkably well constrained. The presence of primary sulfur suggests that chondrule precursors started at temperatures $< 650\,\mathrm{K}$ (Rubin et al. 1999; Krot et al. 2009). The lack of isotopic fractionation of S suggests that they were subsequently heated to the liquidus temperature within less than 10 minutes (Tachibana & Huss 2005). They were then heated to a few hundred K above their liquidus temperature ($\sim 1800\,\mathrm{K}$), in order to retain just a few nucleation sites (Hewins et al. 2005). The chondrules then cooled to below the liquidus within minutes, at rates $> 10^4\,\mathrm{K\,hr^{-1}}$. Such high cooling rates are necessary for the retention of Na (Yu & Hewins 1998). While still partially molten, the cooling rates dropped suddenly for most chondrules, cooling at rates $10 - 1000\,\mathrm{K\,hr^{-1}}$ (Hewins et al. 2005; Miyamoto et al. 2009) through their crystallization temperatures. In order to stabilize the melt against evaporation that was too rapid, the melting of chondrules took place in the presence of moderately high pressure gas. The total pressures during chondrule melting probably exceeded $10^{-3}\,\mathrm{atm}$ (Miura et al. 2002).

The sizes of the regions in which chondrules formed have been estimated by noting the lack of isotopic fractionation of K, Fe, Mg and Si. The chondrule melts must have been in equilibrium

with their own vapor for these gases to avoid fractionation. This requires a large region ($\gg 10^3$ km in size) so that the vapor does not diffuse away (Cuzzi & Alexander 2006). At the same time, the density of chondrules must have been $1 - 10\,\mathrm{m}^{-3}$ (Cuzzi & Alexander 2006), a number consistent with the frequency of compound chondrules, chondrules that collided and stuck while partially molten (Gooding & Keil 1981).

Finally, the mechanism that melted chondrules must have acted multiple times in the same vicinity, because some chondrules contain relicts of previous generations of chondrules (Jones et al. 2000). Additionally, the variations in Al-Mg and Pb-Pb systematics in chondrules suggest the chondrule formation mechanism spanned several Myr (Wadhwa & Russell 2000; Wadhwa et al. 2007; Hutcheon et al. 2009).

Identifying the mechanism that melted chondrules is key to probing the conditions and processes at play in the solar nebula. Any model of chondrule formation must be tested against the experimental and theoretical constraints. Few models have been developed to the point where they can make such detailed predictions and fewer still have passed them. To date, the shock model of chondrule formation is the most successful.

2. Formation of Chondrules in Solar Nebula Shocks

The nebula shock model, first proposed by Wood (1963), was successively developed by Hood & Horanyi (1991, 1993), Connolly & Love (1998), Iida et al. (2001), DC02, Ciesla & Hood (2002; hereafter CH02), and Miura & Nakamoto (2006). DC02 was the first shock model to include a proper treatment of radiative transfer and a dust opacity that was distinct from chondrules, important effects. Additionally DC02 included the effects of hydrogen dissociation and recombination. The treatment by CH02 was very similar, although it did not include dust (or hydrogen dissociation and recombination effects). CH02 independently reached many of the same conclusions as DC02, such as predicting chondrule cooling rates $\sim 10 - 100\,\mathrm{K\,hr}^{-1}$. Neither of these models included line cooling, the cooling of the gas due to emission of infrared radiation by water molecules. Line

cooling was included in the model of INSN, but only in the optically thin limit. In addition, they did not include dust. INSN found typical cooling rates $\sim 10^4\,\mathrm{K\,hr^{-1}}$. If INSN were correct, it would mean that the cooling rates of chondrules in solar nebula shocks are incompatible with experimental constraints. The review by Desch et al. (2005) identified proper treatment of line cooling as the major impediment to progress in shock models. In addition, Desch et al. (2005) pointed out the that proper treatment of the opacity of solids and the correct determination of the input radiation field were needed to overcome major shortcomings in existing shock models. A true test of the nebula shock model must include these physical effects.

In this study, we have addressed all of the problems with previous shock models that were identified in the review of Desch et al. (2005). We have determined the proper treatment for the input radiation field (Chapter 2, §4). We have calculated the necessary boundary conditions in the 1-D approximation, and found that they are not appropriate for use under the conditions believed to exist in the solar nebula. Yet we have found that because of the radiative diffusion timescale over the scale of our computational domain, it is justifiable to set the post-shock temperature equal to the ambient, pre-shock temperature. We have developed an accurate approximation to the wavelength-dependent opacity of solids (Chapter 2, §5), and implemented this approximation in our updated shock code. Additionally, we have utilized a temperature-dependent evaporation rate to properly account for the evaporation of micron-sized dust (Chapter 2, §6). Most important, we have determined the amount of molecular line emission from H_2O (Chapter 4), and have included a detailed treatment of its effects in our updated shock model (Chapter 5).

After the correction of the boundary condition for input radiation and the inclusion of realistic dust opacities and evaporation, we found that slightly higher shock speeds than those of DC02 (8 km $\mathrm{s^{-1}}$ instead of 7 km $\mathrm{s^{-1}}$) were necessary to completely melt chondrules. Our results show that the evaporation of dust occurs not only at the shock front, but in the pre-shock region as well. Naively, based on simple, incomplete, toy models, we believed that the inclusion of line cooling would result in a major increase in the cooling rates following the shock (from 10 - 10^2

K hr^{-1} to $> 10^4$ K hr^{-1}), because of the the low opacity resulting from the evaporation of dust. Surprisingly, our results have shown that molecular line cooling has very little effect on the gas, and almost no effect on the thermal histories of chondrules. Although, line cooling should be extremely effective immediately following the passage of the shock (due to the high temperature of the gas and low column densities of H_2O), this is the region where the gas is already cooling very rapidly due to dissociation of hydrogen. Shortly thereafter, energy is added to the gas through recombinations of hydrogen, moderating the cooling due to line emission. In effect, the presence of hydrogen buffers the gas against line cooling. [NB: Buffering by hydrogen was originally considered by Scott et al. (1996) as a mechanism limiting chondrule peak temperatures]. By the time hydrogen recombinations are no longer of importance to the energetics, high column densities have reduced the line cooling rates dramatically (see Morris et al. 2009). Because of the low rate of thermal exchange between the gas and chondrules, this means that molecular line cooling has basically no effect on the cooling rates of chondrules.

The results from our updated shock model presented in this study meet almost all the observational constraints on chondrule formation as outlined in Tables 1 and 2. It is plausible that shocks due to gravitational instabilities or X-ray flares occurred multiple times in the solar nebula, as localized events. Chondrules melted by shocks would retain evidence of the magnetic field of their environment as they cooled through their Curie temperatures. Compression of the post-shock gas creates a high-pressure environment for chondrule formation. Shocks efficiently melt the solids in their path, leading to high abundances of chondrules. Once cooled, chondrules would mix with nearby local dust, prior to the incorporation into parent bodies. With respect to the thermal histories of chondrules, our results show that chondrules reach peak temperatures $\sim$ 2000 K, experience initial rapid cooling (several x 10^4 K hr^{-1}), and cool through their crystallization temperature ranges ($\sim$ 1400 - 1800 K) at rates of 10 - 1000 K hr^{-1}, consistent with experimental constraints. The results in our canonical case, with a chondrule concentration of $\mathcal{C} = 10$, do not meet the constraint on the pre-shock heating time of chondrules necessary for the retention

of volatiles and prevention of the fractionation of sulfur. However, our results with $\mathcal{C} = 30$ and $\mathcal{C} = 50$ (Figures 65 and 66) (Table 20, Case 17) show that with higher chondrule concentrations, the duration of pre-shock heating is reduced; with $\mathcal{C} = 100$ the nebula shock model will more than likely meet this observational constraint.

3. Chondrule Concentrations

Compound chondrules are believed to form when newly melted chondrules stick together while still partially molten. Based on the frequency of compound chondrules ($\sim 5\%$), chondrule densities have been estimated at $\sim$ 1-10 m^{-3} (Gooding & Keil 1981; Ciesla et al. 2004a). Chondrule densities of $\sim$ 10 m^{-3} over regions of $\sim 10^3$ km are needed in order to prevent the isotopic fractionation of volatiles during melting (Cuzzi & Alexander 2006). For chondrules of radii 300 μm, at a chondrules-to-gas mass ratio of 5 x 10^{-3} (the solar dust-to-gas ratio), a density of only $\sim$ 0.2 m^{-3} is achieved in the post-shock region in our model. Therefore, it appears that chondrules probably formed in clumps, where the density of chondrules was orders of magnitude above the solar dust-to-gas ratio. It has been suggested that chondrules could be concentrated into clumps by turbulence, resulting in chondrule concentrations as high as $\mathcal{C} = 10^4$, with the most likely value $\mathcal{C} \sim 10^2$ (Cuzzi et al. 1993; Cuzzi et al. 2001; Hogan & Cuzzi 2001; Cuzzi et al. 2008). Alexander et al. (2008) have argued for even higher chondrule concentrations ($\mathcal{C} \sim 10^5$), based on the discovery of primary Na in olivine phenocrysts in chondrules. Maintaining a high partial pressure of Na vapor in the gas, as the chondrules cooled, is the only way to stabilize the chondrule melt against the loss of this volatile. Alexander et al. (2008) invoke high concentrations of chondrules to do just that, even though they acknowledge that the chondrule densities necessary are unrealistically high, based on our current understanding of the solar nebula. Regardless, clearly an increase in the chondrule concentration used in our model, from $\mathcal{C} = 10 - 30$ to a higher value, is justified and warranted.

4. Weaknesses of the Model

We are imposing steady-state conditions in the frame of the shock, but we can't impose radiative equilibrium anywhere within the computational region because of the rapidity of the changes in gas properties. This necessitates the use of a Λ-iteration approach in the calculation of the radiation field, leading to very slow convergence ($\sim 10^3$ iterations), which is certainly not ideal. A new approach is needed that includes time derivatives, probably requiring a radiative hydrodynamics simulation. Additionally, (in part due to the use of a Λ-iteration approach) the position of the dust evaporation front is numerically difficult to resolve. This is a well-known problem (Chick & Cassen 1997), which in the case of chondrule formation in nebular shocks, affects the pre-heating of chondrule precursors.

5. Future Work

In most models of chondrule formation, including the one presented in this thesis, the assumption is made that chondrite parent bodies formed at 2-3 AU, the present location of the asteroid belt. Our assumption that chondrules formed at 2-3 AU has influenced our choice of ambient temperature, pre-shock densities, and shock speeds. However, chondritic parent bodies that were incorporated into the terrestrial planets may have formed interior to the present-day asteroid belt. We would like to expand our parameter space to include temperatures, pre-shock gas densities, and shock speeds (consistent with gravitational instabilities or other models) that are appropriate for locations interior to 2 AU. In doing so, we anticipate that our model can be better utilized to predict the regions in the solar nebula where chondrule formation in nebular shocks is possible.

We propose to investigate a different explanation for the high partial pressure of Na in chondrule-forming regions. Desch (2009, personal communication) has suggested the following: We envision a scenario as depicted in Figure 67, in which a shock overruns a clump of chondrules of

limited spatial extent. Based on Cuzzi et al. (2008), we assume $\mathcal{C} \sim 10^4$ on scales $\sim 10^3 - 10^4$ km, and lower concentrations ($\mathcal{C} \sim 10 - 100$) on much larger scales, $\sim 10^4 - 10^5$ km. According to the calculations of DC02, the concentrations in the heart of the clump are sufficient (for a given shock speed $\approx 7 - 8$ km s^{-1}) to completely evaporate all chondrules in the clump. Outside the heart of the clump, chondrule concentrations are lower, and for the same shock speed, chondrules are likely to melt normally without evaporating. After chondrules in each region are shocked, there are several hours, during which the normally melted chondrules and the vapor within the clumps can commingle. One possibility is that chondrule vapor can move outward. In the time it takes chondrules to cool (a few hours), it is unlikely that diffusion can carry this vapor much farther than a few km, but the elevated gas pressures (from chondrule vapor) could potentially drive an outward expansion, carrying the vapor thousands of kilometers in a few hours. An alternative possibility is that chondrules are *focused* into the clumps. In clumps like the one depicted in Figure 67, chondrules are a significant fraction of the gas mass, increasing the overall density of material in this region. The shock ends up propagating more slowly through the clump than the surrounding gas, and the shock front is expected to assume the geometry depicted in Figure 67. The trajectories of chondrules entering the shock are therefore refracted, and chondrules are focused into the clump, *after* the clump has experienced its peak heating. Therefore, some fraction of chondrules should experience otherwise normal thermal histories indicative of moderate chondrule concentrations, but in the presence of very high pressures of chondrule vapor, that can only arise from regions of higher chondrule concentration.

This scenario may resolve the quandary of Alexander et al. (2008). Because chondrules in the clumps totally evaporate, the requisite Na vapor pressure can be met by evaporating a solids density in the post-shock region of only 1 g m^{-3}. This equates to about 0.1 g m^{-3} before the shock. For 300 μm-sized chondrules, this implies a chondrule density of ≈ 300 m^{-3} and $\mathcal{C} \sim 10^4$ in the pre-shock gas. This is near the upper limit of chondrule concentrations thought attainable by turbulent concentration, but still achievable, and is consistent with the scenario envisioned here.

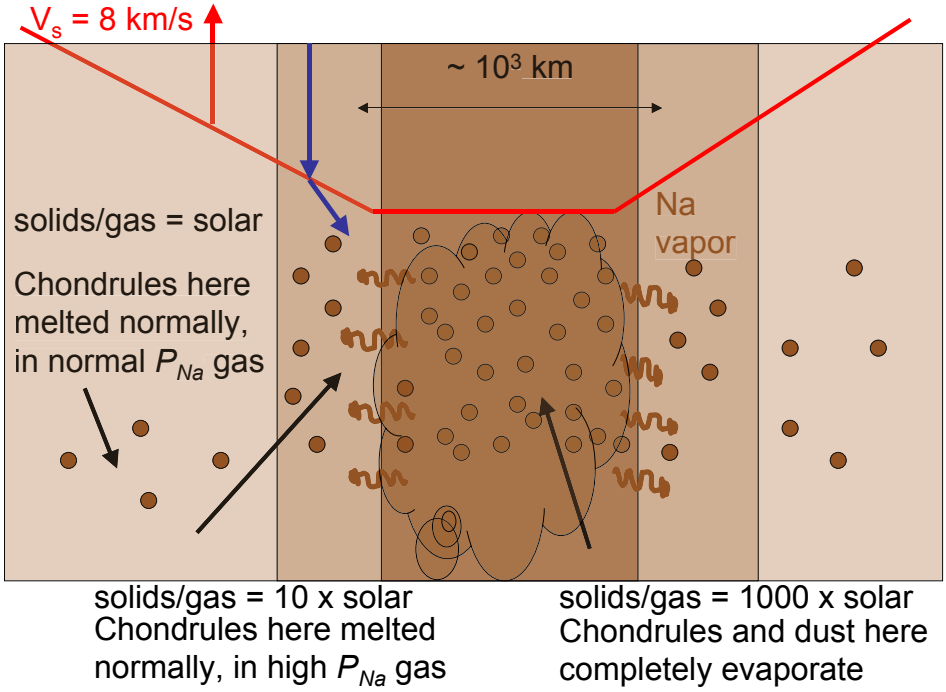

FIG. 67 — Possible solution to the dilemma posed by the discovery by Alexander et al. (2008) that chondrule melts contained volatile Na. If a shock overtook a region of varying chondrule densities, chondrules in the densest regions would be likely to fully evaporate, generating a cloud of Na vapor. The shock front (red) is slowed as it passes through clumps, and bends. Chondrules not in the densest parts of the clumps, as they are overrun by the shock, find their trajectories deflected toward the clump (blue). Chondrules can start to melt normally but then find themselves in a cloud of Na vapor characteristic of much denser regions, with Na partial pressures high enough to stabilize the melt against Na loss. (Desch 2009, personal communication).

A more quantitative analysis to test this hypothesis requires a shock code that can handle motions parallel to the shock front as well as radiative transfer in 2-D cylindrical geometry.

2-D radiative transfer must also be implemented in order to develop a quantitative model for testing the idea that bow shocks driven by planetesimals on eccentric orbits are the mechanism that melted chondrules. Current shock models assume planar shock fronts over large scales ($> 10^5$ km) and therefore invoke a 1-D approach. This is appropriate for shocks due to gravitational instabilities, but not bow shocks, because bow shocks are only a few times the diameter of the planetesimal in scale. No previous model of chondrule formation by bow shocks (Ciesla et al.

2004b; Hood et al. 2009) has included the necessary 2-D radiative transfer. We propose to modify PERSEUS, the existing 2-D hydrodynamics code developed by the Desch research group at Arizona State University (Ouellette et al. 2007), to model chondrule formation in dense clumps and bow shocks.

Our shock code can also be adapted to investigate the thermal processing of ices and icy grains. This modified shock code might be combined with a protoplanetary disk code to produce theoretical spectral to compare to observations of real disks. Recent observations of water emission may be diagnostic of shocks (Carr & Najita 2007, Watson et al. 2007). If so, one of the major objections to the shock model for chondrule formation, that there is no observational evidence for shocks, would be rendered moot.

REFERENCES

[1] Alexander, C. M. O., Grossman, J. N., Ebel, D. S., & Ciesla, F. J. 2006, Science, 320, 1617

[2] Amelin, Y., Krot, A. N., Hutcheon, I. D., & Ulyanov, A. A. 2002, Science, 297, 1678

[3] Anders, E., & Grevesse, N. 1989, Geochim. Cosmochim. Atca, 53, 197

[4] Avrett, E. H., & Hummer, D. G. 1965, MNRAS, 130, 295

[5] Boley, A. C., Durisen, R. H., & Pickett, M. K. 2005, Chondrites and the Protoplanetary Disk, 341, 839

[6] Boley, A. C., & Durisen, R. H. 2008, ApJ, 685, 1193

[7] Boss, A. P. 1996, Chondrules and the Protoplanetary Disk, 257

[8] Boss, A. P. 2001, ApJ, 563, 367

[9] Boss, A. P. 2005, ApJ, 629, 535

[10] Boss, A. P., & Durisen, R. H. 2005, Chondrites and the Protoplanetary Disk, 341, 821

[11] Bouvier, A., Blichert-Toft, J., Moynier, F., Vervoort, J. D., & Albarède, F. 2007, Geochim. Cosmochim. Atca, 71, 1583

[12] Bouvier, A., & Wadhwa, M. 2009, Lunar and Planetary Institute Science Conference Abstracts, 40, 2184

[13] Bowers, R. L., & Deeming, T. 1984, *Astrophysics. Volume 1 - Stars* (Boston: Jones and Bartlett Publishers, Inc)

[14] Burkhardt, C., Kleine, T., Bourdon, B., Palme, H., Zipfel, J., Friedrich, J. M., & Ebel, D. S. 2008, Geochim. Cosmochim. Atca, 72, 6177

[15] Carr, J. S., & Najita, J. R. 2008, Science, 319, 1504

[16] Chaussidon, M., & Gounelle, M. 2006, Meteorites and the Early Solar System II, 323

[Cherchneff et al 1992] Cherchneff I., Barker J. R. and Tielens A. G. G. M. (1992) Polycyclic aromatic hydrocarbon formation in carbon-rich stellar atmospheres. *Astrophys. J.* **401**, 269-287.

[17] Chick, K. M., & Cassen, P. 1997, ApJ, 477, 398

[18] Ciesla, F. J., & Hood, L. L. 2002, Icarus, 158, 281

[19] Ciesla, F. J., Lauretta, D. S., Cohen, B. A., & Hood, L. L. 2003, Science, 299, 549

[20] Ciesla, F. J., Lauretta, D. S., Hood, L. L. 2004 Meteoritics and Planetary Science 39, 531-544.

[21] Ciesla, F. J., Hood, L. L., & Weidenschilling, S. J. 2004, Meteoritics and Planetary Science, 39, 1809

[22] Ciesla, F. J. 2005, Chondrites and the Protoplanetary Disk, 341, 8

[23] Ciesla, F. J., & Cuzzi, J. N. 2006, Icarus, 181, 178

[24] Ciesla, F. J. 2006, Meteoritics and Planetary Science, 41, 1271

[25] Collin-Souffrin, S., Delache, P., Frisch, H., & Dumont, S. 1981, A&A, 104, 264

[26] Connolly, H. C., Jr., & Hewins, R. H. 1991, Geochim. Cosmochim. Atca, 55, 2943

[27] Connolly, H. C., Jr., & Desch, S. J. 2004, Chemie der Erde / Geochemistry, 64, 95

[28] Connolly, H. C., Jr. 2005, Chondrites and the Protoplanetary Disk, 341, 215

[29] Connolly, H. C., Jr., Desch, S. J., Ash, R. D., & Jones, R. H. 2006, Meteorites and the Early Solar System II, 383

[30] Connelly, J. N., Amelin, Y., Krot, A. N., & Bizzarro, M. 2008, ApJ, 675, L121

[31] Cuzzi, J. N., Dobrovolskis, A. R., & Champney, J. M. 1993, Icarus, 106, 102

[32] Cuzzi, J. N., Hogan, R. C., Paque, J. M., & Dobrovolskis, A. R. 2001, ApJ, 546, 496

[33] Cuzzi, J. N., & Alexander, C. M. O. 2006, Nature, 441, 483

[34] Cuzzi, J. N., Hogan, R. C., & Shariff, K. 2008, ApJ, 687, 1432

[35] Davis, A. M., Alexander, C. M. O., Nagahara, H., & Richter, F. M. 2005, Chondrites and the Protoplanetary Disk, 341, 432

[36] Dehart, J. M., & Lofgren, G. E. 1996, Geochim. Cosmochim. Atca, 60, 2233

[37] Desch, S. J. 2000, Lunar and Planetary Institute Science Conference Abstracts, 31, 1923

[38] Desch, S. J., & Cuzzi, J. N. 2000, Icarus, 143, 87

[39] Desch, S. J., & Connolly, H. C., Jr. 2002, Meteoritics and Planetary Science, 37, 183

[40] Desch, S. J., Borucki, W. J., Russell, C. T., & Bar-Nun, A. 2002, Reports on Progress in Physics, 65, 955

.

[41] Desch, S. J., Ciesla, F. J., Hood, L. L., & Nakamoto, T. 2005, Chondrites and the Protoplanetary Disk, 341, 849

[42] Desch, S. J. 2007, ApJ, 671, 878

[43] Dumont, A.-M., Collin, S., Paletou, F., Coupé, S., Godet, O., & Pelat, D. 2003, A&A, 407, 13

[44] Ebel, D. S., Weisberg, M. K., Hertz, J., & Campbell, A. J. 2008, Meteoritics and Planetary Science, 43, 1725

[45] Fedkin, A. V., & Grossman, L. 2006, Meteorites and the Early Solar System II, 279

[46] Fedkin, A. V., Grossman, L., & Ghiorso, M. S. 2006, 37th Annual Lunar and Planetary Science Conference, 37, 2249

[47] Fedkin, A. V., & Grossman, L. 2007, Lunar and Planetary Institute Conference Abstracts, 38, 2014

[48] Gammie, C. F. 1996, ApJ, 462, 725

[49] Gullbring, E., Hartmann, L., Briceno, C., & Calvet, N. 1998, ApJ, 492, 323

[50] Güttler, C., Poppe, T., Wasson, J. T., & Blum, J. 2008, Icarus, 195, 504

[51] Grossman, J. N. 1988, Meteorites and the Early Solar System, 680

[52] Hayashi, C. 1981, Progress of Theoretical Physics Supplement, 70, 35

[53] Henning, T., & Stognienko, R. 1996, A&A, 311, 291

[54] Hewins, R. H. 1997, Annual Review of Earth and Planetary Sciences, 25, 61

[55] Hewins, R. H., & Connolly, H. C., Jr. 1996, Chondrules and the Protoplanetary Disk, 197

[56] Hewins, R. H., Connolly, H. C., Lofgren, G. E., Jr., & Libourel, G. 2005, Chondrites and the Protoplanetary Disk, 341, 286

[57] Hezel, D. C., & Palme, H. 2008, Earth and Planetary Science Letters, 265, 716

[58] Hollenbach, D., & McKee, C. F. 1979, ApJS, 41, 555

[59] Hogan, R. C., & Cuzzi, J. N. 2007, Physical Review E, 75, 056305

[60] Hood, L. L., & Horanyi, M. 1991, Icarus, 93, 259

[61] Hood, L. L., & Horanyi, M. 1993, Icarus, 106, 179

[62] Hood, L. L., Ciesla, F. J., & Weidenschilling, S. J. 2005, Chondrites and the Protoplanetary Disk, 341, 873

[63] Hood, L. L., Ciesla, F. J., Artemieva, N. A., Marzari, F., & Weidenschilling, S. J. 2009, Lunar and Planetary Institute Science Conference Abstracts, 40, 1775

[64] Hummer, D. G., & Rybicki, G. 1971, Ann. Rev. Astron. Astrophys., 9, 237

[65] Hummer, D. G., & Rybicki, G. B. 1982, ApJ, 254, 767

[66] Huss, G. R. 1988. Lunar and Planetary Institute Science Conference Abstracts 19, 521.

[Hutcheon et al.)] Hutcheon, I. D., et al. 2009, Geochim. Cosmochim. Atca, in press

[67] Hutchison, R., Bridges, J. C., & Gilmour, J. D. 2005, Chondrites and the Protoplanetary Disk, 341, 933

[68] Iida, A., Nakamoto, T., Susa, H., & Nakagawa, Y. 2001, Icarus, 153, 430

[69] Jacobsen, B., Yin, Q.-Z., Moynier, F., Amelin, Y., Krot, A. N., Nagashima, K., Hutcheon, I. D., & Palme, H. 2008, Earth and Planetary Science Letters, 272, 353

[70] Jones, R. H., & Lofgren, G. E. 1993, Meteoritics, 28, 213

[71] Jones, R. H., Lee, T., Connolly, H. C., Jr., Love, S. G., & Shang, H. 2000, Protostars and Planets IV, 927

[72] Jones, R. H., Grossman, J. N., & Rubin, A. E. 2005, Chondrites and the Protoplanetary Disk, 341, 251

[73] Jørgensen, U. G., Jensen, P., Sørensen, G. O., & Aringer, B. 2001, A&A, 372, 249

[74] Keil, K., Stoeffler, D., Love, S. G., & Scott, E. R. D. 1997, Meteoritics and Planetary Science, 32, 349

[75] Kita, N. T., Huss, G. R., Tachibana, S., Amelin, Y., Nyquist, L. E., & Hutcheon, I. D. 2005, Chondrites and the Protoplanetary Disk, 341, 558

[76] Klerner, S., & Palme, H. 2000, Meteoritics and Planetary Science Supplement, 35, 89

[77] Kropf, A., & Pack, A. 2008, Lunar and Planetary Institute Science Conference Abstracts, 39, 2222

[Krot et al.)] Krot, A. N., et al. 2009, Geochim. Cosmochim. Atca, in press

[78] Lauretta, D. S., Nagahara, H., & Alexander, C. M. O. 2006, Meteorites and the Early Solar System II, 431

[79] Lenzuni, P., Gail, H.-P., & Henning, T. 1995, ApJ, 447, 848

[80] Levy, E. H. 1988, Meteorites and the Early Solar System, 697

[81] Li, A., & Greenberg, J. M. 1997, A&A, 323, 566

[82] Liffman, K., & Brown, M. 1995, Icarus, 116, 275

[83] Liffman, K., & Brown, M. J. I. 1996, Chondrules and the Protoplanetary Disk, pages 285-302, 285

[84] Liffman, K. 2009, ApJ, 694, L41

[85] Lodders, K. 2003, Meteoritics & Planetary Science, vol. 38, Supplement, abstract no.5272, 38, 5272

[86] Lugmair, G. W., & Shukolyukov, A. 2001, Meteoritics and Planetary Science, 36, 1017

[87] Marzari, F., & Weidenschilling, S. J. 2002, Icarus, 156, 570

[88] Mathews, W. G. 1992, ApJ, 386, 90

[89] Mihalas, D. 1978, San Francisco, W. H. Freeman and Co., 1978. 650 p.,

[90] Mihalas, D., & Mihalas, B. W. 1984, New York, Oxford University Press, 1984, 731 p.,

[91] Miura, H., Nakamoto, T., & Susa, H. 2002, Icarus, 160, 258

[92] Miura, H., & Nakamoto, T. 2006, ApJ, 651, 1272

[Miyamoto et al.)] Miyamoto, M., Mikouchi, T., & Jones, R. H. 2009, Meteoritics and Planetary Science, 44, 521

[93] Morris, M. A., Desch, S. J., & Ciesla, F. J. 2009, ApJ, 691, 320

[94] Nakamoto, T., Hayashi, M. R., Kita, N. T., & Tachibana, S. 2005, Chondrites and the Protoplanetary Disk, 341, 883

[95] Nelson, A. F., & Ruffert, M. 2005, Chondrites and the Protoplanetary Disk, 341, 903

[96] Neufeld, D. A., & Kaufman, M. J. 1993, ApJ, 418, 263

[97] Palme, H., Spettel, B., & Ikeda, Y. 1993, Meteoritics, 28, 417

[98] Palme, H., & Jones, A. 2005, Meteorites, Comets and Planets: Treatise on Geochemistry, Volume 1, 41

[99] Pilipp, W., Hartquist, T. W., Morfill, G. E., & Levy, E. H. 1998, A&A, 331, 121

[100] Plume, R., et al. 2004, ApJ, 605, 247

[101] Prinn, R. G., & Fegley, B. 1987, Annual Review of Earth and Planetary Sciences, 15, 171

[102] Rothman, L. S., et al. 1987, Appl. Opt., 26, 4058

[103] Rubin, A. 1999, Geochim. Cosmochim. Atca, 63, 2281

[104] Rudraswami, N. G., Goswami, J. N., Chattopadhyay, B., Sengupta, S. K., & Thapliyal, A. P. 2008, Earth and Planetary Science Letters, 274, 93

[105] Russell, S. S., Hartmann, L., Cuzzi, J., Krot, A. N., Gounelle, M., & Weidenschilling, S. 2006, Meteorites and the Early Solar System II, 233

[106] Rybicki, G. B., & Lightman, A. P. 1979, *Radiative Processes in Astrophysics* (New York: Wiley-Interscience)

[107] Sanders, I. S. 1996, Chondrules and the Protoplanetary Disk, 327

[108] Scott, E. R. D., Love, S. G., & Krot, A. N. 1996, Chondrules and the Protoplanetary Disk, 87

[109] Scott, E. R. D., & Krot, A. N. 2005, ApJ, 623, 571

[110] Shang, H., Shu, F. H., & Lee, T. 1996, Astronomical Society of the Pacific Conference Series, 122, 191

[111] Shu, F. H., Shang, H., & Lee, T. 1996, Science, 271, 1545

[112] Shu, F. H., Shang, H., Glassgold, A. E., & Lee, T. 1997, Science, 277, 1475

[113] Shu, F. H., Shang, H., Gounelle, M., Glassgold, A. E., & Lee, T. 2001, ApJ, 548, 1029

[114] Sorby,H. C. 1877, Nature, 15, 495

[115] Sobolev, V. V. 1960, Cambridge: Harvard University Press, 1960,

[116] Tachibana, S., Huss, G. R., Miura, H., & Nakamoto, T. 2004, Lunar and Planetary Institute Conference Abstracts, 35, 1549

[117] Tachibana, S., & Huss, G. R. 2005, Geochim. Cosmochim. Atca, 69, 3075

[118] Taylor, G. J., Scott, E. R. D., & Keil, K. 1983, Chondrules and their Origins, 262

[119] Urey, H. C. 1967, Icarus, 7, 350

[120] Urey, H. C., & Craig, H. 1953, Geochim. Cosmochim. Atca, 4, 36

[121] Wadhwa, M., & Russell, S. S. 2000, Protostars and Planets IV, 995

[122] Wadhwa, M., Amelin, Y., Davis, A. M., Lugmair, G. W., Meyer, B., Gounelle, M., & Desch, S. J. 2007, Protostars and Planets V, 835

[123] Wadhwa, M., Amelin, Y., Bizzarro, M., Kita, N., Kleine, T., Lugmair, G. W., & Yin, Q. 2007, Chronology of Meteorites and the Early Solar System, 173

[124] Wasson, J. T. 2008, Icarus, 195, 895

[125] Watson, D. M., et al. 2007, Nature, 448, 1026

[126] Weidenschilling, S. J., Marzari, F., & Hood, L. L. 1998, Science, 279, 681

[127] Weisberg, M. K., McCoy, T. J., & Krot, A. N. 2006, Meteorites and the Early Solar System II, 19

[128] Wood, J. A. 1963, Icarus, 2, 152

[129] Wood, J. A. 1985, Protostars and Planets II, 687

[130] Yasuda, S., & Nakamoto, T. 2008, Meteoritics and Planetary Science Supplement, 43, 5145

[131] Yu, Y., Hewins, R. H., & Eiben, B. A. 1995, Meteoritics, 30, 604

[132] Yu, Y., & Hewins, R. H. 1998, Geochim. Cosmochim. Atca, 62, 159

[133] Zaghloul, M. R. 2007, MNRAS, 375, 1043

APPENDIX A

LINE COOLING AND OPTICAL DEPTH

The cooling per line is given by the expression

$$\frac{\Lambda ul}{n_{H_2O}} = \frac{n_u}{n_{H_2O}}\, A_{ul}\, h\nu_{ul}, \tag{A.1}$$

where (in LTE)

$$\frac{nu}{n_{H_2O}} = \frac{n_l}{n_{H_2O}}\, \frac{g_u}{g_l}\, e^{-h\nu/kT}, \tag{A.2}$$

and the Einstein coefficient, A_{ul} is given by

$$A_{ul} = \frac{2h\nu^3}{c^2}\, \frac{B_{lu} g_l}{g_u}. \tag{A.3}$$

Substituting Eq. A.2 and Eq. A.3 into Eq. A.1 gives

$$\begin{aligned}
\frac{\Lambda ul}{n_{H_2O}} &= \left(\frac{n_l}{n_{H_2O}}\, e^{-h\nu/kT}\right)\, \left(\frac{2h\nu^3}{c^2}\, B_{lu}\right)\, h\nu \\
&= \frac{n_l}{n_{H_2O}}\, \frac{h\nu}{4\pi}\, B_{lu} \left(\frac{8\pi h\nu^3}{c^2}\, e^{-h\nu/kT}\right) \\
&= \frac{n_l}{n_{H_2O}}\, \frac{h\nu}{4\pi}\, B_{lu}\, \left(1 - e^{-h\nu/kT}\right) \left(\frac{8\pi h\nu^3}{c^2}\, \frac{e^{-h\nu/kT}}{1 - e^{-h\nu/kT}}\right) \\
&= \frac{n_l}{n_{H_2O}}\, \frac{h\nu_{lu}}{4\pi}\, B_{lu}\, \left(1 - e^{-h\nu/kT}\right) (4\pi B_\nu(T))
\end{aligned} \tag{A.4}$$

What we are given in the SCAN-H_2O line list is linestrength. The 1.2 million lines of spectral data included in the line list cover a range in wavelength from $\sim$ 6700 Å to 25 μm. The data consist of the following: the wavenumber at line center, ν_0, in cm^{-1}, the temperature-independent line strength, S_0, in km/mol, and the excitation energy, E_{low}, in cm^{-1}. From the temperature-independent line strength, S_0, given in the list, the temperature-dependent linestrength, $S(T)$, is calculated as follows:

$$S(T) = \frac{S_0 \ \exp\left(-E_{low}\frac{hc}{kT}\right)\left(1 - \exp\ \left(-\nu_0\frac{hc}{kT}\right)\right)}{Q_{vib}(T)Q_{rot}(T)}. \tag{A.5}$$

The vibrational partition function, Q_{vib}, is given for temperatures ranging from 200 K to 8000 K, in increments of 200 K, in the documentation for the SCAN-H_2O line list. We have interpolated values for Q_{vib} using a quadratic spline. The rotational partition function, Q_{rot}, is calculated with a subroutine provided in the documentation for the SCAN-H_2O line list. $S(T)$, as shown by Eq. A.5, is in units of km/mol, and we wish to have $S(T)$ in $\text{cm}^2 \cdot \text{Hz}$, so we must convert wavenumber to frequency which gives

$$S(T,\nu) = 10^5 \ \cdot \ S_0 \ \frac{c}{N_A}, \tag{A.6}$$

where N_A is Avogadro's number, and we have converted from km to cm. This results in a conversion factor where

$$S(T,\nu) = 4.98 \text{ x } 10^{-9} \ S_0 = S(T). \tag{A.7}$$

The left side of Eq. A.4 is just $S(T)$, as given by Eq. A.5, so in terms of linestrength

$$\begin{aligned} \frac{\Lambda ul}{n_{H_2O}} &= S(T)\left(\frac{8\pi h\nu^3}{c^2}\ \frac{1}{e^{-h\nu/kT}-1}\right) \\ &= S(T)\left(8\pi\ \frac{\nu^2}{c^2}\ kT\ \frac{h\nu/kT}{e^{-h\nu/kT}-1}\right) \\ &= S(T)\left(\frac{8\pi}{\lambda^2}\ kT\ \frac{h\nu/kT}{e^{h\nu/kT}-1}\right). \end{aligned} \tag{A.8}$$

According to Plume et al. (2004), the optical depth to line center is given by

$$\tau_0 = N_l \, \frac{g_u}{g_l} \, \frac{A_{ul}}{\sqrt{\pi}} \, \frac{\lambda^3}{8\pi} \, \frac{\left(1 - e^{-h\nu/kT}\right)}{\Delta v}, \tag{A.9}$$

where $\Delta v = (2kT/m)^{1/2}$ and the Einstein coefficients, A_{ul} and B_{lu} are given as follows:

$$A_{ul} = \frac{2h\nu^3}{c^2} \, B_{ul} \; = \; \frac{2h\nu^3}{c^2} \, \frac{g_l}{g_u} \, B_{lu}, \tag{A.10}$$

which gives the gas optical depth as

$$\tau_0 = N_l \, \frac{1}{\sqrt{\pi}} \, \frac{1}{8\pi} \, \frac{c^3}{\nu^3} \, \frac{2h\nu^3}{c^2} \, \frac{B_{lu}}{\Delta v} \left(1 - e^{-h\nu/kT}\right). \tag{A.11}$$

In local thermodynamic equilibrium (LTE),

$$N_l = N_{H_2O} \, \frac{g_l \, \exp\left(-E_{low}/kT\right)}{Q_{vib}(T) Q_{rot}(T)}, \tag{A.12}$$

which gives

$$\tau_0 = N_{H_2O} \, \frac{g_l \, \exp\left(-E_{low}/kT\right)}{Q_{vib}(T) Q_{rot}(T)} \, \frac{1}{4\pi} \, \frac{hc}{\sqrt{\pi}} \, \frac{B_{lu}\left(1 - e^{-h\nu/kT}\right)}{\Delta v}. \tag{A.13}$$

Integrating over all frequencies, and normalizing to $\Delta\nu_0 = \Delta v/c \; \nu_0$ gives the temperature-dependent line strength

$$S_{ul} = S(T) = \frac{n_l}{n_{H_2O}} \, \frac{h\nu}{4\pi} \, B_{lu} \left(1 - e^{-h\nu/kT}\right), \tag{A.14}$$

where the units are cm^2 Hz $\mathrm{molecule}^{-1}$, resulting in the gas optical depth to line center

$$\tau_0 = N_{H_2O} \, \frac{S_{ul}}{\sqrt{\pi} \, (\Delta v/c) \, \nu_0}. \tag{A.15}$$

We want the frequency-integrated optical depth, however, which is given by

$$\tau_0 = N_{H_2O} \, \frac{S_{ul}}{(\Delta v/c)\, \nu_0}. \tag{A.16}$$

APPENDIX B

DISSOCIATION AND RECOMBINATION

The following is taken from DC02:

In the gas phase, H atoms can combine to form H_2 molecules. Because H_2 is a nonpolar molecule, it cannot radiate away the excess chemical energy of formation by allowed transitions, and H_2 formation must proceed by three-body reactions, with either H atoms or H_2 molecules as the catalysts. Once formed, H_2 molecules are dissociated by collisions with H atoms or other H_2 molecules. The net rate at which H atoms recombine in the gas phase is (Cherchneff *et al.* 1992):

$$R = +n_{\rm H}^2 \left(a_1 n_{\rm H_2} + a_2 n_{\rm H}\right) - n_{\rm H_2} \left(a_3 n_{\rm H_2} + a_4 n_{\rm H}\right), \tag{B.1}$$

$$a_1 = 8.72 \times 10^{-33} \left(\frac{T_{\rm g}}{300\,{\rm K}}\right)^{-0.6} {\rm cm^6\,s^{-1}}, \tag{B.2}$$

$$a_2 = 1.83 \times 10^{-31} \left(\frac{T_{\rm g}}{300\,{\rm K}}\right)^{-1} {\rm cm^6\,s^{-1}}, \tag{B.3}$$

$$a_3 = 1.50 \times 10^{-9} \exp\left(-\frac{46350\,{\rm K}}{T_{\rm g}}\right) {\rm cm^3\,s^{-1}}, \tag{B.4}$$

$$a_4 = 3.75 \times 10^{-8} \left(\frac{T_{\rm g}}{300\,{\rm K}}\right)^{-0.5} \exp\left(-\frac{53280\,{\rm K}}{T_{\rm g}}\right) {\rm cm^3\,s^{-1}}. \tag{B.5}$$